TAMPEREEN TEKNILLINEN YLIOPISTO
TAMPERE UNIVERSITY OF TECHNOLOGY

Heli Hytti

Energy Efficient Measurement and Signal Processing for Self-powered, Lamb-wave-based Structural Health Monitoring System

Julkaisu 916 • Publication 916

Tampere 2010

Tampereen teknillinen yliopisto. Julkaisu 916
Tampere University of Technology. Publication 916

Heli Hytti

Energy Efficient Measurement and Signal Processing for Self-powered, Lamb-wave-based Structural Health Monitoring System

Thesis for the degree of Doctor of Science in Technology to be presented with due permission for public examination and criticism in Sähkötalo Building, Auditorium S4, at Tampere University of Technology, on the 12th of November 2010, at 12 noon.

Tampereen teknillinen yliopisto - Tampere University of Technology
Tampere 2010

ISBN 978-952-15-2443-1 (printed)
ISBN 978-952-15-2462-2 (PDF)
ISSN 1459-2045

Abstract

Ultrasonic waves have been applied in non-destructive testing for decades. Development of new sensors and transducers for actuating and detecting the ultrasonic guided waves has made the ultrasonic structural health monitoring more viable both technically and economically than it has been in the past. However, from both the economical and technical point of view, the wiring needed for powering the measurement system and transferring the collected data is seldom acceptable. The demand for wireless and self-powered, energy efficient systems is continuously increasing.

This thesis contributes to development of a structural health monitoring system suitable for continuous use in industrial applications. The suggested monitoring system integrates a well-known piezoelectric actuator and sensor technique for Lamb wave based defect detection with wireless data transfer, power harvesting and data analysis in an affordable manner. Low power production in the local power harvesting dominates the design of both the components and the operating principle of the integrated system.

The main contributions of this thesis are 1) specifications for a new, energy efficient measurement system, where only a few key samples are measured from the piezoelectric transducer response to ultrasonic guided waves and the response is then reconstructed from these samples, 2) repeatability analysis of the measurements and the defect indicating parameters calculated from them, and 3) enhanced defect detection and location method based on changes in variance of the response and the repeatability of defect location. The defect location method is based on the reconstruction algorithm for probabilistic inspection of defects suggested by Zhao et al. [Zha2007a] and developed further for improved function with small number of piezoelectric transducers and minimized amount of measurement data.

Preface

The work presented in this thesis was carried out at the Department of Automation Science and Engineering at the Tampere University of Technology (TUT), Finland, during the years 2006 – 2009, in co-operation with the VTT Technical Research Centre of Finland.

When I first was introduced with the idea of this "damage sense" research project back in 2004, I found it very interesting and had no idea what I was actually getting myself into. Had I known that, I would probably have been very, very afraid. It took a couple of years to get the financing for the project, so it wasn't until the spring of 2006 we got to start the actual work. Rather soon I found myself up to my neck in the swamp of challenging questions like, "what on Earth have I gotten myself into" and "what are these Lamb waves, anyway?" But, luckily enough, we can only see a couple of steps ahead instead of the whole mess, and one by one the questions found their answers, until my colleagues at VTT and I were able to put together our first version of a self-powered, energy efficient Lamb wave based structural health monitoring system.

I would like to express my gratitude for fruitful co-operation to my fellow researchers at the VTT: project manager, M.Sc. Mikko Lehtonen, and researchers M.Sc. Tatu Muukkonen, M.Sc. Henrik Huovila, M.Sc. Klaus Känsälä, M.Sc. Marko Korkalainen and M.Sc. Kalle Määttä. I also want to thank my supervisor, Prof. Risto Ritala, for his valuable comments, suggestions and constructive criticism considering the manuscript of this thesis. My colleagues in the former Institute of Measurement and Information Technology I thank for the open exchange of professional knowledge, as well as the refreshing albeit sometimes (if not usually) absurd coffee break conversations, which in their part make our little community so fun to work in.

I would like to thank the reviewers, Prof. Keith Worden (University of Sheffield, U.K.) and Prof. Erkki Ikonen (Aalto University School of Science and Technology), for their constructive comments and suggestions, which helped me to greatly improve this thesis.

Significant funding and support for the research project related to this thesis have been obtained from the Finnish Funding Agency for Technology (Tekes), FY Composites Oy, Metso Paper Oy, Wärtsilä Oy, and Finnish Air Force. The financial support of the Paper Manufacturing Graduate School is also gratefully acknowledged.

Finally, I am happy to say that there is neither need, nor reason for me to apologise to my family for neglecting them during this project (I checked with them). Ari and Anna, I love you both very much. These past few years have been very hard for us as a family, but with Lord's help we have kept going, day by day, and we still will. And Ari, this work would have been very much harder for me, had you not been willing to take loving care of our little angel at home, even though it has not always been a very easy job.

Psalm 23: A Psalm of David.
"The Lord is my shepherd; I shall not want. He makes me to lie down in green pastures; He leads me beside the still waters. He restores my soul; He leads me in the paths of righteousness For His name's sake. Yea, though I walk through the valley of the shadow of death, I will fear no evil; For You are with me; Your rod and Your staff, they comfort me. You prepare a table before me in the presence of my enemies; You anoint my head with oil; My cup runs over. Surely goodness and mercy shall follow me All the days of my life; And I will dwell in the house of the Lord Forever." (NKJV)

Tampere, September 2010

Heli Hytti

Contents

List of Symbols

a	piezoelectric wafer active sensor (PWAS) radius
A_i	area of surface i
c_G	group velocity of Lamb wave
c_L	velocity of longitudinal wave
c_P	phase velocity of Lamb wave
c_R	velocity of Rayleigh wave
c_T	velocity of transverse wave
$\mathbf{C}, C_{ijkl}$	elastic constant tensor a.k.a. stiffness matrix
d	half-thickness of a plate
δ_{ij}	Kronecker's delta
Δ	dilatation
e	Neper's number
$\mathbf{e_i}$	unit vector in direction x_i
E_i	Young's modulus in x_i direction
$\boldsymbol{\varepsilon}$	strain tensor
ε_{ii}	normal strain in x_i direction
ε_{ij}	shear strain in the plane $x_i - x_j$
f	frequency
f_c	centre actuation frequency
f_i	body force in direction i
ϕ	scalar potential
G_{ij}	shear modulus in the plane $x_i - x_j$
h	height
$H_k(x)$	cubic Hermite basis function k
i	imaginary unit
J_i	Bessel function of order i

k	wave number
k_f	wave number in fluid
k_L	longitudinal wave number
k_R	Rayleigh wave number
k_T	transversal wave number
$\mathbf{L}$	transformation matrix
λ	Lamé constant (Lamé's first parameter) for the material; also wavelength
μ	Lamé constant (Lamé's second parameter) for the material
$\mathbf{n}$	unit vector normal to a plane; also wave propagation direction
ν	Poisson's ratio for isotropic material
ν_{ij}	Poisson's ratio in the plane $x_i - x_j$
$\mathbf{r}$	position vector
ρ	density for the material; also correlation coefficient
$\boldsymbol{\sigma}$	stress tensor
σ^2	variance
σ_{ii}	normal stress in x_i direction
σ_{ij}	shear stress in the plane $x_i - x_j$
t	time
$\mathbf{T_n}$	traction
$\mathbf{u}$	displacement vector
u_i	displacement in x_i direction
$\nabla\mathbf{u}$	displacement matrix
V	volume
V_p	peak voltage
$\boldsymbol{\omega}$	rotation tensor
ω	angular frequency
$\boldsymbol{\psi}$	vector potential

List of Abbreviations

ACESS	Acellent Smart Suitcase^{TM}
A/D	Analog-to-Digital
ANN	Artificial Neural Network
AWR	Autonomous Wireless Receiver
AWT	Autonomous Wireless Transmitter
CWT	Continuous Wavelet Transform
DFT	Discrete Fourier Transform
EMAT	Electromagnetic Acoustic Transducer
EUSR	Embedded Ultrasonic Structural Radar
FFT	Fast Fourier Transform
FPSLIC	Field Programmable System Level Integrated Circuit
FRF	Frequency Response Function
LLW	Leaky Lamb wave
NDT	Non-Destructive Testing
PCA	Principal Component Analysis
PVDF	Polyvinylidene fluoride
PWAS	Piezoelectric Wafer Active Sensor
PWVD	Pseudo Wigner-Ville Distribution
PZT	Led-Zirconium-Titanate ceramic
RAPID	Reconstruction Algorithm for Probabilistic Inspection of Defects
RF	Radio Frequency
RMS	Root Mean Square
SH	Shear Horizontal
SHM	Structural Health Monitoring
S/H	Sample and Hold
STFT	Short-Time Fourier Transform
SVM	Support Vector Machine
TOF	Time of Flight

WPAN	Wireless Personal Area Network
WVD	Wigner-Ville Distribution

1. Introduction

1.1 Structural health monitoring vs. non-destructive testing

The modern developed world depends heavily on a complex and extensive system of infrastructure (roads, bridges, sewers, buildings) and technology (transportation, factories, mills etc.). Examples of critical structural components requiring careful condition monitoring are support structures in bridges and buildings, rails, crane booms, bearings in rotating machines and fuselage joints. Without satisfactory inspection and monitoring of these kinds of critical structural components, the problems may not become apparent until they are in extreme need of repair. Unnoticed deterioration in critical structures may lead to disastrous results, or at least to expensive replacements or reconstruction projects.

If it is not possible to inspect the integrity of any given structure visually, non-destructive testing (NDT) has traditionally been used for inspection. NDT generally refers to a one-time assessment of the condition of materials in the structure using equipment external to the structure, for example ultrasonic, acoustic emission or eddy current measurements or X-ray or thermographic imaging [Sta2004]. Inspecting large structures takes generally a long time and can only be carried out during maintenance breaks.

Emergence of new materials and innovative structures as well as the development in sensors, data acquisition systems, communication technology and data processing has lead to increasing application of structural health monitoring (SHM) systems [Giu2008a]. SHM is a non-destructive, in-situ structural evaluation method that uses several types of sensors, embedded in or attached to the structure. SHM inspects continuously or repeatedly, during the normal operation, the condition of the structure or its key components based on the response of various types of loads. The benefits of the SHM are based on the fact that it reduces maintenance costs and extends the life span of the structure. SHM is applied in structures that are difficult or otherwise not practical to access using conventional non-destructive testing methods. It also addresses the problem of aging structures, which is a major concern of the engineering community.

Today, different SHM techniques are applied for example in civil infrastructures [Cha2003, Muf2008], offshore wind energy plants [Fri2008], wind turbines [Chi2008], loadings of a hull [Kid2002] and ship joints [Her2005]. SHM techniques are also strongly emerging in aircraft integrity monitoring [Sta2004, Giu2008b].

References to the relevant literature based on extensive survey concerning this field of research to date are made throughout the thesis.

1.2 Guided waves and their applications to structural health monitoring

Guided waves are electromagnetic or acoustic waves that require a boundary as well as a source of energy for their existence. Examples of guided waves are surface waves (Rayleigh waves), Lamb waves and interface waves.

In 1885, the English physicist John William Strutt, 3rd Baron Rayleigh showed theoretically that waves can be propagated over the plane boundary between an elastic half-space and a vacuum or sufficiently rarefied medium (for example, air). The amplitude of the waves decays rapidly with depth, penetrating only to a depth of about one wavelength [Ray1885]. These waves, known now as Rayleigh or surface waves, comprise the principal type of wave observed in earth tremors. In ultrasonic range, the Rayleigh waves can be used in the detection of surface and near-surface defects in different materials. Propagation velocity of the Rayleigh waves is independent on frequency.

Another type of elastic waves that has found applications in ultrasonic testing is the Lamb wave, first described by English mathematician Horace Lamb in 1917 [Lam1917]. Lamb waves propagate in a solid plate or layer with free boundaries. The wave displacements occur both in the direction of wave propagation and perpendicularly to the plane of the plate. Propagation velocity of the Lamb waves depends on the product of frequency and plate thickness. The overall character and behaviour of the Lamb waves is much more complicated than those of Rayleigh waves, but the advantage of Lamb waves in monitoring the structural integrity is that they cover the entire thickness of the material, not just the surface [Vik1967]. Lamb waves also travel long distances with little attenuation.

Ultrasonic waves have been applied in non-destructive testing for decades. In thin-wall structures, like metallic plates or composite laminates used for example in aircrafts, hulls, or windmill propeller blades, actuating an ultrasonic wave into the structure results in guided waves. One of the major limitations in transforming Lamb-wave NDT techniques into SHM methodologies has been the bulky size and high cost of the conventional NDT transducers. Permanent installation of conventional NDT transducers onto a structure is not feasible. Development of new sensors and transducers, for example piezoelectric wafer active sensors (PWASs), for actuating and detecting the guided waves, has made the ultrasonic SHM more viable both technically and economically.

1.3 Research problem

Aerospace, civil, and mechanical engineering industries are using more and more optimized structural solutions. The main goal is to achieve required structural loading capacity with the lightest and most energy efficient solutions possible, yet avoiding to overdimension the structures. Ensuring the reliability of the structure in even unexpected loading situations is thus very important, and deterioration of structural health and its significance needs to be detected and evaluated in the earliest possible state.

One part of the structural optimization is the increasing use of composite materials. Composites offer advantages such as low weight, corrosion resistance, high fatigue strength, and faster assembly. Composites are used as materials ranging from making aircraft structures to medical equipment, and space vehicles to home building. However, there are also some limitations and drawbacks in using composites instead of metals. For example, composites do not have a high combination of strength and fracture toughness compared to metals. For this reason, e.g. in commercial airlines, the use of composites is generally limited to secondary structures such as rudders and elevators made of graphite/epoxy for the Boeing 767 and landing gear doors made of Kevlar–graphite/epoxy. Composites are also used in panels and floorings of airplanes [Kaw2006]. Lamb waves have been found to be suitable for inspecting the integrity of composite structures as well as metallic structures.

The new, progressive structures need to be equipped with an embedded “sense” for observing the loading and defect status of the structure and a control and decision making system supporting it. This “defect sense” should provide all information needed for evaluating the significance of the defect, such as the information about defect existence, its size, location, and growth rate. From both the economical and technical point of view, wiring needed for powering the measurement system and transferring the collected data is seldom acceptable. The demand for wireless and self-powered, energy efficient systems is continuously increasing.

The research problem to which this thesis contributes is to develop a structural health monitoring system suitable for continuous use in industrial applications. The suggested monitoring system integrates piezoelectric actuator and sensor technique for Lamb wave based defect detection with wireless data transfer, power harvesting, online data check and analysis in an affordable manner. Low power production in the local power harvesting dominates the design of both the components and the operating principle of the integrated system [Muu2008].

Research groups around the world are working on wireless and self-powered, energy efficient SHM systems. During this research project, for example Zhao et al. [Zha2007a,b] and Lallart et al. [Lal2008] introduced their suggestions for integrated, wireless and self-powered structural health monitoring schemes, which are described more closely in Chapter 5.4 along with comparisons to the system developed in this research project.

1.4 Energy harvesting methods

Energy autonomous devices without external power supply wires can be classified as follows:

- A self powered device: electric energy is harvested from some physical phenomenon in the environment of the device.
- A wirelessly powered device: A transmitter sends the energy to a receiver via means of light, magnetic field, radio waves, etc.

- A generator powered device: Energy generator includes structures that have been constructed for instance between moving and stationary parts of a machine for generating electric energy.
- A power storage powered device: Includes batteries, super capacitors, fuel cells, etc.

The ultimate goal in applying energy autonomous sensors and devices is to achieve a totally maintenance free all-wireless system without battery replacement or recharging that is also easy to install. In the research project to which this thesis contributes, the intended system application targets were e.g. mobile vehicles and rotating machines. For these kinds of application targets, the self-powering of the device is the optimal solution.

The most common energy converters for energy harvesting are based on

- Photovoltaics (solar cells)
- Thermoelectricity (e.g. Seebeck/Peltier elements, pressure/temperature converters)
- Electromechanics (e.g. electromagnetic/electrostatic/piezoelectric vibration converters, gyroscopic converters)
- Electromagnetism (magnetic/electric/RF field converters)

1.4.1 Photovoltaics

Photovoltaic conversion is the direct conversion of sunlight into electricity with no intervening heat engine. Photovoltaic devices are simple in design and require very little maintenance. They can be constructed as standalone systems to give outputs from microwatts to megawatts. Photovoltaic devices have been used as the power sources from calculators to satellites and even megawatt-scale power plants [Gos2007].

The main constraint on the efficiency of a solar cell is related to the band gap of the semiconductor material of a photovoltaic cell. A photon of light with energy equal to or greater than the band gap of the material is able to free-up one electron when absorbed into the material. However, the photons that have energy either less or more than the band gap are not useful for this process. When absorbed on the cell, they end up to produce heat. These reasons account for a theoretical maximum limit on the efficiency of a conventional single-junction photovoltaic cell to less than 25%. The actual efficiency is even lower because of reflection of light from the cell surface, shading of the cell due to current collecting contacts, internal resistance of the cell, and recombination of electrons and holes before they are able to contribute to the current.

At present, photovoltaic module efficiencies are as high as 15-20% [Lew2007]. Recently a team of scientists from the California Institute of Technology has created a new type of flexible solar cell that enhances the absorption of sunlight. The silicon wire arrays created in the research project are able to convert between 90 and 100 percent of the photons they absorb into electrons [Kel2010].

Applicability of photovoltaic energy harvesting in indoor industrial applications is limited. Although photovoltaics can produce 100 mW/cm^2 in direct sunlight, they produce only about 100 μW/cm^2 in a typically illuminated office, and even less in a dim environment [Pri2009].

1.4.2 Thermoelectricity

Thermoelectric energy harvesting utilizes the heat energy flow between some objects with temperature difference. A fraction of the heat flow through a thermoelectric element is converted to electric energy. Even with large heat flow, however, the extractable power is typically low due to low Carnot and material efficiencies. In addition, limited heat availability will also limit the power produced. The efficiency of a thermoelectric generator increases nearly linearly with temperature difference. In energy harvesting applications, where the temperature difference ΔT is small the efficiency is almost directly proportional to the ΔT across the thermoelectric. For good bismuth telluride devices, the efficiency is approximately 0.04% for each 1K of ΔT [Pri2009].

Typical thermoelectric generator is a matrix of thermoelectric couples consisting of n-type and p-type semiconductor elements. The elements are connected electrically in series and thermally in parallel. When connected between objects with different temperatures, heat flows through the thermoelectric element and a small voltage is generated at every semiconductor block. Those blocks are connected in series to create a voltage with a practical voltage level.

An electronic controller is needed for controlling the electric loading of the element and to convert the voltage to a practical level. Typically the output voltage levels, especially with smaller temperature differences, are low, less that 1V. A boost converter is needed for increasing the voltage level to practical supply voltage levels.

1.4.3 Electromechanics

Electromechanical energy harvesting is based on converting ambient vibration into electrical energy. For example, large machines and mobile vehicles can act as vibration sources. Typical machine vibration spectrum consists of spikes on some harmonic frequencies, and a wide band base vibration. Depending on the device the frequency of the spikes can also vary for instance as a function of motor speed.

The basic principle on which almost all electromagnetic generators are based is Faraday's law of electromagnetic induction. In most linear vibration generators, the motion between the coil and the magnet is in a single direction, and the magnetic field is produced by a permanent magnet and has no time variation. Power is extracted from the generator by connecting the coil terminals to a load resistance and allowing a current to flow in the coil. This current creates its own magnetic field which acts to oppose the field giving rise to it. The interaction between the field caused by the induced current and the field from the magnets gives rise to a force which opposes the motion. It is by acting against this electromagnetic force that the mechanical energy is transformed into electrical energy [Pri2009].

The electromagnetic force is proportional to the current and hence the velocity and is expressed as the product of an electromagnetic damping and the velocity. In order to extract the maximum power in the form of electrical energy, an important goal for the design of a generator is the maximization of the electromagnetic damping.

Most of the present energy harvesting devices operate in narrow band mode. They use a mass spring resonant principle, which enables efficient energy harvesting at a predefined vibration frequency (mechanical resonator) [Pri2009]. In the case of wide band vibration the resonance frequency have to be adjusted to one of the higher frequency spikes. The rest of the vibration will be left unharnessed. Another option for broadband vibrations that has been researched is to use piezoelectric energy harvesting [Adh2009, Pri2009]. The amount of generated power varies greatly between the devices demonstrated by the year 2009. Normalized power, i.e. the stated power output of the device normalized to 1 m/s^2 acceleration, varies between $2 \cdot 10^{-6}$ and 16000 [Pri2009]. However, the comparison of normalized power is not nearly enough for selecting a generator for a specific application, since it ignores frequency (which is governed by the application) and it does not reflect the bandwidth of the generator. In practice, the bandwidth of a device is as an important consideration as peak power output in determining the suitability of a generator for a given application.

1.4.4 Electromagnetism

Electric and magnetic fields emitted by power wires can be utilised in energy harvesting of nearby sensors. This can be applied e.g. in condition monitoring of power plants, power grids and power transmission systems.

Capacitive energy harvesters such as in [Zhu2008] can be formed by putting a harvesting plate into electric field around a high-voltage terminal. The plate becomes a capacitive divider between the high-voltage terminal and the environment that is connected to the ground potential or to different phase high voltage. Thus, energy can be harvested from the voltage between the plate and the ground or from the voltage between the plate and the high-voltage terminal. Because of the low operating frequency (50/60 Hz), the source impedance of the terminal is very high. For this reason, an AC/DC converter circuit with high input voltage (hundreds or even thousands volts) is needed between the harvesting plate and the application payload.

Inductive energy harvesters based on Faraday's law of electromagnetic induction can be formed by putting a harvesting toroidal coil around a high-current wire. Because of the low operating frequency (50/60 Hz), the terminal voltage and the source impedance of the harvesting coil are typically low. This sets special demands to the AC/DC converter between the harvesting coil and the application payload, which has to be able to operate with remarkably low input voltages [Zhu2009].

1.5 Hypothesis

In present SHM applications based on Lamb waves, signal analysis generally requires both acquiring a large number of data samples and relatively high computational capacity. This makes the wireless and self-powered operation of the SHM systems difficult. The hypothesis of the thesis is that it is possible to develop a small-sized, self-powered, energy efficient Lamb wave based SHM system with minimized data sampling and energy efficient signal analysis for challenging applications in e.g. mobile vehicles or rotating machines.

1.6 Contribution

The results presented in this thesis are the outcome of a co-operation project between VTT Technical Research Centre of Finland and Tampere University of Technology. The energy harvester element was designed and implemented at VTT. The final prototype measurement board was designed and implemented at VTT according to the measurement specifications set by the author.

The main contributions of this thesis are as follows:

- Analysis of repeatability and defect detection applicability of peak-to-peak voltage, variance and correlation coefficient calculated from piezoelectric wafer active sensor (PWAS) responses to Lamb wave modes in thin (1 mm) and thick (10 mm) aluminium plates. Repeatability is a property unique to each measurement system and should be studied for determining the defect detection thresholds values for each statistical parameter.
- Presentation of a new, energy efficient Lamb wave based SHM system, where only a few key samples are measured from the PWAS response to Lamb waves, and the response is then reconstructed from these samples. Compared to using a high sampling rate which in general is a necessary requirement for measuring high-frequency signals, energy is saved both in measuring and transmitting data. The precise contribution of the author to the development of the system is described in Chapter 5.3.
- Comparison of statistical parameters estimated from a reconstructed response and from a reference response measured at high sampling rate showing the reliability of the reconstruction method.

- Enhanced defect detection and location method based on changes in variance of the PWAS response. Defect location method is based on the reconstruction algorithm for probabilistic inspection of defects suggested by Zhao et al. [Zha2007a] and developed further for improved function with small number of PWASs. The repeatability of locating the defects with this method is also analysed.

1.7 Structure of the thesis

The structure of the thesis is divided in four parts. In Chapter 2, the research problem and the experimental setup are presented. In Chapters 3-4, the properties and the behaviour of the guided, in particular Lamb waves in isotropic media are reviewed to the extent relevant to understanding the principles and problematics of guided wave based SHM.

The properties of the elastic waves in any solid material depend on the elastic properties of the material, e.g. its order of material symmetry. In composite laminates, these properties may vary from layer to layer. Chapter 3 reviews the theory considering deformations in elastic solids, including the tensor transformations in coordinate system rotations required for calculating the Lamb wave mode propagation velocities in a composite laminate.

Chapter 4 reviews the theory of ultrasonic waves in single-layer, isotropic media. The stress-free boundary conditions determine the type of ultrasonic waves that can propagate in a structure. In plate-like structures, these are Lamb waves and shear horizontal waves. The number of Lamb wave modes existing in a structure, as well as the physical properties of those modes, depends on the elastic properties of the structure, its dimensions, and the applied actuation frequency. The PWAS based Lamb wave actuation and detection technique is also reviewed, including the mode selective actuation theory and the PWAS sensitivity with respect to the Lamb wavelength. This relatively extensive theoretical background is needed for understanding the characteristics of the Lamb waves in different materials and their interaction with discontinuities (defects) in a structure. The theory is the foundation for optimizing the measurement and signal analysis methods for defect detection.

In Chapter 5, the energy efficient measurement method utilizing signal reconstruction is presented. Chapter 6 is a review of signal analysis methods applied in Lamb wave based

SHM. It also includes the presentation of an enhanced defect location method. In Chapter 7, the repeatability and defect indication capability of some statistical signal parameters are studied, and the applicability of the suggested energy efficient method is verified by comparing the analysis results calculated from the reconstructed signal with those calculated from a reference signal.

2. Research problem and experimental set-up

The fundamental goal of structural health monitoring is to detect incipient defects in structures before they cause any problems. In addition to detecting the existence of a defect, its location, size and rate of growth are of interest. The goal of the research project to which this thesis contributes was to develop a self-powered structural health monitoring system suitable for continuous use in industrial applications. The requirements for the final system were as follows:

- energy efficiency
- piezoelectric actuating and sensing of Lamb waves
- simple actuation burst generation
- minimized data sampling
- wireless data transfer
- self-powering through power harvesting
- detecting and locating defects through efficient signal analysis

Low power production in the local power harvesting sets the guidelines for the design of this integrated system [Muu2008]. When designing defect detection based on the propagation of Lamb waves the key question is which parameters to extract from the measurements so that the existence, type, severity and location of defect are indicated with required accuracy and reliability. In practice the design is a trade-off between reliability and computability when the energy available for accessing data and computing the defect information is constrained.

Theoretical study of the Lamb wave properties and the results of experiments described below were used for

- selecting an actuation burst that is energy efficient to generate and results in a PWAS response suitable for defect detection
- deciding what are the key features of the Lamb wave response for minimizing the number of measured data samples and for reconstructing the response from these samples for further analysis

- determining the computationally most energy efficient parameters estimated from the Lamb wave response that can be used to indicate existence of a defect and their repeatability in different structures
- enhancing a correlation-based defect location algorithm presented by Zhao et al. [Zha2007a] for improved operation with small number of PWASs.

A commonly used setup for experimenting with the defect detection using guided waves is first to attach actuators and sensors to a structure with a simple geometry, e.g. metallic or composite plates or beams, before proceeding to more complex geometries and actual application targets, e.g. aircraft wings [Lan2007, Lu2006, Lee2003, Wan2007, Yan2005, Ng2009]. These kinds of simple geometries are also practical cases for simulations.

The work was started with studying the Lamb wave propagation in different test structures with simple geometries. Several laboratory experiments were made in order to study the Lamb wave behaviour together with piezoelectric actuation and sensing technique. The starting point of the study was the need to locate defects in both thin and thick metallic structures as well as in different composite structures. The measurement system used in the experiments was Acellent Smart Suitcase^{TM} (ACESS) SCS-3200. ACESS SCS-3200 system is a measurement computer equipped with CompuGen 1100 (CG1100) arbitrary waveform generator board, CompuScope 1450 (CS1450) data acquisition board, amplifiers and measurement and analysis software for PWAS based SHM [Ace2009, GaG2009]. The representative specifications of CG1100 and CS1450 boards are listed in Tables 1 and 2.

The main limitations of the ACESS SCS-3200 system are incapability of pulse-echo type measurements and crosstalk between the signal generator board and data acquisition board. The latter feature causes the actuation signal burst to show in the measured response. The actuation burst duration is $T = n/f_c$ where n is the number of periods in the burst and f_c is the actuation frequency. If T exceeds the time of arrival of the fastest Lamb wave modes at the sensor, their effect on the response is buried under the actuation burst. This sets a lower limit to actuation frequency that can be used in each measurement case.

Table 1. Representative specifications of CG1100 board

Output	1 per card
Amplitude	10Vp-p into 50Ohm, 20Vp-p into 1KOhm
Resolution	12 bits
Accuracy	±2% excluding offset
Conversion Rates	80MHz, 40MHz, 20MHz, ...
Output Frequency	61 uHz to 10 MHz
Buffer Depth	1 Million samples
Full Scale Output Range	±100mV, ±200mV, ±500mV, ±1V, ±2V, ±5V

Table 2. Representative specifications of CS1450

Inputs per card	2, Channel A and B
Resolution	14 bits
Bandwidth	25 MHz
Abs. Max Amplitude	±5 Volts (continuous), ±15 Volts (for 1 msec)
DC Accuracy	±0.5% of full scale
Sampling Rate (Single Ch.)	50 M Samples/sec max, 1 KS/sec – 50 MS/sec.
Sampling Rate (Dual Ch.)	25 M Samples/sec max., 1 KS/sec – 25 MS/sec.
Memory Depth	1 Million 14-bit samples

The piezoelectric sensors used in the experiments were disc-shaped, 0.25 mm thick, with a diameter of 6.35 mm, and made of APC 850 material [APC2009].

Test plate 1 was a 500 mm × 500 mm, 1 mm thick aluminium plate. Four piezos were attached to it symmetrically, 150 mm from the plate edges (Figure 1a). Test plate 2a was a 10 mm thick aluminium plate with the same size as plate 1. In this plate, the four piezos were attached slightly unsymmetrically so that one of them was only 100 mm from one edge (Figure 1b). Test plate 2b is geometrically identical to plate 2a. The Lamb wave responses from these plates were compared in order to study the effect of PWASs contact to the plate on the response. It is very difficult to make the fastenings of the PWASs to the structure surface identical, and even very small differences in fixing agent layer thickness and spread across the PWAS surface result in differences between the actuating and sensing functions of different

PWASs. Therefore the intact structure reference measurement from each signal path between the PWASs has to be kept in store. One attempt to create reference-free SHM system for an isotropic material was presented in [Ant2008]. The idea there was to use several identical signal paths between PWAS pairs and compare the responses measured from them at each round of measurements. However, making the responses identical required several rounds of detaching and replacing the PWAS sensors until their contacts to the structure surface were identical. This is not practical or even possible in industrial applications where the sensors may be installed between composite laminates or under protective coating. The ceramic PWASs are also very fragile and once they are fastened to a surface, they can not be detached without breaking them.

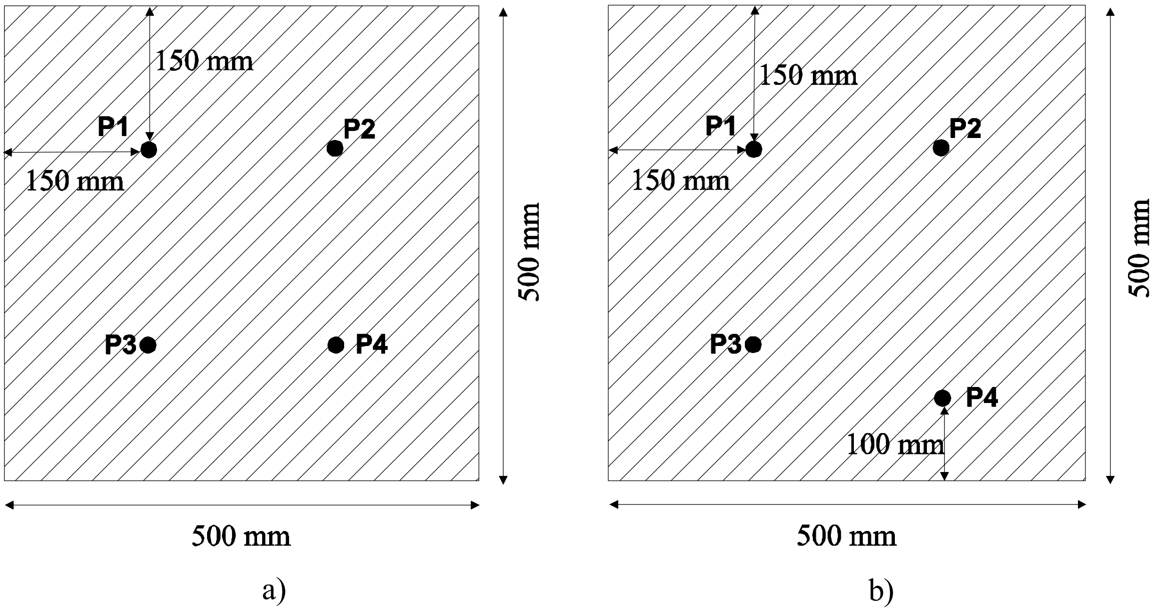

Figure 1. Experimental setups.

a) Test plate 1: 1 mm aluminium plate, b) Test plate 2: 10 mm aluminium plate.

The Lamb wave responses were first measured from an intact plate between every possible actuator-sensor pair using the pitch-catch technique. For system repeatability study, the first measurements were repeated 50 times consequently. Repeatability is a measure of variation in results when the measurements are repeated with the same equipment within a short period of time. It is important to know the repeatability of the Lamb wave response when the structure is intact, in order to be able to separate changes induced by defects from normal variation. In later experiments, average of 5 repeated measurements was taken. Also the effect of actuation burst shape on the measured response was studied.

For defect detection experiments, both test plates were then damaged by drilling a hole into them. The locations of the defects are shown in Figure 2. The diameter of the defect was increased as follows: 1 mm – 2 mm – 3 mm – 5 mm – 10 mm. The Lamb wave responses from every signal path were measured again after each step.

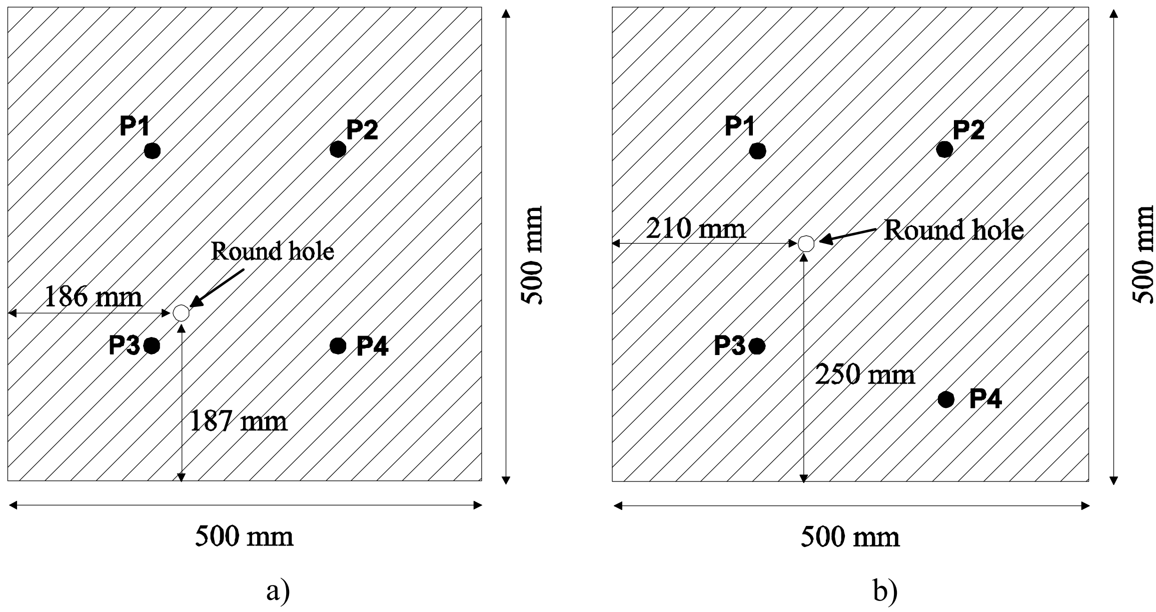

Figure 2. Location of defects in the test plates. a) Test plate 1, b) Test plate 2.

Test plate 2 was later damaged further by adding another 10 mm hole to it for testing the measurement system prototype developed in this project. The system is described in Chapter 5.

Test plate 3 was a 800 mm × 800 mm, 1 mm thick aluminium plate. Six piezos were attached to it as shown in Figure 3a. Piezos P3b and P4b were used for testing pulse-echo type measurements such that P3-P3b and P4-P4b formed an actuator-sensor pair. Again, the responses from each signal path were first measured in an intact plate. Then the plate was damaged with a knife blade, causing a crack of size 1 mm × 10 mm, and the measurements were repeated.

The effect of using SMART Layer® instead of separate piezos was tested with a 800 mm × 800 mm, 1 mm thick aluminium plate shown in Figure 3b (test plate 4). SMART Layer® is a thin dielectric film with an array of durable, networked piezoelectric sensors, which are of the same type as the separate piezos used in the other test plates [Ace2009]. The sensors were located 337 mm from the plate edges. The responses from each signal path were measured only in an intact plate.

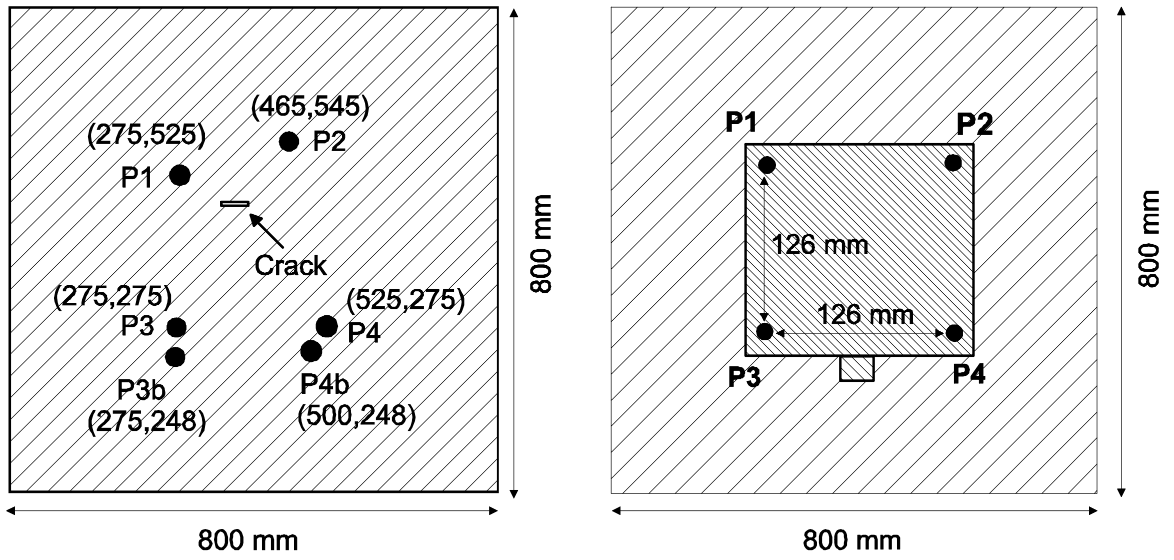

a) b)

Figure 3. a) Location of the piezos and the defect in test plate 3, b) Location of the SMART Layer® piezos in test plate 4.

In the above test cases, the size of the defect was relatively large, considering the SHM objective to detect defects in their early stage. This is due to the frequency range used in the measurements, as well as the size of the PWASs. With the frequencies used in tests, the wavelengths vary from a few millimetres to tens of millimetres, and small cracks do not affect the waves. For smaller defects, higher frequency-thickness product resulting in smaller wavelengths is needed before the waveforms are affected by the defects enough to be recognized as off-reference waveforms. Therefore, an aluminium test beam with variable width and thickness, shown in Figure 4, was used for simulating a more real-life SHM objective, detecting an initiating crack in a metallic structure. The beam was mounted on a material testing system, where it was dynamically loaded until it cracked and finally broke completely. Initiation of the crack was verified using eddy current measurement, before it was visible to the eye. Lamb wave measurements were repeated between the loading cycles.

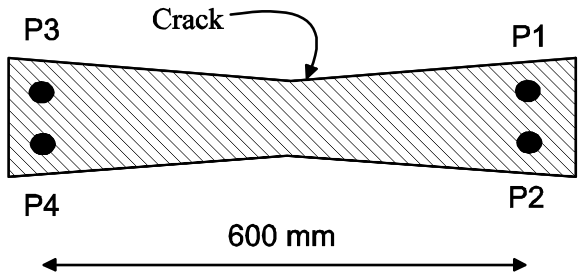

Figure 4. Aluminium test beam with variable thickness.

MATLAB® [Mat2009] and related toolboxes: Wavelet Toolbox, Signal Processing Toolbox, Time-Frequency Toolbox [TFT2008] and DiscreteTFDs [TFD1999, O'Ne1998] were used for mathematical analysis and algorithm implementation in this thesis. MATLAB® programs for calculating and plotting the phase and group velocity dispersion curves and particle direction plots for different wave types were implemented by the author.

3. Deformations in elastic solids

This chapter reviews tensor calculus relevant to the thesis. Many physical quantities are naturally regarded as correspondences between two sets of vectors. Such quantities are examples of tensors [Kol2002]. The tensors needed in analysing the deformation in elastic solids are strain, stress and elastic constant tensor, also known as stiffness matrix.

Mathematically tensors are defined as a set of functions of the coordinates of any point in space that transform linearly between coordinate systems [Kun2003]. For a three dimensional space there are 3^r components, where r is the rank. A tensor of zero rank is a scalar, of rank one, a vector, and of rank two, a matrix.

3.1 Displacement, stress and strain

When a force is applied to a solid body, the body is deformed. Let us consider two points, P and Q in the reference state (R) of the body (Figure 5). After deformation they are in positions P* and Q*. Displacement of points P and Q are denoted by vectors **u** and **u** + **du**, respectively. Position vectors for P, Q, P* and Q* are **r**, **r** + **dr, r*** and **r*** + **dr***, respectively. Displacement and position vectors are related as follows:

$$\begin{aligned}&\mathbf{r}^* = \mathbf{r} + \mathbf{u}\\ &\mathbf{r}^* + \mathbf{dr}^* = \mathbf{r} + \mathbf{dr} + \mathbf{u} + \mathbf{du}\\ &\therefore \mathbf{dr}^* = \mathbf{dr} + \mathbf{du}\end{aligned} \tag{1}$$

Divided into Cartesian components, Eq. (1) can be written as

$$\left(dx_1^*\mathbf{e_1} + dx_2^*\mathbf{e}_2 + dx_3^*\mathbf{e}_3\right) = \left(dx_1\mathbf{e_1} + dx_2\mathbf{e}_2 + dx_3\mathbf{e}_3\right) + \left(du_1\mathbf{e_1} + du_2\mathbf{e}_2 + du_3\mathbf{e}_3\right) \tag{2}$$

where $\mathbf{e_1}$, $\mathbf{e_2}$ and $\mathbf{e_3}$ are unit vectors in x_1, x_2 and x_3 directions, respectively.

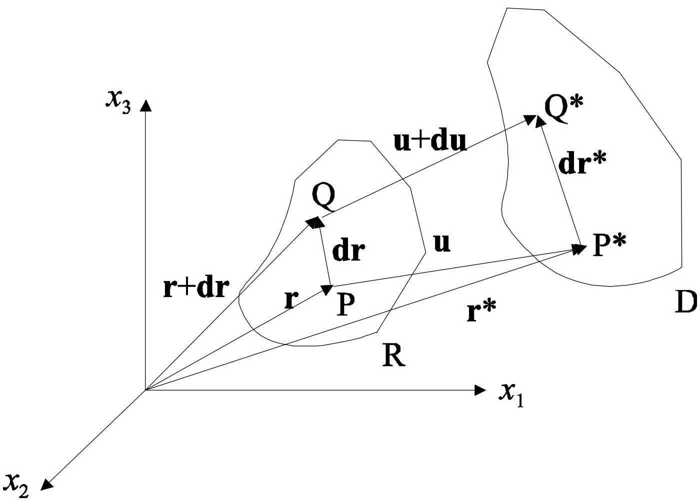

Figure 5. Deformation of a body.

In tensor notation this is

$$\sum_{i=1}^{3} dx_i^* = \sum_{i=1}^{3}\left(dx_i + du_i\right) \tag{3}$$

Applying the chain rule into Eq. (3) gives

$$\sum_{i=1}^{3} dx_i^* = \sum_{i=1}^{3}\left(dx_i + \frac{\partial u_i}{\partial x_1}dx_1 + \frac{\partial u_i}{\partial x_2}dx_2 + \frac{\partial u_i}{\partial x_3}dx_3 \right) = \sum_{i=1}^{3} dx_i + \sum_{i,j=1}^{3}\frac{\partial u_i}{\partial x_j}dx_j \tag{4}$$

In matrix form, Eq. (4) can be written as

$$\mathbf{dr^*} = \mathbf{dr} + \left(\nabla\mathbf{u}\right)^{\mathrm{T}}\,\mathbf{dr} \tag{5}$$

where $\mathbf{dr} = \left[dx_1, dx_2, dx_3\right]^{\mathrm{T}}$ and $\nabla\mathbf{u}$ is the gradient of vector $\mathbf{u}$. The displacement matrix $\nabla\mathbf{u}$ can be presented as a sum of symmetric matrix $\boldsymbol{\varepsilon}$ and antisymmetric matrix $\boldsymbol{\omega}$ where

$$\varepsilon_{ij} = \frac{1}{2}\left(\frac{\partial u_i}{\partial x_j} + \frac{\partial u_j}{\partial x_i}\right), \quad \omega_{ij} = \frac{1}{2}\left(\frac{\partial u_i}{\partial x_j} - \frac{\partial u_j}{\partial x_i}\right) \tag{6}$$

Then Eq. (5) takes the form

$$\mathbf{dr}^* = \mathbf{dr} + \boldsymbol{\omega}^{\mathrm{T}}\mathbf{dr} + \boldsymbol{\varepsilon}^{\mathrm{T}}\mathbf{dr} \tag{7}$$

The second term in Eq. (7) represents the rigid rotation about the translated point (rotation tensor). The third term represents the deformation of the material and is called the strain tensor.

Each diagonal term of the strain tensor matrix ($i = j = 1$, 2 or 3) has the significance of compressing or stretching the material into direction of one of the main axis (tensile stress). For example, $\varepsilon_{11} = \partial u_1 / \partial x_1$ is the extension per unit length in the x_1 direction.

The off-diagonal terms correspond to shear strain, which acts parallel to the surface of a material that it is acting on. For example, if an infinitesimal rectangle in the x_1-x_2 plane is subjected to shear strain, it becomes a parallelogram.

Let us now study the effect of internal forces acting on a hypothetical unit cube in an elastic material. These forces lead to deformation of the cube, which can be described by the strain tensor. Using this description, it is possible to formulate a three-dimensional equivalent of Hooke's law for a relation between the forces and the deformations.

Force per unit area on a surface is called traction. In order to define traction at a point, its three components must be given and the plane on which it is defined must be identified. The traction can be denoted as $\mathbf{T_n}$, where the superscript $\mathbf{n}$ denotes the unit vector normal to the plane on which the traction is defined. $\mathbf{T_n}$ has three components that correspond to the force per unit area in x_1-, x_2-, and x_3- directions.

Stress is similar to traction in the sense that both are defined as force per unit area. The only difference is that the stress components are defined normal or parallel to surface, while traction components may have an arbitrary direction. Traction $\mathbf{T_n}$ can be divided into two stress components: normal and shear stress, σ_{nn} and σ_{ns}. Traction on a plane and its components are shown in Figure 6.

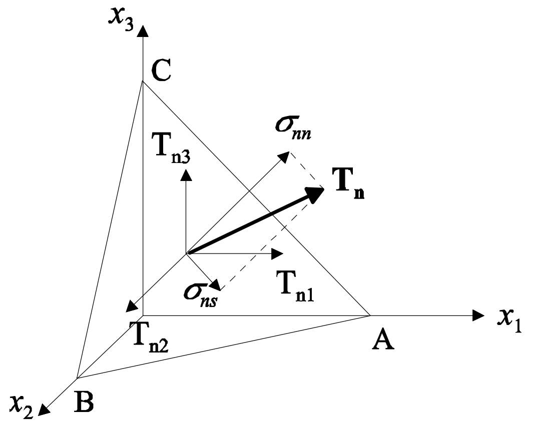

Figure 6. Traction T_n can be divided into three components T_{ni} or two components: normal and shear stress, σ_{nn} and σ_{ns}.

The normal stress component gives rise to compressive or tensile stresses, σ_{ii}, and the tangential components give rise to shear stresses, σ_{ij}. Stress tensor components are shown in Figure 7. The first subscript indicates the direction of stress value, and the second subscript indicates the normal to the plane on which the stress component is defined.

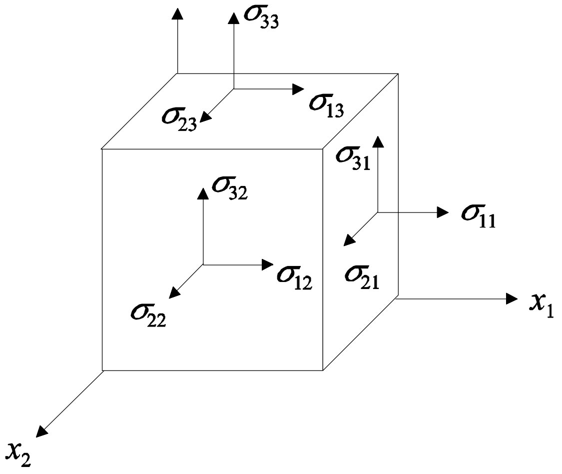

Figure 7. Stress tensor components. In σ_{ij}, *i* indicates direction of the stress and *j* indicates the normal of the plane on which the stress component is defined.

Consider the situation shown in Figure 8 where traction $\mathbf{T_n}$ is applied to the plane ABC. In static equilibrium, the sum of the forces is zero. For example in x_1 –direction,

$$\sum F_1 = T_{n1}A - \sigma_{11}A_1 - \sigma_{12}A_2 - \sigma_{13}A_3 + f_1 V = 0 \tag{8}$$

where A is the area of surface ABC, A_1, A_2 and A_3 are the areas of the other three surfaces BOC, AOC and AOB, respectively, and f_1 is the body force per unit volume (e.g. gravity) in the x_1 direction.

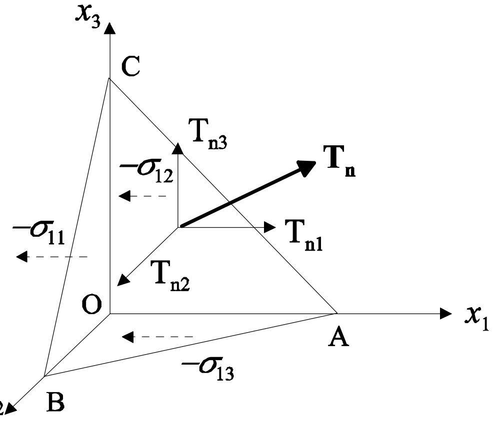

Figure 8. Traction components on plane ABC and x_1 –direction stress components on planes AOC, BOC and AOB.

Let **n** denote the unit vector normal to the plane ABC. Then $A_i = n_i A$ and $V = (Ah)/3$, where h is the height of the tetrahedron OACB measured from the apex O. The Eq. (8) can be written as

$$T_{n1} - \sigma_{11}n_1 - \sigma_{12}n_2 - \sigma_{13}n_3 + f_1 \frac{h}{3} = 0 \tag{9}$$

When the plane ABC becomes infinitesimally small, the tetrahedron height h goes to zero and Eq. (9) is simplified to

$$T_{n1} = \sigma_{11}n_1 + \sigma_{12}n_2 + \sigma_{13}n_3 = \sum_{j=1}^{3} \sigma_{1j} n_j \tag{10}$$

Traction-stress equations for x_2 and x_3 directions can be derived accordingly. Combining the results leads to

$$T_i = \sum_{j=1}^{3} \sigma_{ij} n_j \tag{11}$$

The condition of static equilibrium leads to symmetry of the stress tensor ($\sigma_{ij} = \sigma_{ji}$). The tensile stresses along any one axis must balance; otherwise the body would be accelerated. This means that there can only be three independent diagonal stresses. The shear stresses must balance in order to avoid rotation, leading to three off-diagonal stresses.

In equilibrium, also the resultant force on the body must be equal to zero. The force acting on each face of an elemental volume is the value of the stress at the centre of the face times the area of the face. For example, the forces acting in the x_1-direction on the cube in Figure 7 are those resulting from tensile stresses, and the x_1 direction projections of the shear stresses.

$$\begin{aligned}
&-\sigma_{11} dx_2 dx_3 + \left(\sigma_{11} + \frac{\partial \sigma_{11}}{\partial x_1} dx_1 \right) dx_2 dx_3 - \sigma_{12} dx_1 dx_3 + \left(\sigma_{12} + \frac{\partial \sigma_{12}}{\partial x_2} dx_2 \right) dx_1 dx_3 \\
&-\sigma_{13} dx_1 dx_2 + \left(\sigma_{13} + \frac{\partial \sigma_{13}}{\partial x_3} dx_3 \right) dx_1 dx_2 + f_1 dx_1 dx_2 dx_3 = 0 \\
&\Leftrightarrow \quad \frac{\partial \sigma_{11}}{\partial x_1} + \frac{\partial \sigma_{12}}{\partial x_2} + \frac{\partial \sigma_{13}}{\partial x_3} + f_1 = 0
\end{aligned} \tag{12}$$

If the body is subjected to a nonzero, time-dependent resultant force, then it will have acceleration $\partial^2 u_i / \partial t^2$. Calculating the corresponding forces in each direction and combining the results leads to force equilibrium equation:

$$\sum_{j=1}^{3} \frac{\partial \sigma_{ij}}{\partial x_j} + f_i = \rho \frac{\partial^2 u_i}{\partial t^2}, \quad i = 1,2,3 \tag{13}$$

where ρ is the mass density.

3.2 Elastic constant tensor

One definition for elasticity of a material is that there is one-to-one correspondence between stress and strain: each of the six components of stress is at any point a linear function of the six components of strain (Hooke's law). The coefficients of those functions are the elastic constants of the material. If this relation is linear, then the material is called linear elastic material. Thus the linear stress-strain relation is expressed through the elastic constant tensor **C**,

$$\sigma_{ij} = C_{ijkl}\varepsilon_{kl} \tag{14}$$

C is also known as stiffness matrix. In matrix form and using only independent stress and strain components, Eq. (14) is expressed as

$$\boldsymbol{\sigma} = \mathbf{C}\boldsymbol{\varepsilon} \tag{15}$$

where $\boldsymbol{\sigma} = \left[\sigma_{11}, \sigma_{22}, \sigma_{33}, \sigma_{23}, \sigma_{31}, \sigma_{12}\right]^{\mathrm{T}}$, $\boldsymbol{\varepsilon} = \left[\varepsilon_{11}, \varepsilon_{22}, \varepsilon_{33}, 2\varepsilon_{23}, 2\varepsilon_{31}, 2\varepsilon_{12}\right]^{\mathrm{T}}$ and

$$\mathbf{C} = \begin{bmatrix} C_{1111} & C_{1122} & C_{1133} & C_{1123} & C_{1131} & C_{1112} \\ C_{2211} & C_{2222} & C_{2233} & C_{2223} & C_{2231} & C_{2212} \\ C_{3311} & C_{3322} & C_{3333} & C_{3323} & C_{3331} & C_{3312} \\ C_{2311} & C_{2322} & C_{2333} & C_{2323} & C_{2331} & C_{2312} \\ C_{3111} & C_{3122} & C_{3133} & C_{3123} & C_{3131} & C_{3112} \\ C_{1211} & C_{1222} & C_{1233} & C_{1223} & C_{1231} & C_{1212} \end{bmatrix}$$

Since *ij* and *kl* go in pairs, a reduced notation is generally used for the elastic constants: $C_{\alpha\beta} \equiv C_{klij}$.

Conversion from regular indices to reduced indices is shown in Table 3.

Table 3. Conversion table from regular indices to reduced indices

α, β	ij, kl
1	11
2	22
3	33
4	23 = 32
5	31 = 13
6	12 = 21

3.3 Orders of material symmetry

Elastic constant tensor C_{ijkl} represents Hooke's law in three dimensions. Since both σ_{ij} and ε_{kl} are symmetric, also C_{ijkl} is symmetric:

$$C_{ijkl} = C_{jikl} = C_{ijlk} = C_{jilk} = C_{klij} \tag{16}$$

This symmetry property leads to general stiffness matrix having only 21 independent constants. The material that has 21 independent elastic constants (i.e. there are no relations between the elastic constants in different directions) is called an anisotropic material [Kaw2006]:

$$\mathbf{C} = \begin{bmatrix} C_{11} & C_{12} & C_{13} & C_{14} & C_{15} & C_{16} \\ C_{12} & C_{22} & C_{23} & C_{24} & C_{25} & C_{26} \\ C_{13} & C_{23} & C_{33} & C_{34} & C_{35} & C_{36} \\ C_{14} & C_{24} & C_{34} & C_{44} & C_{45} & C_{46} \\ C_{15} & C_{25} & C_{35} & C_{45} & C_{55} & C_{56} \\ C_{16} & C_{26} & C_{36} & C_{46} & C_{56} & C_{66} \end{bmatrix} \tag{17}$$

Many natural and synthetic materials possess material symmetries, i.e. their elastic properties are invariant under some rotations and/or reflections due to their microscopic structure. Such symmetries reduce the number of independent elastic constants.

If the material is invariant under reflection with respect to a plane, for example plane x_1-x_2, with direction x_3 normal to this plane, then the stiffness matrix reduces to

$$\mathbf{C} = \begin{bmatrix} C_{11} & C_{12} & C_{13} & 0 & 0 & C_{16} \\ C_{12} & C_{22} & C_{23} & 0 & 0 & C_{26} \\ C_{13} & C_{23} & C_{33} & 0 & 0 & C_{36} \\ 0 & 0 & 0 & C_{44} & C_{45} & 0 \\ 0 & 0 & 0 & C_{45} & C_{55} & 0 \\ C_{16} & C_{26} & C_{36} & 0 & 0 & C_{66} \end{bmatrix} \tag{18}$$

Such material is called monoclinic, and has only 13 independent elastic constants. An example of monoclinic material is feldspar.

If the material has three mutually perpendicular planes of material symmetry, it is called orthotropic. For orthotropic materials, the stiffness matrix is of the form

$$\mathbf{C}=\begin{bmatrix} C_{11} & C_{12} & C_{13} & 0 & 0 & 0 \\ C_{12} & C_{22} & C_{23} & 0 & 0 & 0 \\ C_{13} & C_{23} & C_{33} & 0 & 0 & 0 \\ 0 & 0 & 0 & C_{44} & 0 & 0 \\ 0 & 0 & 0 & 0 & C_{55} & 0 \\ 0 & 0 & 0 & 0 & 0 & C_{66} \end{bmatrix} \tag{19}$$

with nine independent elastic constants. Examples of orthotropic material are a unidirectional lamina with fibres arranged in a rectangular array, a wooden bar, and rolled steel.

If there is a plane of material isotropy in one of the planes of an orthotropic body, e.g. plane x_2-x_3, and direction x_1 is normal to that plane, then the stiffness matrix is

$$\mathbf{C}=\begin{bmatrix} C_{11} & C_{12} & C_{12} & 0 & 0 & 0 \\ C_{12} & C_{22} & C_{23} & 0 & 0 & 0 \\ C_{12} & C_{23} & C_{22} & 0 & 0 & 0 \\ 0 & 0 & 0 & \dfrac{C_{22}-C_{23}}{2} & 0 & 0 \\ 0 & 0 & 0 & 0 & C_{55} & 0 \\ 0 & 0 & 0 & 0 & 0 & C_{55} \end{bmatrix} \tag{20}$$

This material is called transversely isotropic with five independent elastic constants. An example of this type of material is a thin unidirectional lamina in which the fibres are arranged in a square or hexagonal array. The elastic properties in the two directions perpendicular to the fibres may be considered to be the same.

The highest order of material symmetry is isotropy. For an isotropic solid,

$$C_{ijkl} = \lambda \delta_{ij} \delta_{kl} + \mu \left(\delta_{ik} \delta_{jl} + \delta_{il} \delta_{jk} \right) \tag{21a}$$

where λ and μ are the Lamé constants for the material, derived from modulus of elasticity, $\sigma_{ii} / \varepsilon_{ii}$, and Poisson's ratio, $-\varepsilon_{jj} / \varepsilon_{ii}$. Thus the isotropic form of **C** is

$$\mathbf{C} = \begin{bmatrix} \lambda+2\mu & \lambda & \lambda & 0 & 0 & 0 \\ \lambda & \lambda+2\mu & \lambda & 0 & 0 & 0 \\ \lambda & \lambda & \lambda+2\mu & 0 & 0 & 0 \\ 0 & 0 & 0 & \mu & 0 & 0 \\ 0 & 0 & 0 & 0 & \mu & 0 \\ 0 & 0 & 0 & 0 & 0 & \mu \end{bmatrix} \tag{21b}$$

Using Hooke's law and the isotropic form of **C**, we obtain

$$\sigma_{ij} = \lambda \delta_{ij} \sum_{k=1}^{3} \varepsilon_{kk} + 2\mu \varepsilon_{ij} \tag{22}$$

3.4 Tensor transformations in coordinate system rotations

The properties of non-isotropic media are dependent upon the direction. Therefore it is often necessary to rotate the original coordinate system about the x_3 axis and recalculate the shears and strains in a rotated coordinate system. This rotation requires also a corresponding transformation of the elastic moduli C_{ijkl} from the old coordinate system to the new coordinate system. In a laminate with several layers, this rotation needs to be done for each layer in order to align the local coordinate systems from each layer [Nay1995].

In a counterclockwise rotation in $x_1' - x_2'$ plane (see Figure 9), the transformation **L** is

$$\mathbf{L} = \begin{bmatrix} \cos\phi & \sin\phi & 0 \\ -\sin\phi & \cos\phi & 0 \\ 0 & 0 & 1 \end{bmatrix} \tag{23}$$

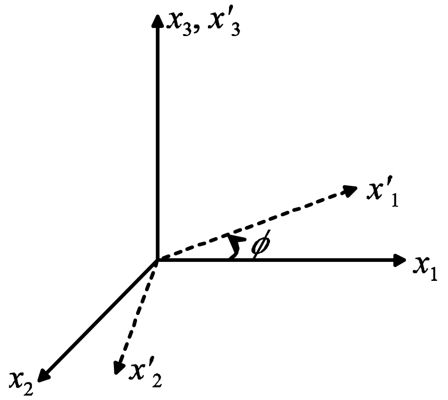

Figure 9. Coordinate rotation e.g. from principal material axes (x'_1, x'_2, x'_3) to global axes (x_1, x_2, x_3).

The elements L_{ij} are the direction cosines between the *i*-th axis in the new coordinate system and the *j*-th axis of the old system.

Consider the stress components in Figure 7. If the coordinate system is rotated, the rotation changes both the direction of stress and the direction of the plane (or normal of that plane) on which the stress is acting. Thus the rotation needs to be done with respect to both of the defining indices, and therefore the transformation

$$\sigma_{kl} = \sum_{i,j=1}^{3} L_{ik} L_{jl} \sigma'_{ij} \tag{24}$$

converts the symmetric second-order stress tensor σ'_{lm} into its representation in the new coordinate system σ_{ik}. For stiffness matrix, the rotation needs to be done with respect to all four defining indices, and the corresponding transformation is

$$C_{mnop} = \sum_{i,j,k,l=1}^{3} L_{mi} L_{nj} L_{ok} L_{pl} C'_{ijkl} \tag{25}$$

For monoclinic media, this results in

$$
\begin{aligned}
C_{11} &= C'_{11}G^4 + C'_{22}S^4 + 4C'_{16}SG^3 + 4C'_{26}S^3G + 2\left(C'_{12} + 2C'_{66}\right)S^2G^2 \\
C_{12} &= C'_{12}\left(S^4 + G^4\right) - 2\left(C_{16} - C_{26}\right)\left(SG^3 - S^3G\right) + \left(C'_{11} + C'_{22} - 4C'_{66}\right)S^2G^2 \\
C_{13} &= C'_{13}G^2 + C'_{23}S^2 + 2C_{36}SG \\
C_{16} &= C'_{16}G^4 - 2C'_{26}S^4 + \left(C'_{12} - C'_{11} + 2C'_{66}\right)SG^3 \\
&\quad + \left(C'_{22} - C'_{12} - 2C'_{66}\right)S^3G - 3\left(C'_{16} - C'_{26}\right)S^2G^2 \\
C_{22} &= C'_{11}S^4 + C'_{22}G^4 - 4C'_{16}S^3G - 4C'_{26}SG^3 + 2\left(C'_{12} + 2C'_{66}\right)S^2G^2 \\
C_{23} &= C'_{23}G^2 - 2C'_{36}SG + C'_{13}S^2 \\
C_{26} &= C'_{26}G^4 - C'_{16}S^4 + \left(C'_{12} - C'_{11} + 2C'_{66}\right)S^3G \\
&\quad + \left(C'_{22} - C'_{12} - 2C'_{66}\right)SG^3 + 3\left(C'_{16} - C'_{26}\right)S^2G^2 \\
C_{33} &= C'_{33} \\
C_{36} &= C'_{36}\left(G^2 - S^2\right) + \left(C'_{23} - C'_{13}\right)SG \\
C_{44} &= C'_{44}G^2 + C'_{55}S^2 - 2C'_{45}SG \\
C_{45} &= C'_{45}\left(G^2 - S^2\right) + \left(C'_{44} - C'_{55}\right)SG \\
C_{55} &= C'_{55}G^2 + C'_{44}S^2 + 2C'_{45}SG \\
C_{66} &= C'_{66}\left(G^4 + S^4\right) - 2\left(C'_{16} - C'_{26}\right)\left(SG^3 - S^3G\right) \\
&\quad + \left(C'_{11} - 2C'_{12} + C'_{22} - 2C'_{66}\right)S^2G^2
\end{aligned}
\tag{26}
$$

where $S = \sin\phi$ and $G = \cos\phi$ [Chr2005].

For media of higher symmetry, values for C_{ij} can be calculated from Eq. (26) by setting the appropriate C'_{kl} values to zero.

3.5 Elastic constants and stiffness matrix

Composite laminas can generally be considered to be at least of orthotropic symmetry. In that case, the stiffness matrix is of the form in Eq. (19).

If the wavelengths of the generated disturbances are large compared to the diameter of individual fibres in each of the lamina, as is usually the case, then each lamina can be modelled by a homogeneous and transversely isotropic material with symmetry axis x_1

(normal to the plane of isotropy, x_2–x_3). For such material, the stiffness matrix is of the form in Eq. (20).

The stiffness matrix elements C_{pq} can be calculated using the elastic constants for the material: shear modulus μ, Poisson's ratio ν, and Young's modulus E. This is easiest to do through the compliance matrix S, which is the inverse of stiffness matrix:

$$\boldsymbol{\sigma} = \mathbf{C}\boldsymbol{\varepsilon} \quad \Leftrightarrow \quad \boldsymbol{\varepsilon} = \mathbf{S}\boldsymbol{\sigma} \tag{27}$$

The components of compliance matrix as a function of elastic constants can be determined by setting each of the stress components σ_{ij} to nonzero one at the time, calculating the resulting strains and using the definitions of the elastic constants [Jon1975, Kaw2006]. For an orthotropic case, this results in compliance matrix of the form

$$\mathbf{S}' = \begin{bmatrix} \frac{1}{E_1} & \frac{-\nu_{12}}{E_1} & \frac{-\nu_{13}}{E_1} & 0 & 0 & 0 \\ \frac{-\nu_{21}}{E_2} & \frac{1}{E_2} & \frac{-\nu_{23}}{E_2} & 0 & 0 & 0 \\ \frac{-\nu_{31}}{E_3} & \frac{-\nu_{32}}{E_3} & \frac{1}{E_3} & 0 & 0 & 0 \\ 0 & 0 & 0 & \frac{1}{G_{23}} & 0 & 0 \\ 0 & 0 & 0 & 0 & \frac{1}{G_{31}} & 0 \\ 0 & 0 & 0 & 0 & 0 & \frac{1}{G_{12}} \end{bmatrix} \tag{28}$$

where E_i is the Young's modulus in x_i' direction, ν_{ij} is the Poisson's ratio in the plane $x_i' - x_j'$, and G_{ij} is the shear modulus in the plane $x_i' - x_j'$. The compliance matrix as well as the stiffness matrix needs to be symmetric and thus

$$\frac{\nu_{ij}}{E_i} = \frac{\nu_{ji}}{E_j} \quad \text{for } i \neq j \tag{29}$$

The stiffness matrix C is the inversion of (28) and is given by

$$
\mathbf{C}' = \begin{bmatrix}
\frac{1-\nu_{23}\nu_{32}}{E_2E_3\Delta} & \frac{\nu_{21}+\nu_{23}\nu_{31}}{E_2E_3\Delta} & \frac{\nu_{31}+\nu_{21}\nu_{32}}{E_2E_3\Delta} & 0 & 0 & 0 \\
\frac{\nu_{21}+\nu_{23}\nu_{31}}{E_2E_3\Delta} & \frac{1-\nu_{13}\nu_{31}}{E_1E_3\Delta} & \frac{\nu_{32}+\nu_{12}\nu_{31}}{E_1E_3\Delta} & 0 & 0 & 0 \\
\frac{\nu_{31}+\nu_{21}\nu_{32}}{E_2E_3\Delta} & \frac{\nu_{32}+\nu_{12}\nu_{31}}{E_1E_3\Delta} & \frac{1-\nu_{12}\nu_{21}}{E_1E_2\Delta} & 0 & 0 & 0 \\
0 & 0 & 0 & G_{23} & 0 & 0 \\
0 & 0 & 0 & 0 & G_{31} & 0 \\
0 & 0 & 0 & 0 & 0 & G_{12}
\end{bmatrix} \tag{30}
$$

where $\Delta = (1-\nu_{12}\nu_{21}-\nu_{23}\nu_{32}-\nu_{12}\nu_{21}-2\nu_{21}\nu_{32}\nu_{13})/(E_1E_2E_3)$.

For transversely isotropic material with x_1' as an axis of symmetry, the stiffness matrix becomes

$$
\mathbf{C}' = \begin{bmatrix}
\frac{E_1(\nu_{23}-1)}{\Delta} & \frac{-E_2\nu_{12}}{\Delta} & \frac{-E_2\nu_{12}}{\Delta} & 0 & 0 & 0 \\
\frac{-E_2\nu_{12}}{\Delta} & \frac{E_2(\nu_{12}\nu_{21}-1)}{(\nu_{23}+1)\Delta} & \frac{-E_2(\nu_{23}+\nu_{12}\nu_{21})}{(\nu_{23}+1)\Delta} & 0 & 0 & 0 \\
\frac{-E_2\nu_{12}}{\Delta} & \frac{-E_2(\nu_{23}+\nu_{12}\nu_{21})}{(\nu_{23}+1)\Delta} & \frac{E_2(\nu_{12}\nu_{21}-1)}{(\nu_{23}+1)\Delta} & 0 & 0 & 0 \\
0 & 0 & 0 & \frac{E_2}{2(\nu_{23}+1)} & 0 & 0 \\
0 & 0 & 0 & 0 & G_{31} & 0 \\
0 & 0 & 0 & 0 & 0 & G_{31}
\end{bmatrix} \tag{31}
$$

where $\Delta = (\nu_{23}+2\nu_{12}\nu_{21}-1)$.

4. Ultrasonic waves in isotropic media

In this chapter, the theory for ultrasonic waves in an isotropic media is reviewed. First, the equations for the dynamics of displacement fields in elastic material are formulated. Then the solutions for bulk waves, shear horizontal waves and Rayleigh surface waves are presented in compact form. The Lamb waves, which are the main consideration of the thesis, are analyzed more thoroughly. The equations for the displacement fields in symmetric and antisymmetric Lamb wave modes are derived. Then the dispersion equations are presented. Motion of different Lamb wave modes is studied. Lamb wave excitation using piezoelectric wafer active sensors is discussed. Finally, the concept of leaky Lamb waves, mode conversion phenomenon and adiabatic modes are presented briefly.

4.1 Field equations and boundary conditions

Substituting the stress-strain relation (22) into the force equilibrium equation (13) and using Eq. (6) gives [Kun2003, Ros1999]

$$\left(\lambda+\mu\right)\sum_{j=1}^{3}\frac{\partial^2 u_j}{\partial x_j \partial x_i}+\mu\sum_{j=1}^{3}\frac{\partial^2 u_i}{\partial x_j^2}+f_i=\rho\frac{\partial^2 u_i}{\partial t^2} \tag{32}$$

In the vector form this can be written as

$$\left(\lambda+\mu\right)\nabla\left(\nabla\bullet\mathbf{u}\right)+\mu\nabla^2\mathbf{u}+\mathbf{f}=\rho\frac{\partial^2\mathbf{u}}{\partial t^2} \tag{33}$$

where ∇ is the gradient, and $\nabla\bullet$ is the divergence of a vector. Using the identity $\nabla^2\mathbf{u}=\nabla\left(\nabla\bullet\mathbf{u}\right)-\nabla\times\nabla\times\mathbf{u}$, where $\nabla\times$ is the curl of a vector, Eq. (33) can also be written as

$$\left(\lambda+2\mu\right)\nabla\left(\nabla\bullet\mathbf{u}\right)-\mu\nabla\times\nabla\times\mathbf{u}+\mathbf{f}=\rho\frac{\partial^2\mathbf{u}}{\partial t^2} \tag{34}$$

which is a three-dimensional wave equation known as Navier's equation.

Since any vector can be written as the gradient of a scalar and the curl of a vector, called scalar (ϕ) and vector ($\boldsymbol{\psi}$) potentials, the displacement vector **u** may be written in form

$$\mathbf{u} = \nabla\phi + \nabla\times\boldsymbol{\psi} \tag{35}$$

which is known as Stokes-Helmholtz decomposition. Since the vector equation (35) has three parameters on the left hand side and four parameters on the right hand side, an additional relation

$$\nabla\bullet\boldsymbol{\psi} = 0 \tag{36}$$

is defined to obtain unique relations between u_1, u_2, u_3 and ϕ, ψ_1, ψ_2, and ψ_3. The potentials can always be selected such that also the relations

$$\begin{aligned} &\nabla\bullet\left(\nabla\times\boldsymbol{\psi}\right) = 0 \\ &\nabla\times\left(\nabla\phi\right) = 0 \\ &\nabla\times\nabla\times\boldsymbol{\psi} = \nabla\left(\nabla\bullet\boldsymbol{\psi}\right) - \nabla^2\boldsymbol{\psi} \end{aligned} \tag{37}$$

hold.

Substituting Eq. (35) in the wave equation Eq. (34) and using relations (37) gives

$$\begin{aligned} &(\lambda+2\mu)\nabla\left(\nabla^2\phi\right) - \mu\nabla\times\left(-\nabla^2\boldsymbol{\psi}\right) + \mathbf{f} = \rho\frac{\partial^2\left(\nabla\phi\right)}{\partial t^2} + \rho\frac{\partial^2\left(\nabla\times\boldsymbol{\psi}\right)}{\partial t^2} \\ &\Rightarrow \nabla\left[(\lambda+2\mu)\left(\nabla^2\phi\right) - \rho\frac{\partial^2\phi}{\partial t^2}\right] + \nabla\times\left[\mu\nabla^2\boldsymbol{\psi} - \rho\frac{\partial^2\boldsymbol{\psi}}{\partial t^2}\right] + \mathbf{f} = 0 \end{aligned} \tag{38}$$

When analysing the propagation of elastic waves in solids, the body forces **f** in Eq. (38) are assumed to be zero. Then Eq. (38) is satisfied if

$$\begin{aligned}
&\nabla^2\phi - \frac{\rho}{\lambda+2\mu}\frac{\partial^2\phi}{\partial t^2} = \nabla^2\phi - \frac{1}{c_L^2}\frac{\partial^2\phi}{\partial t^2} = 0 \\
&\nabla^2\boldsymbol{\psi} - \frac{\rho}{\mu}\frac{\partial^2\boldsymbol{\psi}}{\partial t^2} = \nabla^2\boldsymbol{\psi} - \frac{1}{c_T^2}\frac{\partial^2\boldsymbol{\psi}}{\partial t^2} = 0
\end{aligned} \tag{39}$$

The wave equations in Eq. (39) have solutions of the form

$$\begin{aligned}
&\phi(\mathbf{x},t) = \phi(\mathbf{n}\bullet\mathbf{x} - c_L t) \\
&\boldsymbol{\psi}(\mathbf{x},t) = \boldsymbol{\psi}(\mathbf{n}\bullet\mathbf{x} - c_T t)
\end{aligned} \tag{40}$$

These equations represent two waves propagating in the **n** direction with the velocity of c_L and c_T, respectively. Hence c_L and c_T are velocities of longitudinal and transverse waves.

The displacement fields of different types of elastic waves can be described through Eqs. (6) (relationship between displacement and strain), (22) (relationship between strain and stress), (35) and (39). Finding the unique solution for the equations for each case requires defining appropriate boundary conditions on the surface of the undeformed body [Ach1975]. The most common boundary conditions are (i) displacement boundary conditions: the three components u_i are prescribed on the boundary, and (ii) traction boundary conditions: the three traction components t_i are prescribed on the boundary with unit normal **n**. Through traction-stress equation (11) this corresponds to conditions on the three components of the stress tensor. In this thesis, appropriate stress-free boundary conditions are applied.

4.2 Bulk waves

When $\boldsymbol{\psi} = 0$ and $\phi \neq 0$, one gets

$$\mathbf{u} = \nabla\phi = \mathbf{n}\phi'(\mathbf{n}\bullet\mathbf{x} - c_L t) \tag{41}$$

where the prime indicates derivative with respect to the argument. The direction of the displacement vector **u** and the wave propagation direction **n** are the same; hence this is the equation for longitudinal waves (Figure 10).

When $\boldsymbol{\psi} \neq 0$ and $\phi = 0$, one gets

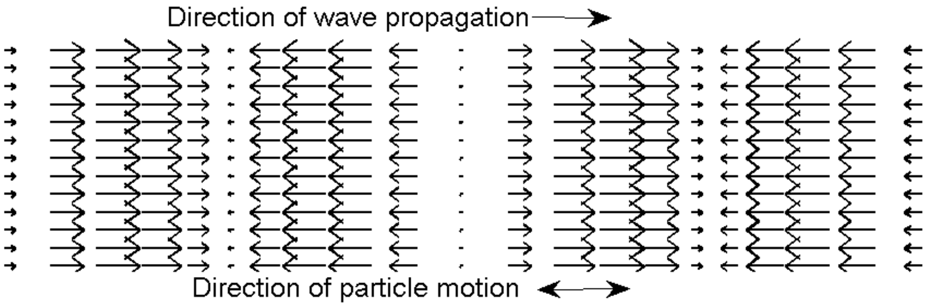

Figure 10. Longitudinal waves.

$$\mathbf{u} = \nabla \times \boldsymbol{\psi} = \nabla \times \boldsymbol{\psi}\left(\mathbf{n} \bullet \mathbf{x} - c_T t\right) \tag{42}$$

The three components of displacement in the Cartesian coordinate system can be written from Eq. (42):

$$\begin{aligned} u_1 &= n_2 \psi_3'\left(\mathbf{n} \bullet \mathbf{x} - c_T t\right) - n_3 \psi_2'\left(\mathbf{n} \bullet \mathbf{x} - c_T t\right) \\ u_2 &= n_3 \psi_1'\left(\mathbf{n} \bullet \mathbf{x} - c_T t\right) - n_1 \psi_3'\left(\mathbf{n} \bullet \mathbf{x} - c_T t\right) \\ u_3 &= n_1 \psi_2'\left(\mathbf{n} \bullet \mathbf{x} - c_T t\right) - n_2 \psi_1'\left(\mathbf{n} \bullet \mathbf{x} - c_T t\right) \end{aligned} \tag{43}$$

Clearly the dot product between **n** and **u** given in Eq. (43) is zero. Hence, the direction of the displacement vector **u** is perpendicular to the wave propagation direction **n**, and thus Eq. (42) corresponds to transversal wave (Figure 11).

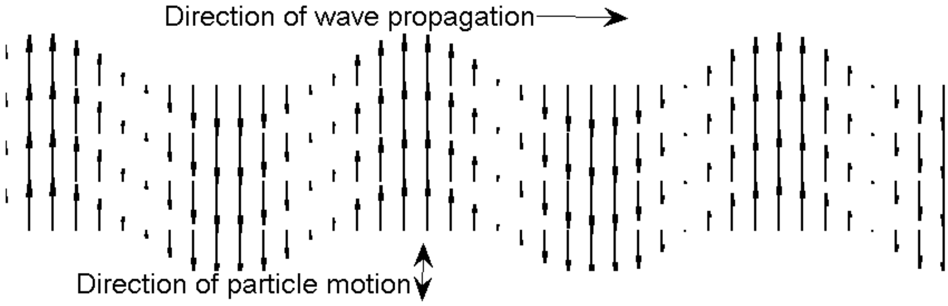

Figure 11. Transversal waves.

If Eq. (42) is simplified to an in-plane problem where the waves propagate in one plane (for example in x_1-x_2 -plane), then the wave potentials for these two type of waves with harmonic time dependence can be written as

$$\begin{aligned}\phi(\mathbf{x},t) &= A\mathrm{e}^{\mathrm{i}\left(k_L x_1 \cos\theta + k_T x_2 \sin\theta\right)}\mathrm{e}^{-\mathrm{i}\omega t} \\ \psi(\mathbf{x},t) &= B\mathrm{e}^{\mathrm{i}\left(k_T x_1 \cos\theta + k_L x_2 \sin\theta\right)}\mathrm{e}^{-\mathrm{i}\omega t}\end{aligned} \tag{44}$$

where $k_L = \omega/c_L$ is the longitudinal wave number, $k_T = \omega/c_T$ is the transversal wave number, and θ is the angle between propagation direction **n** and x_1 axis. In air, sound travels in longitudinal waves. In solids, molecules can vibrate in several directions, resulting in different wave modes. Longitudinal and transversal waves are the modes of so-called bulk acoustic waves, and they travel in unbounded solids independently at different velocities.

In bounded solids, i.e. half-spaces or plates, bulk waves are repeatedly reflected from the boundaries. Therefore they are not applicable for studying thin-walled samples, or for the surface layer of a sample, since the reflection from a defect is masked by reflection from the surface. In these kinds of structures, Rayleigh or Lamb waves are the relevant ones.

4.3 Shear horizontal waves

Longitudinal and transversal waves have the common property that both the wave propagation and the particle displacements occur in the same plane, e.g. in x_1-x_2 –plane. If the waves propagate in certain plane, but the particle displacements occur in direction perpendicular to this plane (e.g. propagation in x_1-x_2 –plane and displacements in x_3 direction, see Figure 12), then the wave motion is called out-of-plane motion. It can be shown that in bulk material, these kinds of waves have the same velocity, c_T, as the in-plane transversal (shear) waves and they, too, generate only shear stress in the medium. The out-of-plane shear waves are called the shear horizontal (SH) waves [Kun2003].

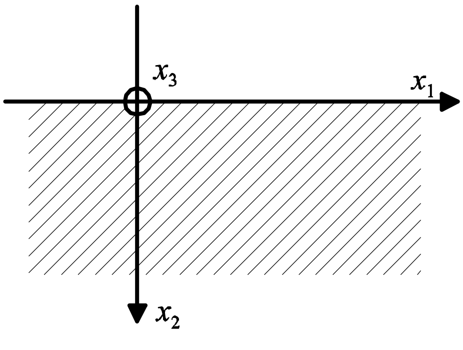

Figure 12. Wave propagation coordinate system.

In plate-like structures, the SH wave motion is governed through the stress-free boundary conditions on the free surfaces. The displacement field in the plate can be expressed as

$$u_3 = \left(Ae^{-\mathrm{i}qx_2} + Be^{\mathrm{i}qx_2}\right)e^{\mathrm{i}(kx_1 - \omega t)} \tag{45}$$

where $q^2 = k_T^2 - k^2$, k_T is the transversal wave number, and A and B are arbitrary constants. From the strain-displacement and stress-strain relations for isotropic material one can show that this displacement field can only produce shear strain and shear stress, σ_{32} and σ_{31}. At the boundary, σ_{32} (stress in x_1-x_3 plane and in x_3 direction) is zero but σ_{31} (stress in x_1-x_2 plane and in x_3 direction) is not.

Let the plate thickness be 2d. Using (6) and (22), the two stress-free boundary conditions, $\sigma_{32} = 0$ at $x_2 = \pm d$ are

(46)

From Eq. (46) we can write

$$\begin{bmatrix} -e^{-\mathrm{i}qd} & e^{\mathrm{i}qd} \\ -e^{\mathrm{i}qd} & e^{-\mathrm{i}qd} \end{bmatrix} \begin{bmatrix} A \\ B \end{bmatrix} = \begin{bmatrix} 0 \\ 0 \end{bmatrix} \tag{47}$$

For nontrivial solution, the determinant of the coefficient matrix must be zero. Hence,

$$\begin{aligned} &-e^{-2\mathrm{i}qd} + e^{2\mathrm{i}qd} = 2\mathrm{i}\sin(2qd) = 0 \\ &\Rightarrow \sin(2qd) = 0 = \sin(m\pi), \quad m = 0,1,2,\ldots \\ &\Rightarrow \sqrt{k_T^2 - k^2} = \frac{m\pi}{2d}, \quad m = 0,1,2,\ldots \end{aligned} \tag{48}$$

mth order SH wave number k_m and wave velocity c_m can then be computed as follows:

$$k_m = \sqrt{k_T^2 - \left(\frac{m\pi}{2d}\right)^2}, \quad m = 0,1,2,\ldots \tag{49a}$$

$$\Rightarrow c_m = \frac{\omega}{k_m} = \frac{\omega}{\sqrt{k_T^2 - \left(\frac{m\pi}{2d}\right)^2}} = \frac{c_T}{\sqrt{1 - \left(\frac{m\pi}{2d}\right)^2 \left(\frac{c_T}{\omega}\right)^2}}, \quad m = 0,1,2,\ldots \tag{49b}$$

Thus the SH waves can exist in several modes, whose wave number, k_m, and wave velocity, c_m, depend on frequency, except for the 0th order mode, which has velocity equal to c_T. Such frequency dependent waves are called dispersive.

For an SH wave mode to exist, $k_T > (m\pi/2d)$. Therefore the number of possible SH modes and their propagation velocity depend on the product of frequency and plate thickness. Figure 13 shows the dispersion curves for the first six SH wave modes in aluminium.

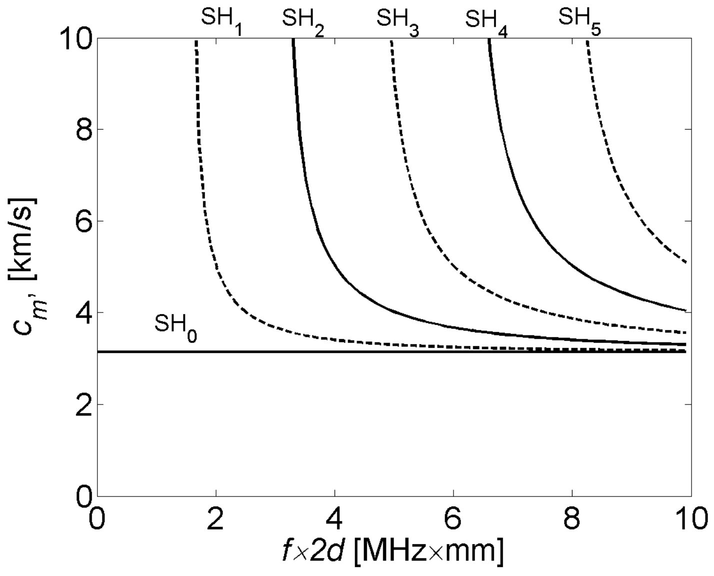

Figure 13. SH wave dispersion curves for aluminium.

4.4 Rayleigh waves

Surface or Rayleigh waves travel on the surface of a relatively thick solid material, penetrating only to a depth of about one wavelength. In Rayleigh waves, particles vibrate in elliptical orbit in the plane perpendicular to the surface; the longitudinal and transversal motions are coupled together and they travel at common velocity [Vik1967].

Let us consider a Rayleigh wave on the boundary between a solid, isotropic, perfectly elastic material and vacuum (or low-density fluid, such as air in atmospheric conditions). The coordinate system for wave propagation is defined so that the solid material occupies the region $x_2 > 0$, the direction of wave propagation coincides with the x_1 axis, the wave displacements occur in the sagittal plane, and the x_3 direction is perpendicular to the sagittal plane (see Figure 12). The boundary conditions for Rayleigh wave problem are that the stresses σ_{22} and σ_{12} go to zero at the boundary of the solid ($x_2 = 0$) (no displacement in the x_1-x_3 plane or x_2-x_3 plane).

Let us define the scalar potential ϕ (longitudinal wave potential) and vector potential $\boldsymbol{\psi}$ (transversal wave potential) of the particle displacements, so that the displacement vector **u** is defined according to Eq. (35).

If the wave propagation plane is the x_1-x_2 plane, the only nonzero component of $\boldsymbol{\psi}$ is in the x_3 direction. The corresponding wave equations from Eq. (39) are

$$\frac{\partial^2\phi}{\partial x_1^2}+\frac{\partial^2\phi}{\partial x_2^2}-\frac{k_L^2}{\omega^2}\frac{\partial^2\phi}{\partial t^2}=0 \tag{50}$$

$$\frac{\partial^2\boldsymbol{\psi}}{\partial x_1^2}+\frac{\partial^2\boldsymbol{\psi}}{\partial x_2^2}-\frac{k_T^2}{\omega^2}\frac{\partial^2\boldsymbol{\psi}}{\partial t^2}=0 \tag{51}$$

where k_L and k_T are longitudinal and transversal wave numbers, respectively:

$$k_L=\omega\sqrt{\frac{\rho}{\lambda+2\mu}}=\frac{\omega}{c_L} \quad \text{and} \quad k_T=\omega\sqrt{\frac{\rho}{\mu}}=\frac{\omega}{c_T}$$

where ω is the angular frequency, λ and μ are the elastic Lamè constants, and ρ is the density of the medium.

The solution for wave equations (50) and (51) corresponding to a plane harmonic wave propagating in the positive x_1 direction with Rayleigh wave number k_R is found through setting

$$\begin{aligned}\phi &= F(x_2)\mathrm{e}^{\mathrm{i}(k_R x_1-\omega t)}\\ \psi &= G(x_2)\mathrm{e}^{\mathrm{i}(k_R x_1-\omega t)}\end{aligned} \tag{52}$$

Substituting these expressions into equations (50) and (51), we obtain two differential equations for the functions $F(x_2)$ and $G(x_2)$:

$$\begin{aligned}&\frac{\partial^2 F(x_2)}{\partial x_2^2}-\left(k_R^2-k_L^2\right)F(x_2)=0\\ &\frac{\partial^2 G(x_2)}{\partial x_2^2}-\left(k_R^2-k_T^2\right)G(x_2)=0\end{aligned} \tag{53}$$

The two linearly independent solutions of the above equations are $\exp(\pm\sqrt{k_R^2-k_L^2}x_2)$ and $\exp(\pm\sqrt{k_R^2-k_T^2}x_2)$. In his original paper [Ray1887], Lord Rayleigh showed that the velocity of propagation for Rayleigh waves is smaller than that of the bulk waves and so $k_L^2, k_T^2 < k_R^2$ holds. Thus the solutions with negative radicals correspond to motion decaying exponentially with depth, that is, a surface wave. Thus the expressions for ϕ and ψ take the form

$$\begin{aligned}\phi &= A\mathrm{e}^{-qx_2}\mathrm{e}^{\mathrm{i}(k_R x_1-\omega t)}\\ \psi &= B\mathrm{e}^{-sx_2}\mathrm{e}^{\mathrm{i}(k_R x_1-\omega t)}\end{aligned} \tag{54}$$

where $q^2=k_R^2-k_L^2$, $s^2=k_R^2-k_T^2$, and A and B are arbitrary constants.

The components u_1 and u_2 of particle displacement along the x_1 and x_2 axes, respectively, and the stress components σ_{11}, σ_{22}, and σ_{12} may be represented as functions of ϕ and ψ using Eqs. (6), (22) and (35). Applying the stress-free boundary conditions leads to potentials

$$\begin{aligned}\phi &= -A\mathrm{e}^{\mathrm{i}(k_R x_1-\omega t)-qx_2}\\ \psi &= \mathrm{i}A\frac{2k_R q}{k_R^2+s^2}\mathrm{e}^{\mathrm{i}(k_R x_1-\omega t)-sx_2}\end{aligned} \tag{55}$$

and to characteristic equation

$$\begin{bmatrix} \left(k_R^2+s^2\right) & -2\mathrm{i}k_R s \\ -2\mathrm{i}k_R q & -\left(k_R^2+s^2\right) \end{bmatrix} \begin{bmatrix} A \\ B \end{bmatrix} = \begin{bmatrix} 0 \\ 0 \end{bmatrix} \tag{56}$$

Eq. (56) has a nontrivial solution if and only if the determinant of the coefficient matrix is zero:

$$\left(k_R^2+s^2\right)^2 - 4k_R^2 qs = 0 \tag{57}$$

The values of the roots of this equation depend only on the Poisson's ratio ν for the given elastic medium. The Rayleigh wave corresponds to the root $\eta_R = k_T/k_R = c_R/c_T$, which lies between zero and one. It can be shown that for any values of ν corresponding to real materials, there exists only one such root, and an approximate expression for this root is [Ach1975]

$$\eta_R = \frac{0.862+1.14\nu}{1+\nu} \tag{58}$$

This approximation also shows that for the Rayleigh wave, η_R and c_R do not depend on the frequency.

Equation (56) describing a Rayleigh wave shows that it consists of two inhomogeneous waves, one longitudinal and one transversal wave, which propagate along the boundary with identical velocities and attenuate exponentially with depth as $\exp(\pm\sqrt{k_R^2-k_L^2}x_2)$ (longitudinal mode) and $\exp(\pm\sqrt{k_R^2-k_T^2}x_2)$ (transversal mode).

The displacement components along the x_1 and x_2 axes are, according to Eq. (35)

$$\begin{aligned} u_{1,R} &= Ak_R\left(\mathrm{e}^{-q_R x_2} - \frac{2q_R s_R}{k_R^2+s_R^2}\mathrm{e}^{-s_R x_2}\right)\sin\left(k_R x_1 - \omega t\right) \\ u_{2,R} &= Aq_R\left(\mathrm{e}^{-q_R x_2} - \frac{2k_R^2}{k_R^2+s_R^2}\mathrm{e}^{-s_R x_2}\right)\cos\left(k_R x_1 - \omega t\right) \end{aligned} \tag{59}$$

Since these displacement components in the Rayleigh wave are shifted by π/2 from another, the trajectories of the particle motions in the wave are ellipses. The displacement field of Rayleigh wave is shown in Figure 14. The attenuation with depth is clearly visible.

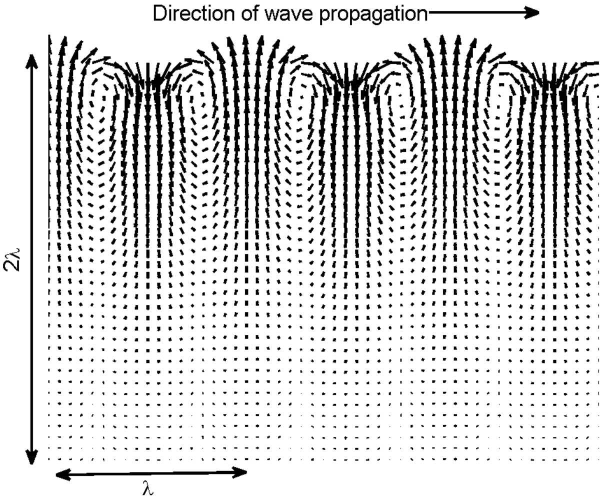

Figure 14. Rayleigh wave particle directions and relative amplitudes at different depths.

4.5 Lamb waves

In structures with two stress-free boundaries there exist specific plate waves, which may have either antiplane or in-plane displacement fields. The former are the shear horizontal (SH) waves, the latter the Lamb waves. Lamb wave is a complex vibrational wave that travels by affecting the material through its entire thickness. This makes it the most important plate wave for SHM applications. The fundamental property of Lamb waves in a plate is that for finite values of the ratio of the Lamb wavelength λ to plate thickness $2d$, the wave number and the propagation velocity depend on frequency, i.e. they are dispersive [Vik1967]. As shown above, Rayleigh waves are not dispersive.

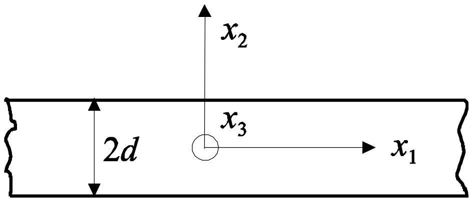

Figure 15. Lamb coordinate system.

The boundary conditions for Lamb wave problem are that the stresses σ_{22} and σ_{12} go to zero at both boundaries of the solid ($x_2 = \pm d$). The coordinate system in shown in Figure 15.

4.5.1 Lamb wave dynamics

With Lamb waves, the expressions for ϕ and ψ can be represented in the form

$$\begin{aligned}\phi &= a\mathrm{e}^{-\mathrm{i}px_2}\mathrm{e}^{\mathrm{i}(kx_1-\omega t)} + b\mathrm{e}^{\mathrm{i}px_2}\mathrm{e}^{\mathrm{i}(kx_1-\omega t)} = A_s\cos(px_2)\mathrm{e}^{\mathrm{i}(kx_1-\omega t)} + B_a\sin(px_2)\mathrm{e}^{\mathrm{i}(kx_1-\omega t)} \\ \psi &= c\mathrm{e}^{-\mathrm{i}qx_2}\mathrm{e}^{\mathrm{i}(kx_1-\omega t)} + d\mathrm{e}^{\mathrm{i}qx_2}\mathrm{e}^{\mathrm{i}(kx_1-\omega t)} = C_s\sin(qx_2)\mathrm{e}^{\mathrm{i}(kx_1-\omega t)} + D_a\cos(qx_2)\mathrm{e}^{\mathrm{i}(kx_1-\omega t)}\end{aligned} \tag{60}$$

where k is the Lamb wave number, $p^2 = k_L^2 - k^2$, $q^2 = k_T^2 - k^2$, k_L and k_T are longitudinal and transversal wave numbers, respectively, and A_s, B_a, C_s and D_a are arbitrary constants. The subscripts s and a stand for symmetric and antisymmetric wave mode, respectively.

With x_2 axis pointing upwards, using Eqs. (6), (22) and (35) we get displacements and stresses

$$\begin{aligned}u_1 &= \frac{\partial\phi}{\partial x_1} + \frac{\partial\psi}{\partial x_2} \\ u_2 &= \frac{\partial\phi}{\partial x_2} - \frac{\partial\psi}{\partial x_1}\end{aligned} \tag{61}$$

$$\begin{aligned}\sigma_{22} &= -\mu\left(k_T^2\phi + 2\left[\frac{\partial^2\phi}{\partial x_1^2} + \frac{\partial^2\psi}{\partial x_1\partial x_2}\right]\right) \\ \sigma_{12} &= \mu\left(2\frac{\partial^2\phi}{\partial x_1\partial x_2} - \frac{\partial^2\psi}{\partial x_1^2} + \frac{\partial^2\psi}{\partial x_2^2}\right)\end{aligned} \tag{62}$$

Substituting Equations (60) into (62) and applying the boundary conditions given above, we obtain a set of linear homogenous equations for the amplitudes A_s, B_a, C_s and D_a:

$$\begin{bmatrix} K\cos(pd) & K\sin(pd) & -2\mathrm{i}kq\cos(qd) & 2\mathrm{i}kq\sin(qd) \\ K\cos(pd) & -K\sin(pd) & -2\mathrm{i}kq\cos(qd) & -2\mathrm{i}kq\sin(qd) \\ -2\mathrm{i}kp\sin(pd) & 2\mathrm{i}kp\cos(pd) & K\sin(qd) & K\cos(qd) \\ 2\mathrm{i}kp\sin(pd) & 2\mathrm{i}kp\cos(pd) & -K\sin(qd) & K\cos(qd) \end{bmatrix} \begin{bmatrix} A_s \\ B_a \\ C_s \\ D_a \end{bmatrix} = \begin{bmatrix} 0 \\ 0 \\ 0 \\ 0 \end{bmatrix} \tag{63}$$

where $K = k^2 - q^2$. The set of equations has a nontrivial solution if and only if the determinant of the coefficient matrix is zero.

By applying the Gaussian elimination, the problem can be simplified into separate symmetric and antisymmetric wave mode problems. Gaussian elimination is an algorithm used e.g. for solving systems of linear equations [Gol1996]. The idea is to eliminate variables and create subsets of equations through elementary row operations (multiplying rows, switching rows, and adding multiples of rows to other rows) on the coefficient matrix. The set of equations has a solution if the subsets of equations have a solution. In this case, adding the second row of the coefficient matrix in Eq. (63) to the first row, and subtracting the fourth row from the third row results in subset of equations with only A_s and C_s terms:

$$\begin{bmatrix} K\cos(pd) & -2\mathrm{i}kq\cos(qd) \\ -2\mathrm{i}kp\sin(pd) & K\sin(qd) \end{bmatrix}\begin{bmatrix} A_s \\ C_s \end{bmatrix} = \begin{bmatrix} 0 \\ 0 \end{bmatrix} \tag{64}$$

Correspondingly, subtracting the second row of the coefficient matrix in Eq. (63) from the first row, and adding the fourth row to the third row results in subset of equations with only B_a and D_a terms:

$$\begin{bmatrix} K\sin(pd) & 2\mathrm{i}kq\sin(qd) \\ 2\mathrm{i}kp\cos(pd) & K\cos(qd) \end{bmatrix}\begin{bmatrix} B_a \\ D_a \end{bmatrix} = \begin{bmatrix} 0 \\ 0 \end{bmatrix} \tag{65}$$

The solution of these subsystems leads to two characteristic equations, determining the eigenvalues of the wave number k:

$$K^2\cos(pd)\sin(qd) + 4k^2pq\sin(pd)\cos(qd) = 0 \tag{66}$$

$$K^2\sin(pd)\cos(qd) + 4k^2pq\cos(pd)\sin(qd) = 0 \tag{67}$$

Coefficients (A_s, C_s) and (B_a, D_a) are the eigenvectors of the homogeneous linear systems (64) and (65) corresponding to the subproblem eigenvalues 0, respectively. Solving these eigenvectors yields

$$\begin{aligned} A_s &= A2\mathrm{i}k_s q_s \cos(q_s d) \\ C_s &= AK_s \cos(p_s d) \end{aligned} \tag{68}$$

$$\begin{aligned} B_a &= A2\mathrm{i}k_a q_a \sin(q_a d) \\ D_a &= -AK_a \sin(p_a d) \end{aligned} \tag{69}$$

where A is arbitrary constant. Inserting Eqs. (68) and (69) into Eq. (62) leads into following relations for the potentials:

$$\begin{aligned} \phi &= 2\mathrm{i}k_s s_s \cos(q_s d)\cos\left(p_s x_2\right)\mathrm{e}^{\mathrm{i}\left(k_s x_1 - \omega t\right)} + 2\mathrm{i}k_a q_a \sin(q_a d)\sin\left(p_a x_2\right)\mathrm{e}^{\mathrm{i}\left(k_a x_1 - \omega t\right)} \\ \boldsymbol{\psi} &= K_s \cos\left(p_s d\right)\sin\left(q_s x_2\right)\mathrm{e}^{\mathrm{i}\left(k_s x_1 - \omega t\right)} - K_a \sin\left(p_a d\right)\cos\left(q_a x_2\right)\mathrm{e}^{\mathrm{i}\left(k_a x_1 - \omega t\right)} \end{aligned} \tag{70}$$

where k_s are the values of k satisfying Eq. (64), k_a are the values satisfying Eq. (65), $p_{s,a} = \sqrt{k_L^2 - k_{s,a}^2}$ and $q_{s,a} = \sqrt{k_T^2 - k_{s,a}^2}$. The displacement components u_1 and u_2 may be calculated from Eqs. (70) with the help of the relations (61):

$$\begin{aligned} u_1 &= u_{1,s} + u_{1,a} \\ u_2 &= u_{2,s} + u_{2,a} \end{aligned} \tag{71}$$

where

$$\begin{aligned} u_{1,s} &= \left\{-2k_s^2 q_s \cos\left(q_s d\right)\cos\left(p_s x_2\right) + q_s\left(k_s^2 - q_s^2\right)\cos\left(p_s d\right)\cos\left(q_s x_2\right)\right\}\mathrm{e}^{\mathrm{i}k_s x_1} \\ u_{2,s} &= \left\{-2\mathrm{i}k_s p_s q_s \cos\left(q_s d\right)\sin\left(p_s x_2\right) - \mathrm{i}k_s\left(k_s^2 - q_s^2\right)\cos\left(p_s d\right)\sin\left(q_s x_2\right)\right\}\mathrm{e}^{\mathrm{i}k_s x_1} \end{aligned} \tag{72}$$

$$\begin{aligned} u_{1,a} &= \left\{-2k_a^2 q_a \sin\left(q_a d\right)\sin\left(p_a x_2\right) + q_a\left(k_a^2 - q_a^2\right)\sin\left(p_a d\right)\sin\left(q_a x_2\right)\right\}e^{\mathrm{i}k_a x_1} \\ u_{2,a} &= \left\{2ik_a p_a q_a \sin\left(q_a d\right)\cos\left(p_a x_2\right) + ik_a\left(k_a^2 - q_a^2\right)\sin\left(p_a d\right)\cos\left(q_a x_2\right)\right\}e^{\mathrm{i}k_a x_1} \end{aligned} \tag{73}$$

The expressions (70) – (73) and Equations (66), (67) describe two groups of waves, which can propagate in the plate independently of one another. The first group of waves, with subscript s, describes waves in which the motion occurs symmetrically with respect to the plane $x_2 = 0$ (that is, the displacement u_1 has the same signs, the displacement u_2 opposite signs in the upper and lower halves of the plate). The second group, with subscript *a*, describes waves in which the motion is antisymmetric with respect to $x_2 = 0$. The displacement fields of symmetric and antisymmetric Lamb wave modes are shown in Figures 16a and 16b.

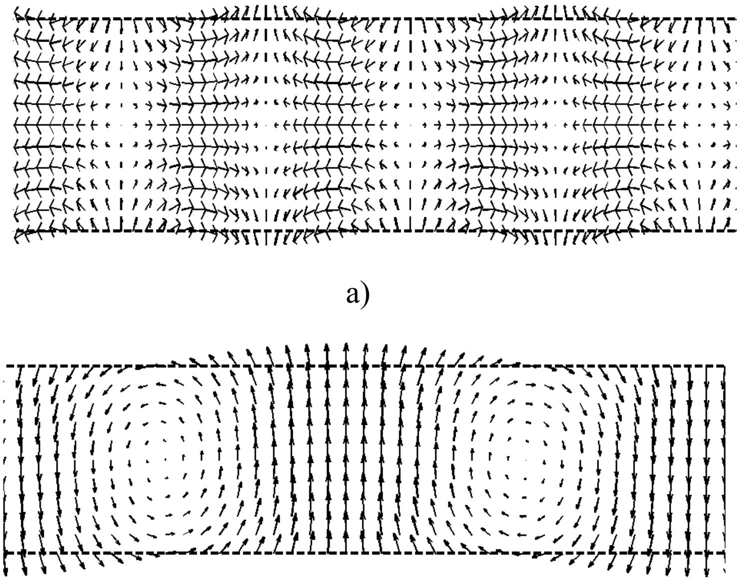
a)

b)

Figure 16. Side view of a plate with a) symmetric, b) antisymmetric Lamb waves.

4.5.2 Velocity dispersion in Lamb waves

The phenomenon of velocity dispersion is related to the concepts of phase and group velocity. Phase velocity c_P is the propagation velocity of a wave front of constant phase. It is the velocity at which the phase of any one frequency component of the wave travels. The phase velocity is given in terms of the wave's angular frequency ω and wave number *k*: $c_p = \omega/k$. If the phase velocities of different frequency components are different, the wave is dispersive.

The physical meaning of group velocity is that it describes the velocity of energy transfer in a wave or the envelope of a wave that is a sum of waves travelling at different phase velocities. If the phase velocities of the frequency components of the wave are approximately the same, the group velocity is approximately the same as the phase velocity (Figure 17a). If the phase velocities are different, the resulting group velocity differs from both of them (Figure 17b).

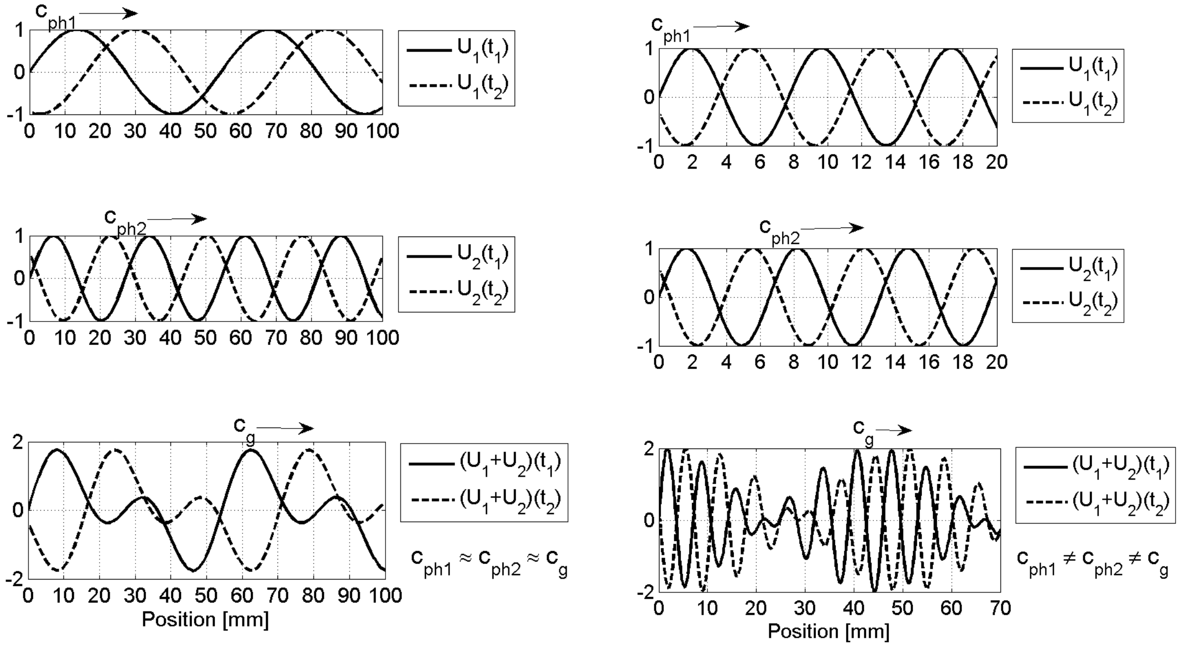

a) b)

Figure 17. a) Group velocity when the phase velocities of the wave components are close to each other. b) Group velocity when the phase velocities of the wave components are far from each other.

In a plate of thickness 2*d* at frequency *ω* there can exist a finite number of symmetric and antisymmetric Lamb waves. These waves have different phase and group velocities and distribution of the displacements throughout the thickness of the plate. The number of symmetric waves is determined by the number of real roots of Eq. (66), the number of antisymmetric waves by the number of real roots of Eq. (67). Every root defines a wave number $k_{s,a}$ or phase velocity $c_{s,a}$ of the corresponding wave.

The phase velocity c_P is the fundamental characteristic of a Lamb wave. When it is known, the wave number can be determined and the stresses and displacements in the Lamb wave at any point of the plate can be calculated. The phase velocity is found by numerical solution of the characteristic equations (66) and (67), which are rewritten for these calculations as function of velocity on the following dimensionless form:

$$\frac{\tan(p_s d)}{\tan(q_s d)} = \frac{-\left(2k_s^2 - k_T^2\right)^2}{4k_s^2 p_s q_s} \quad \text{for symmetric mode} \qquad (74)$$

$$\frac{\tan(q_a d)}{\tan(p_a d)} = \frac{-\left(2k_a^2 - k_T^2\right)^2}{4k_a^2 p_a q_a} \quad \text{for antisymmetric mode} \tag{75}$$

where k_L and k_T are longitudinal and transversal wave numbers, respectively, and $p_{s,a} = \sqrt{k_L^2 - k_{s,a}^2}$, $q_{s,a} = \sqrt{k_T^2 - k_{s,a}^2}$. In very thin plates and/or at low frequencies, Eqs. (66) and (67) have only one root each. These roots correspond to the so-called zero-order symmetric (S_0) and antisymmetric (A_0) normal modes, respectively. At definite values of product ωd new roots appear, corresponding to higher Lamb wave modes. At these critical points, the wave numbers $k_{s,a} \to 0$ and phase velocities $c_{s,a} \to \infty$, respectively, and thus $p \to k_L$ and $q \to k_T$. From Eq. (74) it can be seen that for symmetric mode, $\tan(pd)/\tan(qd)$ goes to infinity if $\cos(pd) = 0$, i.e. if $pd = n\pi/2$, $n = 1,3,5\ldots$ or $\sin(qd) = 0$, i.e. $qd = n\pi$, $n = 0,1,2,\ldots$ For the antisymmetric mode, there is inverse relationship. The relations between these critical thicknesses and transverse and longitudinal wave numbers are thus as follows [Vik1967]:

$$\left.\begin{aligned} 2d &= \frac{\pi n}{k_L}, \quad n = 1,3,5\ldots \\ 2d &= \frac{2\pi n}{k_T}, \quad n = 1,2,3\ldots \end{aligned}\right\} \text{for symmetric modes} \tag{76}$$

$$\left.\begin{aligned} 2d &= \frac{2\pi n}{k_L}, \quad n = 1,2,3\ldots \\ 2d &= \frac{\pi n}{k_T}, \quad n = 1,3,5\ldots \end{aligned}\right\} \text{for antisymmetric modes.} \tag{77}$$

The total number of symmetric modes N_s that may propagate in a plate of given thickness $2d$ at the frequency ω is

$$N_s = 1 + \left[\frac{2dk_T}{2\pi}\right] + \left[\frac{2dk_L}{2\pi} + \frac{1}{2}\right] \tag{78}$$

and the total number of antisymmetric modes N_a is

$$N_a = 1 + \left[\frac{2dk_L}{2\pi}\right] + \left[\frac{2dk_T}{2\pi} + \frac{1}{2}\right] \tag{79}$$

The brackets in the Eqs. (78) and (79) indicate rounding to the nearest smaller integer.

For example, Lamè constants for aluminium are $\lambda = 61.4 \cdot 10^9$ Pa and $\mu = 25.0 \cdot 10^9$ Pa, and $\rho = 2.70 \cdot 10^3$ kgm^{-3}. Thus the wave numbers for $\omega = 2 \cdot \pi \cdot 200\ \text{kHz} \approx 1.257 \cdot 10^6$ rad/s are

$$k_L = \frac{2\pi}{\lambda_L} = \omega\sqrt{\frac{\rho}{\lambda + 2\mu}} \approx 196\ \text{m}^{-1} \quad \text{and} \quad k_T = \frac{2\pi}{\lambda_T} = \omega\sqrt{\frac{\rho}{\mu}} \approx 413\ \text{m}^{-1}$$

If aluminium plate thickness is $2d$ = 1 mm, then N_s = 1 and N_a = 1; that is, only modes S_0 and A_0 exist. Mode S_1 appears at about 3 MHz, mode A_1 at about 1.5 MHz (both resulting from transverse wave).

The group velocity c_G for each Lamb wave mode can be calculated from the relation

$$c_G = c_P - \lambda \frac{dc_P}{d\lambda} = \frac{d\omega}{dk} \tag{80}$$

Dispersion curves for Lamb wave phase velocity and group velocity for aluminium are shown in Figure 18.

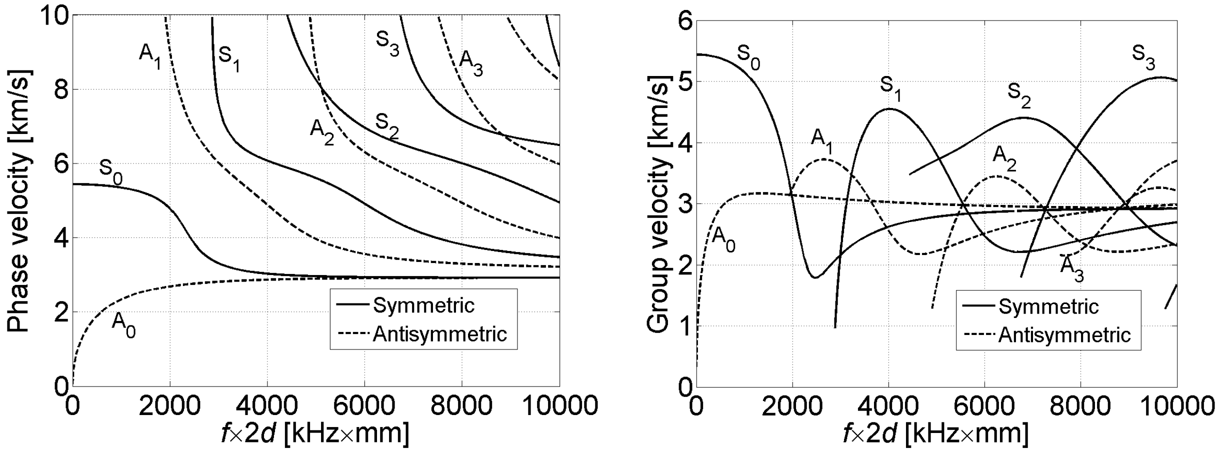

a) b)

Figure 18. Dispersion curves for aluminium. a) Phase velocity, b) group velocity.

4.5.3 Lamb wave motion

When the dispersion of Lamb waves is known, it is possible to study the motion of different wave modes. To characterize the wave motion, it is sufficient to know the displacement along x_1 and x_2 axes throughout the plate. The stress in the wave is then determined by the displacement.

For very small plate thickness (or low frequency), mode S_0 represents a longitudinal and A_0 represents a transversal wave. On the plate surface, the ratio of amplitudes in particle motions, u_1/u_2, for S_0 and A_0 waves as a function of frequency for a 1 mm aluminium plate is shown in Figure 19. It is clearly seen that at lower frequencies, the particle movement in x_1-direction is dominant in the S_0 wave mode. In the A_0-mode, the transversal component in x_2 direction is the stronger one, but the dominance is less pronounced than in the S_0 mode.

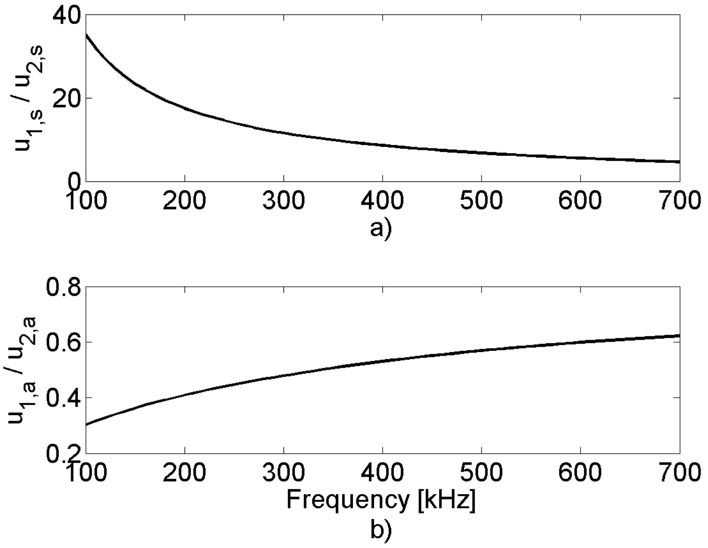

Figure 19. Particle motion amplitude ratios in a) S_0 and b) A_0 wave modes in 1 mm aluminium plate.

As the plate thickness is increased, the wave modes S_0 and A_0 become increasingly alike, and like Rayleigh wave. In a thick plate the displacements are localized near the free boundaries of the plate. The amplitudes of the normal and tangential displacement in the modes S_0 and A_0 as a function of depth for a 10 mm thick aluminium plate with $\nu = 0.33$, $\lambda = 61.4$ GPa, $\mu = 25.0$ GPa, and $\rho = 2700$ kgm^{-3} and at 570 kHz frequency, are shown in Figure 20. The displacement amplitudes are normalized according to the amplitudes of the corresponding waves at the surface. Figure 20 also shows the corresponding curves for the Rayleigh wave (subscript R). It is clearly seen that the largest differences in the depthwise distributions of the displacements are observed in the middle of the plate.

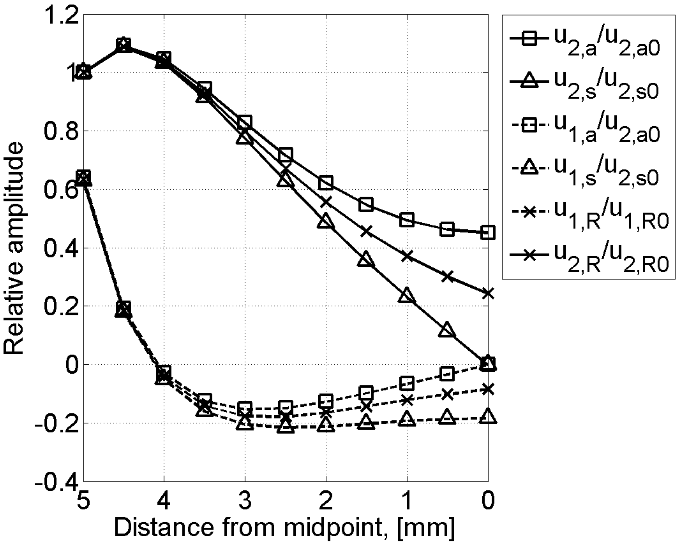

Figure 20. Relative Lamb and Rayleigh wave amplitudes in x_1 and x_2 directions.

If the plate thickness and signal frequency are such that higher order wave modes exist, the wave motion becomes rather complicated. At the critical values of $k_T d$ (defined by Eqs. 76-77), the generated Lamb wave is a purely longitudinal or purely transversal standing wave formed by two waves propagating in the opposite directions of x_2 axis. For larger-than-critical values of $k_T d$, the directions of propagation of these two waves are rotated from the x_2 axis towards the positive x_1 axis. Due to reflection from the plate boundaries, the resulting Lamb wave is composed of four components or partial waves: two longitudinal and two transversal waves. The projections of all the wave numbers on the x_1 axis are the same, while the stresses on the bounding planes are equal to zero.

With a given plate thickness, the amplitude of horizontal and vertical displacements of the different Lamb wave modes as a function of depth varies with frequency. In the example case of 10 mm thick aluminium plate at 570 kHz frequency, wave modes S_0, S_1, S_2, A_0, A_1 and A_2 coexist. Their horizontal (u_1) and vertical (u_2) displacements at different depths are shown in

Figures 21a-d. It is clearly seen that the different wave modes contribute different amounts to displacements and, therefore, strains on the plate surface.

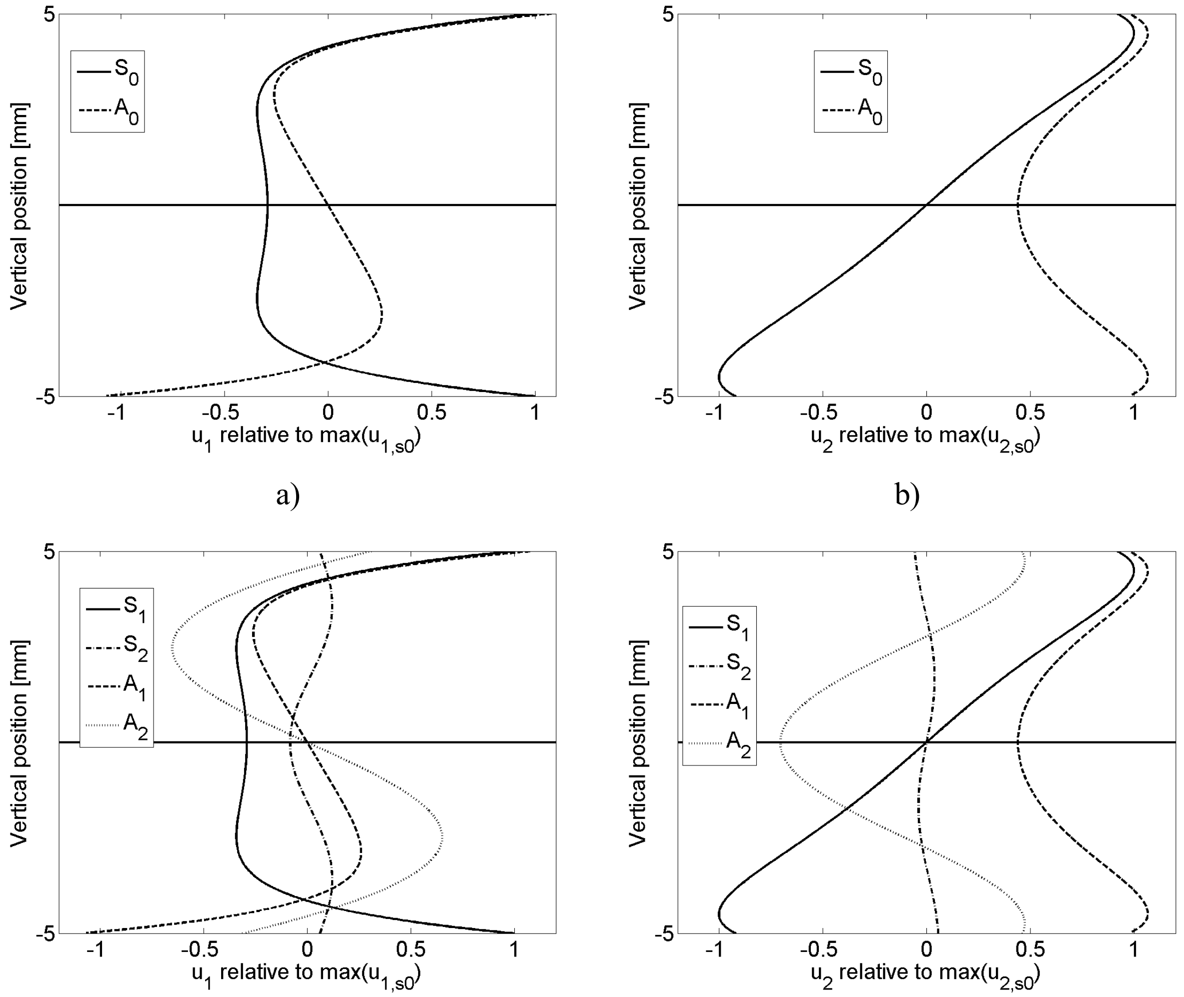

a)

b)

c)

d)

Figure 21. Horizontal (u_1) and vertical (u_2) displacements of different Lamb wave modes as a function of vertical position in a 10 mm aluminium plate at 570 kHz frequency. a) u_1 of S_0 and A_0 modes, b) u_2 of S_0 and A_0 modes, c) u_1 of S_1, S_2, A_1 and A_2 modes, d) u_2 of S_1, S_2, A_1 and A_2 modes. Horizontal and vertical displacements are shown relative to maximum amplitude of $u_{1,s0}$ and u_{2s0}, respectively.

4.5.4 Lamb wave actuation and tuning

In practice, Lamb waves are generated by causing perturbations to the surface of the plate. The most commonly used actuators are angled piezoelectric wedge transducers ([Zhu1998], [Wil2001]), comb transducers ([Pel1996]) and electromagnetic acoustic transducers (EMATs;

[Ale1987]). Other options that have been explored in recent years for NDT are Hertzian contact transducers ([Deg1996]) and lasers ([Pie1998]). However, while these types of transducers function well in tests determining need for maintenance when the structure is not in active use, they are not compact enough to be permanently onboard the structure during its operation as is required in SHM applications [Rag2007b].

During the past decade, piezoelectric wafer active sensors (PWASs) for actuating and detecting structural waves have been explored in several studies [Giu2002a, Lu2006, Ng2009, Nie2005, Gre2005, Zha2007a-b, Yu2005]. PWASs are small, inexpensive, nonintrusive, unobtrusive, and minimally invasive. They can be mounted on the surface of existing structures, inserted between the layers of lap joints, or placed inside composite materials [Giu2005].

In Lamb wave applications, PWASs couple their in-plane motion, resulting from the piezoelectric effect, with the Lamb wave particle motion on the material surface. They can act both as actuators and detectors of Lamb waves. Unlike the conventional narrow-band ultrasonic transducers, PWASs are broadband devices and can be tuned into selected Lamb modes. The PWAS operation principle for wave actuation is shown in Figure 22.

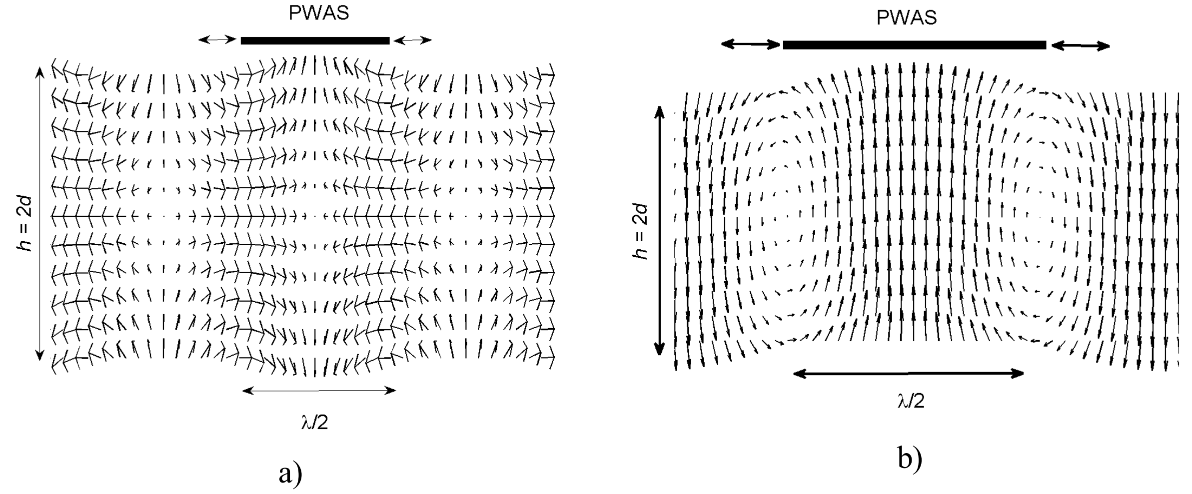

Figure 22. PWAS operation for actuating a) symmetric, b) antisymmetric Lamb wave mode.

Until the recent years, most of the progress in utilizing the PWAS technology for active structural health monitoring has been achieved empirically. However, a comprehensive modelling of the interaction between the PWAS, the structure, and the Lamb waves is needed as an essential design tool. These modelling studies have been conducted by e.g. Giurgiutiu et al. [Giu2002a, Giu2005] and Nieuwenhuis et al. [Nie2005, Gre2005].

PWASs may be square, rectangular or disc-shaped. The expressions for Lamb wave strain and displacement under PWAS actuation were first published by Giurgiutiu ([Giu2002a]) for rectangular PWAS. Giurgiutiu and Greve et al. ([Gre2005]) also studied the sensitivity of Lamb wave S_0 and A_0 mode detection with respect to PWAS size. Giurgiutiu's analytical solution predicted that a transducer of width $2a$ would generate maximum and minimum response, for Lamb wave mode i, at particular frequencies. The frequencies correspond to the cases where the transducer width, $2a$, equals an odd number of half-wavelengths or even number of half-wavelengths, respectively.

In their simulations, Greve et al. found that the rectangular PWAS sensitivity for S_0 mode is almost constant in that frequency range where the half-wavelength of the acoustic wave is longer than the PWAS's length and the wafer functions as an ideal strain sensor. At higher frequencies, such a PWAS is more than a half wavelength long, and the strain reverses sign along the transducer, leading to decreased sensitivity. PWAS sensitivity to A_0 mode is different, since in that case, strain is inversely proportional to phase velocity. The phase velocity of the A_0 mode is strongly frequency-dependent and decreases toward zero at low frequencies. Therefore, the A_0 sensitivity increases strongly with decreasing frequency.

The PWASs used in the experiments for this thesis, however, were disc-shaped. For disc-shaped actuators, the equations have been derived in axisymmetric cylindrical coordinates [Rag2004]. The equations of motion take the form

$$\left(\lambda+\mu\right)\frac{\partial\Delta}{\partial r}+\mu\nabla^2 u_r-\mu\frac{u_r}{r^2}=\rho\frac{\partial^2 u_r}{\partial t^2} \tag{81}$$

$$\left(\lambda+\mu\right)\frac{\partial\Delta}{\partial x_2}+\mu\nabla^2 u_{x_2}=\rho\frac{\partial^2 u_{x_2}}{\partial t^2} \tag{82}$$

where

$$\Delta = \left(\frac{\partial u_r}{\partial r} + \frac{u_r}{r} + \frac{\partial u_{x_2}}{\partial x_2} \right) \tag{83}$$

is the dilatation. In cylindrical coordinates

$$\nabla^2 \equiv \left(\frac{\partial^2}{\partial r^2} + \frac{1}{r}\frac{\partial}{\partial r} + \frac{\partial^2}{\partial x_2^2} \right) \tag{84}$$

The solutions for Eqs. (81) and (82) follow Bessel functions in *r* and harmonic functions in *t*:

$$\begin{aligned} u_r &= A\frac{k}{q^2 - s^2}\cosh(qx_2)J_1(kr)e^{-i\omega t} \\ u_{x_2} &= -A\frac{q}{q^2 - s^2}\sinh(qx_2)J_0(kr)e^{-i\omega t} \end{aligned} \tag{85}$$

Hence the dilatation from Eq. (83) is

$$\Delta = A\frac{\mu}{\lambda + \mu}J_0(kr)e^{-i\omega t}g\left(qx_2\right) \tag{86}$$

where

$$g\left(qx_2\right) = \begin{cases} \cosh\left(qx_2\right) & \text{for symmetric motion} \\ \sinh\left(qx_2\right) & \text{for antisymmetric motion} \end{cases} \tag{87}$$

Substituting Eqs. (85)-(87) into (81) and (82) an noting

$$\begin{aligned} \alpha^2 &= k_L^2 - k^2 = -q^2, \quad q = \mathrm{i}\alpha \\ \beta^2 &= k_T^2 - k^2 = -s^2, \quad s = \mathrm{i}\beta \end{aligned}$$

results in displacement equations

$$\begin{aligned} u_{r,s} &= A_s^* J_1(kr)\mathrm{e}^{\mathrm{i}\omega t}\left[2k^2\beta\cos(\beta d)\cos(\alpha x_2) - \beta\left(k^2 - \beta^2\right)\cos(\alpha d)\cos(\beta x_2) \right] \\ u_{2,s} &= A_s^* J_0(kr)\mathrm{e}^{\mathrm{i}\omega t}\left[2k\alpha\beta\cos(\beta d)\sin(\alpha x_2) + k\left(k^2 - \beta^2\right)\cos(\alpha d)\sin(\beta x_2) \right] \end{aligned} \tag{88}$$

where

$$A_s^* = \frac{A}{2k\beta\left(\beta^2 - \alpha^2\right)\cos(\beta d)} \tag{89}$$

for the symmetric case and

$$\begin{aligned} u_{r,a} &= A_a^* J_1(kr)\mathrm{e}^{\mathrm{i}\omega t}\left[-2k^2\beta\sin(\beta d)\sin(\alpha x_2) + \beta\left(k^2 - \beta^2\right)\sin(\alpha d)\sin(\beta x_2)\right] \\ u_{2,a} &= A_a^* J_0(kr)\mathrm{e}^{\mathrm{i}\omega t}\left[2k\alpha\beta\sin(\beta d)\cos(\alpha x_2) + k\left(k^2 - \beta^2\right)\sin(\alpha d)\cos(\beta x_2)\right] \end{aligned} \tag{90}$$

where

$$A_a^* = \frac{-A\mathrm{i}}{2k\beta\left(\beta^2 - \alpha^2\right)\sin(\beta d)} \tag{91}$$

for the antisymmetric case.

Raghavan and Cesnik [Rag2004] showed the relationship between the PWAS radius a and resulting Lamb wave strain ε_r and displacement u_r on the plate surface to be

$$\varepsilon_r\big|_{x_2=h} = -\pi\mathrm{i}\frac{a\tau_0}{\mu}\mathrm{e}^{\mathrm{i}\omega t} \times \left[\sum_{k_S}\frac{J_1(k_S a)}{k_s}\frac{N_S(k_S)}{D_S'(k_S)}H_1^{(2)}(k_S r) + \sum_{k_A}\frac{J_1(k_A a)}{k_A}\frac{N_A(k_A)}{D_A'(k_A)}H_1^{(2)}(k_A r)\right] \tag{92}$$

$$u_r\big|_{x_2=h} = -\pi\mathrm{i}\frac{a\tau_0}{\mu}\mathrm{e}^{\mathrm{i}\omega t} \times \left[\sum_{k_S}J_1(k_S a)\frac{N_S(k_S)}{D_S'(k_S)}H_1^{(2)}(k_S r) + \sum_{k_A}J_1(k_A a)\frac{N_A(k_A)}{D_A'(k_A)}H_1^{(2)}(k_A r)\right] \tag{93}$$

where

$$N_s = k_S\beta_S\left(k_S^2 + \beta_S^2\right)\cos(\alpha_S h)\cos(\beta_S h) \tag{94}$$

$$D_s = \left(k_S^2 - \beta_S^2\right)^2\cos(\alpha_S h)\sin(\beta_S h) + 4k_S^2\alpha_S\beta_S\sin(\alpha_S h)\cos(\beta_S h) \tag{95}$$

$$D_s' = \frac{dD_S}{dk_S} \tag{96}$$

$$N_A = k_A \beta_A \left(k_A^2 + \beta_A^2\right) \cos(\alpha_A h) \cos(\beta_A h) \tag{97}$$

$$D_A = \left(k_A^2 - \beta_A^2\right)^2 \sin(\alpha_A h) \cos(\beta_A h) + 4 k_A^2 \alpha_A \beta_A \cos(\alpha_A h) \sin(\beta_A h) \tag{98}$$

$$D'_A = \frac{dD_A}{dk_A} \tag{99}$$

J_1 is the Bessel function of the first kind of order 1, $H_1^{(2)}$ is the complex Hankel function of order 1, of the second type, τ_0 is the amplitude of the excitation stress applied to the plate, and h is the half-thickness of the plate.

For example, for a 1 mm thick aluminium plate with $2a$ = 6.35 mm disc-shaped PWA sensors, the resulting radial strain and displacement at the surface as a function of frequency are shown in Figure 23.

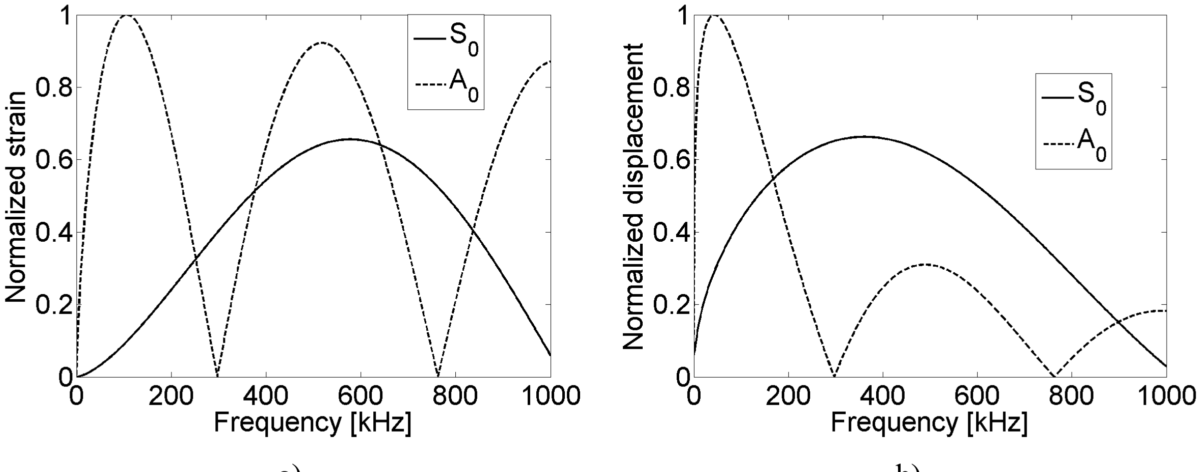

a) b)

Figure 23. a) Strain response, b) displacement response.

Raghavan and Cesnic also studied the actuating and sensing efficiency of the PWASs and found that for disc-shaped actuators, there is no one single optimum diameter value a for maximizing sensor response as such. The PWAS response is proportional to an oscillating function of a. By choosing higher values of a that yield local extrema, one can in principle keep increasing the magnitude of sensor response to harmonic excitation. However, the power consumption of the actuator increases with the actuator size. Hence, the choice of actuator length for the largest local maximum depends on the power available to drive the actuator.

4.5.5 Leaky Lamb waves

When a plate is immersed in a fluid, the acoustic energy is no longer trapped inside the plate; it leaks into the surrounding medium. Hence the guided waves generated in this case are called leaky Lamb waves (LLW) [Kun2004]. The boundary conditions for fluid-solid interface are as follows: the shear stress σ_{12} should be zero, and the normal stress and displacement components, σ_{22} and u_2, should be continuous across the interface. The leads to dispersion equation for symmetric LLW modes:

$$\begin{aligned}&-4k_s^2 p_s q_s \mathrm{i}\sin(p_s d)\cos(q_s d) - \left(2k_s^2 - k_T^2\right)^2 \cos(p_s d)\mathrm{i}\sin(q_s d)\\ &= -\frac{\rho_f p_s k_T^4}{\rho p_f}\sin(p_s d)\sin(q_s d)\end{aligned} \tag{100}$$

and for antisymmetric modes:

$$\begin{aligned}&-4k_s^2 p_s q_s \cos(p_s d)\mathrm{i}\sin(q_s d) - \left(2k_s^2 - k_T^2\right)^2 \mathrm{i}\sin(p_s d)\cos(q_s d)\\ &= \frac{\rho_f p_s k_T^4}{\rho p_f}\cos(p_s d)\cos(q_s d)\end{aligned} \tag{101}$$

where $p_f = \sqrt{k_f^2 - k_{s,a}^2}$, and ρ_f is the density of the fluid. Notice that if the right hand side of the equations vanishes (the plate is in the vacuum), these equations are simplified into those given in (66) and (67).

Viktorov [Vik1967] showed that for a solid plate immersed in a liquid, one additional real root of the dispersion equation appears at every frequency for a phase velocity value that is less than the longitudinal wave velocity in the fluid or the transversal wave velocity in the solid. This wave mode at the fluid-solid interface is known as Scholte or Stonely-Scholte wave mode [Sto1924, Sch1942]. Other than this additional mode, the presence of fluid (e.g. water) does not significantly affect the other Lamb wave modes.

When the plate is immersed in air, Lamb waves leak energy into air and thus they are strictly speaking leaky Lamb waves. However, the intensity of the energy leaking into the surrounding air in atmospheric pressure is very small. Therefore it is generally ignored and the waves in plates immersed in air are treated as Lamb waves.

4.5.6 Mode conversion

When Lamb waves are reflected from a free edge of a plate, they are partially reflected as the original wave mode and partially as the other wave modes that can exist on that frequency and plate thickness. In reflection the total energy is preserved. This phenomenon is known as mode conversion. It is well known that the mode conversion from a symmetric scatterer (like the plate edge) can only occur within the same family modes as the incident mode; that is, incident antisymmetric modes can only be converted to other antisymmetric modes, and symmetric modes only to symmetric modes [Cho1996].

If the frequency is low and/or the plate is thin so that only S_0 and A_0 wave modes exist, the reflected waves are of the same mode as the incident waves. In thicker plates or at higher frequencies, the incident waves are partially converted into other wave modes. This phenomenon is very complicated to analyse and model. Cho and Rose [Cho1996] developed a 2-D elastodynamic boundary element method for mode conversion studies and applied it to a steel plate in a frequency-thickness range where A_0 and A_1, and S_0, S_1 and S_2 modes exist. They found that the reflection factor of incident A_0 wave is 1 below the cut-off frequency of the A_1 mode as expected, and then decreases rapidly to its minimum when most of the energy converts to A_1 mode. After this point, the direction of mode conversion changes from A_1 to A_0, and eventually the A_0 mode becomes again the dominant reflected mode. The similar trends can be found in the A_1 incidence case, only vice versa – the reflected A_1 mode here is at its minimum where, in the A_0 incidence case, it was at its maximum.

The symmetric mode conversion analysis revealed a dominant interaction between S_0 and S_2 modes in a manner similar to antisymmetric case, while the S_1 mode is nearly independent on the other two modes and is hardly affected by the mode conversion phenomenon.

Mode conversion problem becomes even more complicated when the waves are partially reflected and transmitted through a discontinuity in the structure (hole, crack, change of thickness etc.). Alleyne and Cawley [All1992] studied the interaction of individual Lamb waves with a variety of defects simulated by notches using finite-element analysis. They showed that the sensitivity of individual Lamb waves to discontinuities (notches) is dependent on the product of frequency and thickness, the mode type (symmetric or antisymmetric), the mode order, and the geometry of the notch. In the case of discontinuities, the mode conversion can also occur from antisymmetric to symmetric mode and vice versa.

For the sake of simpler NDT analysis, it is advisable to use the *fd* range where only S_0 and A_0 modes exist, if possible.

4.5.7 Adiabatic waves

As stated before, at a given frequency *f*, each Lamb wave propagating in a plate with constant thickness $2d$, has a constant phase velocity and a constant wave number. When the plate or structure under study is of slowly varying thickness, guided waves are called adiabatic modes [Arn1986, Gal1998]. An adiabatic mode adapts to the thickness variation: its phase velocity and wave number change continuously during propagation, depending on the local thickness so that the instantaneous velocity equals the Lamb phase velocity corresponding to the local frequency-thickness product.

When a guided wave at a given frequency is propagating downslope in the direction of thickness decreasing, it will reach its thickness cut-off if the thickness becomes small enough. El-Kettani et al. have shown through numerical simulations and experimental results that such wave is reflected and propagates upslope in the plate, and that it can give rise to another guided wave which can continue its propagation downslope [Elk2004].

5. Energy efficient solutions for measuring and reconstructing Lamb wave response

5.1 Introduction

The complicated dependence of Lamb wave propagation velocity on frequency, wave modes and structure geometry makes the analysis of measured PWAS responses to wave-induced strains rather cumbersome. The physics of Lamb waves have been reviewed in Chapters 3-4.

The Shannon sampling theorem applied directly to ultrasonic SHM defect detection leads to the requirement of high sampling rate and therefore large amount of data. A theoretical minimum sampling rate e.g. for a response containing frequency components up to 500 kHz is 1 MS/s. In practice, this theoretical minimum does not suffice for defect detection purposes, and even though the measurement periods are generally of the order of hundreds of microseconds, the number of data samples is several hundreds or thousands. In a self-powered, integrated on-line SHM system transferring data wirelessly, the limited supply of power prevents high sampling rates and large amounts of data. The aim of this chapter is to show that with appropriate sampling and signal reconstruction, the defects can be detected and their location estimated with only a small number of samples measured from the Lamb wave response [Hyt2008].

5.2 Actuation burst

Lamb waves propagate with a high velocity, and different modes have different velocities and dispersion properties. This affects both on the waveform measurement time and amplitude resolution and the selection of the actuation burst shape, frequency and duration. In order to find optimal actuation burst in the sense of power optimization of the measurement system, PWAS responses to different actuation burst waveforms were studied experimentally using ACESS SCS-3200 measurement system and a test plate made of aluminium with four PWASs fastened to it [Ace2009].

The most commonly used actuation signal is a *n*-period Hanning modulated sinusoid burst:

$$V_a(t) = \frac{1}{2}\left(1 - \cos\frac{2\pi t}{T}\right)\sin(2\pi f_c t), \quad 0 \le t \le T \tag{102}$$

where f_c is the centre actuation frequency and $T = n/f_c$ is the duration of the burst. The magnitude of the Fourier transform of this signal is [Ben1986, Rag2004]

$$\begin{aligned}|V_a(f)| = \frac{n}{2f_c}\Bigg| & \operatorname{sinc}\left(\frac{2\pi n}{f_c}(f - f_c)\right) + (-1)^{2n+1}\operatorname{sinc}\left(\frac{2\pi n}{f_c}(f + f_c)\right) \\ & + \frac{1}{2}\left\{\operatorname{sinc}\left(\frac{2\pi n}{f_c}\left(f - \frac{2n-1}{2n}f_c\right)\right) + (-1)^{2n+1}\operatorname{sinc}\left(\frac{2\pi n}{f_c}\left(f + \frac{2n-1}{2n}f_c\right)\right)\right\} \\ & + \frac{1}{2}\left\{\operatorname{sinc}\left(\frac{2\pi n}{f_c}\left(f - \frac{2n+1}{2n}f_c\right)\right) + (-1)^{2n+1}\operatorname{sinc}\left(\frac{2\pi n}{f_c}\left(f + \frac{2n+1}{2n}f_c\right)\right)\right\}\Bigg|\end{aligned} \tag{103}$$

where $\operatorname{sinc}() = \sin()/()$. The result of (103) is shown in Figure 24.

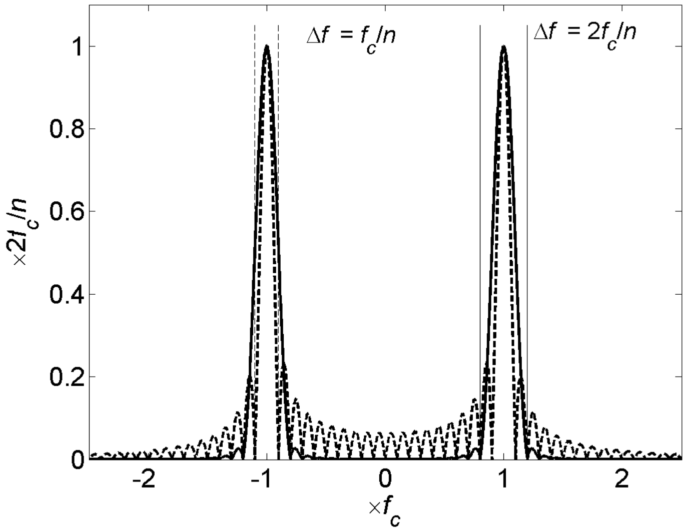

Figure 24. Relationship between actuation burst duration and its frequency bandwidth. f_c is the centre actuation frequency. Dashed line: sinusoidal burst without modulation; uniform line: Hanning-modulated burst.

The first two terms on the right-hand side in Eq. (103) correspond to the contribution of the unmodulated sinusoid truncated to a burst with a boxcar window, and the last four terms are due to the Hanning window. From Eq. (103) and Figure 24 it can be seen that the peak value of $|V_a(f)|$ is $n/(2f_c)$. The width of the principal lobe in the frequency domain of the unmodulated burst is f_c/n and of the modulated burst, $2f_c/n$. These relations can be used to control the frequency bandwidth of the excitation signal in order to reduce dispersion. A five-period burst is widely used for its good dispersion characteristics [Roh1999, Ihn2004].

The generation of the actuation burst must also be analyzed from the energy efficiency point of view. Technically the simplest and therefore also most energy efficient waveform to generate is a positive square wave, which is a simple on-off signal. Filtering a square wave with a band-pass filter was also tested in order to produce an actuation burst resembling the Hanning-modulated sinusoid. However, implementing an analog active band-pass filter requires more electronic components and increases energy consumption. Also, the filtered burst had a vibrating “tail” which disturbed the measurements. Therefore the suitability of simple square wave burst for Lamb wave actuation was analyzed and tested. The actual difference in the energy consumption was not simulated or tested.

A square wave can be presented as a Fourier series

$$V_a(t) = \frac{4}{\pi}\sum_{k=1}^{\infty}\frac{1}{2k-1}\sin(2\pi(2k-1)f_c t), \quad 0 \le t \le T \tag{104}$$

The magnitude of the Fourier transform of this signal truncated to a burst with a boxcar window is

$$\begin{aligned}|V_a(f)| = \frac{n}{2f_c}\frac{4}{\pi}\Bigg|&\operatorname{sinc}\left(\frac{2\pi n}{f_c}(f-f_c)\right)+(-1)^{2n+1}\operatorname{sinc}\left(\frac{2\pi n}{f_c}(f+f_c)\right)\\ &+\frac{1}{3}\left\{\operatorname{sinc}\left(\frac{2\pi n}{3f_c}(f-3f_c)\right)+(-1)^{2n+1}\operatorname{sinc}\left(\frac{2\pi n}{3f_c}(f+3f_c)\right)\right\}\\ &+\frac{1}{5}\left\{\operatorname{sinc}\left(\frac{2\pi n}{5f_c}(f-5f_c)\right)+(-1)^{2n+1}\operatorname{sinc}\left(\frac{2\pi n}{5f_c}(f+5f_c)\right)\right\}+\ldots\Bigg|\end{aligned} \tag{105}$$

The result of (105) is shown in Figure 25. The peak value of $|V_a(f)|$ is $4n/(2\pi f_c)$. The width of the harmonic frequency lobe centred at kf_c in the frequency domain of the modulated burst is kf_c/n, where $k = 1,3,5\ldots$. Thus the width of the centre frequency lobe equals that of an unmodulated sinusoid burst. Since the Lamb waves are dispersive, the wide frequency band of the square wave with the harmonic frequencies $f_c*(2k-1)$ may cause problems. However, the harmonic components do not in practice cause problems because their frequencies are so high that the corresponding PWAS response amplitudes are much lower than those of the centre frequency due to that PWAS is less sensitive at short wavelengths (high frequencies). Therefore the positive square wave burst is comparable with the sinusoid burst for Lamb wave actuation.

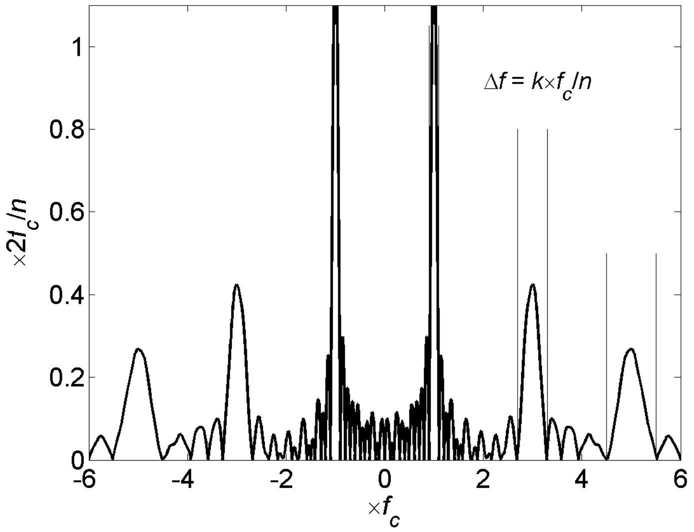

Figure 25. Relationship between the square wave actuation burst duration and its frequency bandwidth. f_c is the centre actuation frequency. *k* is an odd integral multiplier of f_c.

The effect of the different actuation bursts on PWAS response was verified experimentally. The result given by 10V peak-to-peak, five-period Hanning modulated actuation burst was compared with the results of an unmodulated sinusoidal 10V peak-to-peak five-period burst and with a 5V peak-to-peak five-period, positive square wave burst, all with centre frequency f_c of 450 kHz (Figure 26). They were amplified 20 dB in ACESS system for actuating the sensors.

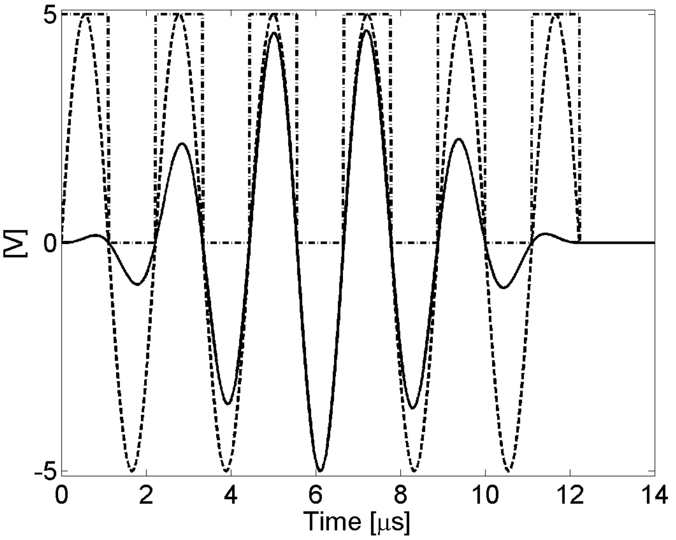

Figure 26. Actuation burst choices.

Figure 27 shows the measured S_0 mode responses for the actuation bursts studied. The effect of modulation is clear: the response attenuates more rapidly and thus the wave modes with velocities close to each other are possibly easier to separate. Responses to the pure sinusoid and positive square wave are close to each other, as expected. The time resolution of their response can be improved by using a shorter actuation burst. As a final outcome of this analysis done by the author, the measurement system developed in this project generates a 3-5 period, 10V peak-to-peak positive square wave burst for PWAS actuation.

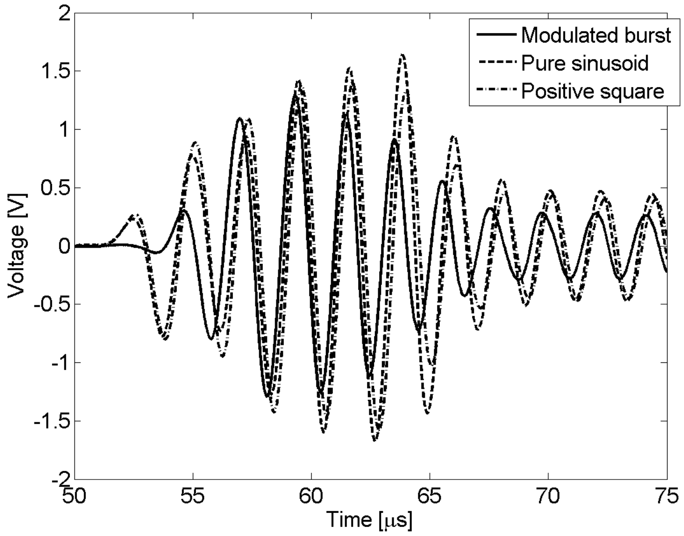

Figure 27. Responses measured with different actuation bursts.

5.3 Developed measurement system prototype

The outcome of the project is the Lamb wave based SHM system prototype, whose operating principle is shown in Figure 28. The system was implemented at VTT Technical Research Centre of Finland. The author's contribution to the development of the system was as follows:

- theoretical analysis and experimental verification of the applicability of a positive square wave actuation burst instead of Hanning modulated sinusoid for Lamb wave based SHM,
- determining the minimum required data samples for signal reconstruction, which are the peak values of the PWAS response half-periods plus a time label for either positive or negative peak value for each period,
- comparing different reconstruction techniques and selecting the one most suitable for the system, and
- determining the required amplitude and phase response characteristics required for the analog band-pass filter used for filtering the PWAS response before sampling it such that the response waveform distortion due to different amplification and phase shift of different frequencies does not lose the wave mode structure of the response for further response analysis.

The measurement system utilizes a Field Programmable System Level Integrated Circuit (FPSLIC) based measurement board developed at VTT in an earlier project. This board was supplemented with a new measurement interface I/O board and PWAS board for actuating and measuring Lamb waves, developed during this project. The I/O board has two 16-bit, 4-channel A/D transformers, 64 Mbit flash memory and a 12-bit, 4-channel D/A transformer for actuation burst generation. The actuation burst is a 3-5 period, 10 V peak-to-peak, 400-430 kHz positive square wave burst generated with a field-effect transistor (FET) circuit.

The measurement principle presented in Figure 28 is based on the assumption that the length of each period of the waveform equals to $1/f_c$ and thus the peak value of each half-period occurs at constant time interval from the zero-crossing point. The clock rate of the FPSLIC timer is f_{clk} = 12 MHz and the actuation burst centre frequency is f_c. This gives $N_t = f_{clk}/f_c$ clock "ticks" per period.

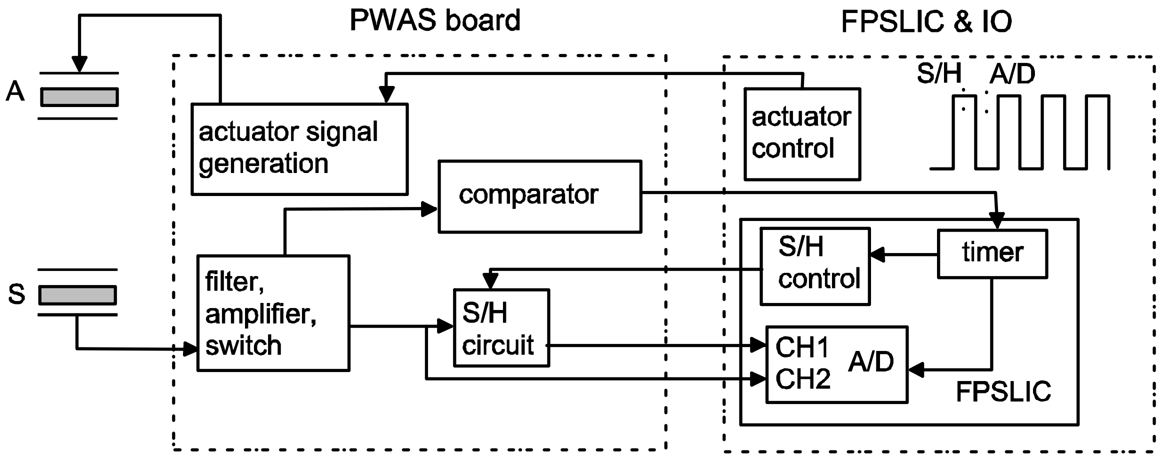

Figure 28. The measurement principle. S/H stands for sample-and-hold circuit, A/D stands for analog-to-digital converter.

The measurement procedure is in summary as follows:

1. Actuator burst frequency, number of periods in burst, and actuator PWAS are selected using FPSLIC.
2. Lamb waves are actuated with the selected PWAS.
3. PWAS response is measured from one of the other PWASs:

3a. PWAS response voltage is filtered with an analog band-pass filter.

3b. The filtered response is directed to analog-to-digital (A/D) converter both directly (channel 2) and through a sample-and-hold (S/H) circuit (channel 1).

3c. The comparator is used to detect the zero-crossing points of the filtered response. When an upward slope zero-crossing is detected, it triggers the 12 MHz FPSLIC timer. After $N_t/4$ timer counts a sample of positive half-period (assumed peak value) is saved into S/H circuit. Then, after $3N_t/4$ timer counts a sample of negative half-period is taken. The two peak values from channels 1 and 2 are read simultaneously. The timer gives the exact time stamp for the negative peak.

One full measurement cycle consists of (1) actuating and sensing ultrasonic waves between four piezoelectric actuator-sensor transducers (total of six different signal paths), (2) tracking down the positive and negative peak values and time stamp from the sensor signal and (3) sending the tracked values via radio to PC for signal reconstruction and analysis.

By using this principle, there are only three data values (positive peak, negative peak and one time stamp) per waveform period to be transferred. The time stamp for the positive peak can be determined as a function of the clock rate of the timer. Theoretical time stamp resolution is 1/12 MHz, i.e. 83 ns. Wireless data transfer is implemented by utilizing commercial 2.4 GHz WPAN (Nanonet) radio technology capable of sending 2 Mbit/s [Nan2006].

As mentioned above, the voltage response from PWAS is band-pass filtered. The amplitude and phase response of the analog wide-band filter are shown in Figure 29. The purpose of the filter is to reduce noise and provide amplification to the response to compensate the low voltage level of the actuation burst. The filter is designed to have a flat amplitude response and linear phase response around the actuation frequency in order to minimize distortion in the response shape. The large bandwidth allows some variation in the actuation frequency. The effect of band-pass filtering to a 450 kHz PWAS response is shown in Figure 30.

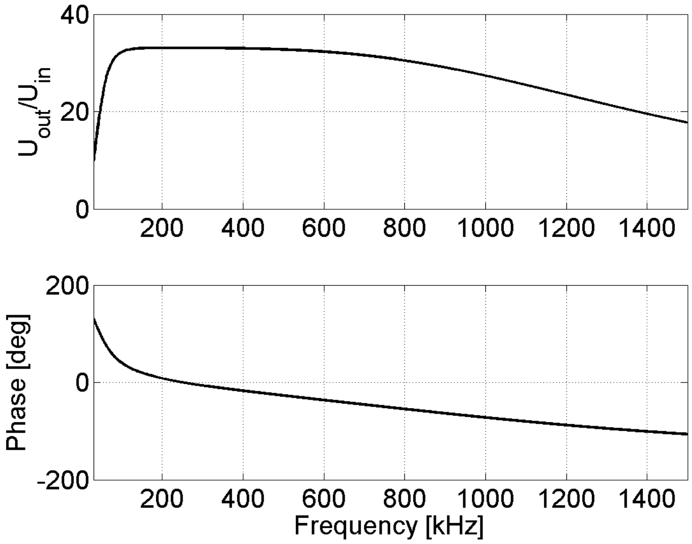

Figure 29. Amplitude and phase response of the band-pass filter used in filtering the PWAS response.

The measurement method can be improved by finding the trigger point at both positive and negative slopes and using a peak detection circuit.

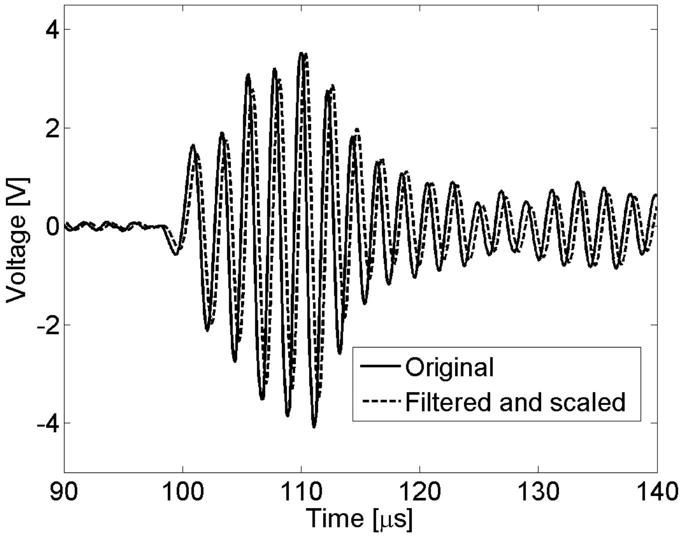

Figure 30. The effect of band-pass filtering to a PWAS response. Actuation burst was 450 kHz, 5-period positive square wave. The amplitude of the filtered signal is scaled to match the original signal for improved visualization of the shape preservation.

5.3.1 Energy consumption and harvesting

With optimized system, the approximate energy consumption for one complete measurement cycle (i.e. Lamb wave actuation and PWAS response measurement from six signal paths) carried out with the system presented in Figure 28 with four PWASs is 3.7 mJ. With Nanonet radio, the maximum amount of data per packet sent is 128 bytes. Each data sample takes 2 bytes, and each transmitted packet can contain approximately 120 bytes, i.e. 60 samples of actual data. Sending one maximum size data packet consumes approximately 150 μJ of energy. In standby mode, the radio consumes approximately 7 mJ, but only 4.4 μJ in sleep mode [Nan2006]. The measurement electronics and the FPSLIC processor card consume approximately 120 mJ of energy when active.

Let us study the data transfer related energy consumption in the following example case. During a 224 μs measurement period of a PWAS response actuated at 450 kHz, the sampling rate of 6.25 MHz provides 1400 samples, whereas the suggested method only takes 258 samples. Reduction in data samples to be transferred is almost 82%. Compared with the near theoretical minimum, 2 MHz, the reduction is about 42% (from 448 to 258 samples). The reduction ratio depends on the waveform, i.e. the number of turning points in the PWAS response. The total number of data points collected from the six signal paths and the amount of transmitted data packets as well as the consumed energy with different sampling rates are shown in Table 4.

Table 4. Number of data points and the energy consumption estimate of wireless data transfer for six signal path measurements at different sampling rates.

Sampling method	Samples	Bytes	Data packets	Energy
Suggested	1548	3096	26	3.8 mJ
2 MHz even	2688	5376	45	6.6 mJ
6 MHz even	8064	16128	135	19.8 mJ
12 MHz even	16128	32256	269	39.5 mJ

The total energy consumption of one measurement cycle with the suggested method is thus approximately (3.8+3.7) mJ = 7.5 mJ. The amount of energy consumed increases in direct proportion with the number of samples transmitted. Therefore, minimizing the number of transmitted samples reduces energy consumption.

The aim of the research project presented in [Muu2008] was to develop a self-powered, Lamb wave based SHM system. From the most common potential ambient energy sources described in Chapter 1.4, vibrations of the surrounding structures were considered the best solution for the SHM application targets within this project. The implemented energy harvesting module consists of a generator, power conversion and energy storage elements. The energy storage element then feeds energy to the measurement and radio module electronics. The harvesting element was designed and implemented at VTT Technical Research Centre of Finland.

The generator element was a low-loss mass-spring resonator. The voltage converter was of double boost structure [Muu2008]. The measurements showed that with vibration of 50 Hz and 8 mm/s peak velocity, the system charges the 3.0 V battery with maximum charging power of 23 mW. Charging power achieved with vibration originating from a vibrating engine frame was 4.5 mW. In this realistic case, the energy harvesting module is able to charge the SHM system in Figure 28 so that one full cycle of measurements can in optimized case be performed every three seconds.

Without power optimization (using higher operating voltage and external voltage regulators), the measurement system prototype consumed 1200 mJ. With this consumption, the charging capacity of the energy harvesting module enables repeating one measurement cycle up to 17 times per hour.

5.4 Comparisons to some competing technologies

Research groups around the world are working on wireless and self-powered, energy efficient SHM systems. For example, Zhao et al. [Zha2007a,b] have suggested a PWAS based defect detection, localization and growth monitoring system for an aircraft wing combined with two different methods for wirelessly interrogating the sensor/actuator network. The first one utilized a pair of reactive coupling monopoles to deliver RF tone-burst interrogation pulses directly to the polyvinylidene fluoride (PVDF) comb transducers for generating ultrasonic guided waves and to receive the response signals from the piezoelectric transducers. In the experiment, they used a Matec® TB-1000 tone-burst signal generator/receiver card to generate 3 MHz, 300 V peak-to-peak windowed sinusoidal pulses to the PVDF transducer through the transmission and onboard monopoles. A Vectronics® active monopole and a Datel® PCI-417M2 40 megasamples per second (MSPS) digitizer were used for receiving and digitizing the return signal. They used time domain averaging to reduce the noise level in the measured response, but it was still relatively high compared with the wired case. In addition, there was a long main-bang in the beginning of the measured signal introduced by the active antenna. This may blind the defect signal if the defect is too close to the transducer. The fundamental deficiency of this approach was the short coupling distance (7-10 cm) for wireless RF energy coupling.

The second approach was a small local diagnostic device that can be embedded in the wing and transmit the digital signals FM-modulated on a 915 MHz carrier. The device had an ultrasonic pulser that was able to generate 350 kHz, 70 V peak-to-peak sinusoidal tone-burst signals, a multiplexed A/D board with a programmable gain amplifier for multi-channel data acquisition, a microprocessor for circuit control and data processing, and a wireless module for data transmission. Power to the electronics is delivered wirelessly at microwave band with an antenna–rectifier (rectenna) array conformed to the aircraft body, providing at least 15 V, 100 mW of DC power, from an 8 W, 100 GHz source at range between 0.5 and 1 m. The tone-burst pulser design was based on a halfbridge series resonant inverter with an isolated output. It was able to generate 70 V peak-to-peak tone-burst pulses every 10 ms, with the centre frequency tunable from 300 to 400 kHz. In order to interface with the transducer network on board, a multiplexer and de-multiplexer (mux–demux) was needed to interrogate each pair of actuator/sensor elements. The developed mux-demux was able to pass 200 V peak-to-peak ultrasonic signals and measure one round of eight-element sensor array within a minute. The estimated power consumption of the system components were as follows: 30 mW for microcontroller unit, 33 mW for 8-bit A/D converter, 30 mW for pulser, 60 mW for mux-demux, 30 mW for RF transmission and 20 mW for RF reception. The time durations for each operation required for energy consumption calculations were not specified.

As an other example, Lallart et al. [Lal2008] suggested a fully integrated, self-powered structural health monitoring scheme applying microgenerators combined with the synchronized switch harvesting on inductor (SSHI) method for harvesting energy from vibration, and Autonomous Wireless Transmitters and Receivers (AWTs and AWRs) for Lamb wave generation and detection. The AWTs are modules with built-in SSHI energy harvesting using piezoelectric patches, piezoelectric Lamb wave actuation with 3.3 V, one-period square burst (typically 50 µs of length), and RF emitter for communication. These operations were managed using an ultra-low power microcontroller (Microchip PIC 16F688 featuring *nanoWatt* technology).

The AWR modules also used the SSHI energy harvesting. The electric energy was stored to a 940 µF capacitor. The AWR had a low-power 433.92MHz RF receiver (Aurel RX-4M30RR01SF), for synchronization with the AWT, and a AM-RF transmitter (433.92MHz Aurel TX-4MDIL) for sending an identifier and the damage control results to the base station. The Lamb wave produced by the AWT was detected with a piezoelectric patch. The signal was processed using a second order filter, a true-RMS IC (Linear Technology LTC1966) and an amplifier. The result of the processing was then sent to the base station, as well as the RF identifier of the AWR. These operations were also supervised by a Microchip PIC16F688 microcontroller. The existence of a defect was estimated by calculating a damage index based on comparisons between the RMS values of the Lamb wave responses in the current and reference state. The total energy needed for one AWT for every SHM interrogation cycle was 1.2 mJ, and for every AWR the corresponding reading was 1.68 mJ. With the aim of performing one structural health interrogation every ten seconds, Lallart et al. discovered that the energy requirements for a system with one AWT and one AWR, both supplied with three harvesting patches, are fulfilled if the magnitude of stress over the harvesting elements exceeds approximately 2 MPa.

Compared with these competing technologies, the suggested measurement system is competitive when the energy efficiency is considered. One significant energy sink is generating the actuation burst, which is different in all three systems (Zhao: 70 V_{pp} sinusoidal burst, Lallart: 3.3 V_{pp}, one period square, the suggested system: 10 V_{pp}, 3-5 period positive square wave). The main difference between the suggested system and the competing ones is that in the suggested system, the PWASs are wired, and only the actuation/detection/radio unit is powered wirelessly. The wiring of the PWASs was not considered an issue in the case of the application targets in this project, but as the system designs presented above show, actuating and sensing the PWASs wirelessly is a strongly emerging concept. It is obvious that the Lallart's local SSHI harvester is better suited for many industrial applications than the Zhao's RF or microwave antenna based method of supplying power to the sensors, since the latter requires an external power transmitter at very close distance from the SHM target. However, the cost for AWR and AWT type sensors per unit is much higher than for a single PWAS, and thus it may still be more economical to use wired PWASs, if possible.

5.5 Signal sampling and reconstruction

As discussed later in Chapters 6 and 7, the relative change in the variance of the first wave mode burst arriving at the sensor suffices for defect indication in isotropic (metallic) structures. However, in anisotropic structures, more advanced signal analysis methods are generally required. Reconstructing the signal from the samples taken from it enables both simple variance analysis and more advanced Lamb wave response analysis, e.g. chirplet analysis.

5.5.1 Fourier series method

The Shannon sampling theorem requires the sampling frequency to be at least twice the highest frequency present in the sampled signal [Pri1981]. This criterion satisfied guarantees correct reconstruction of a signal from its Fourier transform when the reconstruction (or signal synthesis) is done on the same time instants as the original signal samples were taken. In practice, the signal duration is limited and since the frequency resolution of its FFT is inversely proportional to the number of samples taken, the error in the estimated frequencies and phases of the signal components results in distorted reconstruction when an arbitrary time scale with smaller sample intervals than the original one is used for reconstruction, as is the case in this application. Therefore a sampling rate of at least 5 times the maximum frequency is recommendable.

An example of this is shown in Figure 31. Centre frequency f_c of the Hanning modulated five-period actuation signal is 450 kHz. Frequency band of the signal is approximately $f_c \pm (f_c/5) =$ 360…540 kHz. Allowing some bandwidth for dispersion and superposing of the wave modes, the theoretical minimum for the sampling rate would then be about 2×1 MHz = 2 MHz. The original signal **x** is reconstructed from the sampled signal $\mathbf{x}_s$ as follows:

Step 1. Calculate the discrete Fourier transform (DFT) of $\mathbf{x}_s$, $\mathbf{F}_{xs}$ [Opp1989]:

$$\mathbf{F}_{xs}(k) = \sum_{n=0}^{N-1} \mathbf{x}_s(n) \mathrm{e}^{-\mathrm{i}(2\pi/N)kn} \;;0 \le k \le N-1 \tag{106}$$

where N is the length of $\mathbf{x}_s$. $\mathbf{F}_{xs}$ is a two-sided DFT, so the second half of it is redundant. The amplitudes of the sinusoid components are thus $2\left|\mathbf{F}_{xs}(k)\right|$.

Step 2. Reconstruct an estimate $\hat{\mathbf{x}}$ for the original signal as a sum of cosines with coefficients $2\left|\mathbf{F}_{xs}(k)\right|$ and phase angles $\angle \mathbf{F}_{xs}(k)$ using arbitrary time scale t:

$$\hat{\mathbf{x}}(t) = \frac{1}{N}\left\{ \mathbf{F}_{xs}(0) + \sum_{k=1}^{N/2} 2\left|\mathbf{F}_{xs}(k)\right| \cos(2\pi f_k t + \angle \mathbf{F}_{xs}(k)) \right\} \tag{107}$$

where $f_k = f_s\, k/N$.

As shown in Figure 31, the Fourier series reconstruction captures the waveform and local peak values almost accurately with sampling rate of 6.25 MHz, but with sampling rate 2.08 MHz, the error is as much as 10% of the peak response value.

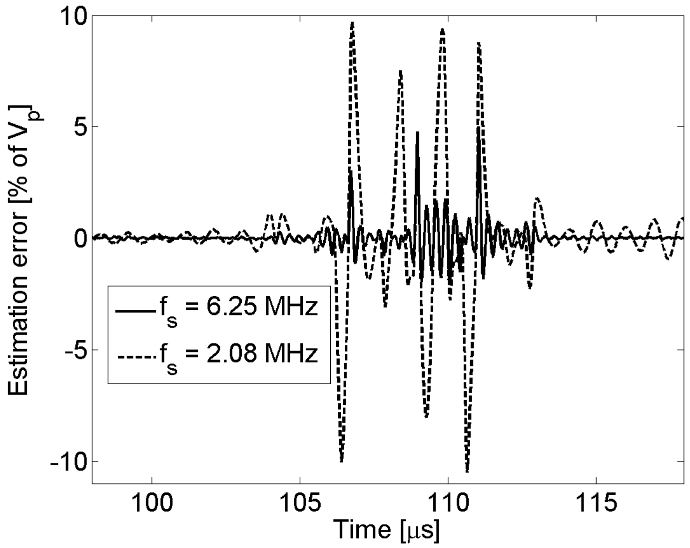

Figure 31. DFT reconstruction errors as percentage of peak response voltage from uniform sampling at different sampling rates. The errors result from the signal in reality containing frequencies higher than twice the sampling rate.

According to the Shannon sampling theorem, there should be no reconstruction error if the sampling rate meets the criterion of being at least twice the highest frequency present in the sampled signal. Spectral analysis of the PWAS response reveals that although the frequency content of the signal is dominantly within the expected range, 300…600 kHz, the signal in reality contains nonzero frequency components even up to 4 MHz. These components, albeit very low in amplitude (0.1…0.25% of the 450 kHz amplitude), result in the reconstruction error seen in Figure 31. Low-pass filtering the response before sampling would ensure that the minimum sampling rate criterion is satisfied and signal reconstruction would be perfect. However, care must be taken in the selection of the analog low-pass filter parameters in order to avoid significant waveform distortion due to different amplification and phase shift of different frequency components of the signal. Figure 32 shows the reconstruction error when the method is applied to a PWAS response filtered with the band-pass filter presented in Figure 29. The upper cut-off frequency for the filter was approximately 1.2 MHz, so the 2.08 MHz sampling frequency is still below the theoretical minimum, but the reconstruction error is significantly reduced from Figure 31. The small error remaining with sampling rate 6.25 MHz is caused by using a reconstruction time scale with smaller sample interval than that of the original sampled signal.

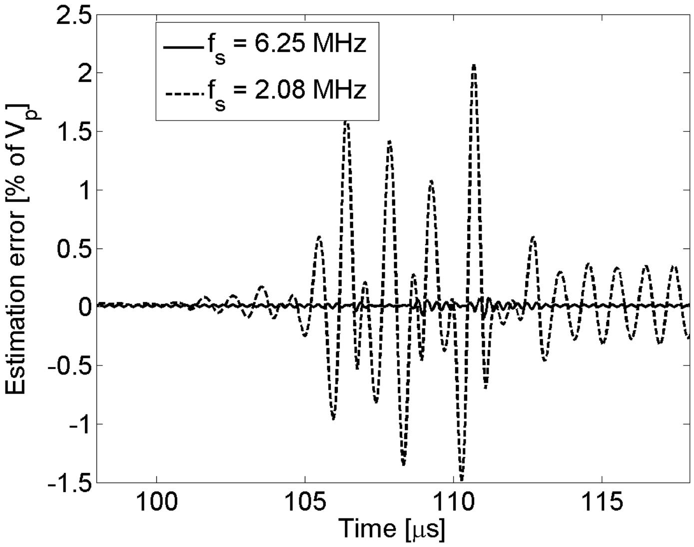

Figure 32. DFT reconstruction errors as percentage of peak response voltage from uniform sampling at different sampling rates. The PWAS response was band-pass filtered before sampling.

The reconstruction based on Fourier series can be implemented using Fast Fourier Transform (FFT). The energy consumption of FFT may become an issue if, in the future, the reconstruction and further signal analysis need to be done within local sensor nodes instead of a computer. Therefore the author suggests a different measurement and reconstruction approach, which is described next.

5.5.2 Monotone piecewise cubic interpolation method

If the turning points (i.e. the local positive and negative peaks) of the waveform and their time stamps are known, the waveform can be reconstructed from them using an interpolation technique. Assuming that short-term variation in frequency (i.e. within time window of length $T = 1/f_c$) is negligible, time stamp t_1 is required only for positive or negative peak, and the time stamp t_2 for the other can be estimated as $t_2 = t_1 + T/4$. By using this principle, there are only three data values (positive peak, negative peak and one time stamp) per waveform period to be transferred.

The time series resulting from the suggested sampling method is at irregular intervals in time. For most signal analysis methods applied to SHM, e.g. for STFT or cross-correlation analysis, the signals are expected to be sampled at regular intervals. Therefore the waveform reconstruction has to be done at regular intervals. Fourier series method could be applied also to irregularly sampled data, but estimating the Fourier transform is in that case a tedious process and thus not suitable for energy efficient solutions (see e.g. [Mas2006, Mas2009]). A simpler reconstruction with samples at irregular intervals is achieved by shape-preserving piecewise cubic interpolation introduced by Fritsch and Carlson in [Fri1980].

Fritsch and Carlson's shape-preserving piecewise cubic interpolation meets the demand of producing a monotonic function to fit monotonic data without generating artefacts, such as "bumps" or "wiggles". It suits very well for reconstructing Lamb wave responses generated with PWAS, which basically consist of near-sinusoid half-periods with varying amplitude and duration. Interpolation is also a rapid and energy efficient reconstruction method.

Let P: $a = x_1 < x_2 < \ldots < x_n = b$ be a partition of the interval $I = [a, b]$. Let $\{f_i : i = 1,2, \ldots ,n\}$ be a given set of monotonic data values at the partition points (knots); that is, we assume either $f_i \le f_{i+1}$ ($i = 1,2,\ldots,n -1$) or $f_i \ge f_{i+1}$ ($i = 1,2,\ldots,n -1$). The goal is to construct on the partition P a piecewise cubic function $p(x) \in \mathcal{C}^1[I]$ such that

$$p(x_i) = f_i, \qquad i = 1,2,\ldots, n \tag{108}$$

and $p(x)$ is monotonic.

In each subinterval $I_i = [x_i, x_{i+1}]$, $p(x)$ is a cubic polynomial which may be represented as follows:

$$p(x) = f_i H_1(x) + f_{i+1} H_2(x) + d_i H_3(x) + d_{i+1} H_4(x) \tag{109}$$

where $d_j = p'(x_j)$, $j = i$, $i + 1$, and the $H_k(x)$ are the cubic Hermite basis functions for the interval I_i:

$$\begin{aligned} H_1(x) &= \phi((x_{i+1} - x)/h_i) \\ H_2(x) &= \phi((x - x_i)/h_i) \\ H_3(x) &= -h_i \psi((x_{i+1} - x)/h_i) \\ H_4(x) &= -h_i \psi((x - x_i)/h_i) \end{aligned} \tag{110}$$

where $h_i = x_{i+1} - x_i$, $\phi(t) = 3t^2 - 2t^3$ and $\psi(t) = t^3 - t^2$.

Let $\Delta_i = \left(f_{i+1} - f_i\right)/h_i$ be the slope of the line segment joining the data to be interpolated. A necessary condition for monotonicity is that

$$\operatorname{sgn}(d_i) = \operatorname{sgn}(d_{i+1}) = \operatorname{sgn}(\Delta_i) \tag{111}$$

Further, if $\Delta_i = 0$, then $p(x)$ is monotonic on I_i if and only if $d_i = d_{i+1} = 0$. Therefore, an algorithm for constructing a piecewise cubic interpolant to $\{(x_i, f_i) : i = 1,2,\ldots,n\}$ is essentially a procedure for calculating the derivative values $d_1, d_2, \ldots, d_n$.

Expanding $p(x)$ about $x = x_i$ we obtain

$$p(x) = \left[\frac{d_i + d_{i+1} - 2\Delta_i}{h_i^2}\right]\left(x - x_i\right)^3 + \left[\frac{-2d_i - d_{i+1} + 3\Delta_i}{h_i}\right]\left(x - x_i\right)^2 + d_i\left(x - x_i\right) + f_i \tag{112a}$$

$$p'(x) = \left[\frac{3\left(d_i + d_{i+1} - 2\Delta_i\right)}{h_i^2}\right]\left(x - x_i\right)^2 + \left[\frac{2\left(-2d_i - d_{i+1} + 3\Delta_i\right)}{h_i}\right]\left(x - x_i\right) + d_i \tag{112b}$$

Let $\alpha_i = d_i/\Delta_i$ and $\beta_i = d_{i+1}/\Delta_i$ be the respective ratios of the endpoint derivatives to the slope of the secant line, i.e. line segment joining the data to be interpolated. Then $d_i + d_{i+1} - 2\Delta_i = \left(\alpha_i + \beta_i - 2\right)\Delta_i$ and $p(x)$ is monotonic if $\alpha_i + \beta_i - 2 \le 0$.

Lemma 1: If $\alpha_i + \beta_i - 2 \le 0$, then $p(x)$ is monotonic in I_i if and only if (111) is satisfied [Fri1980].

Next we observe that $p'(x)$ has a unique extremum at

$$x^* = x_i + \frac{h_i}{3}\left[\frac{2\alpha_i + \beta_i - 3}{\alpha_i + \beta_i - 2}\right] \tag{113}$$

and

$$p'(x^*) = \phi(\alpha_i, \beta_i)\Delta_i \tag{114}$$

where

$$\phi(\alpha_i, \beta_i) = \alpha - \frac{1}{3}\frac{(2\alpha + \beta - 3)^2}{(\alpha + \beta - 2)} \tag{115}$$

Lemma 2: If $\alpha_i + \beta_i - 2 > 0$, and (111) is satisfied, then $p(x)$ is monotonic in I_i if and only if one of the following conditions is satisfied [Fri1980]:

(i) $2\alpha_i + \beta_i - 3 \le 0$;

(ii) $\alpha_i + 2\beta_i - 3 \le 0$; or

(iii) $\phi(\alpha_i, \beta_i) \ge 0$

As a consequence of Lemmas 1 and 2 it is possible to construct monotonicity region $\mathcal{M}$, i.e. the region of acceptable values for α_i and β_i (hence d_i and d_{i+1}) to produce a monotonic interpolant on I_i.

The algorithm can be briefly described as follows:

Step 1. Initialize the derivatives d_i, $i = 1,2,\ldots,n$ such that $\mathrm{sgn}(d_i) = \mathrm{sgn}(d_{i+1}) = \mathrm{sgn}(\Delta_i)$. If $\Delta_i = 0$, set $d_i = d_{i+1} = 0$.

Step 2. To preserve monotonicity also in I_{i-1}, select a subset $\mathcal{S} \subset \mathcal{M}$ such that

a) If $(\alpha, \beta) \in \mathcal{S}$, then $(\alpha_i^*, \beta_i^*) \in \mathcal{S}$ whenever $0 \le \alpha^* \le \alpha$ and $0 \le \beta^* \le \beta$

b) If $(\alpha, \beta) \in \mathcal{S}$, then $(\beta, \alpha) \in \mathcal{S}$

Then, for each interval I_i in which $(\alpha_i, \beta_i) \notin \mathcal{S}$, modify d_i and d_{i+1} to d_i^* and d_{i+1}^* such that $0 \le \alpha_i^* \le \alpha_i$, $0 \le \beta_i^* \le \beta_i$, and $(\alpha_i^*, \beta_i^*) \in \mathcal{S}$.

Thus an algorithm for monotonic piecewise cubic interpolation has three basic components:

(i) an initialization procedure for Step 1;

(ii) the choice of a subregion $\mathcal{S}$ satisfying properties a) and b);

(iii) the selection of an algorithm for mapping (α_i, β_i) to (α_i^*, β_i^*) for Step 2.

There are several possible choices for subregion $\mathcal{S}$. The smoothest results are produced with $\mathcal{S}$ being a circle of radius 3 centred at the origin. One procedure for modifying the derivative values in Step 2 is to construct the line joining the origin to the point (α_i, β_i). Let (α_i^*, β_i^*) be the point of intersection of this line with the boundary of $\mathcal{S}$. Then $d_i^* = \alpha_i^* \Delta_i$ and $d_{i+1}^* = \beta_i^* \Delta_i$. Then for $\mathcal{S}$, $\alpha_i^* = \tau_i \alpha_i$, $\beta_i^* = \tau_i \beta_i$, where $\tau_i = 3 \big/ \sqrt{\alpha_i^2 + \beta_i^2}$.

Figure 33 shows the result when this interpolation technique is applied to an accurate peak value sampled sequence (reconstruction 1). In Figure 34, error between the 25 MHz reference and sequence interpolated with three different methods (linear, spline and piecewise cubic interpolation) is shown. It is clearly seen that the suggested piecewise cubic method produces overall the smallest estimation error. The largest error occurs at the slopes of the waveform where there cubic polynomial estimate does not quite suffice to imitate the original, sinusoid waveform. It must also be noted that the accuracy of the method is greatly dependent on the accuracy of peak value detection. The waveform periods are not of constant length, especially where the different wave modes and reflections from discontinuities in the structure are superposed.

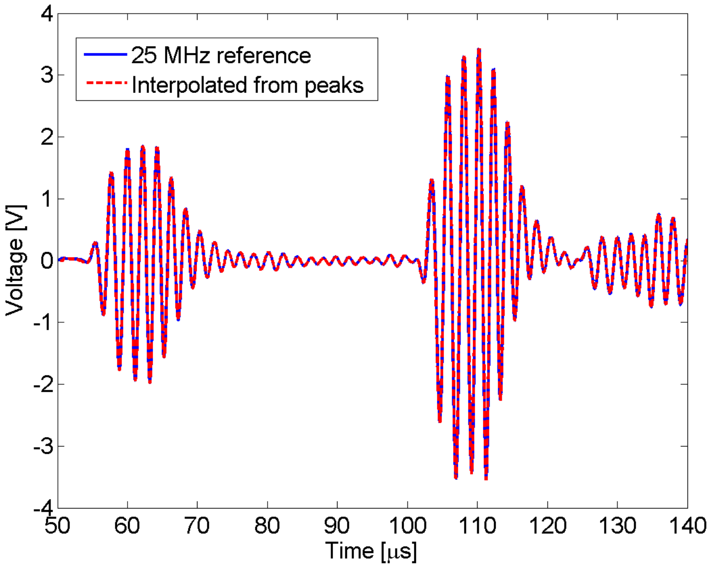

Figure 33. Interpolation result compared to reference measurement.

If the peak detection, however, is based on the aforementioned assumption that short-term variation in frequency (i.e. within time window of length $T = 1/f_c$) is negligible, and estimates for peak values and their time stamps are picked at constant intervals after a zero-crossing trigger point, the method does not always in practice give accurate peak values and may even miss some peaks if the period is short enough. An example of the results of constant period length assumption (reconstruction 2) is shown in Figure 35.

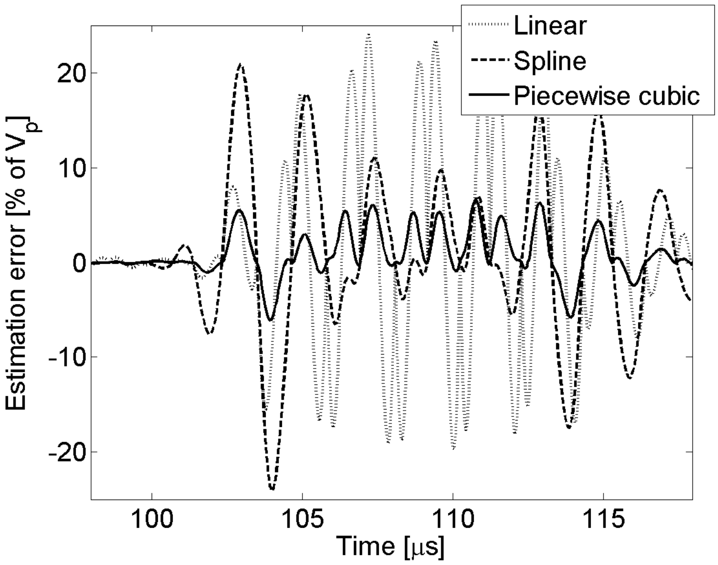

Figure 34. Interpolation errors from different methods.

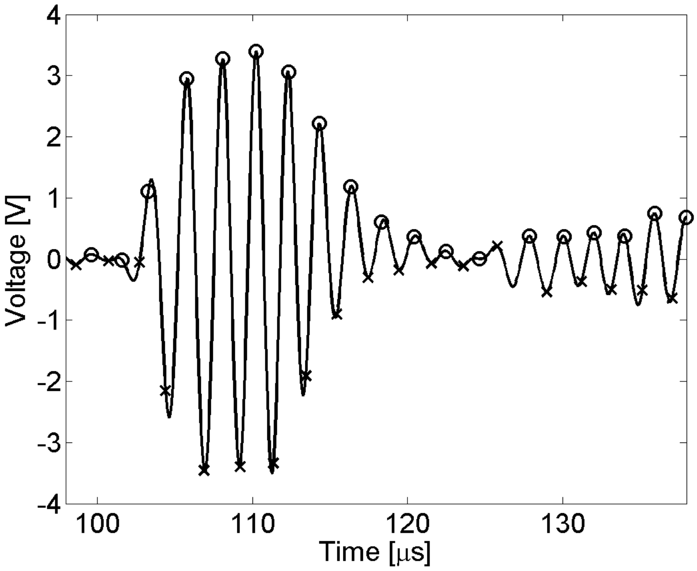

Figure 35. Example of sampling results with the suggested method.

5.5.3 Method verification

The applicability of this reconstruction method to Lamb wave based SHM can be verified by comparing the signal analysis results between a signal reconstructed from the peak values and a reference signal measured from the same target sampled at a high rate. As an example, let us study the test measurements with test plate 2 (Figure 1b). The reference is selected to be the superposed S_1 and S_2 mode response to 450 kHz actuation frequency.

The times of arrival, were calculated for different wave modes on signal path P1→P4 ($s \approx 320$ mm). The results are shown in Table 5. Time period selected for analysis is 72 – 106 μs.

Table 5. Estimated times of arrival (TOA) for different wave modes in path P1→P4.

Wave mode	TOA [μs]
S_1	72
S_2	92
A_0	106
S_0	117
A_1	145

Peak amplitudes and signal variances calculated from the reference signal measured at 25 MHz sampling rate and from reconstructed signals as a function of defect size are show in Table 6. Reconstruction 1 corresponds to reconstruction from an accurate peak value sampled sequence, and reconstruction 2 corresponds to reconstruction from a measurement based on constant period length assumption.

Table 6 shows a very good match between the parameter values estimated from the reference signal and reconstruction 1. With reconstruction 2, the absolute values of the parameters differ more from the reference values, especially those of the burst variance. However, the trend in the change of the variance with increasing defect diameter is similar to that of the reference measurement and thus also reconstruction 2 is capable of indicating the existence of defect and even the increase in its size.

Table 6. Defect indicator parameter comparison: relative V_p and σ^2.

Defect diameter [mm]	V_p			σ^2		
	Reference	Reconst. 1	Reconst. 2	Reference	Reconst. 1	Reconst. 2
0	0.249 V	0.246 V	0.242 V	0.013 V^2	0.013 V^2	0.011 V^2
1	0.920	0.924	0.941	0.831	0.843	0.926
2	0.902	0.905	0.915	0.769	0.776	0.825
3	0.847	0.852	0.855	0.678	0.685	0.735
5	0.791	0.790	0.794	0.614	0.626	0.680
10	0.630	0.636	0.634	0.401	0.404	0.440

Correlation coefficient comparison is represented in Table 7. Correlation coefficient ρ between the length N intact reference signal x_I and damaged state signal x_D is defined as

$$\rho = \frac{1}{N} \frac{\sum_{k=1}^{N} \left(x_I(k) - \mu_I \right) \left(x_D(k) - \mu_D \right)}{\sigma_I \sigma_D} \tag{116}$$

where μ_I, μ_D are the mean values, and σ_I, σ_D are the standard deviations of the intact and damaged state signals, respectively.

Table 7. Correlation coefficient comparison.

Defect diameter [mm]	ρ		
	Reference	Reconst. 1	Reconst. 2
1	0.995	0.958	0.998
2	0.998	0.973	1.000
3	0.997	0.997	0.999
5	0.987	0.953	0.996
10	0.984	0.978	0.984

Data normalization reduces significantly the effect of attenuation caused by defect when compared with the intact reference status. Reduction in correlation coefficient with increasing defect size originates mainly in possible delays and waveform distortion caused by the defect.

The defect locating algorithm presented in detail in Chapter 6 compares the relative variance to a preset significance threshold to determine the shape of the spatial probability distribution at each signal path, and then uses the relative variance to determine the weight of that distribution. Examples of the locating results using the reference measurement and the two reconstructions with defect diameters 3m and 5 mm for test plate 2 are shown in Figure 36. The white circle with cross at (210,250) mm marks the correct location of the defect, and the green cross denotes the estimated location of the defect. It is clearly seen from Figure 36, that the relative variance values from the three methods result in equal defect locating results, despite the differences in the absolute values of the variances resulting from the different methods.

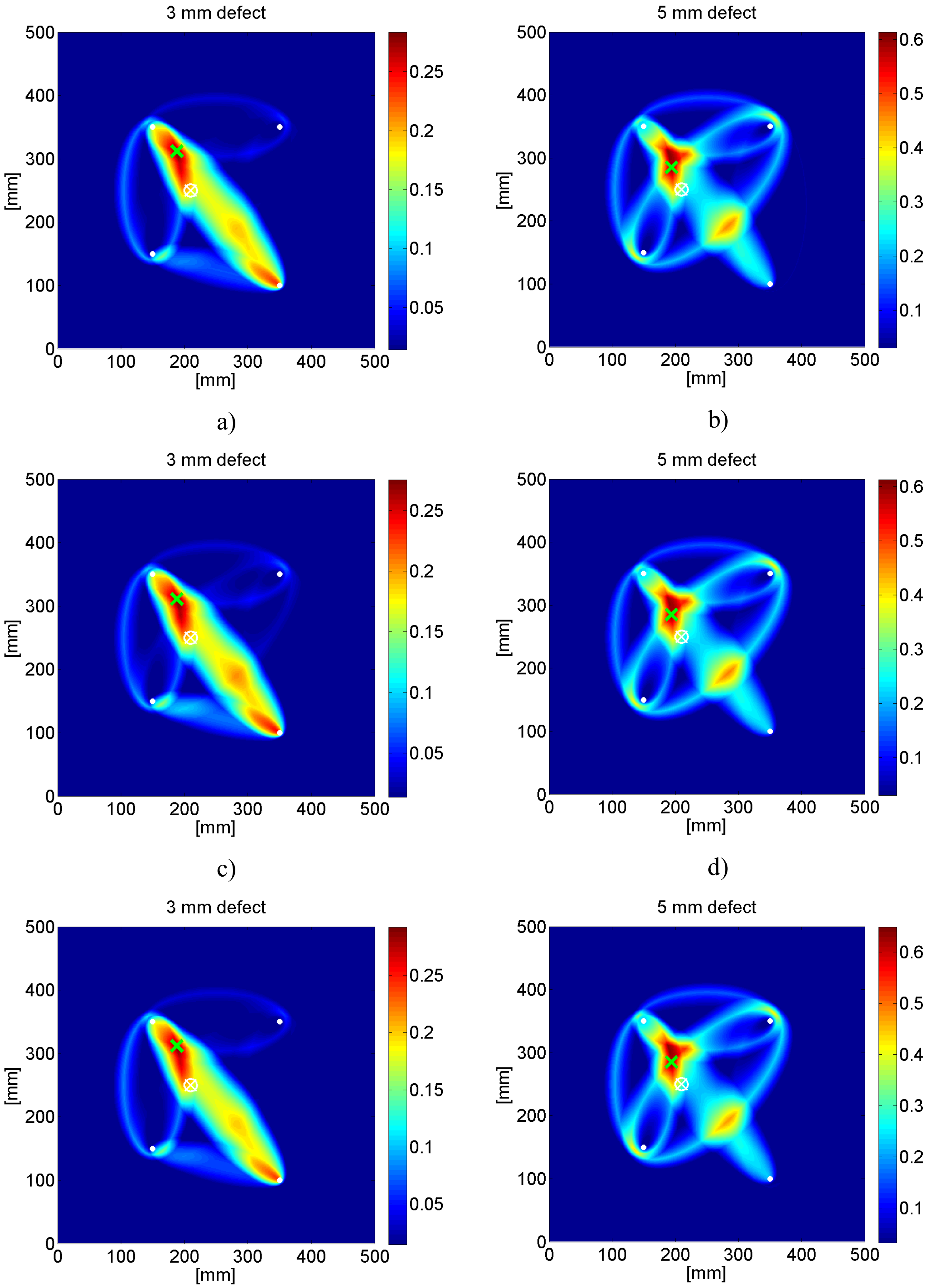

a) b) c) d) e) f)

Figure 36. Comparison of defect locating results using 25 MHz sampling rate (a, b), reconstruction 1 (c, d) and reconstruction 2 (e, f) in test plate 2.

6. Signal analysis methods for detecting and locating defects

In this chapter, the most commonly used signal analysis methods and defect indicating parameters both in time domain, frequency domain and join time-frequency domain for defect detection are reviewed. A method for locating a defect based on simple statistical signal parameters is presented.

6.1 Basic methods

The task of setting up defect detection using Lamb waves is the selection of appropriate parameters extracted from the measurements that can reliably indicate the existence, type, severity and location of defect. Generally, the analysis is a trade-off between the amount of required data and computation, and the reliability of the defect analysis results. Raghavan and Cesnik have written a comprehensive review on guided-wave based SHM including the applied signal processing methods [Rag2007b]. This subsection discusses shortly the most commonly used signal analysis methods for Lamb wave based defect detection.

6.1.1 Time domain analysis

The simplest statistical parameters of the Lamb wave response that can be used for detecting an existing defect are time domain amplitude measures: mean, maximum, minimum and peak-to-peak values of the response. Root Mean Square (RMS) or variance of the response gives indication of the average Lamb wave energy. Higher order statistical moments (skewness and kurtosis) can also be used [Sta2004]. Although these higher order moments have been useful in detecting e.g. faults in bearings, they are not so useful when applied to Lamb wave data. Analysis of correlation coefficient between successive measurements is also used for detecting defects.

The ability of the time domain amplitude parameters to indicate defects is strongly affected by the ratio of Lamb wavelength to the size of defect and also by the location of the defect with respect to the actuator-sensor path.

6.1.2 Frequency domain analysis

Signals can be presented in the frequency domain. The distribution of the signal variance over frequencies from zero (DC) to half of the sampling frequency is called the power spectrum. For a discrete (sampled) signal $x(n)$ of length M, the estimate for power spectrum $R(\omega_k)$ is defined as

$$R(\omega_k) = \frac{1}{M}\left|\sum_{n=0}^{M-1} x(n)e^{-\mathrm{i}\omega_k n}\right|^2 \; ; k = 0,1,\ldots,N-1 \tag{117}$$

where $\omega_k = 2\pi k/N$ and N is the length of the discrete Fourier transform (in the most simple case, $N = M$). The square root values of the spectrum give the amplitudes of the corresponding signal components. The relationships of these amplitudes can be used to describe differences between spectra in different defect conditions [Bie2001, Sta2004]. Two parameters used in structural defect detection and defined by the signal component amplitudes are the arithmetic mean,

$$A_m = 20\log\left(\frac{1}{N}\sum_{i=1}^{N}\frac{A_i}{10^{-5}}\right) \tag{118}$$

and the geometric mean,

$$G_m = \frac{1}{N}\left(\sum_{i=1}^{N} 20\log\left(\frac{A_i}{\sqrt{2}\cdot 10^{-5}}\right)^2\right) \tag{119}$$

where A_i is the amplitude of the ith Fourier coefficient of frequency spectrum and 10^{-5} is a scaling factor used to compensate for generally small values of A_i. Another spectrum based parameter used especially for detecting defects in composites is the damage index,

$$DI = \left| 1 - \frac{FD^{\mathrm{T}} * FD}{FI^{\mathrm{T}} * FI} \right| \tag{120}$$

where *FD* and *FI* are the frequency response function (FRF) amplitude vectors for the damaged and reference structure, respectively [Ban2007, Ban2009, Mal2009]. The FRF's are obtained using either a sinusoidal pulse (simulating an impulse response) or a chirp signal for actuating the Lamb waves.

6.2 Advanced signal analysis methods

6.2.1 Joint time-frequency analysis

As an example, let us study test plate 2 shown in Figure 1b. The following examples of time-frequency analysis are on pitch-catch measurements on signal path P1→P4 with 450 kHz actuation frequency. At this frequency-thickness product, three symmetric and two antisymmetric Lamb wave modes coexist in the plate. Their group velocities are listed in Table 8. The order of arrival of wave modes at the sensor P4 is S_1, S_2, A_0, S_0 and A_1. Reflections of some of the faster wave modes from the plate edges arrive at the sensor before modes S_0 and A_1 arrive directly from the actuator P1.

Table 8. Group velocities of existing Lamb wave modes in aluminium at *fd* = 4500 kHz×mm

Mode	c_G, [m/s]
S_0	2728
S_1	4445
S_2	3467
A_0	3019
A_1	2207

Figure 37 shows the measured pitch-catch responses from the selected path. The solid vertical lines show the estimated direct time of arrival for the symmetric wave modes. The dashed lines show the arrival of antisymmetric wave modes. The dash-dot lines show first arriving reflections from different plate edges. The different modes arriving from different sources are superposed.

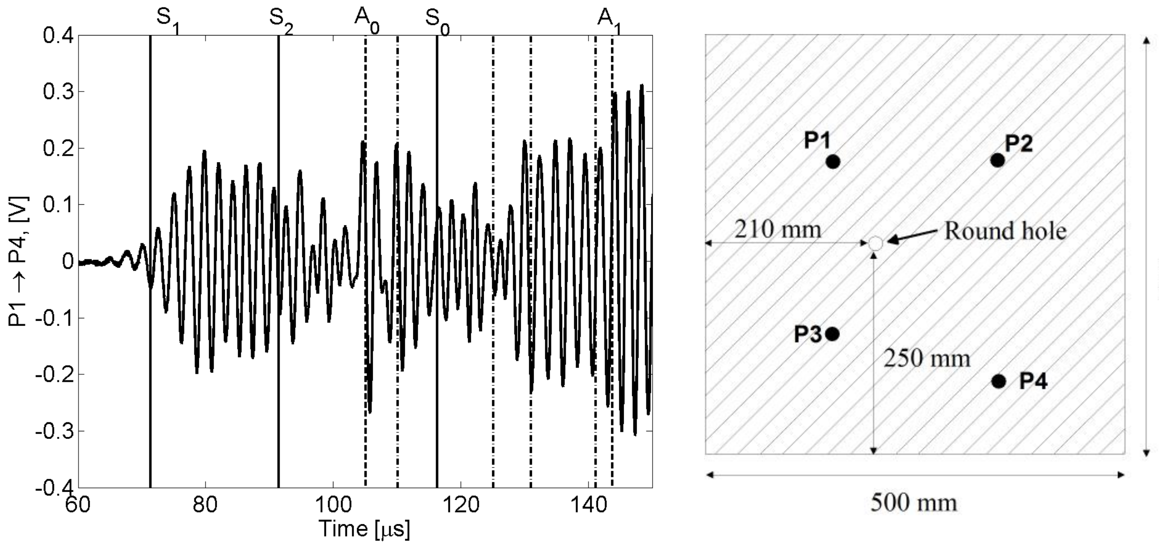

Figure 37. Pitch-catch response from path P1→P4 in damaged test plate 2. The dash-dot lines approximately at 100 μs, 125 μs, and 130 μs show the first arriving S_1 mode reflections from the lower, left/right and upper plate edge, respectively. The dash-dot line at 140 μs shows the first arriving S_2 mode reflection from the lower plate edge.

Spectrograms

Fourier transform of a time domain signal describes which frequencies are present in the signal, and gives the amplitudes and the phases of those frequency components. Generally, with the Fourier transform stationarity of the signal is assumed; i.e. the probability distribution and frequency content of the signal are assumed not to change over time or position. Therefore the Fourier transform reveals the frequency components present in the signal, but does not specify whether they are present throughout the signal or only during some period of it. However, when the signals originate from a dynamic process, like e.g. the Lamb wave responses discussed here, they are usually not stationary but their statistical properties and frequency vary over time. With nonstationary signals, it is often desirable to study their frequency content with respect to time.

The simplest method to represent the frequency content of the signal with respect to time is the spectrogram, which is calculated using the short-time Fourier transform (STFT) [Opp1989]. In STFT, the signal is divided into short segments and the frequency spectrum of each segment is calculated separately using FFT. The results from each segment are then combined to form a spectrogram (square of the absolute value of STFT) of the signal. Since the frequency resolution of FFT depends on the length of the available data, this method leads to a compromise between time and frequency resolution. The shorter the data segments, the better the time resolution but the worse the frequency resolution. A workaround for this problem is to use long data segments overlapping in time. The bandwidth of the STFT is uniform in frequency domain. STFT has been applied to Lamb wave based SHM by e.g. Prasad et al. ([Pra2003]), and Ihn and Chang ([Ihn2004]).

Mathematically discrete time STFT of a finite-length signal $x(n)$ is expressed as

$$\mathrm{STFT}(n,k)=\sum_{m=0}^{L-1} x(n+m)w(m)\mathrm{e}^{-\mathrm{i}(2\pi/N)km}\;;0\le k\le N-1 \tag{121}$$

where $w(m)$ is so-called window function with length L and the number of frequency sampling points $N \geq L$. The shape of the selected window function may be rectangular, but generally a weighted window, for example Hanning type window, $w(m)=0.5\left(1-\cos\left(2\pi m/L-1\right)\right)$; $m = 0\ldots L-1$ is used in order to reduce the effects caused by calculating FFT from limited number of data points.

Figure 38 shows the spectrograms of the signal measured from path P1→P4 when the plate is intact (Figure 38a) and with 5 mm defect at location (210,250) mm from the lower left corner (Figures 37,38b). Hanning window of length 55.6 μs was applied. The time resolution was 2.8 μs so that the overlap of transformed areas was 95%. Sampling interval was 55.6 μs/8192 and thus each transformed sample consisted of 8192 signal values and each spectrum had 4096 discrete frequencies. Figure 38 shows that the frequency content of the signal is distributed around the actuation frequency 450 kHz. The effect of the selection of estimation parameters on the time-frequency resolution is illustrated e.g. in [Giu2008a].

The effect of defect can be seen as decreased spectral power at around 80 μs where the S_1 wave mode arrives directly from the actuator, and increased spectral power between 130-140 μs where several wave modes arriving directly or reflected from the plate edges and the defect are superposed.

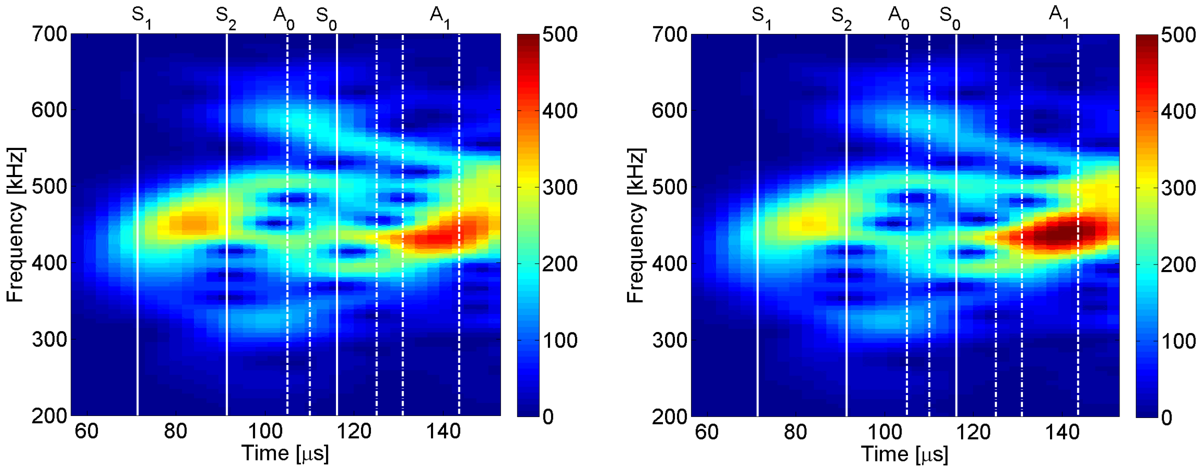

a)

b)

Figure 38. Spectrograms of the signal in Figure 37. a) Undamaged plate, b) 5 mm defect. The frequency band originally ranging between 0…12.5 MHz is shown only between 200…700 kHz, where the spectral power is concentrated. The step between frequency points is 6.1 kHz. Wave mode arrivals are indicated as in Figure 37.

Wavelets

More refined method for joint time-frequency representation of a signal is to use wavelets. In wavelet analysis, the signal is represented as a sum of scaled (dilated) and time-shifted (translated) elementary functions $\psi\left(a^{-1}(t-b)\right)$, where $\psi(t)$ is called the mother wavelet [Qia1996]. Scaling the function in time domain results in inversely scaling in frequency domain.

The continuous wavelet transform, CWT is defined as

$$\mathrm{CWT}(a,b)=\frac{1}{\sqrt{|a|}}\int s(t)\psi^{*}\left(\frac{t-b}{a}\right)dt, \qquad a\neq 0 \tag{122}$$

If $\psi(t)$ is centred at time zero and its Fourier transform around frequency ω_0, then its dilation and translation $\psi\left(a^{-1}(t-b)\right)$ is centred at time b and its Fourier transform around frequency ω_0/a, respectively. Both time resolution of the basis function and frequency resolution of its Fourier transform are functions of the scaling factor. Thus, the correspondence between wavelet scales and frequency as revealed by wavelet analysis can be described as follows:

- Low scale *a* → Compressed wavelet → Rapidly changing details → High frequency *ω*.
- High scale *a* → Stretched wavelet → Slowly changing, coarse features → Low frequency *ω*.

The ratio of the bandwidth and centre frequency is constant [Sta2004, Qia1996].

A simple presentation of continuous wavelet analysis is as follows:

1. Take a wavelet and compare it to a section at the start of the original signal.
2. Calculate a number, `C`, that represents how closely correlated the wavelet is with this section of the signal. The higher `C` is, the more the similarity. If the signal energy and the wavelet energy are equal to one, `C` may be interpreted as a correlation coefficient. The results depend on the shape of the chosen wavelet.
3. Shift the wavelet to the right and repeat steps 1 and 2 until you've covered the whole signal.
4. Scale (stretch) the wavelet and repeat steps 1 through 3.
5. Repeat steps 1 through 4 for all scales.

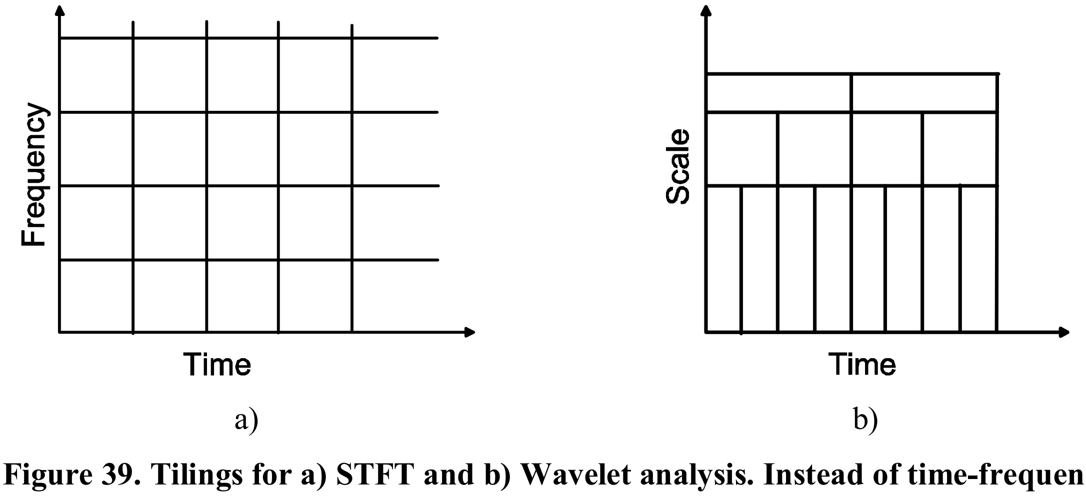

a) b)

Figure 39. Tilings for a) STFT and b) Wavelet analysis. Instead of time-frequency region, Wavelet analysis uses logarithmic time-scale region.

Figure 39a shows the relationship between time and frequency for STFT. For a chosen data segment length, frequency bandwidth is the same at all frequencies. Wavelet analysis does not operate in time-frequency region, but rather in a logarithmic time-scale region (Figure 39b). The connection between scale and frequency can be described in terms of pseudo-frequency F_a corresponding to scale a:

$$F_a = \frac{F_c}{a \cdot \Delta} \tag{123}$$

where F_c is the centre frequency of a wavelet in Hz, a is a scale and Δ is the sampling period.

There are a number of different complex and real-valued functions used as wavelets. Examples are given in [Dau1992]. One of the most widely used functions in the continuous wavelet analysis, including Lamb wave based SHM applications [Sta2004], is the Morlet wavelet (Figure 40),

$$\psi(t) = e^{\mathrm{i}\omega t} e^{-|t|^2/2} \tag{124}$$

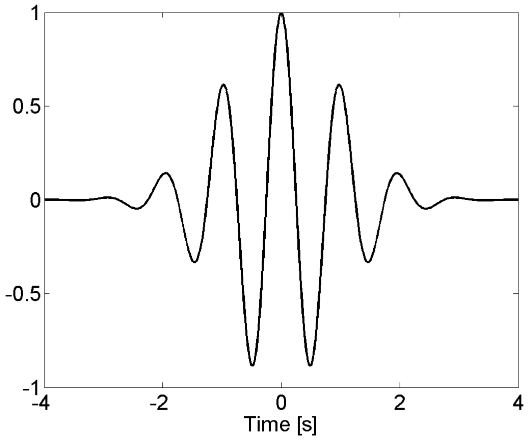

Figure 40. Morlet mother wavelet, *f* = 1 Hz.

Wavelets have been used for de-noising the Lamb wave responses [Yu2005], and feature extraction and feature selection purposes [Sta2004]. In Figure 41, the Morlet wavelet coefficients of scales 20…70 corresponding to pseudo-frequencies 1,02 MHz…290 kHz, respectively, for the signal from path P1→P4 when the plate is intact (Figure 41a) and with 5 mm defect (Figure 41b) are shown. Visual inspection shows e.g. some decrease in the wavelet coefficients between 70…90 µs (direct arrival of the symmetric wave modes) and increase between 130…140 µs (reflections from the plate edges) between the two states.

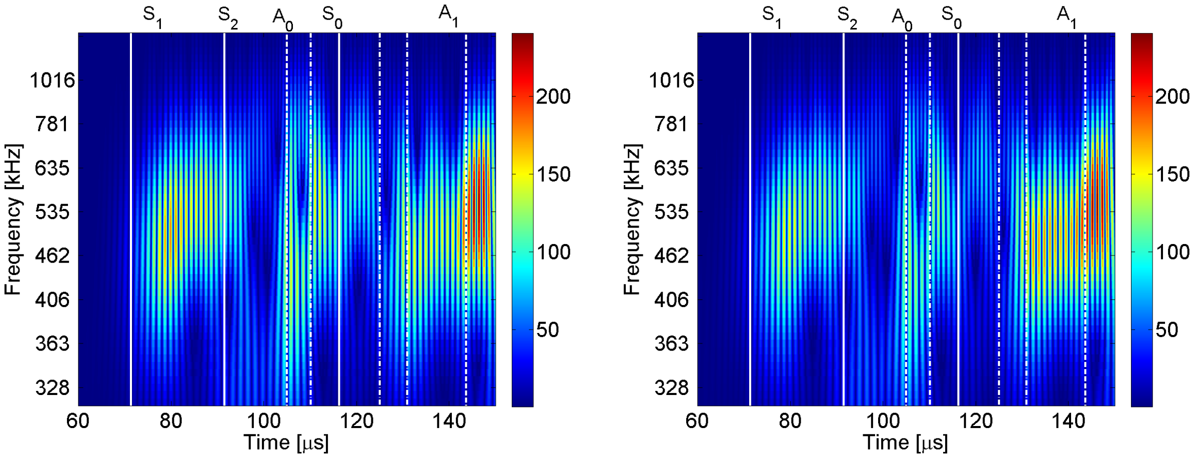

a) b)

Figure 41. Morlet wavelet coefficients at pseudo-frequencies 290 kHz…1.02 MHz of the signal in Figure 37. a) Undamaged plate, b) 5 mm defect. Wave mode arrivals are indicated as in Figure 37.

Chirplets

The time-frequency distribution of any individual wavelet is concentrated around the central time and frequency (Figure 42). This is not the best possible match for dispersive signals, which propagate at frequency-dependent velocity. Their time-frequency distribution is more like an ellipse with its main axes direction depending on whether the velocity increases or decreases with frequency. These kinds of signals have a better match with chirplets, which are, in a way, wavelets with changing frequency.

In 1993, Mallat and Zhang introduced the matching pursuit algorithm for decomposing any signal f into a linear expansion of waveforms that are selected from a redundant dictionary D of functions [Mal1993]. A similar algorithm was proposed independently by Qian and Chen [Qia1994]. The decomposition is done by successive approximations of the signal f with orthogonal projections on elements $g \in D$ so that the vector f is decomposed into $f = \langle f, g \rangle g + Rf$, where $\langle f, g \rangle = \int_{-\infty}^{\infty} f(t) g^*(t)\, dt$, and Rf is the residual vector after approximating f in the direction of g. At each iteration, g is selected so that $\|Rf\|$ is minimized, and at the next iteration, the projection is done on Rf. The implicit assumption in the works by Mallat and Qia was that the signals are unimodal and non-dispersive; the time-frequency atoms were stationary in nature, like wavelets.

In 2001, Gribonval introduced a computationally efficient algorithm for matching pursuits using a dictionary consisting of Gaussian modulated chirplet atoms, which have linear time–frequency ridges [Gri2001]. These chirplet atoms are of the form

$$k_{(a,b,\omega,c)}(t) = \frac{1}{\sqrt{a}} g\left(\frac{t-b}{a}\right) \exp\left[\mathrm{i}\left(\xi(t-b) + \frac{c}{2}(t-b)^2 \right) \right] \tag{125}$$

where a is the scale of the atom, b is the time centre of the atom, c is the chirp rate of the atom, ξ is the frequency centre of the atom and $g(t) = 2^{1/4} \mathrm{e}^{-\pi t^2}$ is a Gaussian modulation window. The instantaneous frequency $\omega(t) = \xi + c(t-b)$ varies linearly with time. Examples of time-frequency distribution of chirplets are given in Figure 43.

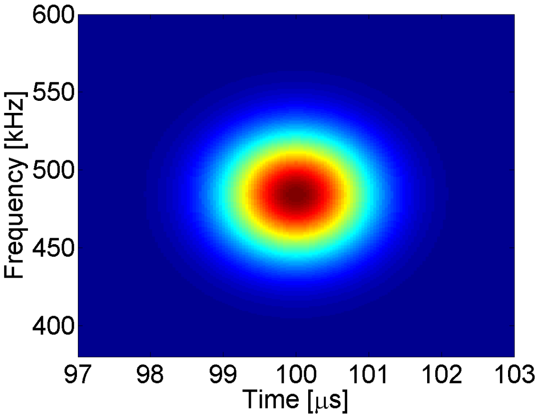

Figure 42. Time-frequency distribution of a wavelet.

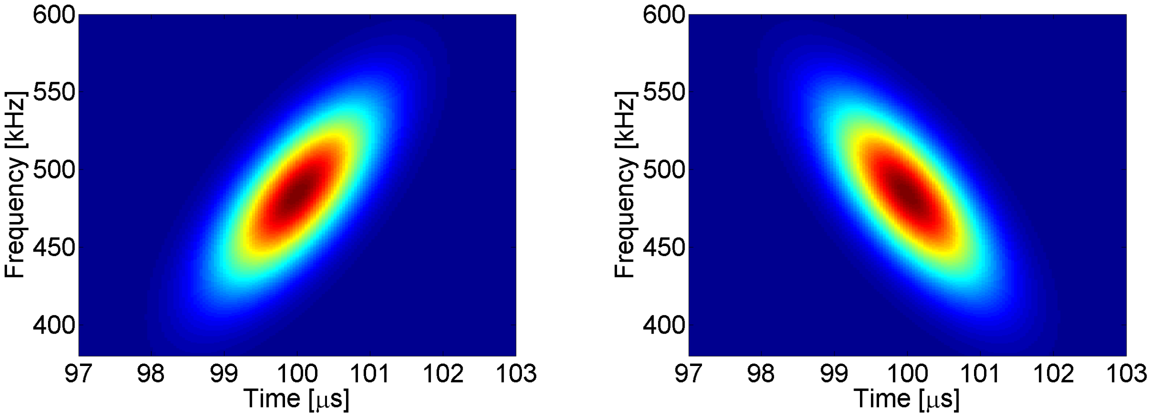

a) b)

Figure 43. Time-frequency distribution of a chirplet with a) increasing, b) decreasing frequency.

In 2007, Raghavan and Cesnik suggested a chirplet matching pursuit based method for analyzing PWAS response for Lamb waves in SHM applications [Rag2007a]. In their method, the signal is iteratively projected onto a large and redundant dictionary of chirplet waveforms. Then the waveform is chosen from that dictionary that is best adapted to the approximate part of the waveform. Finally, the signal is approximated as a sum of these best matching chirplets. The number of iterations, i.e. the number of selected chirplet atoms, is determined by the required approximation accuracy; e.g. the variance of the difference between the original signal and its approximation, called the residual signal.

Figure 44 shows the reduction in residual variance with increasing number of iterations, or chirplets matched to the signal in Figure 37. The signal was de-trended before decomposition. After 20 iterations, the variance of the residual signal is only 3% of the original signal and further iterations reduce it only slightly. The first 20 chirplets are selected to form an approximation of the original signal.

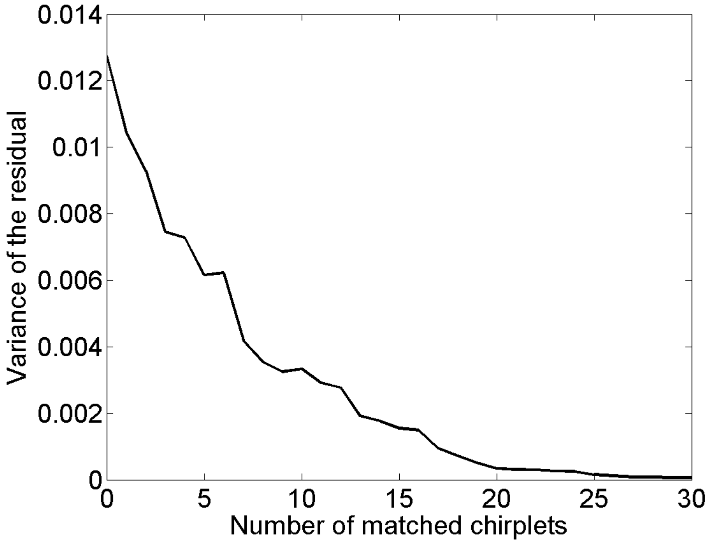

Figure 44. Variance of the residual signal with respect to the number of matched chirplets.

Figure 45 shows the 20 estimated chirplet components for the signal in Figure 37.

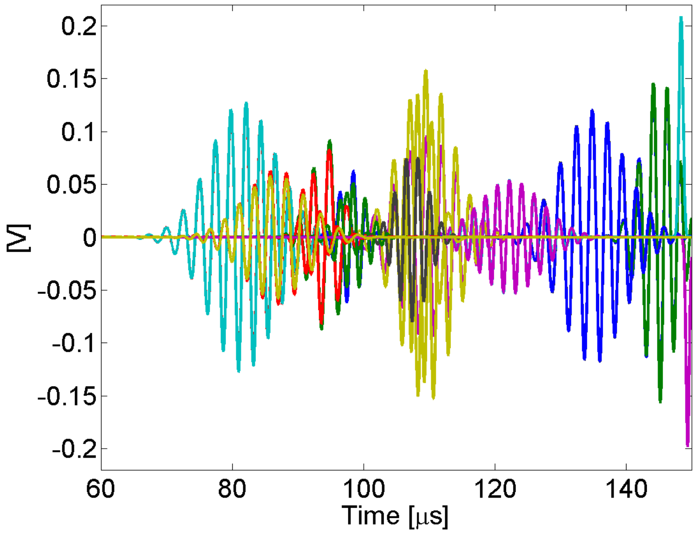

Figure 45. Chirplet components of the signal in Figure 37.

The difference between the final signal estimate (that is, the sum of the individual chirplets) and the original signal is shown in Figure 46.

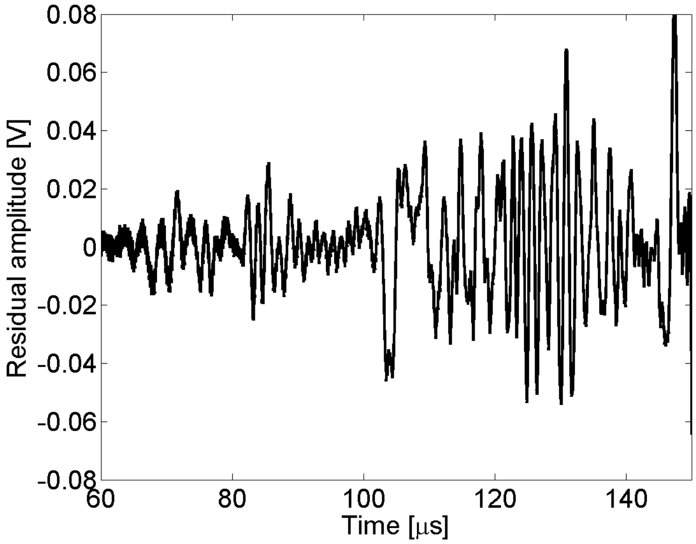

Figure 46. Difference between the signal in Figure 37 and its chirplet sum estimate.

Wigner-Ville method

The concept of Wigner distribution was originally developed for the area of quantum mechanics by Wigner in 1932 [Wig1932] and was introduced for signal analysis by Ville 15 years later [Vil1948]. It is now commonly known as the Wigner-Ville distribution (WVD) [Qia1996]. Generally, for any complex function x the time-dependent WVD is defined

$$\mathrm{WVD}_x(t,\omega) = \int_{-\infty}^{\infty} x\left(t+\frac{\tau}{2}\right) x^*\left(t-\frac{\tau}{2}\right) \mathrm{e}^{-\mathrm{i}\omega\tau} d\tau \tag{126}$$

where * denotes the complex conjugate. WVD maps a one-dimensional function of time into two-dimensional function of time and frequency and is real-valued. Some of the main properties of WVD are as follows [Qia1996]:

- Energy conservation: energy of x, E_x, is obtained by integrating the WVD over time-frequency plane,

  $$E_x = \int_{-\infty}^{\infty}\int_{-\infty}^{\infty} \mathrm{WVD}_x(t,\omega)\, dt\, d\omega$$

- Marginal properties: the energy spectral density, $|X(\omega)|^2$, and the instantaneous power, $|x(t)|^2$, can be obtained as marginal distributions of WVD:

  $$\int_{-\infty}^{\infty} \mathrm{WVD}_x(t,\omega)\, dt = |X(\omega)|^2$$

  $$\int_{-\infty}^{\infty} \mathrm{WVD}_x(t,\omega)\, d\omega = |x(t)|^2$$

- Wide-sense support conservation: if a signal has a compact support in time (respectively in frequency), then its WVD also has the same compact support in time (respectively in frequency):

  $$x(t) = 0, |t| > T \quad \Rightarrow \quad \mathrm{WVD}(t,\omega) = 0, |t| > T$$
  $$X(\omega) = 0, |\omega| > B \quad \Rightarrow \quad \mathrm{WVD}(t,\omega) = 0, |\omega| > B$$

- Unitarity: the unitarity property expresses the conservation of the scalar product from the time-domain to the time-frequency domain (apart from the squared modulus):

  $$\left| \int_{-\infty}^{\infty} x(t) y^*(t)\, dt \right|^2 = \int_{-\infty}^{\infty}\int_{-\infty}^{\infty} \mathrm{WVD}_x(t,\omega)\mathrm{WVD}_y^*(t,\omega)\, dt\, d\omega$$

As the WVD is a bilinear function of the signal x, the quadratic superposition principle applies, i.e. for $x(t) = x_1(t) + x_2(t)$, the WVD is

$$\mathrm{WVD}_x(t,\omega) = \mathrm{WVD}_{x1}(t,\omega) + \mathrm{WVD}_{x2}(t,\omega) + 2\,\mathrm{Re}\left\{\mathrm{WVD}_{x1,x2}(t,\omega)\right\} \tag{127}$$

where $\mathrm{WVD}_{x1,x2}(t,\omega)$ is the cross-WVD of x_1 and x_2. The same principle applies with every quadratic distribution, e.g. the spectrogram. However, one can show [Hla1991] that with spectrograms these interference terms are restricted to those regions of the time-frequency plane where the auto-spectrograms overlap. If the signal components $x_1(t)$ and $x_2(t)$ are sufficiently distant so that their spectrograms do not overlap significantly, then the interference term will nearly be identically zero. In the case of WVD, auto-terms are, in general, relatively smooth, but the cross-terms are strongly oscillated, and they are nonzero regardless of the time-frequency distance between the two signal terms. These interference terms are troublesome since they may overlap with auto-terms and thus make it difficult to visually interpret the WVD image.

Figure 47 shows the WVD of the sum of the chirplets in Figure 45, i.e. the approximation of the signal in Figure 37. The cross-term interference pattern is clearly visible for example across the whole presented frequency band around 120 µs, and the individual chirplet atoms are difficult to locate.

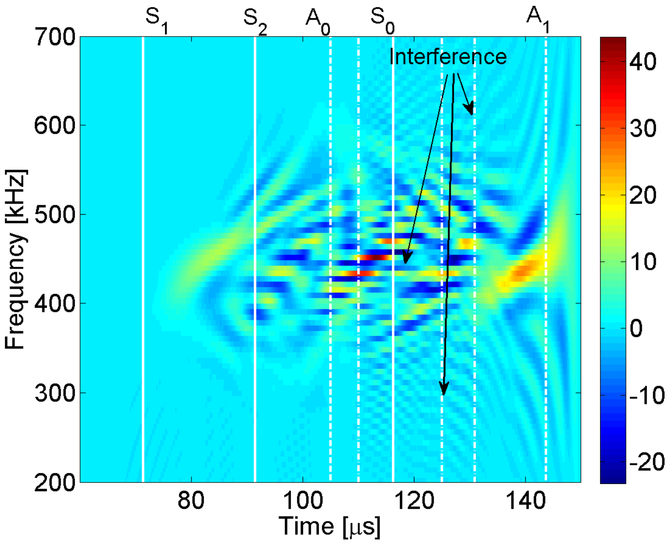

Figure 47. WVD of the sum of the chirplets in Figure 45. $\Delta f = 6.1$ kHz. The arrows point to examples of the cross-term interference areas. Wave mode arrivals are indicated as in Figure 37.

In real applications, evaluation from minus infinite to plus infinite is impossible. To overcome this problem, we can impose a running window $h(t)$, leading to the new distribution:

$$\mathrm{PWVD}_x(t,\omega) = \int_{-\infty}^{\infty} h(\tau)\, x\left(t+\frac{\tau}{2}\right) x^*\left(t-\frac{\tau}{2}\right) \mathrm{e}^{-\mathrm{i}\omega\tau} d\tau \tag{128}$$

which is called the pseudo Wigner-Ville distribution (PWVD) [Qia1996]. This windowing operation will result as frequency smoothing in time domain. Thus the oscillating cross-term interferences will be attenuated in the PWVD compared to the WVD. However, the marginal properties, the unitarity, and the frequency-support conservation of WVD are lost.

Figure 48 shows PWVD of the sum of the chirplets in Figure 45. Number of data points in the signal is 2251. In Figure 48a, the length of the window *h*(*t*), N_h, is 113 points, in Figure 48b it is 225 points. If *h*(*t*) is short, the smoothing function will be narrow in time and wider in frequency, leading to a good time resolution but bad frequency resolution, and the frequency-widths of the auto-terms are increased.

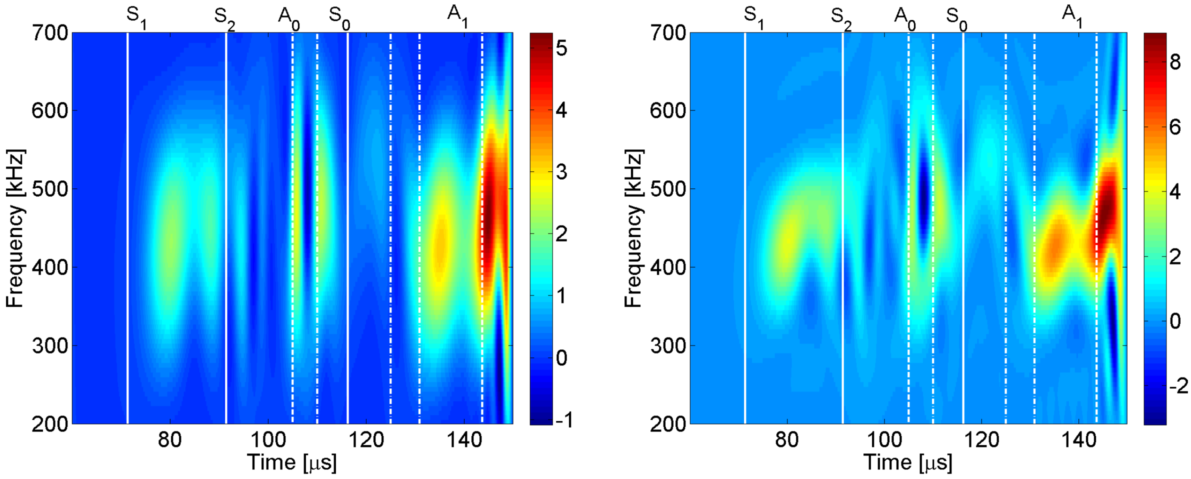

a) b)

Figure 48. PWVD of the sum of the chirplets in Figure 45. a) N_h = 113, b) N_h = 225. Δf = 6.1 kHz. Shorter *h*(*t*) results in increased frequency-width of the auto-terms. Wave mode arrivals are indicated as in Figure 37.

The WVD of the sum of the chirplets provides improved visualization of the Lamb wave response content compared to spectrogram and wavelet analysis. However, estimating the WVDs of individual chirplets separately and displaying them together gives even better view of signal content. It must be kept in mind, though, that this is only a visualization aid and can only give a general idea of e.g. distribution of signal energy between the chirplet atoms. The sum of WVDs of individual chirplets both from the signal from an undamaged plate and from the same signal path with 5 mm defect are shown in Figure 49.

The effect of the defect on signal can be seen for example at the first arriving wave mode, S_1, at around 80 μs. The shape of the chirplet WVD changes because different frequencies and wavelengths in the burst pass through the defect differently. At around 90 μs, the decreasing chirplet from S_2 wave mode is barely visible but better separated from S_1 mode in the defected plate because its longer wavelength passes through the defect almost unaffected, unlike S_1. There is also significant difference at the point where the first reflections from the plate edges arrive at the sensor, at 110 μs.

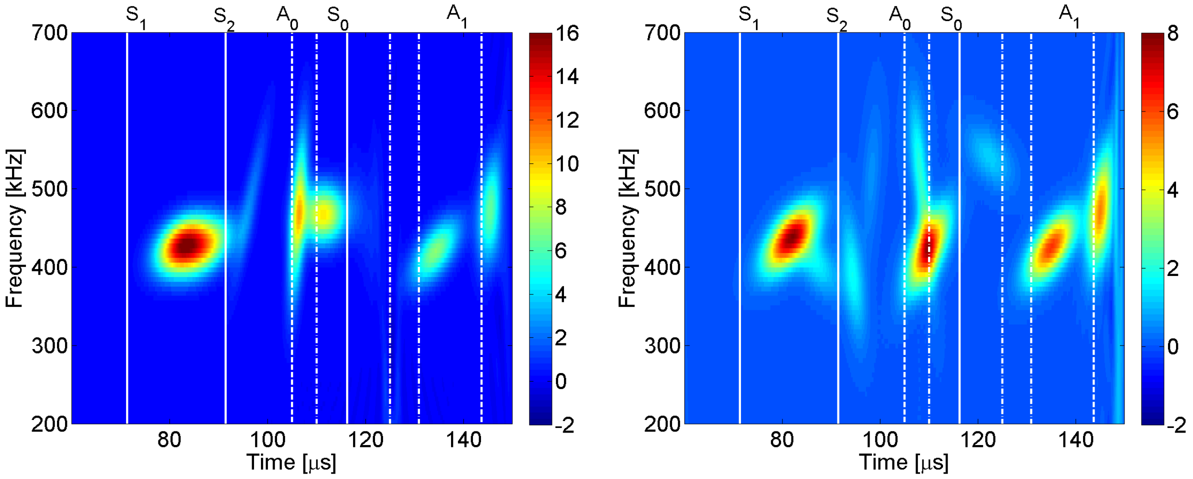

a) b)

Figure 49. The sum of WVDs of individual chirplets in Figure 45 from path P1→P4. a) Undamaged plate, b) 5 mm defect. Wave mode arrivals are indicated as in Figure 37.

The Wigner-Ville distribution (WVD) of the individual chirplets represents the time-frequency distribution of the signal without disturbing interferences that are typical for WVDs calculated directly from the original signal.

Yu and Giurgiutiu applied some of these methods in their embedded ultrasonic structural radar (EUSR) system [Yu2005]. First they applied discrete wavelet transform for signal de-noising. Secondly, after constructing the EUSR data, they used the short-time Fourier transform (STFT) and continuous wavelet transform (CWT) for the time-frequency analysis. Eventually they chose continuous wavelet transform to filter out from the original signal the component with the excitation signal's frequency. Third, they applied the cross correlation method and Hilbert transform to the signals to extract the time of flight (TOF) of the wave packets from a crack. Finally, they applied the Hilbert transform again to the EUSR data to extract the envelopes for final inspection result visualization.

6.2.2 Some other applied methods

Principal component analysis (PCA) has been extensively applied to structural defect analysis. PCA transforms a number of possibly correlated variables into uncorrelated variables, called the principal components, which are linear combinations of the initial variables x_i [Jol2002].

Let $\mathbf{X} \in \Re^{m \times n}$ be a matrix with zero-mean variables x_i of length m as its columns, so that X_{ji} is the jth sample of ith variable. Then the covariance matrix, $\mathbf{S_X}$, of $\mathbf{X}$ can be calculated as

$$\mathbf{S_X} = \frac{\mathbf{X}^{\mathrm{T}}\mathbf{X}}{m-1} \tag{129}$$

The principle of PCA is to find such linear combination of variables x_i, $i = 1 \ldots n$ that contains as large a part as possible of the variation of the variables x_i. Thus the task is to find the linear combination $\mathbf{Xp}$ with the maximum variance $D^2(\mathbf{Xp})$. Vector $\mathbf{p}$ is a scaling vector which defines the weight of the effect of each variable on the linear combination variance.

PCA divides the data matrix into components

$$\mathbf{X} = \mathbf{t}_1\mathbf{p}_1^{\mathrm{T}} + \mathbf{t}_2\mathbf{p}_2^{\mathrm{T}} + \ldots + \mathbf{t}_k\mathbf{p}_k^{\mathrm{T}} + \mathbf{E} = \mathbf{T}_k\mathbf{P}_k^{\mathrm{T}} + \mathbf{E} \tag{130}$$

where $k \le \min\{m,n\}$, $\mathbf{T}_k \in \Re^{m \times k} = [\mathbf{t}_1\ \mathbf{t}_2 \ldots \mathbf{t}_k]$ are the scores, $\mathbf{P}_k \in \Re^{n \times k} = [\mathbf{p}_1\ \mathbf{p}_2 \ldots \mathbf{p}_k]$ are the loadings, and $\mathbf{E} \in \Re^{m \times n}$ is the residual matrix. The scores are orthogonal,

$$\mathbf{t}_i^{\mathrm{T}}\mathbf{t}_j = 0, \quad i \neq j$$

and the loadings are orthonormal,

$$\mathbf{p}_i^{\mathrm{T}}\mathbf{p}_j = 0, \quad i \neq j$$
$$\mathbf{p}_i^{\mathrm{T}}\mathbf{p}_j = 1, \quad i = j$$

It can be shown that the variance of each consecutive linear combination, $D^2\left(\mathbf{X}\mathbf{p}_i\right)$ is maximized when the loadings $\mathbf{p}_i$ are the eigenvectors of the covariance matrix $\mathbf{S}_\mathbf{X}$**:**

$$\mathbf{S}_\mathbf{X}\mathbf{p}_i = \mathbf{p}_i\lambda_i \tag{131}$$

where λ_i is the eigenvalue corresponding to the eigenvector $\mathbf{p}_i$. Thus the principal components are obtained from the eigenvalue decomposition of the covariance matrix $\mathbf{S}_\mathbf{X}$**,**

$$\mathbf{S}_\mathbf{X} = \mathbf{P}_k\mathbf{\Lambda}\mathbf{P}_k^{\mathrm{T}} \tag{132}$$

where $\mathbf{\Lambda}$ = diag(λ_i) is a diagonal matrix containing the eigenvalues λ_i of $\mathbf{S}_\mathbf{X}$. Together, the eigenvalues λ_i explain the total variance of the variables x_i:

$$\sigma_\mathbf{X}^2 = \mathrm{trace}(\mathbf{S}_\mathbf{X}) = \mathrm{trace}(\mathbf{\Lambda}) = \sum_{i=1}^{n}\lambda_i \tag{133}$$

The scores $\mathbf{t}_i$ are orthogonal projections of the original data $\mathbf{X}$ into subspace spanned by the loading vectors $\mathbf{p}_i$:

$$\mathbf{X}\mathbf{p}_i = \mathbf{t}_i \tag{134}$$

Thus the score matrix $\mathbf{T}_k = \mathbf{X}\mathbf{P}_\mathrm{k}$, and the score covariance matrix is

$$\frac{\mathbf{T}_k^{\mathrm{T}}\mathbf{T}_k}{m-1} = \frac{1}{m-1}\left(\mathbf{X}\mathbf{P}_k\right)^{\mathrm{T}}\left(\mathbf{X}\mathbf{P}_k\right) = \mathbf{P}_k^{\mathrm{T}}\frac{\mathbf{X}^{\mathrm{T}}\mathbf{X}}{m-1}\mathbf{P}_k = \mathbf{P}_k^{\mathrm{T}}\mathbf{S}_\mathbf{x}\mathbf{P}_k = \mathbf{P}_k^{\mathrm{T}}\mathbf{P}_k\mathbf{\Lambda}\mathbf{P}_k^{\mathrm{T}}\mathbf{P}_k = \mathbf{\Lambda} \tag{135}$$

Eq. (135) shows that the variance of the original data is distributed among the score vectors so that the variances of the score vectors $\sigma_{\mathbf{t}_i}^2$ are the eigenvalues λ_i of the covariance matrix $\mathbf{S}_\mathbf{X}$. The share of the total variance of the *j*th principal component is then $\lambda_j \Big/ \sum_{i=1}^{n}\lambda_i$.

The first principal component, containing the largest quantity of information, is the eigenvector corresponding to the largest eigenvalue, and so on. In order to reduce dimensionality, the components containing least amount of information can be eliminated, and only the first l eigenvectors are chosen, leading to a l dimensional data set.

Mujica et al. have proposed a method to enhance the structural defect assessment by combining Q-statistics and T^2-statistics with PCA [Muj2008]. Q-statistic is a measure of the difference between a sample and its projection into the PCA model. Q-statistic of the ith variable is defined by $Q_i = e_i e_i^{\mathrm{T}}$, where e_i is the ith column of $\mathbf{E}$, i.e. the principal component model error of the ith variable. Hotelling's T^2-statistics is a measure of variation in each sample within the PCA model. T^2-statistics of the ith variable is defined by $T_i^2 = t_i \mathbf{\Lambda}^{-1} t_i^{\mathrm{T}}$.

Different conditions of the features extracted and selected indicate the state of structural health and correspond to different classes, each with their specific patterns of features. The use of artificial neural networks (ANNs) is the most popular classification and pattern recognition technique for guided wave based defect detection [Rag2007b]. Su and Ye extracted spectrographic features from Lamb wave signals in the time–frequency domain to construct a defect parameter database, which was then used offline to train a multilayer feedforward ANN [Su2004]. Challis et al. applied ANNs to estimate the geometrical parameters of an adhered aluminium T-joint using ultrasonic Lamb waves. The frequency spectrum of received signals was applied as input to conventional feedforward networks, which were trained using the delta rule with momentum [Cha1996]. Legendre et al. used a neural classifier to characterize ultrasonic Lamb wave signals to test metallic welds. This was based on a multilayered ANN, which was trained by selected feature sets chosen to be representative signals for each weld class [Leg2001]. Zhao et al. used a new type of pattern classifier, the support vector machine (SVM), to classify defects such as porosity, surface notches, and subsurface cracks in metal matrix composite sheets [Zha2004].

6.3 Summary of the defect detection parameters

The most commonly used defect indicating parameters are

- In time domain: mean, maximum, minimum, peak-to-peak, Root Mean Square (RMS) and variance of the response, correlation coefficient

- In frequency domain: arithmetic and geometric mean of the spectral peak amplitudes
- In joint time-frequency domain: distribution of signal energy in time and frequency, which can be described by local amplitude of spectrogram, wavelet coefficients, or WVD of chirplet atoms
- Principal components and corresponding eigenvalues of the response.

The least amount of computation and thus the best energy efficiency is achieved through using a combination of time domain parameters for defect detection. For more profound analysis of the behaviour of the wave modes in the structure, chirplet decomposition method combined with WVD analysis is informative but computationally burdening approach. The repeatability and capability to indicate defects of peak-to-peak amplitude, variance and correlation coefficient is studied more closely in Chapter 7.

6.4 Locating defects

The main objectives of SHM are to indicate existence of defects and to locate them with accuracy specific to the application. Furthermore, determining type, size and growth rate of the defect is often needed in order to decide if the defect should be repaired immediately or if it can wait till, for example, the next scheduled maintenance break.

Various methods have been applied to defect locating problem, and only a few of them are mentioned here as typical examples. A common principle for ultrasonic detection of boundaries, e.g. defects, in a structure is to use pulse-echo measurements, where the same transducer is used for both actuating and sensing the ultrasonic wave. When an ultrasonic wave hits a boundary, it is partly reflected, and by analyzing the time of arrival of the reflections, the distance between the sensor and the boundary can be determined.

A phased array technique based on pulse-echo Lamb wave measurements has been applied e.g. by Purekar et al. [Pur2004] and Giurgiutiu et al. [Giu2003, Giu2008a]. Phased array is a group of sensors located at distinct spatial locations in which the relative phases of the sensor signals are varied in such a way that the effective propagation pattern of the array is reinforced in a desired direction and suppressed in undesired directions [Giu2008a]. The array acts as a spatial filter, attenuating all signals except those propagating from certain directions.

So-called beamforming algorithms are used to focus the array's signal-receiving or signal-transmitting abilities in a particular direction. Giurgiutiu et al. developed this approach into an Embedded Ultrasonic Structural Radar (EUSR) algorithm for large area interrogation [Giu2002b, Giu2008b].

It is not always possible to use the pulse-echo method, and the defects need to be detected from a pitch-catch Lamb wave response, where one transducer is actuating the signal and another is the sensor. Su and Ye [Su2004, Su2005] suggested using digital damage fingerprints (DDF) extracted from the pitch-catch Lamb wave data, stored in damage parameter database and then used as an input for a multilayer feedforward artificial neural network. DDF contains characteristic components in a filtered Lamb wave signal, including characteristic amplitudes, time and frequency, and rising/attenuating durations.

Raghavan and Cesnik [Rag2007] discussed the triangulation method in isotropic plate structures. In triangulation method for locating the defect, one needs three piezoelectric transducers: one at the time is an actuator and the other two are used as sensors. The time-of-flight from the actuator to the defect and back to one of the sensors is determined, yielding the distance d travelled by the pulse. The locus of all possible locations of the defect is an ellipse with the actuator and the sensor at its foci and d as the major axis. By exciting each actuator in turn and using the others as sensors, three such ellipses can be drawn and the defect is located at their intersection. Raghavan and Cesnik set the pre-condition to this method that the PWASs are sensitive only to one Lamb wave mode when used as sensors.

Mal et al. have suggested a vibration and wave propagation based SHM system especially for composite structures [Mal2005, Ban2007, Ban2009, Mal2009]. Their method is based on measuring the frequency response function (FRF) of the structure. The FRF depends on the mass, damping and stiffness properties of the structure, and any changes in these properties produce changes in the FRF. The presence and extent of the damage can be determined by measuring and calculating the FRF of the dynamic response of the structure at multiple points before and after the defect appears. As a defect indicating parameter, they used the damage index defined in Eq. (120). The FRFs were measured by using a sinusoidal pulse as an actuation signal to simulate an impulse response, and taking the FFT of the receiving sensor response. The measurements were repeated several times to improve the statistical reliability of the method. A coupled Student's Test [Ben1986, Mon2000] was applied to verify that the measurement sets from the reference and damaged structure belonged to different structural configurations.

Ng and Veidt presented Lamb-wave-based defect detection technique for composite laminates [Ng2009]. Because the wave propagation velocity depends on the direction on propagation in composites, they evaluated the existence and location of defect by measuring the scatter signals, i.e. the difference between the signals measured in current and reference state. In an undamaged state, the scatter signal should be zero. They then used cross-correlation analysis between the envelopes of the actuation and scatter signal to estimate the arrival time of the wave scattered from a defect at the sensor. This corresponds to the wave travel time from actuator to the defect and then from defect to the sensor, taking into account the changes in wave propagation velocity when the direction of propagation changes. The arrival times, $T_{ab}(x,y)$, for waves propagating from actuator a to sensor b trough each point (x,y) of the structure are first calculated. If a defect exists, the value of the cross-correlation function between the envelopes of the actuator and scatter signals will get its maximum value at time delay T_d. The defect can be located at any point (x,y) with $T_{ab}(x,y) = T_d$. The defect localization image was finally created by superimposing the power flux (square of the cross-correlation value at time delay $T_{ab}(x,y)$) of all actuator and sensor signal paths.

6.4.1 Correlation based method

As discussed above, the simplest signal parameters indicating existence of defect in a path between two PWASs are time-domain amplitude measures, amplitude, variance and cross-correlation coefficient. The longer the measurement period, the more the waveform contains superposition of different wave modes travelling through different paths and reflections from structure edges etc. Only the first wave mode burst arriving at the sensor is therefore selected for the analysis because it has travelled directly from the actuator to the sensor and is in that sense "pure" wave and thus easy to interpret [Hyt2008].

Zhao et al. suggested a simple correlation coefficient based method for locating defect in an aircraft wing using a network of PWASs [Zha2007a]. This defect locating method is applicable only to isotropic structures, where the Lamb wave velocity is independent on the direction of propagation. Their eight PWASs were located circularly around a structural "hot spot" where defects are most likely to appear. Types of defect experimented with were simulated corrosion and artificial saw-cut defect in a rivet hole. Lamb wave responses both under normal conditions and in damaged state were measured along every possible signal path so that, one by one, each one of the PWASs was acting as an actuator and the rest of the sensors were detectors. Due to reciprocity, the signal from actuator i to sensor j should be identical to the signal from actuator j to sensor i, and thus only $N(N-1)/2$ data sets would be needed for a N PWAS network.

It is assumed that given the same environmental and measurement conditions, the differences between signals under present and normal conditions are attributed to the defect initiation. The probability that a defect exists at a given point can thus be estimated according to the degree of the signal changes and according to how much a defect at that position affects the signal path. The effect of defects on Lamb wave propagation has been studied both through simulations and physical experiments [Lee2007a,b, McK1999, Fro2002]. It has been shown that a defect causes scattering of the Lamb wave modes, and the propagation direction of the scattered waves as well as the amount of Lamb wave energy passing through the defect depends on the ratio of the wavelength to the defect size. When a defect is located directly at the actuator-sensor path, the measured response is attenuated and delayed. If the defect is located off the path but close to it, the scattered wave modes are superposed with the wave modes propagating directly from actuator to sensor. The further the defect is away from the direct path, the more the signal change decreases. The effect of structural defects on the Lamb waveforms is further discussed in Chapter 7.6.

The defect distribution probability within the sensor network can then be expressed as a linear sum of all the signal changes of every possible transmitter-receiver pair. A simple linearly decreasing elliptical spatial distribution with actuator and sensor PWAS in the focal points shown in Figure 50 is assumed.

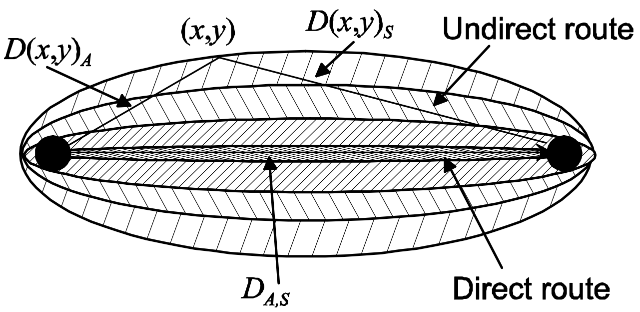

Figure 50. Spatial distribution ellipse.

This distribution between the actuator-sensor pair is defined using the ratio of the sum of distance of the point (x, y) to the transmitter i, $D(x,y)_A$, and receiver j (the focal radii) , $D(x,y)_S$, to the distance between the transmitter and receiver, $D_{A,S}$:

$$RD_{ij}(x,y) = \frac{D(x,y)_A + D(x,y)_S}{D_{A,S}} = \frac{\sqrt{(x-x_i)^2+(y-y_i)^2}+\sqrt{(x-x_j)^2+(y-y_j)^2}}{\sqrt{(x_j-x_i)^2+(y_j-y_i)^2}} \tag{136}$$

The size of the effective elliptical distribution area is controlled with parameter $\beta > 1$ by defining

$$R_{ij}(x,y) = \begin{cases} RD_{ij}(x,y) & \text{when } RD_{ij}(x,y) < \beta \\ \beta & \text{when } RD_{ij}(x,y) \geq \beta \end{cases} \tag{137}$$

Too small value for β results in artefacts, too large value results in poor resolution. Zhao et al. recommend $\beta \approx 1.05$.

The RAPID (Reconstruction Algorithm for Probabilistic Inspection of Defects) algorithm suggested by Zhao et al. [Zha2007a] can be summarized as follows: Let X be the reference signal, Y the new signal and N be the number of PWAS elements in an array cluster of a sensor network.

Step 1. Calculate the correlation coefficient between X and Y:

$$\rho = \frac{C_{XY}}{\sigma_X \sigma_Y} = \frac{\sum_{k=1}^{K} (X_k - \mu_X)(Y_k - \mu_Y)}{K \sigma_X \sigma_Y} \tag{138}$$

where K is the length of the data sets X and Y, μ_X and μ_Y are their mean values, and σ_X and σ_Y are their standard deviations, respectively.

Step 2. Calculate the signal difference coefficient A_{ij} of the sensor pair S_{ij} (i = actuator, j = sensor):

$$A_{ij} = 1 - \rho_{ij} \tag{139}$$

Step 3. Estimate the defect probability at position (x,y) within the reconstruction region $P(x, y)$ as

$$P(x,y) = \sum_{i=1}^{N-1} \sum_{j=i+1}^{N} P_{ij}(x,y) = \sum_{i=1}^{N-1} \sum_{j=i+1}^{N} A_{ij} \left[\frac{\beta - R_{ij}(x,y)}{\beta - 1} \right] \tag{140}$$

where $P_{ij}(x, y)$ is the defect distribution probability estimation from the actuator- sensor pair S_{ij}.

When $R_{ij}(x, y) = 1$, i.e. the point (x, y) is in the direct line between the actuator and the sensor, $P_{ij}(x, y) = A_{ij}(x, y)$; when $R_{ij}(x, y) = \beta$, i.e. the point (x, y) is on the boundary of the effective distribution area, $P_{ij}(x, y) = 0$.

Generally, if a defect occurs, a set of sensor pairs will be affected, and the resulting defect distribution probability image will show largest probability for the point where the defect is located.

Although Zhao uses the term “probability”, $P(x,y)$ or $P_{ij}(x, y)$ is not a value of probability in strictly statistical sense. It is some real number between 0 and R, where R is limited by the number of direct paths between PWASs crossing each other at the given point. This number varies depending on the number of PWASs and their locations with respect to each other. Rather than statistical probability, this method researches the plausibility of a defect to be located at any given point in the structure. If there are changes in the PWAS responses in some local area of the structure, it is likely that some structural change has occurred in that area.

Table 9. Correlation coefficients for each path with 5 mm and 10 mm defects.

Path	ρ, 1 mm	ρ, 3 mm	ρ, 5 mm
P1 → P2	0.998	0.999	0.998
P1 → P3	0.999	0.999	0.997
P1 → P4	0.995	0.997	0.986
P2 → P3	0.997	0.994	0.982
P2 → P4	0.996	0.998	0.996
P3 → P4	0.995	0.995	0.996

Correlation coefficients for different signal paths in the test plate 2 shown in Figure 2b with 1 mm, 3 mm and 5 mm defects are shown in Table 9. The only significant changes in correlation coefficient in Table 9 are on paths P1→P4 and P2→P3 when the defect diameter is 5 mm. The RAPID algorithm results for $\beta = 1.05$ on each path for 1 mm, 3 mm and 5 mm defects are shown later in Figure 51. With only four PWASs, the algorithm tends to result in maximum value at either one of the sensors or in the middle of the sensor area.

6.4.2 Enhanced method

The author suggests that the RAPID algorithm can be enhanced by utilizing the knowledge about the signal amplitude and variance changes instead of only about the correlation coefficients. Decrease in the amplitude and variance of the signal means that the defect is on or very near the signal path. The larger the defect is with respect to the wavelength, the larger the decrease in the amplitude and variance. Increase in amplitude and variance means that the defect is somewhere near the signal path, reflecting more power to the sensor end. This information can be used for setting the parameter β and for defining the shape of the probability distribution area separately for each path. The results of the defect location can also be improved by using only the paths closest to the defect according to the indicating parameters.

Table 10. Relative change in peak amplitude and burst variance for each path for 1 mm, 3 mm and 5 mm defects.

Path	1 mm		3 mm		5 mm	
	V_{peak}	σ^2	V_{peak}	σ^2	V_{peak}	σ^2
P1 → P2	1.02	1.06	1.02	1.03	1.06	1.13
P1 → P3	1.05	1.07	1.08	1.05	1.14	1.17
P1 → P4	1.00	1.00	0.92	0.82	0.86	0.74
P2 → P3	0.97	1.01	0.97	1.02	1.05	1.21
P2 → P4	1.00	1.02	0.99	1.02	1.02	1.05
P3 → P4	0.97	0.91	0.97	0.92	0.99	0.99

Relative changes in peak amplitudes and burst variances for each signal path at 450 kHz frequency for defects with diameter 1 mm, 3 mm and 5 mm in test plate 2 are shown in Table 10. At that frequency, the wavelength of the S_1 mode is approximately 13 mm and the wavelength of S_2 mode 21 mm. Thus the defect size is small with respect to the wavelength and the waves are scattered relatively evenly around the defect [McK1999]. The relative variation both in amplitude and variance under normal conditions is between 0.9…1.1 (see Chapter 7). The only changes exceeding this variation are the attenuation in variance for 3 mm and 5 mm defect at signal paths P1→P4, which is closest to the defect, and amplification in variance at signal paths P1→P2, P1→P3 and P2→P3. The amplification is caused by scattering from the defect. As a quadratic parameter, burst variance has better sensitivity for small changes in Lamb wave responses than the peak amplitude.

The selection of generic significance thresholds for each parameter has a great effect on result of defect location because it determines the weighing of the signal paths in the locating algorithm. Therefore, the variation in variance ratios from each signal path under reference condition needs to be known. The other important parameters are the width of the probability ellipse, β, and the periphery of the probability ellipse if the defect is not directly on the path. The suggested enhancements to the RAPID algorithm are as follows:

If there is increase in the variance, the size of the effective elliptical distribution area is defined as

$$R_{ij}\left(x,y\right)=\begin{cases}\left|RD_{ij}\left(x,y\right)-1.1\right|+1.1 & \text{when } \left|RD_{ij}\left(x,y\right)-1.1\right|+1.1<\beta \\ \beta & \text{when } \left|RD_{ij}\left(x,y\right)-1.1\right|+1.1\geq\beta\end{cases} \tag{141}$$

and the corresponding defect probability at position (*x*,*y*) within the reconstruction region *P*(*x*, *y*) as

$$P\left(x,y\right)=\sum_{i=1}^{N-1}\sum_{j=i+1}^{N}A_{ij}\left[\frac{\beta-R_{ij}\left(x,y\right)}{\beta-1.1}\right] \tag{142}$$

where *N* is the number of PWAS elements in an array cluster of a sensor network. Thus the maximum probability is on the periphery of an ellipse and decreases linearly to both directions from that periphery. The periphery of the ellipse (maximum probability is at $RD_{ij}(x,y)=1.1$) is selected such that the waves scattered from a defect near that periphery reach the sensor within the period of time selected for the analysis, i.e. before the first antisymmetric wave mode arrives at the sensor. The value for β is selected to set a width of the distribution around the periphery of the ellipse. Value $\beta\approx$ 1.2 is recommended.

Let *X* be the reference signal and *Y* the new signal. Let the ranges of variation of the variance under reference conditions be $[\sigma^2_{\min},\sigma^2_{\max}]$. The limits of the range depend on the repeatability of the measurements and are discussed in the next chapter. Let the current variance ratio be σ^2_R.

Step 1. Calculate the variance ratio, $\sigma_R^2=\sigma_Y^2/\sigma_X^2$ between *X* and *Y*.

Step 2. Calculate the signal difference coefficient A_{ij} of the sensor pair S_{ij} (*i* = actuator, *j* = sensor):

$$A_{ij}=1-c_{ij} \tag{143}$$

where

$$c_{ij}=\begin{cases}\sigma_{\mathrm{R}}^2 & \text{when } \sigma_{\mathrm{R}}^2<\sigma_{\min}^2 \\ 2-\sigma_{\mathrm{R}}^2 & \text{when } \sigma_{\mathrm{R}}^2>\sigma_{\max}^2 \\ 1 & \text{when } \sigma_{\min}^2\leq\sigma_{\mathrm{R}}^2\leq\sigma_{\max}^2\end{cases}$$

Step 3. Estimate the defect probability at position (*x*,*y*) within the reconstruction region *P*(*x*, *y*):

- If $\sigma_R^2 < \sigma_{\min}^2$, set β = 1.05 and calculate $R_{ij}(x,y)$ according to Eq. (137) and $P(x,y)$ according to Eq. (140)
- Else if $\sigma_R^2 > \sigma_{\min}^2$, set β = 1.2 and calculate $R_{ij}(x,y)$ according to Eq. (141) and $P(x,y)$ according to Eq. (142)

Step 4 (optional): Based on the changes in parameters, select the three signal paths closest to the defect.

When only a small number of PWASs is used, both algorithms result by nature in spatial defect probability distribution with local maxima, whose values differ from each other. The defect location estimate is selected to coincide with the global maximum value. If the defect has very small effect on the estimation parameters, and the values of spatial probability values are small, this often results in the global maximum being found on or near of one of the PWASs, where the distributions from the other PWASs are summed.

The defect location results for defect diameters 1mm, 3 mm and 5mm using both Zhao's method and the suggested enhanced method with variance reference values $[\sigma_{\min}^2, \sigma_{\max}^2]$ = [0.99, 1.01] for the test plate 2 are shown in Table 11 and Figure 51. The correct location for the defect is (210,250) mm from the lower left corner of the plate (Figure 2b).

Table 11. Estimated defect locations and estimation errors for Zhao's method and enhanced method for defect diameters 1 mm, 3 mm and 5 mm in test plate 2.

Defect size	Estimated (Zhao)	Error (Zhao)	Estimated (enhanced)	Error (enhanced)
1 mm	(350,100) mm	205 mm	(142,358) mm	128 mm
3 mm	(150,150) mm	117 mm	(188,312) mm	66 mm
5 mm	(239,239) mm	31 mm	(194,285) mm	38 mm

The defect location results for defect diameters 1mm, 3 mm and 5mm using both Zhao's method and the suggested enhanced method with variance reference values $[\sigma_{\min}^2, \sigma_{\max}^2]$ =

[0.99, 1.01] for the test plate 1 (Figure 2a) are shown in Table 12 and Figure 52. The correct location for the defect is (186,187) mm from the lower left corner of the plate (Figure 2a).

Table 12. Estimated defect locations and estimation errors for Zhao's method and enhanced method for defect diameters 1 mm, 3 mm and 5 mm in test plate 1.

Defect size	Estimated (Zhao)	Error (Zhao)	Estimated (enhanced)	Error (enhanced)
1 mm	(350,350) mm	231 mm	(350,350) mm	231 mm
3 mm	(150,350) mm	167 mm	(188,188) mm	2 mm
5 mm	(150,350) mm	167 mm	(188,188) mm	2 mm

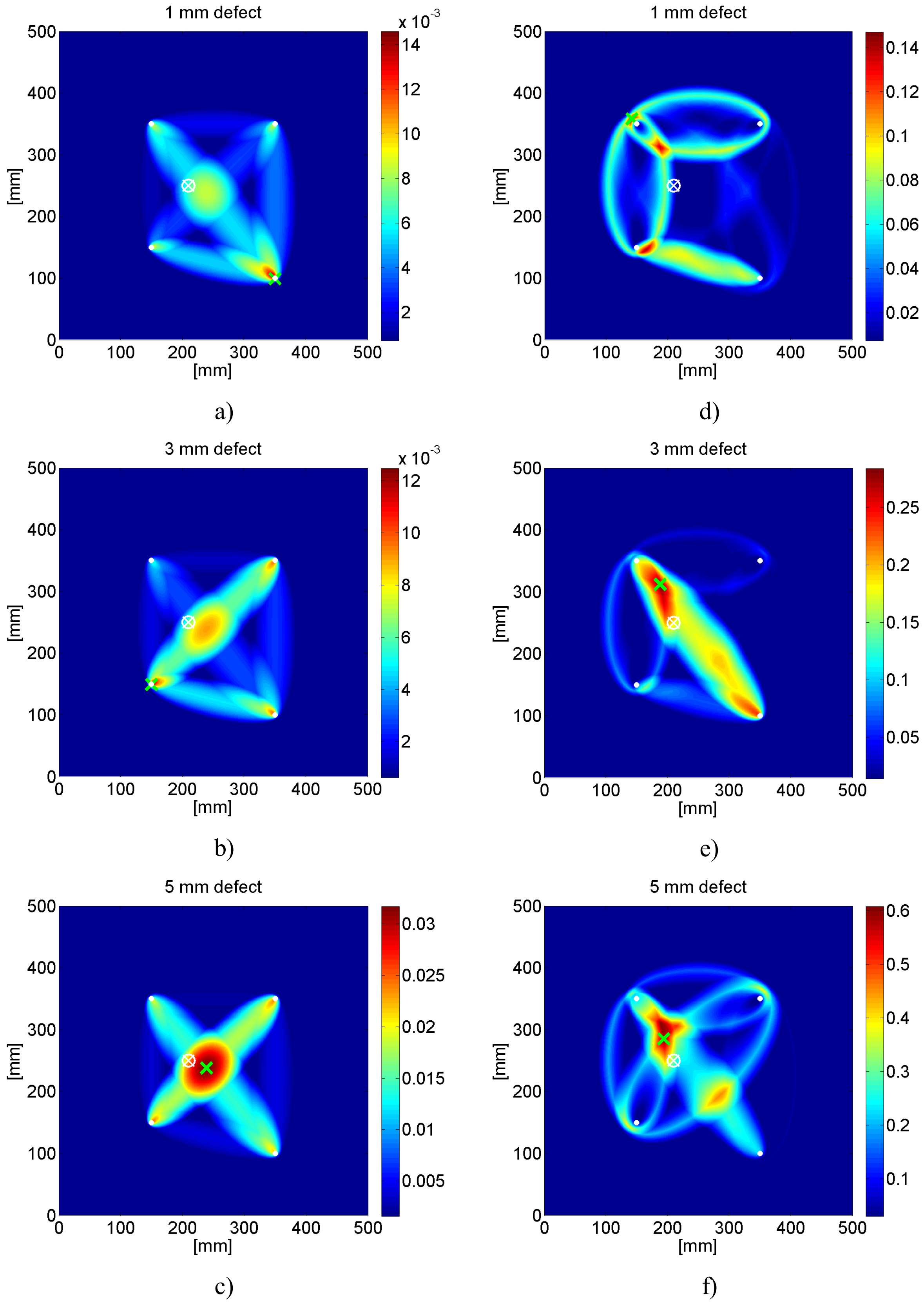

Figure 51. Defect locating results for defect diameters 1 mm, 3 mm and 5 mm from test plate 2. a)...c): Zhao's method, d)…f): enhanced method. The white circle and cross indicate the correct defect location. The green cross indicates the estimated location.

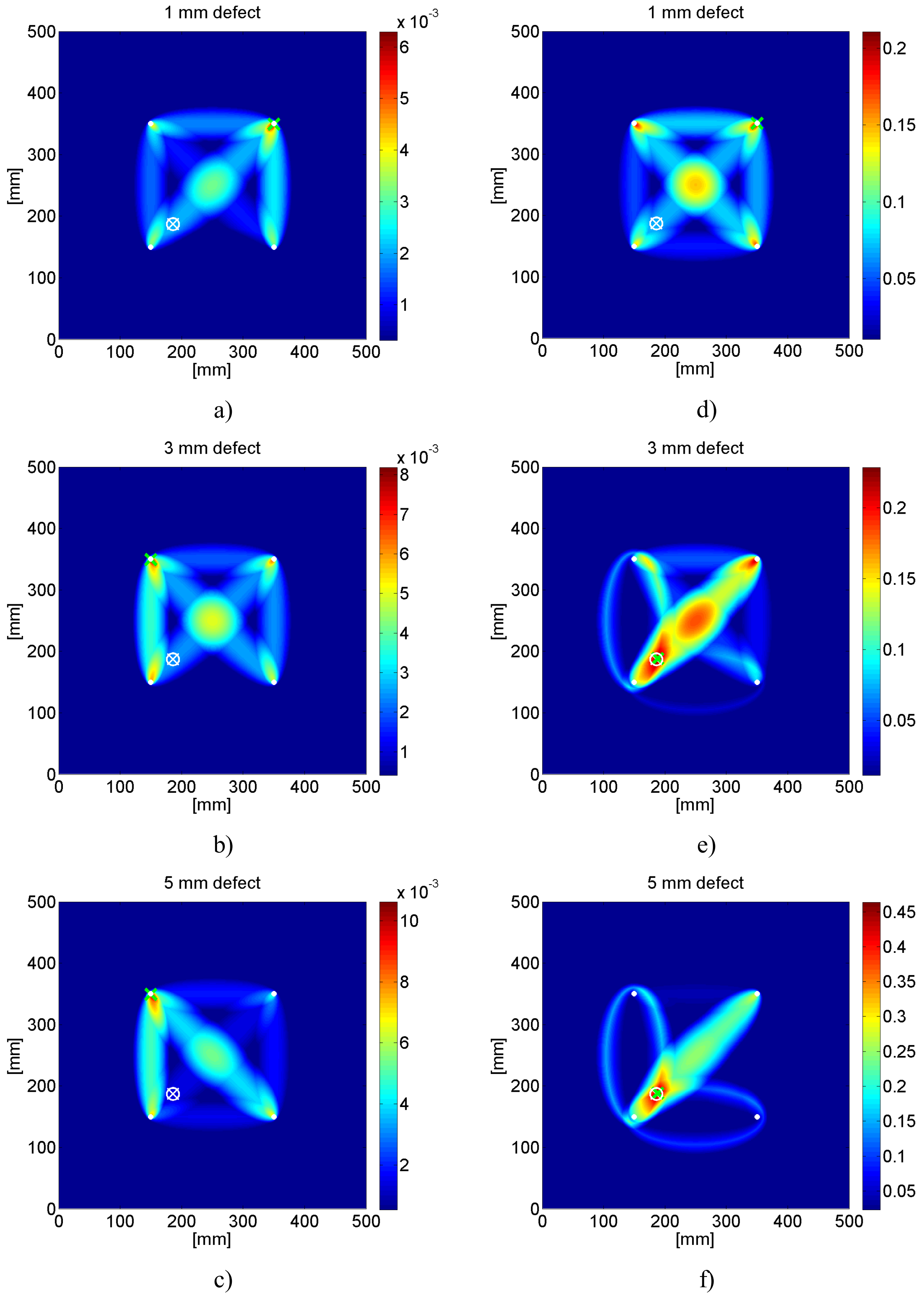

a) d) b) e) c) f)

Figure 52. Defect locating results for defect diameters 1 mm, 3 mm and 5 mm from test plate 1. a)...c): Zhao's method, d)…f): enhanced method. The white circle and cross indicate the correct defect location. The green cross indicates the estimated location.

6.4.3 Crack detection

Like holes, cracks resulting e.g. from metal fatigue form discontinuities in a structure and alter the Lamb wave propagation. The difference between cracks and holes with respect to the Lamb waves is the defect shape and the ratio of the defect size to the Lamb wavelength. The cracks are generally very narrow and tend to elongate with time in a loaded structure. They, as well as holes and other material discontinuities like corrosion, can be detected by studying their effect on Lamb wave characteristics when the wavelength used is small enough with respect to the defect size [Bie2001, Lu2006]. Lamb wave scattering from cracks is studied e.g. by Chang and Mal [Cha1999] and Flores-López and Gregory [Flo2006].

The enhanced method was tested with the same parameters as above on test plate 3, with a 1 mm × 10 mm crack. The results are shown in Figure 53. The centre of the crack was at (365,470) mm. The locating algorithm estimates the defect to be at (323,475) mm. The error is approximately 42 mm.

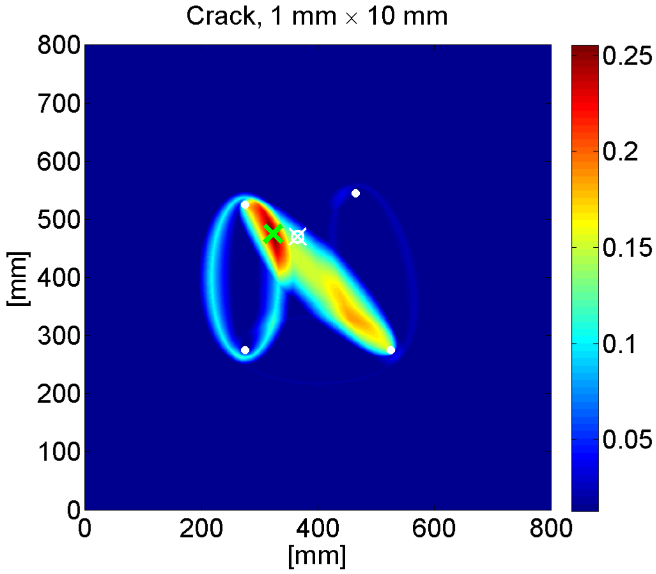

Figure 53. Defect locating results for a crack in test plate 3. The white circle and cross indicate the correct defect location. The green cross indicates the estimated location.

For the long and narrow aluminium test beam shown in Figure 4, the width of the elliptical distribution defined in Equation (141) was too large to fit within the beam. For this case, the elliptical distribution was redefined as

$$R_{ij}(x,y)=\begin{cases}\left|RD_{ij}(x,y)-1.01\right|+1.01 & \text{when } \left|RD_{ij}(x,y)-1.01\right|+1.01<\beta \\ \beta & \text{when } \left|RD_{ij}(x,y)-1.01\right|+1.01\geq\beta\end{cases} \tag{144}$$

and the corresponding defect probability at position (x,y) within the reconstruction region $P(x, y)$ as

$$P(x,y)=\sum_{i=1}^{N-1}\sum_{j=i+1}^{N}A_{ij}\left[\frac{\beta-R_{ij}(x,y)}{\beta-1.01}\right] \tag{145}$$

Parameter β was set to 1.03 instead of 1.2. The defect locating results for 700 kHz actuation frequency with variance reference values [$\sigma^2_{\min}$, $\sigma^2_{\max}$] = [0.99, 1.01] are shown in Figure 54. The shape of the beam is approximated with a uniform width. The four piezos were located as follows: P1 at (x,y) = (10,650) mm, P2 at (90,650) mm, P3 at (10,50) mm and P4 at (90,50) mm from the lower left corner.

Table 13. Relative change in peak amplitude and burst variance for each path for invisible crack under no load, visible crack under no load and visible crack under 50 kN static pull.

Path	Invisible crack		Visible crack		Visible with pull	
	V_{peak}	σ^2	V_{peak}	σ^2	V_{peak}	σ^2
P1 → P3	0.98	0.93	0.86	0.82	0.70	0.58
P1 → P4	0.94	0.95	0.76	0.78	0.85	0.73
P2 → P3	0.94	0.97	0.90	0.95	0.91	1.01
P2 → P4	1.01	1.06	0.98	1.01	0.82	0.85

The relative changes with respect to the intact reference in the peak amplitude and burst variance for each measured signal path for an invisible crack under no load, visible crack under no load and visible crack under 50 kN static pull are shown in Table 13. The wavelengths of the different Lamb wave modes at the crack location are in this case several millimetres, which is large compared to the crack dimensions. The arrival times of the different wave modes at the crack location are hard to estimate because of the adiabatic nature of the waves in a structure with varying thickness. The part of the PWAS response used for the analysis was in this case selected manually to be the first burst arriving at the sensor.

Table 13 shows that the effect of the crack on the Lamb wave response is larger on the signal paths close to the crack, i.e. the paths P1 → P3 and P1 → P4 as can be expected. The effect is also clearly detectable in spite of the small defect size-to-wavelength ratio.

The most notable result in this case is that even the invisible crack can be detected with the enhanced method. The error location estimate is near the midpoint of the beam, where the signal paths cross, which in this case also is close to the defect. However, the weight of the probability distribution is slightly more to the left hand side, where the crack appeared.

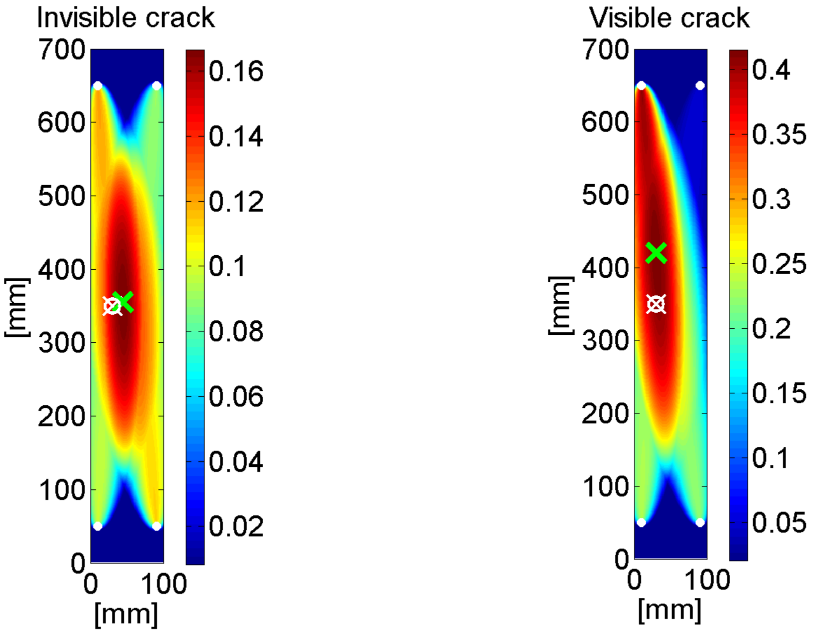

a) **b)**

Figure 54. Defect locating results for a stress induced crack in the aluminium test beam. a) Invisible crack, verified with eddy current measurement, b) visible crack (no pull). The white circle and cross indicate the correct defect location. The green cross indicates the estimated location.

6.5 Defect location tests using measurement system prototype

The measurement system prototype presented in Chapter 5 was tested on test plates 2 and 2B. Because the prototype was implemented after the defect detection tests on test plate 2 with ACESS system, the reference signals were measured from the plate with existing 10 mm defect at location (210,250) mm. Then another 10 mm defect was added to location (291,298) mm and the PWAS responses were again measured from each signal path. The actuation frequency was 428 kHz, and at that frequency, modes S_0, S_1, A_0 and A_1 exist in 10 mm plate. Of these, the S_1 mode has the highest group velocity and the A_0 mode the second highest. The part of the response corresponding to S_1 mode was used for analysis. Locating algorithm parameters were selected the same as in the examples above, $[\sigma^2_{\min}, \sigma^2_{\max}] = [0.99, 1.01]$. The relative changes in the burst variance for each signal path are shown in Table 14. Path P2→P3 experiences significant attenuation as can be expected. The superposing of the scattered waves from the two holes in the plate results in amplified response in almost all of the other paths.

Table 14. Relative change in burst variance for additional 10 mm defect in test plate 2.

Path	σ^2
P1 → P2	1.34
P1 → P3	0.87
P1 → P4	1.33
P2 → P3	0.54
P2 → P4	1.31
P3 → P4	1.30

The defect locating result in test plate 2 is presented in Figure 55. The estimation result is (305,310) mm, approximately 18 mm off the correct location. The red circle and cross indicate the location of the defect existing prior to the reference measurements. The white circle and cross indicate the added defect. The green cross indicates the estimated location for the added defect.

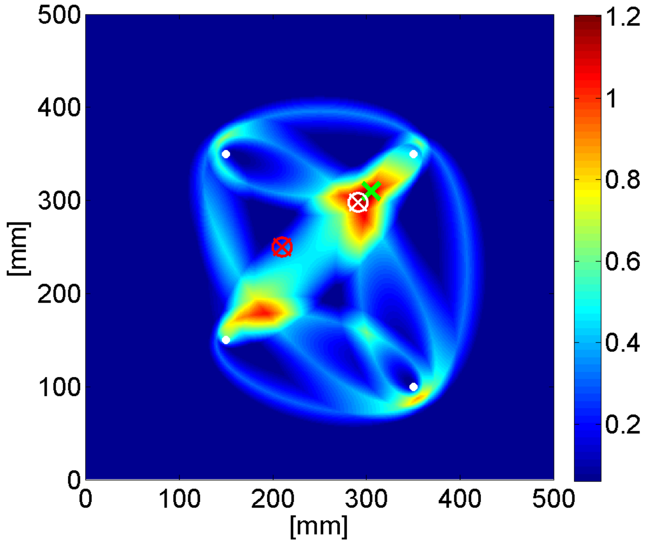

Figure 55. Defect location result in 10 mm thick aluminium plate with two defects (red cross: old, white cross: new) using energy efficient measurement method (test plate 2).

The construction of test plate 2B was identical to test plate 2. This plate was still intact and the reference signals were thus measured in a normal reference state. Then a 10 mm defect was added to location (259,185) mm and the PWAS responses were again measured from each signal path. Again, the part of the response corresponding to S_1 mode was used for analysis. Locating algorithm parameters were selected the same as in the previous examples. The relative changes in the burst variance for each signal path are shown in Table 15. There is attenuation in the path P1→P4 and amplification in the path P2→P3, as expected. In this case, the signal path P3→P4 experiences relatively strong attenuation, although amplification would be expected due to wave scattering. This results in added probability weight to the path P3→P4 and increased error in location estimate.

Table 15. Relative change in burst variance for 10 mm defect in test plate 2B.

Path	σ^2
P1 → P2	0.98
P1 → P3	0.96
P1 → P4	0.92
P2 → P3	1.18
P2 → P4	0.99
P3 → P4	0.85

The defect locating result in test plate 2B is presented in Figure 56. The estimation result is (200,138) mm, approximately 75 mm off the correct location.

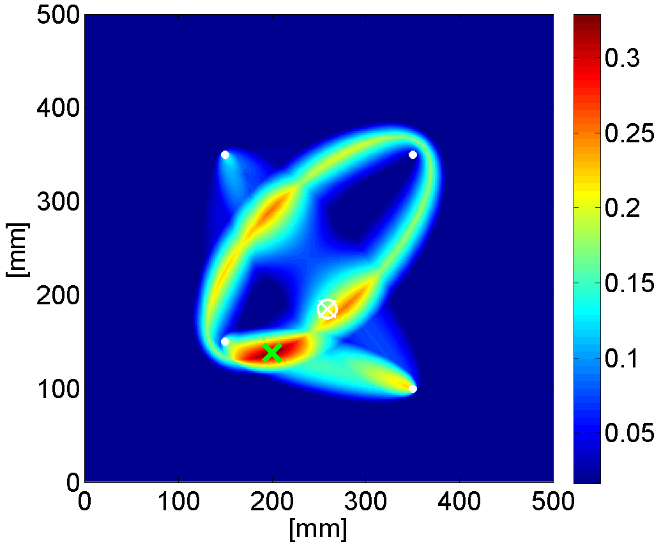

Figure 56. Defect location result in 10 mm thick aluminium plate using energy efficient measurement method (test plate 2B). The white circle and cross indicate the actual location of the defect. The green cross indicates the estimated location.

7. Defect indicating parameters and repeatability

7.1 Introduction

In order to decide if the change in the parameter value indicates defect, it is necessary to know the repeatability characteristics of the measurement method applied. Repeatability is defined as the closeness of agreement between independent results obtained with the same method on identical test material, under the same conditions (same operator, same apparatus, same laboratory and after short intervals of time). The measure of repeatability is the standard deviation [IUP1997]. The calculated values for the parameters generally vary between consecutive measurements. The repeatability of the defect measurements with the Acellent Smart Suitcase^{TM} (ACESS) SCS-3200 was analyzed.

In this chapter, the effect of structure thickness and temperature on the Lamb wave response is first reviewed; thickness because of its importance in selecting the appropriate part of the response for defect analysis, and temperature because of its effect on the parameters selected to indicate defects. Then the repeatability of the Lamb wave responses and amplitude, variance and correlation coefficient estimated from them is analyzed.

7.2 PWAS response with respect to structure thickness

The inherently complex nature of the Lamb waves travelling in a structure makes the analysis of measured responses very complicated. There are always at least two different wave modes (S_0 and A_0) travelling at different velocities and with different amount of wave dispersion. The number of existing wave modes and the behaviour of each mode across the cross section of the structure investigated, e.g. the resulting surface strain, vary according to the product of frequency and thickness. Figure 57 shows the surface amplitude ratio u_1/u_2 of particle motion (parallel and perpendicular to the plate surface, respectively) for S_0 and A_0 waves at different products of frequency and plate thickness, *fd*, in a 1mm thick aluminium plate. Above the *fd* value 1000 kHz×mm, the symmetric mode in the thin plate is considerably less longitudinal than in lower values of *fd*. With the antisymmetric mode, the effect is weaker but the longitudinal component becomes relatively stronger when *fd* value increases.

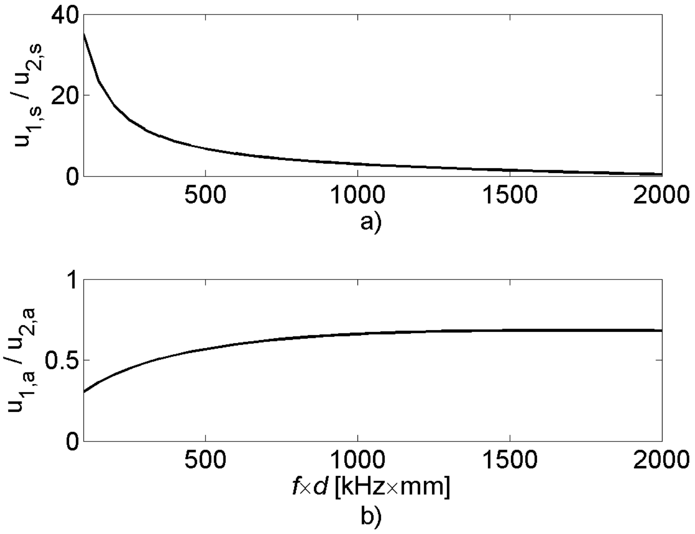

Figure 57. Particle motion amplitude ratios in a) S_0 and b) A_0 wave modes as a function of the product of frequency and plate thickness in 1 mm aluminium plate.

In the thick plate, the symmetric mode is more longitudinal throughout the studied frequency band, and around 2100 kHz×mm it is almost purely longitudinal. The other wave modes have similar behaviour when they appear (Figure 58).

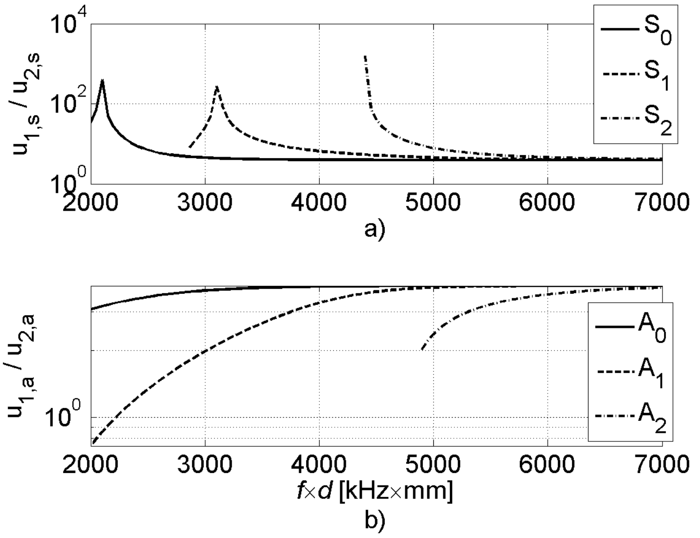

Figure 58. Particle motion amplitude ratios in a) S_0, S_1 and S_2 and b) A_0, A_1 and A_2 wave modes as a function of the product of frequency and plate thickness in aluminium.

Since the PWASs respond to the surface strain instead of the displacement normal to the surface, it might seem that the response is dominated by the wave mode having the stronger longitudinal displacement component. However, the critical factor is the wavelength of the mode with respect to the PWAS diameter as discussed in Chapter 4.5. Figure 59 shows the wavelengths of S_0 and A_0 mode in 1 mm thick aluminium plate. These are the only two wave modes that may exist simultaneously in 1 mm plate in the frequency range studied. The half-wavelength of A_0 mode is equal to or smaller than the PWAS diameter, and thus the surface strain induced by the A_0 mode reverses its sign within the PWAS area, resulting in weak response. In the frequency range up to 500 kHz, the half-wavelength of S_0 mode is larger than or equal to the PWAS diameter. Thus the S_0 mode induces stronger surface strain than A_0 mode and dominates the PWAS response. Above 500 kHz, the effect of S_0 mode reduces but remains stronger than that of A_0 mode. The maximum response is gained at the frequency where the diameter of the PWAS equals the half-wavelength of the mode.

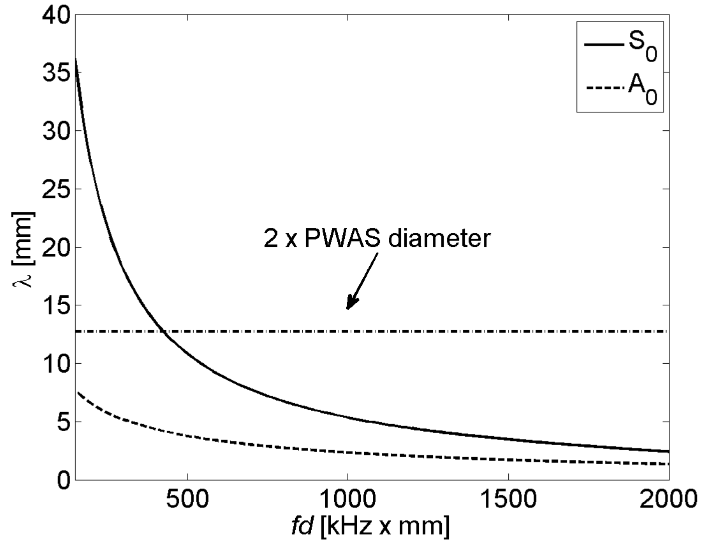

Figure 59. Wavelengths for different Lamb wave modes in 1 mm thick aluminium plate.

In 10 mm plate, the situation is more complicated since in the frequency range studied, up to eight Lamb wave modes (four symmetric and four antisymmetric) may exist simultaneously. Figure 60 shows the wavelengths of the different modes in a 10 mm thick aluminium plate. The optimal match between half-wavelength and the PWAS diameter is gained with different modes at different frequencies.

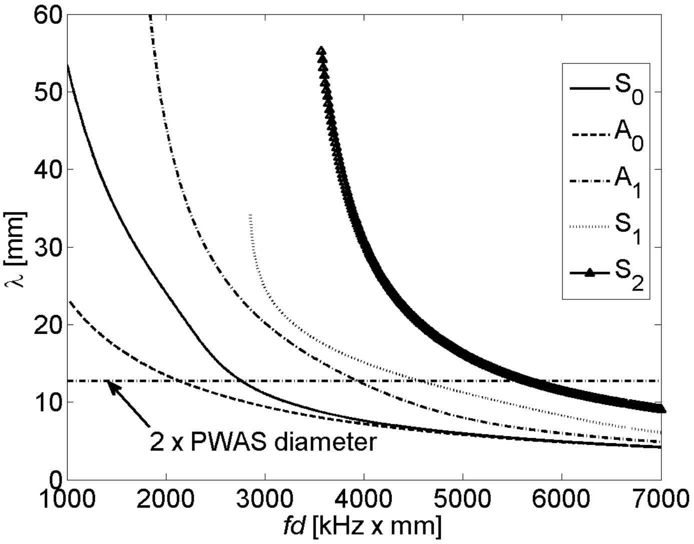

Figure 60. Wavelengths for different Lamb wave modes in 10 mm thick aluminium plate.

In addition to the sensitivity of the PWAS response to the wavelengths of the different wave modes, the separability of the modes from a response needs to be considered. Recall the group velocity dispersion curves from Chapter 4:

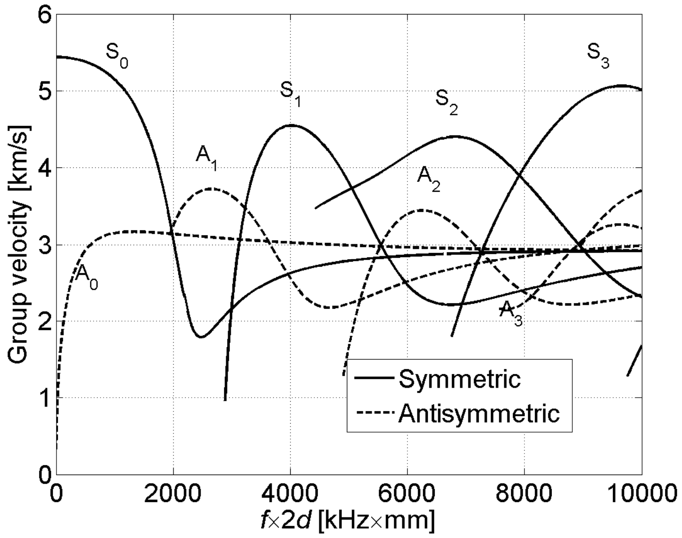

Figure 61. Group velocity dispersion curves for aluminium.

Below *fd* = 2000 kHz×mm, only S_0 and A_0 wave modes exist, and they have different group velocities. Thus they are easily separable from the PWAS response by their time of arrival at the sensor. However, if two or more wave modes arrive at the sensor simultaneously, their effects are superposed. From Figure 61 it is easy to see, that e.g. at *fd* = 2000 kHz×mm the modes S_0, A_0 and A_1 have almost equal group velocities and thus can not be seen separately in the PWAS response. From Figure 60 it can be deduced, that the response results dominantly from A_0 mode, which has the optimal wavelength at that *fd* value. At *fd* = 4500 kHz×mm, modes S_0, S_1, S_2, A_0 and A_1 exist, but they all have different group velocities and can be seen separately in the PWAS response. The strongest response can be expected from S_1 mode, which has the optimal wavelength (Figure 60).

The effect of these Lamb wave properties in practical PWAS measurements is demonstrated in Figures 62 - 64. Figure 62 shows PWAS response to a 600 kHz actuation signal measured from path P2→P3 in test plate 1 (Figure 1a), i.e. the low frequency-times-thickness case. The distance between the actuator and the sensor was approximately 283 mm. Solid line at 52 μs marks the arrival of the S_0 wave directly from actuator to sensor. Dash-dotted line at 93 μs marks the corresponding time for the A_0 wave. The response for the A_0 wave mode is much weaker than for the S_0 wave, as expected (see Figure 61). At 100 μs (dashed line), S_0 mode reflections from every edge of the plate arrive simultaneously due to the symmetric location of the PWAS discs on the plate, resulting in a cumulative response (see Figure 1a).

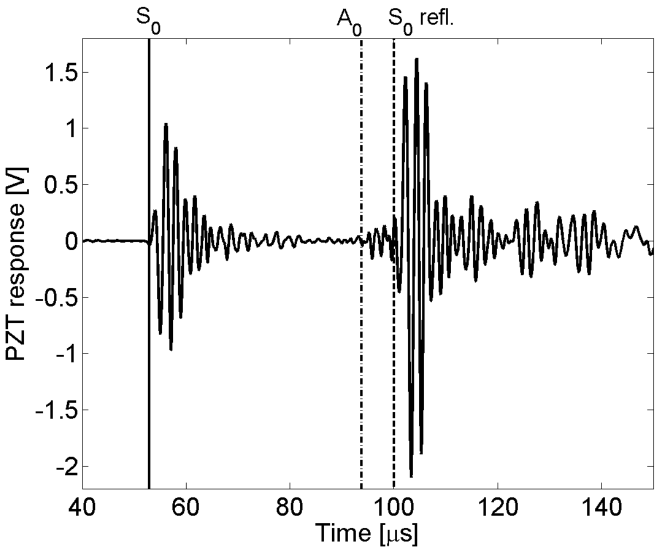

Figure 62. PWAS response from path P2→P3 in test plate 1 (1 mm aluminium).

Figure 63 shows the response to a 150 kHz actuation signal measured from path P2→P3 in test plate 2 (see Figure 1b), i.e. the product between frequency and thickness is 2.5 times higher than in Figure 62. Location of the actuator and sensor was as in the case of 1 mm plate. At this frequency and thickness, only S_0 and A_0 modes exist. The overall response is weaker than in 1 mm plate. Solid line at 61 μs marks the direct arrival of the S_0 mode, dash-dotted line at 88 μs the corresponding time for A_0 mode. Dashed line at 116 μs shows when the S_0 mode reflections from the edges meet; dotted line at 169 μs marks the corresponding time for A_0 mode. As expected from Figure 60, the PWAS is more sensitive to antisymmetric mode than to the symmetric mode.

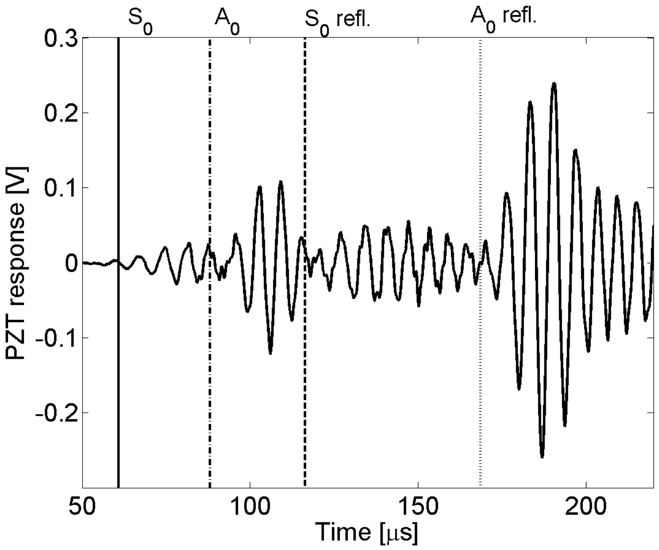

Figure 63. PWAS response from path P2→P3 in test plate 2 (10 mm aluminium plate), *f* = 150 kHz.

Figure 64 shows the response to a 450 kHz actuation signal measured from test plate 2 (see Figure 1b), i.e. the product between frequency and thickness is 3 times higher than in Figure 62. The direct arrivals of the wave modes are marked as follows: solid line with downward pointing triangles at the ends at 63 μs: S_1 mode, solid line with upward pointing triangles at the ends at 81 μs: S_2 mode, solid line at 102 μs: S_0 mode, dash-dotted line at 92 μs: A_0 mode, dash-dotted line with diamonds at the ends at 127 μs: A_1 mode. Dashed lines show when the symmetric mode reflections from the edges meet; dotted lines mark the corresponding time for antisymmetric modes. As expected from Figure 60, the PWAS is most sensitive to S_1 mode, which alone results in peak response value of 0.4 V. The sensitivity for S_0 and A_0 modes is equal, with a peak response value of 0.3 V. All other modes are superposed with each other or the edge reflections.

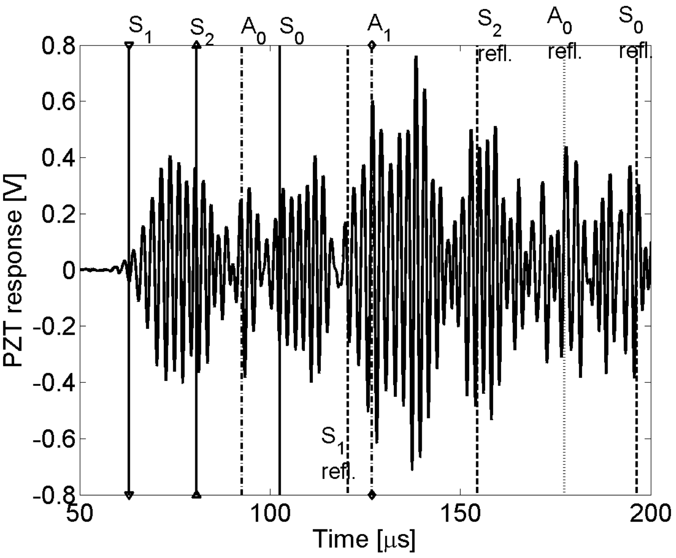

Figure 64. PWAS response from a 10 mm aluminium plate, *f* = 450 kHz.

Figures 62 - 64 also demonstrate that, depending on the sensor locations and reflection-causing discontinuities in the structure under investigation (edges, joints, defects etc.), waves of different modes and/or from different sources may arrive to the sensor rather simultaneously. It is very difficult to separate these coinciding waves from each other.

7.3 Effect of temperature on PWAS response

Another parameter affecting the signal analysis results is temperature. Both the density and the modulus of elasticity of material depend on temperature (Figure 65).

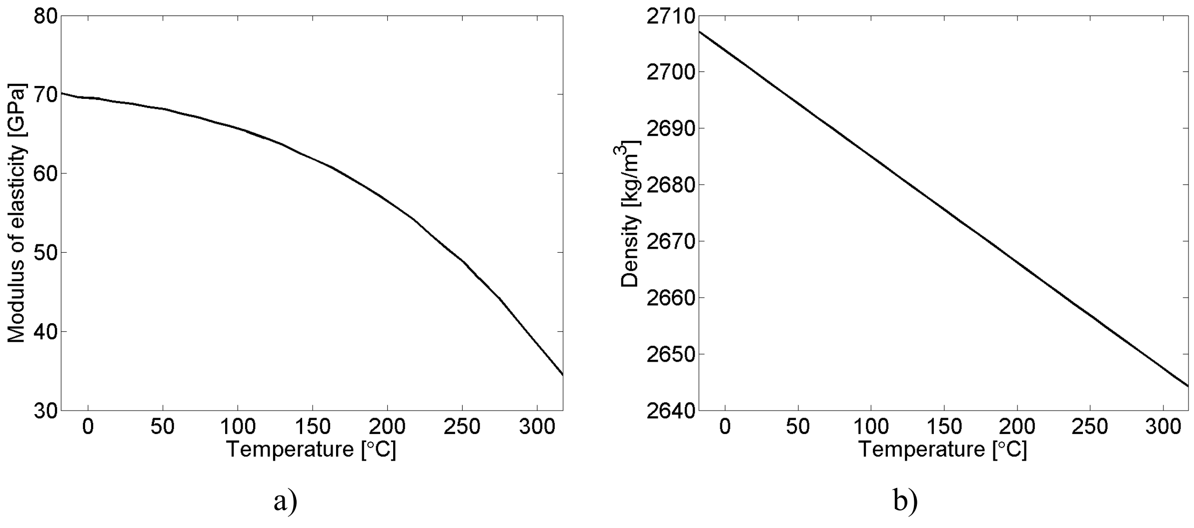

Figure 65. a) Modulus of elasticity and b) density of aluminium vs. temperature.

As the ultrasonic wave velocity depends on density and modulus of elasticity, see Eq. (39), they depend also on temperature [MIL2003]. Even though the changes of material properties for e.g. aluminium in the temperature range of 0 – 100℃ are less than 5%, they may be relevant in SHM applications [Pur2007].

Longitudinal and transversal wave velocities in aluminium as functions of temperature are shown in Figure 66.

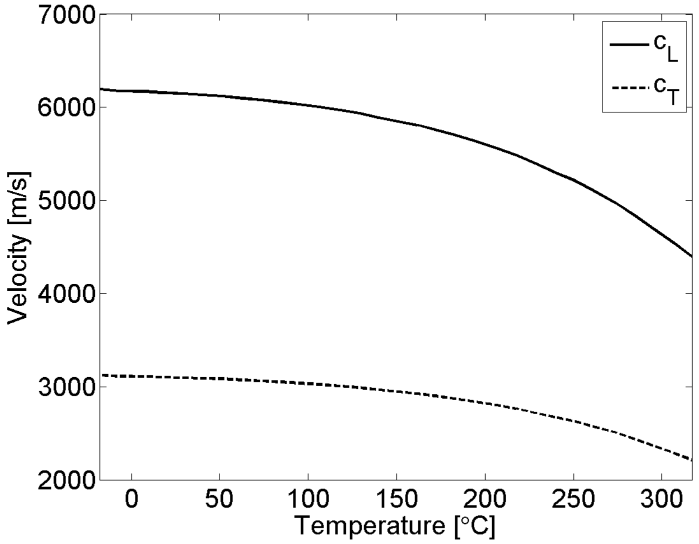

Figure 66. Temperature dependence of longitudinal (c_L) and transversal (c_T) wave velocities.

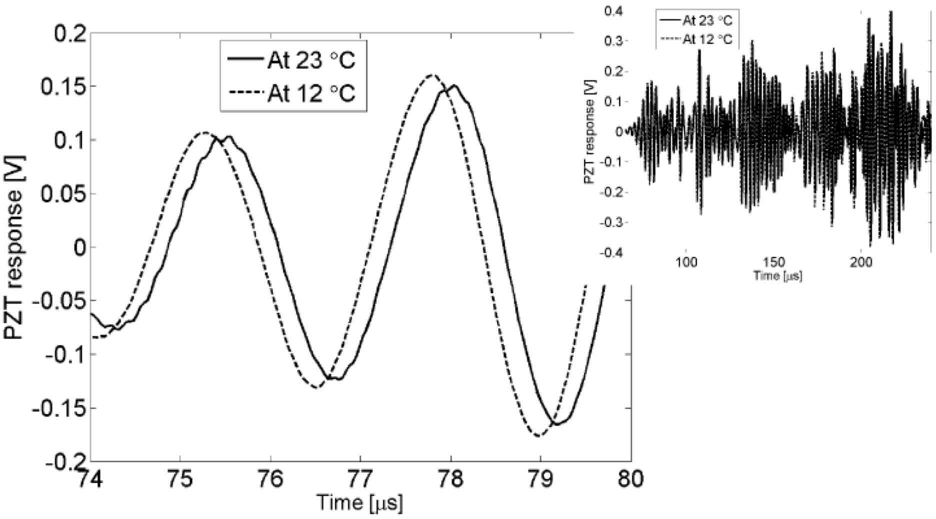

Figure 67. Practical effect of temperature change on response measured from test plate 2 (10 mm aluminium). Actuation frequency is 400 kHz.

An example of the effect of temperature change on Lamb wave propagation is shown in Figure 67. The measurement was made at normal room temperature (23℃), and at 12℃. At lower temperature, both the wave velocity and amplitude are higher. The decrease in thermal noise in measurement electronics can also been seen as a smoother response.

7.4 Repeatability of the PWAS response

Test plates 1 and 2 presented in Chapter 2 were tested for repeatability of the PWAS responses and the statistical parameters estimated from them. Four PWASs were attached to both plates (Figure 1a,b). Actuator signal in the test measurements was a 100 V peak-to-peak, five-period Hanning modulated sinusoid with centre frequencies from 200 kHz to 800 kHz at 50 kHz steps. The generated Lamb wave response was measured for each actuator-sensor pair $N = 50$ times successively. The sampling rate f_s was 25 MHz and the number M of samples taken was 6000. From these N successive measurements $\mathbf{x}_i$, $i = 1 \ldots N$, an average $\bar{\mathbf{x}} = \sum_{i=1}^{N} \mathbf{x}_i \big/ N$ was calculated and each one of the measurements $\mathbf{x}_i$ was then compared with $\bar{\mathbf{x}}$. The repeatability of the responses was tested by estimating the variances $\sigma_{r,i}^2$ of the residual signals $\mathbf{x}_i - \bar{\mathbf{x}}$,

$$\sigma_{r,i}^2 = \frac{1}{M-1} \sum_{i=1}^{M} \left(\mathbf{x}_i - \bar{\mathbf{x}}\right)^2 \qquad (146)$$

The calculations were repeated for each signal path and at every studied frequency.

For each signal path, the variance σ_n^2 of $\bar{\mathbf{x}}$ was calculated at every studied frequency and used as a measure of the total PWAS response energy for an individual path. The mean response variance $\sigma_m^2 = \sum_{n=1}^{M} \sigma_n^2 \big/ M$, where M is the number of different signal paths, is a measure of the average PWAS response energy at a given frequency.

The mean residual variance $\bar{\sigma}_r = \sum_{i=1}^{N} \sigma_{r,i} \big/ N$ for 1 mm plate is shown in Figure 68. Figure 68a shows that the absolute value of the residual variance is proportional to the mean response variance σ_m^2 (black line). The vertical bars show the results from each signal path. Figure 68b shows the residual variance relative to the response variance σ_n^2 on the given signal path.

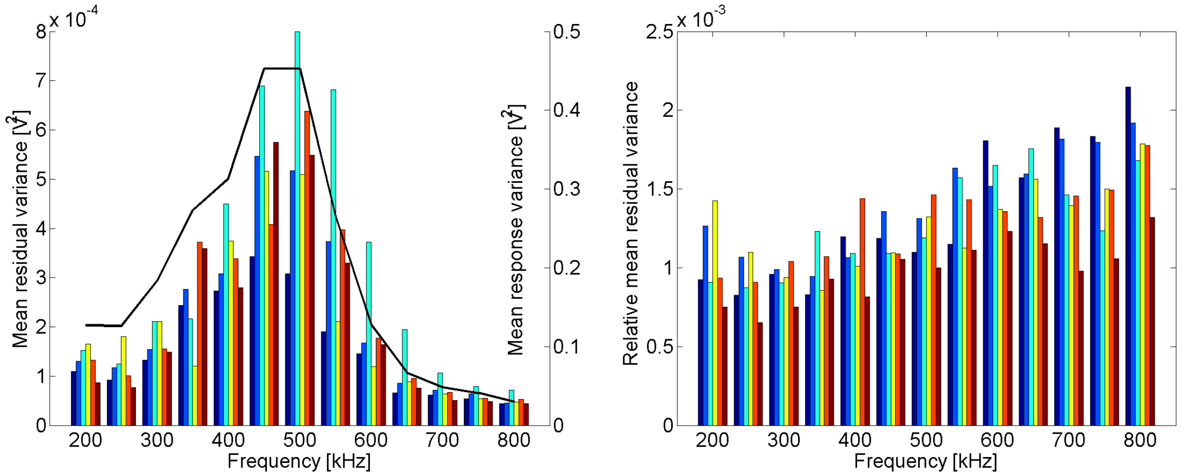

a) b)

Figure 68. PWAS response residual variance as a function of frequency for 1 mm Al plate. a) $\bar{\sigma}_r$ and mean response variance σ_m^2, b) $\bar{\sigma}_r$ relative to response variance σ_n^2.

The corresponding results for 10 mm plate are shown in Figure 69. At low frequencies, there is larger variation between the different signal paths than in the 1 mm plate. The relative residual variance is almost an order of magnitude larger than in 1 mm plate.

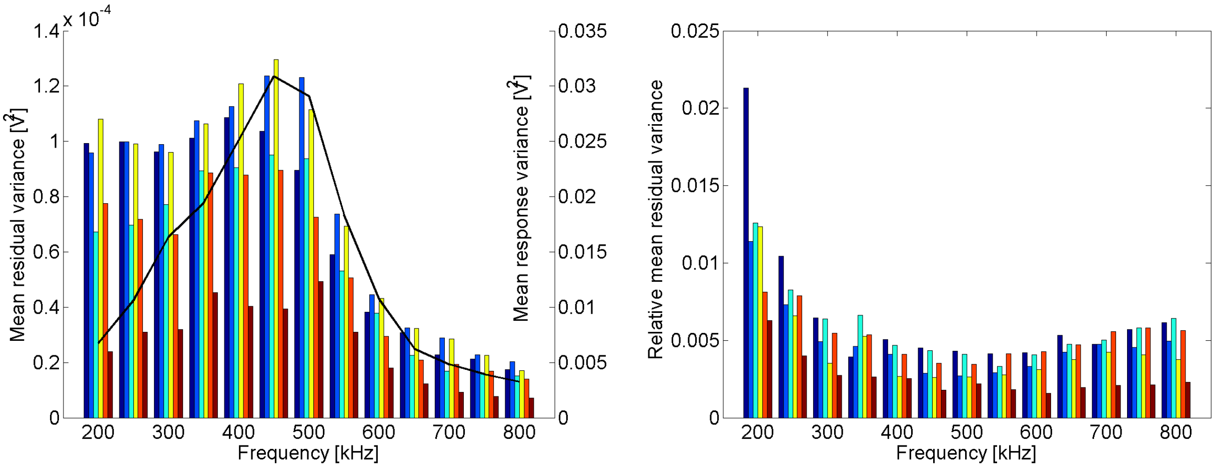

a) b)

Figure 69. PWAS response residual variance as a function of frequency for 10 mm Al plate. a) $\bar{\sigma}_r$ and mean response variance σ_m^2, b) $\bar{\sigma}_r$ relative to response variance σ_n^2.

7.5 Repeatability of the statistical parameters

As stated above, the longer the measurement period is, the more the waveform contains superposition of different wave modes travelling through different paths and reflections from structure edges etc. Only the first wave mode burst arriving at the sensor is therefore selected for the parameter analysis for easy interpretation.

7.5.1 Test plate 1

In the test plate 1 (1 mm aluminium plate) within the studied frequency range, the group velocity of S_0 mode is always higher than that of A_0 mode. The times of arrival for S_0 mode and A_0 mode at the sensor for each actuator-sensor pair were estimated. Then the time period containing only S_0 mode, $\mathbf{x}_{i,S0}$ and $\overline{\mathbf{x}}_{S0}$, was selected for the analysis. From Figure 59 it can be deduced that the best sensitivity for PWAS is for S_0 mode at 500 kHz. Experimental result verifies this (Figure 70). In 1 mm plate, with a 100 V peak-to-peak actuation burst the response generated by the S_0 mode reached maximum amplitudes of above 2 V.

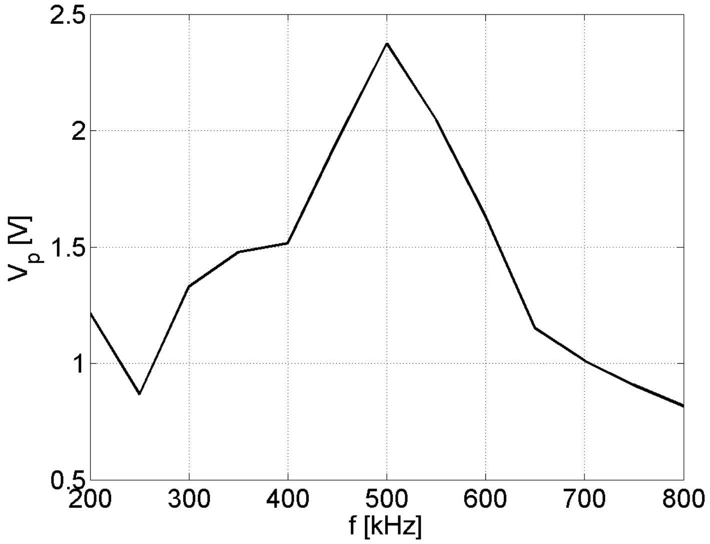

Figure 70. Peak S_0 mode voltage as a function of frequency measured from signal path P1→P4 in test plate 1.

The peak amplitude V_p of each measurement $\mathbf{x}_{i,S0}$ relative to the peak amplitude of the average response $\overline{\mathbf{x}}_{S0}$ was calculated from each signal path. The variations of the results are shown in Figure 71a as a function of frequency. The lower the response amplitude is, the higher the relative variation. Then the variance σ^2 of each measurement $\mathbf{x}_{i,\mathrm{S0}}$ relative to the variance of the average response $\overline{\mathbf{x}}_{S0}$ was calculated from each signal path. The variations of the results are shown in Figure 71b as a function of frequency. Again, the lower the response amplitude is, the higher is the relative variation.

The third statistical parameter analyzed is the correlation coefficient ρ between each of the measurements $\mathbf{x}_{i,\mathrm{S0}}$ and the average response $\overline{\mathbf{x}}_{S0}$. It was calculated from each signal path:

$$\rho = \frac{\sum_{k=1}^{K}\left(\mathbf{x}_i(k) - \mu_{\mathbf{x}i}\right)\left(\overline{\mathbf{x}}(k) - \mu_{\overline{\mathbf{x}}}\right)}{\sigma_{\mathbf{x}i}\sigma_{\overline{\mathbf{x}}}} \tag{147}$$

where K is the number of PWAS response samples. The variations of the results are shown in Figure 72 as a function of frequency. The correlation is nearly perfect at every frequency.

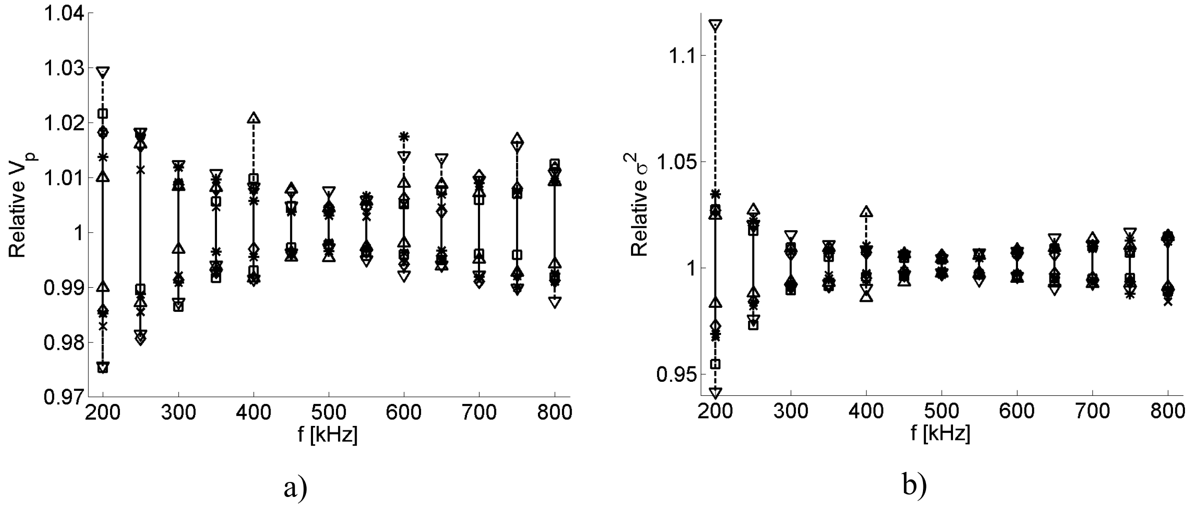

Figure 71. a) The variation of relative S_0 mode burst peak amplitudes, b) The variation of relative S_0 mode burst variances of each signal path as a function of frequency in test plate 1.

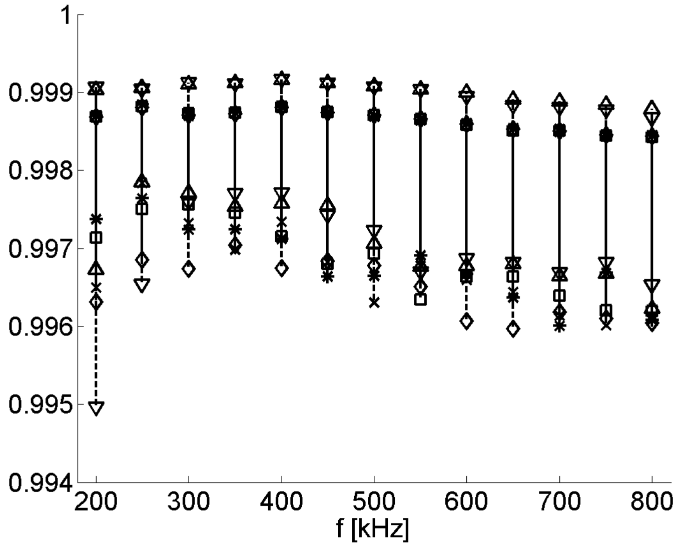

Figure 72. The variation of correlation coefficients between measurement $\mathbf{x}_{i,S0}$ and $\overline{\mathbf{x}}_{S0}$ of each signal path as a function of frequency in test plate 1.

7.5.2 Test plate 4

The corresponding analysis was also made for test plate 4 (1 mm aluminium with SMART Layer®, see Figure 3b). The peak voltage of S_0 mode burst as a function of frequency on signal path P1→P3 is shown in Figure 73.

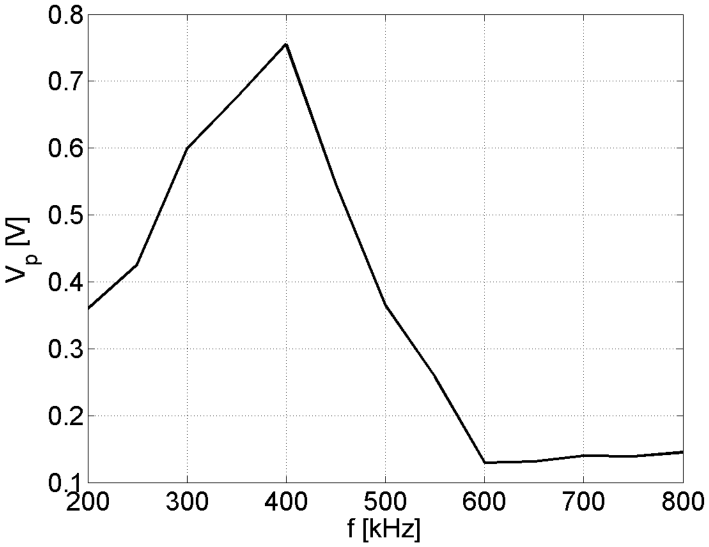

Figure 73. Peak S_0 mode voltage as a function of frequency measured from signal path P2→P3 in test plate 4.

The results for S_0 mode burst peak amplitude and variance are shown in Figure 74. Again, the relative variation of the parameters is smallest when the amplitude is highest. The achieved peak amplitude is much lower than in test plate 1 although the plate material and thickness are the same; with SMART Layer®, the responses are attenuated.

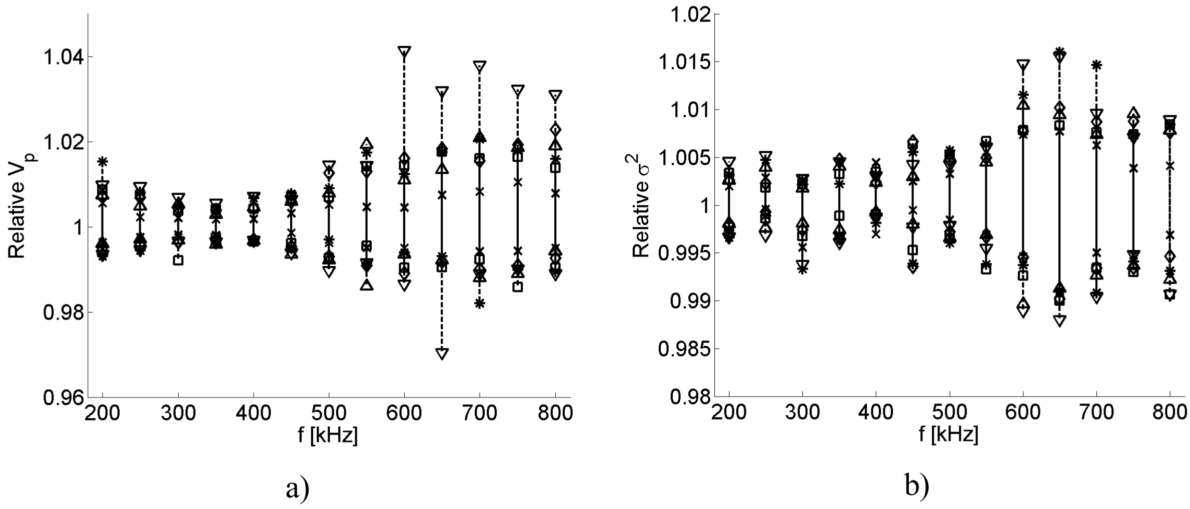

Figure 74. a) The variation of relative S_0 mode burst peak amplitudes, b) The variation of relative S_0 mode burst variances of each signal path as a function of frequency in test plate 4.

7.5.3 Test plate 2

In the test plate 2 (10 mm aluminium), the situation is less straightforward. Within the studied frequency range, the number of existing modes, their group velocities, and their wavelengths with respect to the PWAS diameter vary significantly (Figures 60, 61). E.g. at 200 kHz (*fd* = 2000 kHz×mm), modes S_0, A_0 and A_1 have almost equal group velocities and thus arrive at the sensor simultaneously. The wavelength of A_0 mode is nearly optimal with respect to PWAS diameter, so it is the main source of the PWAS response, but the other two modes add their effect to the response. At some frequencies the differences between the group velocities of the modes are so large that the reflections from the plate edges of the mode with highest velocity may arrive at the sensor before the slower modes arrive at it directly from the actuator. Therefore the time period selected for the analysis is in 10 mm case determined by the arrival of the two modes with highest group velocities at the sensor. If some other modes arrive at the sensor during this period, they affect the results as well.

Figure 75 shows the peak voltage of the selected response period as a function of frequency for signal path P1→P4. The peak voltage varies according to the superposition of different modes and the PWAS sensitivity to them.

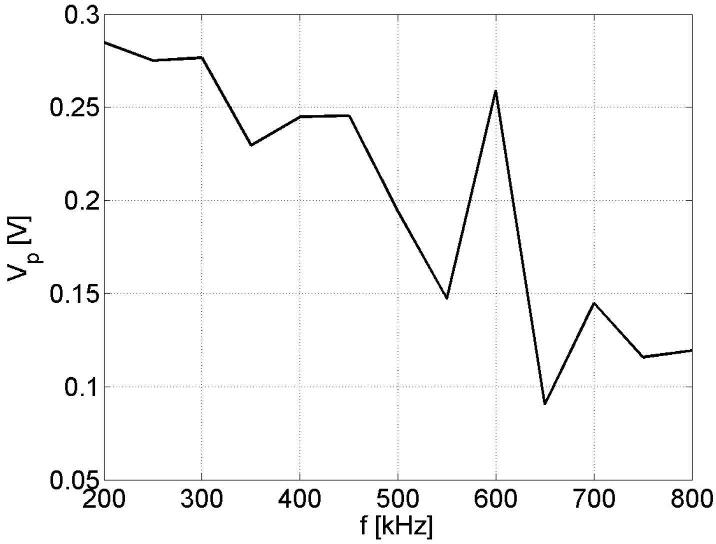

Figure 75. Peak burst voltage as a function of frequency measured from signal path P1→P4 in test plate 2.

The results for relative peak amplitude variation, relative burst variance variation, and correlation coefficient analysis are shown in Figures 76 and 77, respectively.

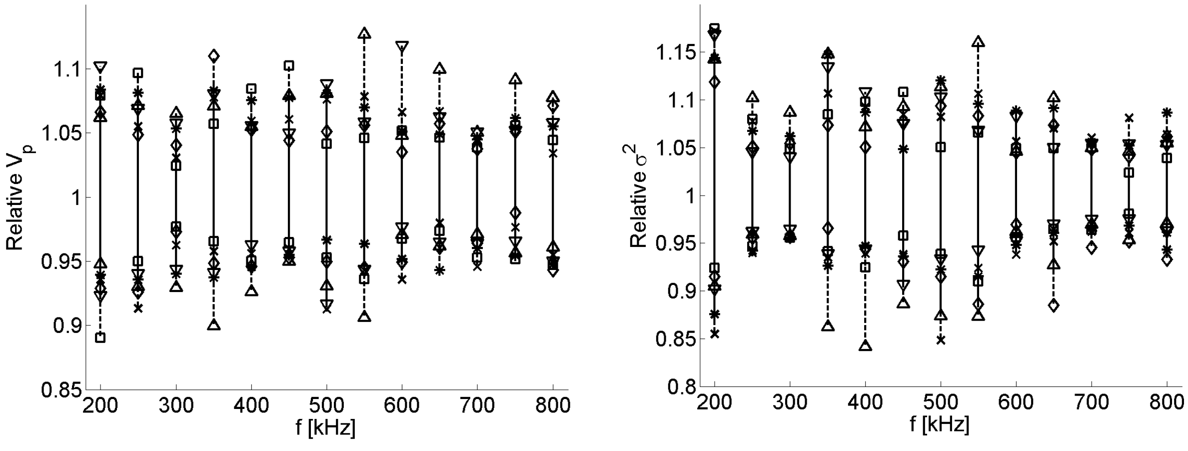

a) b)

Figure 76. a) The variation of relative burst peak amplitudes, b) The variation of relative burst variances of each signal path as a function of frequency in test plate 2.

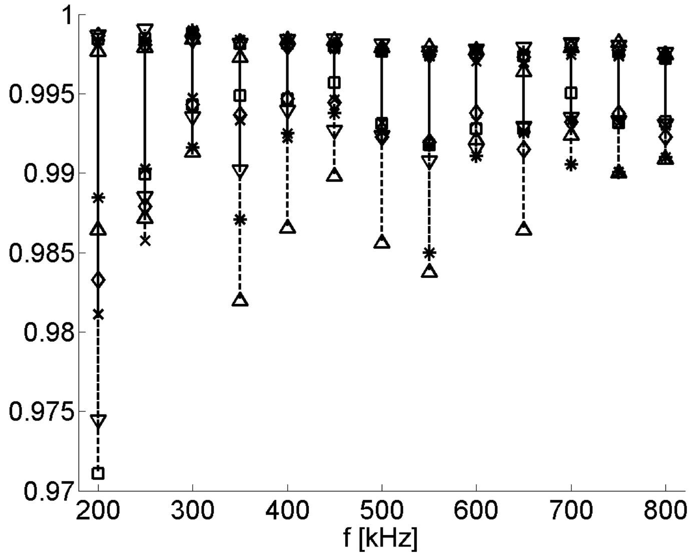

Figure 77. The variation of correlation coefficients of each signal path as a function of frequency in test plate 2.

There is no obvious correspondence between the response amplitude and the relative variation of the parameters. The relative variation is also larger than in test plates 1 and 4. This results from the increased complexity of the Lamb waveform, when several modes are superposed.

7.6 Effect of defect on indicating parameters

As stated earlier in Chapter 6.4.1, the effect of defects on Lamb wave propagation has been studied both through simulations and physical experiments [e.g. Lee2007a,b, McK1999, Fro2002]. When an elastic wave reaches an interface between two media, e.g. a hole or a crack in a metal, the wave can be partly reflected, partly refracted and possibly diffracted [Ach1975]. The distribution among these depends on the material properties, type of incident wave, shape of the scatterer (plate edge, crack, hole etc.) and the ratio of the wavelength to the defect size. Also mode conversions, discussed considering Lamb waves in Chapter 4.5.6, generally occur at the interfaces.

It has been shown that the propagation direction of Lamb waves scattered from a defect as well as the amount of wave energy passing through the defect in a given structure depends on the ratio of the wavelength to the defect size. McKeon et al. studied the Lamb wave scattering from a through-structure hole [McK1999]. They found that a small hole, with diameter of order $D \leq \lambda$, scatters the incident wave relatively evenly around the hole, and from a larger hole the scattered wave is directed largely to 90° and 270° angle from the incident wave. This means that when a defect is located directly at the actuator-sensor path, the measured response is attenuated and delayed with respect to the reference state, and the effect increases with the increasing defect size (or decreasing wavelength). If the defect is located off the path but close to it, the scattered wave modes are superposed with the wave modes propagating directly from actuator to sensor. Circular PWAS sends a wave front identically in every direction in an isotropic structure. Since the wave scattered from the defect has possibly different wave mode structure (due to the mode conversion phenomenon) as well as the time of flight from the wave arriving to the sensor directly from the actuator, the two waves are not identical in their amplitude and phase structure. Hence, their superposition is likely to be more complicated waveform than the original, with higher variance. The further the defect is away from the direct path, the smaller is its effect on the measured PWAS response.

For each test case, one frequency was selected for further analysis of the effect of a defect to peak amplitude, variance and correlation coefficient. For test plate 1, 500 kHz was selected for the optimal PWAS sensitivity for S_0 mode and smallest relative variation in the parameters. For test plate 2, the separability of the modes in the measured response (i.e. the differences in group velocities) and the PWAS sensitivity to their wavelengths were considered from Figures 60 and 61, and 450 kHz frequency was selected for the analysis also in 10 mm plate. At that frequency, the S_1 and S_2 modes arrive at the sensor before any of the antisymmetric modes, and the wavelength of S_1 mode is nearly optimal for the PWAS sensitivity [Giu2005]. In this case, the time period containing only S_1 and S_2 modes was selected for the analysis.

The test plates were damaged by drilling a hole into both of them. The diameter of the hole was increased as follows: 1 mm – 2 mm – 3 mm – 5 mm – 10 mm. The Lamb wave responses at every signal path were measured again after each increase of defect size. The response from each path was measured five times successively and the results were averaged for the final parameter comparison in order to reduce the effect of measurement noise. The location of the defect in the test plates was selected differently, as shown in Figure 2. In the test plate 1, the defect is located directly on the signal path between sensors 2 and 3, and very close to sensor 3. This location was selected to ensure a strong and easily interpretable effect on the response at the early stage of the project. In the test plate 2, the defect is very close to, but not directly on, the path between sensors 1 and 4. It is also close to the path between sensors 2 and 3. The location was selected to have detectable, but less dominant, effect on several signal paths.

7.6.1 Results for test plate 1

The repeatability analysis results for 1 mm plate at 500 kHz frequency are shown in Table 16. The reference used for determining the relative variation of the parameters was $\bar{\mathbf{x}}_{S0}$ measured from an intact plate. The differences in the reference values between the signal paths result from the random differences in PWAS-plate contacts. The distribution of the set of 50 parameter values for each signal path was tested for normality using the chi-squared goodness-of-fit test [Ben1986]. The testing procedure is as follows:

- Let N be the number of independent observations from a random variable x with probability density function $p(x)$.
- Let the N observations be divided into K class intervals, which together from a frequency histogram.
- The number of observations, f_i, falling within the ith class interval is called the observed frequency.
- The number of observations that would be expected to fall within the ith class interval if the true probability density function of x would be $p(x_0)$ is called the expected frequency, F_i in the ith class interval.
- To measure the total discrepancy for all class intervals, the squares of individual class discrepancies $f_i - F_i$ are normalized by the associated expected frequencies and summed to obtain the sample chi-squared statistics:

$$X^2 = \sum_{i=1}^{K} \frac{\left(f_i - F_i\right)^2}{F_i} \tag{148}$$

- Since any deviation of $p(x)$ from $p(x_0)$ will cause X^2 to increase, an upper tail test of fitting is used. The region of acceptance is $\chi^2 \leq \chi^2_{n;\alpha}$, where $\chi^2_{n;\alpha}$ is the value of chi-squared distribution with degrees of freedom n at level of significance α. If $\chi^2 \leq \chi^2_{n;\alpha}$ holds, the hypothesis is accepted at the α level of significance.

If a variable x is normally distributed, then the 95% confidence interval for its mean value μ_x is $\mu_x \pm 1.96\sigma_x$, where σ_x is the standard deviation of the variable x. In this case, the number of independent samples was $N = 50$, number of class intervals was $K = 10$, and degrees of freedom $n = K - 3 = 7$. The normality was tested at 0.05 level of significance with $\chi^2_{7;0.05} = 14.07$. The calculated χ^2 values along with 95% confidence intervals for variance and peak voltage values for each signal path are shown in Table 16.

The relative variation in parameters between the measurements is in this case very small, between 0.99...1.01 times the reference value. Thus for example relative variance value 0.95 could indicate defect on or near the signal path. The measurements are almost perfectly correlated.

Table 16. Repeatability results for test plate 1 (1 mm aluminium). χ^2 is the value of chi-squared statistics. If $\chi^2 < 14.07$, the distribution is normal with 95% level of significance. CI = confidence interval, $\mu_x \pm 1.96\sigma_x$.

Path	σ^2			V_p			ρ
	Ref. [V^2]	χ^2	95% CI	Ref. [V]	χ^2	95% CI	
A1 → S4	0.510	3.58	1.001±0.004	2.374	1.43	1.000±0.003	0.997…0.999
A2 → S3	0.226	12.14	1.001±0.004	1.656	8.61	1.002±0.005	0.997…0.999
A1 → S2	0.503	1.09	1.001±0.002	2.099	4.79	1.001±0.003	0.997…0.999
A3 → S4	1.029	3.22	1.001±0.003	2.691	7.88	1.000±0.003	0.996…0.999
A1 → S3	0.552	1.70	1.001±0.004	2.195	3.56	1.001±0.003	0.997…0.999
A2 → S4	0.607	2.43	1.002±0.003	2.161	7.04	1.000±0.003	0.997…0.999

If several measurements have been made both in healthy and damaged structure, a coupled Student's test can be used for testing if two sample sets belong to different structural configurations (e.g. healthy or damaged) with a given confidence level [Mon2000]. Given the mean values, standard deviations and number of samples of two different sets of data, the test provides a number, t, related to the probability that the difference between the two means is random. This number is then compared to the value obtained from the Student t distribution corresponding to the same chosen confidence level and number of degrees of freedom. If the experimentally evaluated t is higher than the value obtained from the distribution, the two data sets can be statistically associated to two different physical conditions with the chosen confidence level.

Let m_1 and m_2 be the means of the two sets of parameters related to healthy and damaged structure, respectively. Let σ_1 and σ_2 be the standard deviations and n_1 and n_2 the number of samples of each set. The number of degrees of freedom of the t-test is $n = n_1 + n_2 - 2$. t is evaluated as

$$t = \frac{|m_1 - m_2|}{\sqrt{A \cdot B}} \tag{149}$$

where

$$A = \frac{n_1 + n_2}{n_1 n_2} \text{ and } B = \frac{(n_1 - 1)\sigma_1^2 + (n_2 - 1)\sigma_2^2}{n_1 + n_2 - 2}$$

t-test results for relative variance for test plate 1 for defect diameters 1 mm and 5 mm are shown in Table 17. Measurements were repeated five times with each defect diameter. Thus $n_1 = 50$, $n_2 = 5$, and the number of degrees of freedom $n = 53$. If the required confidence level is 95%, the corresponding value of Student t distribution with $\alpha = 0.025$ is needed for reference, and it is $t_{53;0.025} \approx 2.01$. If the evaluated t values are larger than this, existence of a defect on or near the signal path can be assumed with 95% confidence level.

If only one sample, m_2, from a damaged state is available, as may be the case in a self-powered, energy efficient SHM system, $n_2 = 5$ and $\sigma_2 = 0$. If $n_1 \gg 1$, Eq. (149) reduces to $t = |m_1 - m_2| / \sigma_1$ and $n = 49$. Applying the condition $t > t_{49;0.025} = 2.01$ leads to $|m_1 - m_2| > 2.01\sigma_1$, that is, m_2 values outside approximately the 95% confidence interval of the reference state are interpreted as originating from a damaged state.

Table 17. Coupled *t*-test results for relative variance for test plate 1 (1 mm aluminium). If *t* > 2.01, defect on or near the signal path is assumed with 95% confidence level.

Path	No defect		1 mm			5 mm		
	m_1	σ_1	m_2	σ_2	t	m_2	σ_2	t
A1 → S4	1.001	0.002	0.925	0.003	83.00	0.978	0.005	22.55
A2 → S3	1.001	0.002	0.932	0.007	56.29	0.776	0.006	210.68
A1 → S2	1.001	0.001	0.927	0.003	109.04	0.962	0.008	32.57
A3 → S4	1.001	0.001	0.965	0.002	54.15	1.097	0.003	134.11
A1 → S3	1.001	0.002	0.955	0.003	49.02	1.145	0.006	124.17
A2 → S4	1.002	0.001	0.934	0.006	67.12	0.984	0.004	21.09

In this case, the *t*-test results get very large values even in the paths that are in reality far away from the defect. Possible reasons for this are discussed below, along with the parameter values as functions of defect diameter.

Figures 78 – 80 show the relative values of the selected parameters as a function of defect diameter. The reference values on each path are those listed in Table 16. The horizontal lines in each figure show the limits of parameter variation from Table 16.

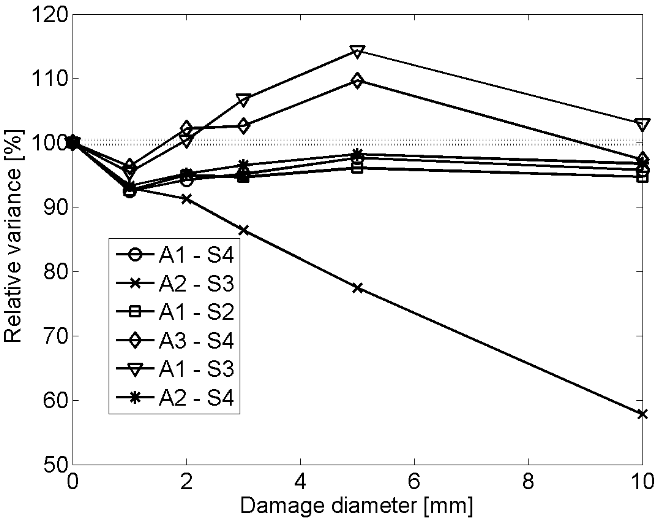

Figure 78. Relative variance as a function of defect diameter in test plate 1.

From Figure 78 it can be clearly seen that the increasing size of the defect is causing almost linear decline in the S_0 mode variance on path A(ctuator)2 – S(ensor)3 as can be expected when the defect is located directly between the sensors. For the paths A1→S4, A1→S2 and A2→S4, which all are located far away from the defect, there is small effect. In the paths A3→S4 and A1→S3, the variance shows significant increase for defect sizes 3 mm and larger. This is due to the scattering of the Lamb wave from the round hole. A small hole, with diameter of order $D \leq \lambda$, scatters the incident wave relatively evenly around the hole, from a larger hole the scattered wave is directed largely to 90° and 270° angle from the incident wave [McK1999]. Thus the wave travelling to or from sensor P3 is scattered from the defect to both sides so that the scattered wave increases the energy (or variance) of the measured response.

Figure 79 shows the relative peak amplitude of the response measured from different paths. Once again, the paths nearest to the defect experience highest relative changes. However, the relative change also in the paths far from the defect is larger than in case of the variance. Thus the peak amplitude is less accurate parameter as defect indicator even though the repeatability analysis gave similar results to both amplitude and variance.

The change in the amplitude and variance on the paths far from the defect is independent on the defect size and possibly indicates the effect of the damaging process itself on the structure. Aluminium conducts heat very efficiently and the heating caused by the plate being drilled may affect the fixing agent of the PWAS. The effect of heating on the contact between the PWAS and the surface could be tested by heating the plate without damaging it, and measuring the PWAS responses before and after heating.

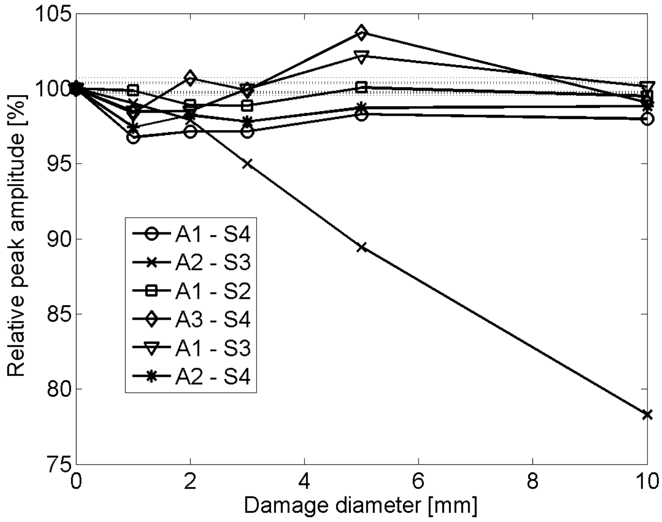

Figure 79. Relative peak amplitude as a function of defect diameter in test plate 1.

The correlation coefficient is a measure of linear statistical dependence between two signals, and thus it is independent on the mean value and scaling of the signal. Thus correlation coefficient is insensitive to attenuation, and if there is no significant change in the shape or phase in the response due to defect, correlation coefficient remains close to 1. The results for correlation coefficient analysis are shown in Figure 80.

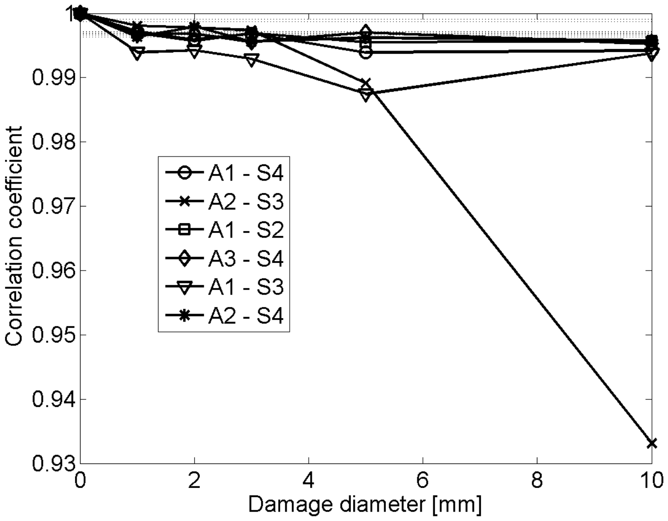

Figure 80. Correlation coefficient as a function of defect diameter in test plate 1.

In this case, large defect directly in the signal path results in a significant change in the correlation coefficient. If the defect is relatively small or off the signal path, its effect on the correlation coefficient is smaller and less pronounced than on the burst variance.

The insensitivity of parameters to defects outside the direct transmission path shows that the location of the PWASs needs to be carefully considered in order to adequately cover the inspection area. Several studies have been published on this area [Lee2003, Lee2007a, Lee2007b, Pur2004].

7.6.2 Results for test plate 2

As stated above, the repeatability of measurements on 10 mm plate is worse than in 1 mm plate due to increased complexity of the Lamb waveform. The repeatability analysis results at 450 kHz for 10 mm plate are shown in Table 18. The relative variation is much higher than in the test plate 1. In this case, e.g. the relative variance would possibly need to be below 0.9

before existence of defect could be assumed. The correlation between the measurements is still nearly perfect. The parameter values at signal path A1→S2 fail the distribution normality test: their $\chi^2 > \chi^2_{7;0.05} = 14.07$. This is caused by two deviating measurement results.

Table 18. Repeatability results for test plate 2 (10 mm aluminium). χ^2 is the value of chi-squared statistics. CI = confidence interval, $\mu_x \pm 1.96\sigma_x$.

Path	σ^2			V_p			ρ
	Ref. [V^2]	χ^2	95% CI	Ref. [V]	χ^2	95% CI	
A1 → S4	0.012	7.81	1.007±0.087	0.245	3.76	1.004±0.053	0.990…0.998
A2 → S3	0.029	4.81	1.003±0.069	0.407	2.63	1.001±0.046	0.993…0.998
A1 → S2	0.044	33.10	1.003±0.062	0.467	50.09	1.002±0.046	0.996…0.998
A3 → S4	0.026	4.15	1.003±0.067	0.399	10.08	1.005±0.042	0.995…0.998
A1 → S3	0.046	2.54	1.003±0.059	0.518	8.42	1.001±0.033	0.995…0.998
A2 → S4	0.026	4.33	1.003±0.053	0.351	5.94	1.004±0.045	0.994…0.998

Table 19. Coupled *t*-test results for relative variance for test plate 2 (10 mm aluminium). If *t* > 2.01, defect on or near the signal path is assumed with 95% confidence level.

Path	No defect		1 mm			5 mm		
	m_1	σ_1	m_2	σ_2	t	m_2	σ_2	t
A1 → S4	1.007	0.045	1.009	0.035	0.12	0.746	0.014	12.90
A2 → S3	1.003	0.035	1.010	0.019	0.44	1.216	0.021	13.30
A1 → S2	1.003	0.031	1.063	0.020	4.20	1.134	0.022	9.09
A3 → S4	1.003	0.034	0.915	0.023	5.59	0.994	0.009	0.58
A1 → S3	1.003	0.030	1.070	0.016	4.93	1.171	0.013	12.39
A2 → S4	1.003	0.027	1.021	0.033	1.38	1.048	0.015	3.59

As an example, *t*-test results for relative variance for signal paths A2→S4 (far from defect), A2→S3 (defect close to the signal path) and A1→S4 (defect closest to the signal path) for defect diameters 1 mm and 5 mm are shown in Table 19. The parameters are the same as in 1 mm plate case: $n_1 = 50$, $n_2 = 5$, the number of degrees of freedom $n = 53$, and $t_{53;0.025} \approx 2.01$. The test identifies the path A1→S4 having a defect even with 1 mm defect diameter. On the other hand, path A2→S4 is diagnosed with possible defect at 5 mm defect diameter, even though it is in reality located far from the defect.

Figures 81 - 83 show the relative values of the selected parameters as a function of defect diameter. The reference values on each path are those listed in Table 18.

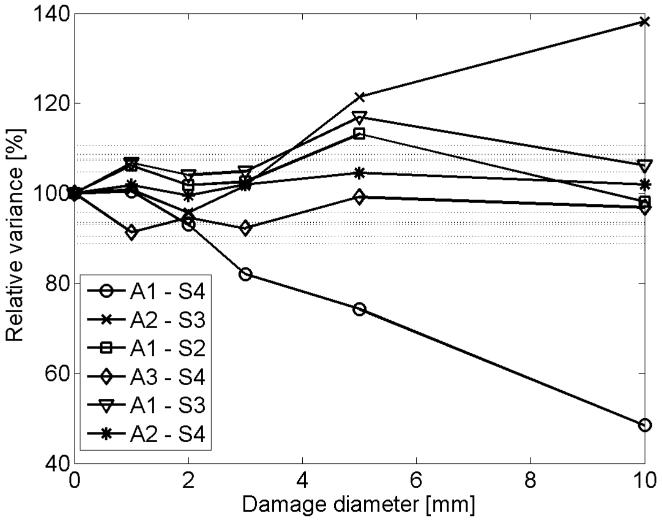

Figure 81. Relative variance as a function of defect diameter in test plate 2.

As could be expected, there is significant decrease in burst variance as a function of defect size in the path A1→S4, which is closest to the defect. Path A2→S3, which passes the defect slightly further away, experiences increase in variance as the incident wave is scattered around the defect. There is also increase in variance in the path A1→S3.

Figure 82 shows the results for relative peak amplitude. Again there is decrease in the parameter value in the path A1→S4 when the defect size is 3 mm or larger. Amplitude in the path A1→S3 increases with defect size due to scattering from the defect. From Figure 83 it can be seen that the correlation coefficient indicates significant separation between the different paths only with defect sizes 5 mm and above. The effect is most significant on the paths A2→S3 and A1→S4 as expected.

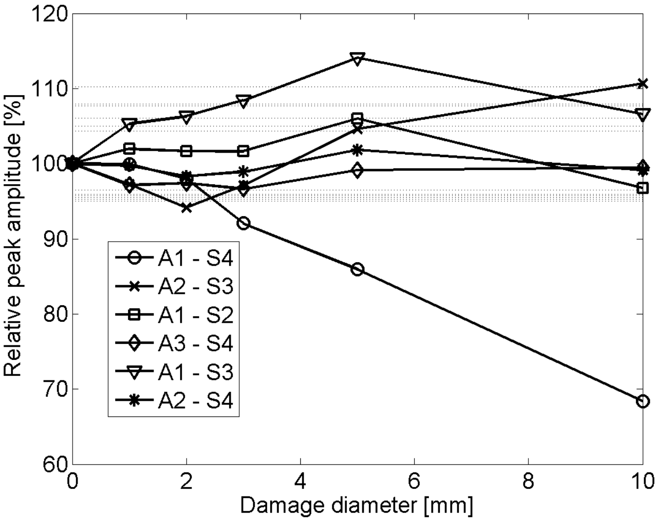

Figure 82. Relative peak amplitude as a function of defect diameter in test plate 2.

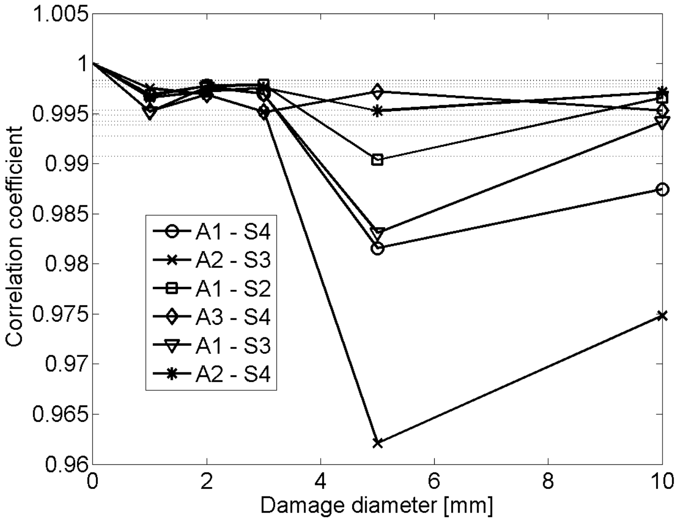

Figure 83. Correlation coefficient as a function of defect diameter in test plate 2.

The variation in all three parameters is generally larger than in test plate 1 also on the paths far away from the defect, due to the weaker repeatability of the responses. However, the most significant changes in the parameters with increasing defect size follow logically the effects of Lamb wave scattering from the defect, and the defect can be detected and located from both test plates as shown in Chapter 6.

Of the simplest defect indicating parameters studied here, the variance of the first easily separable wave mode burst or bursts arriving at the sensor is the most consistent indicator of existence and size of a defect. Peak amplitude and correlation coefficient may provide supporting information in determining the existence, size and distance from the direct signal path of possible defects.

7.7 Effect of measurement repeatability on locating defect

Repeatability of the statistical parameters calculated from the PWAS responses depends on the signal level and complexity. If it is not possible to avoid superposing of several wave modes within the signal period used for the analysis, strictly set defect indication thresholds for the detection algorithm increases the probability of false positive diagnoses. E.g. the limits for allowed relative variation in burst variance used for defect location in Chapter 6, $[\sigma^2_{\min}, \sigma^2_{\max}]$ = [0.99, 1.01], are quite strict for test plate 2 where these limits correspond approximately to 30% confidence interval of normal variation; i.e. 70% of the relative variance values measured from an intact structure fall outside these limits. On the other hand, as can be seen in Figure 81, the burst variance in different signal paths falls easily within the 95% confidence interval of a healthy structure even in damaged structure. If more deviation from the reference is allowed according to the 95% confidence interval of a healthy 10 mm plate, the location algorithm detects e.g. in 3 mm defect case only the path closest to the defect, resulting in estimated location of "somewhere between sensors P1 and P4". If this kind of level of locating accuracy is sufficient for the SHM application, then the allowed variation level can be set more loosely. However, since the defect locating algorithm puts weight to the signal paths in direct proportion to the relative change in the burst variance, the paths with smaller change have smaller effect on the locating result in any case.

The repeatability of defect locating was tested by taking three separate PWAS response measurements from all six signal paths with each defect size, resulting in $3^6 = 729$ response combinations for each defect size. The defect location was then estimated and the estimation error as millimetres calculated. The histograms of the estimation errors and the estimated locations for test plate 1 with defect diameters 1, 3 and 5 mm are shown in Figure 84. The corresponding results for test plate 2 are shown in Figure 85. The correct defect location is marked with a circle, the locations of PWASs with plus signs, and the defect location estimates are marked with crosses.

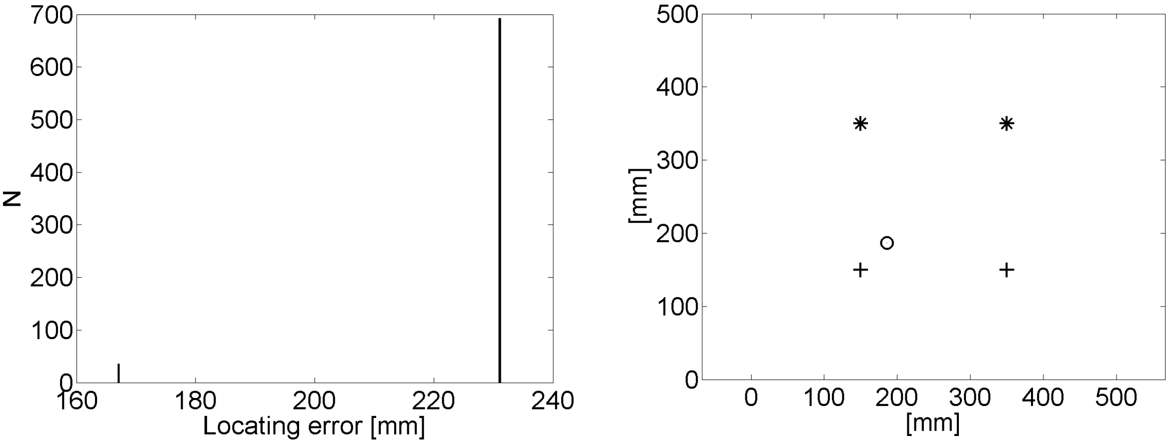

a) Error histogram, 1 mm

d) Estimated locations, 1 mm

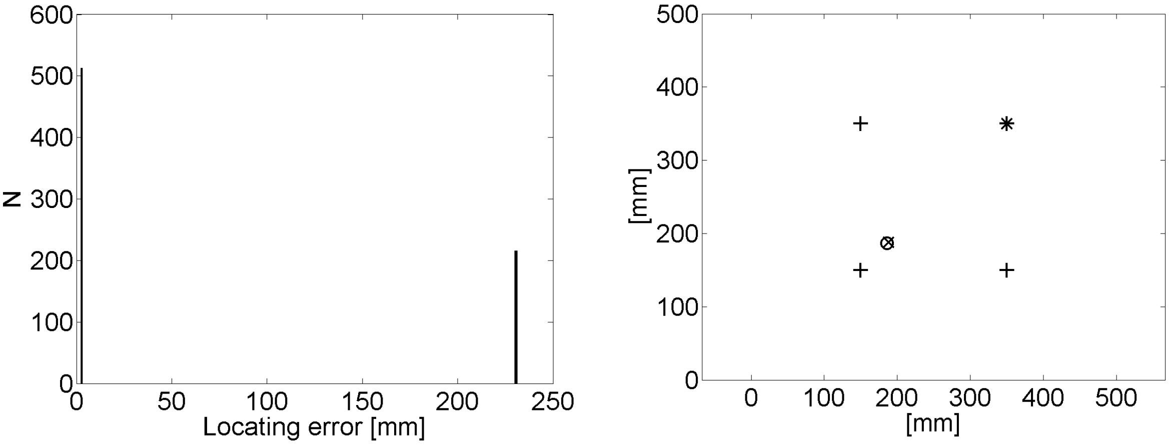

b) Error histogram, 3 mm

e) Estimated locations, 3 mm

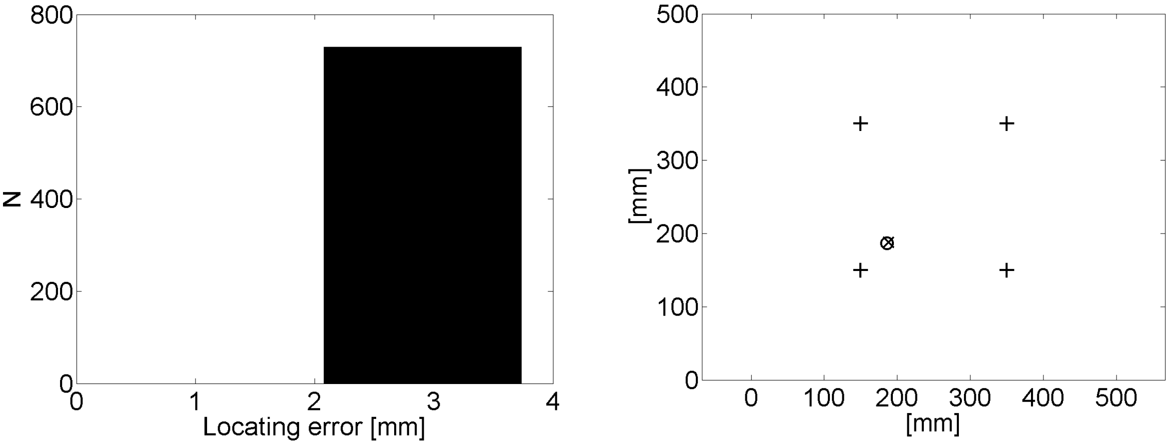

c) Error histogram, 5 mm

f) Estimated locations, 5 mm

Figure 84. Defect location estimate error histograms (a…c) and estimated locations (d...f) with defect diameters 1mm, 3 mm and 5 mm for test plate 1. The circle marks the correct defect location, the plus signs mark the locations of PWASs, and the defect location estimates are marked with crosses.

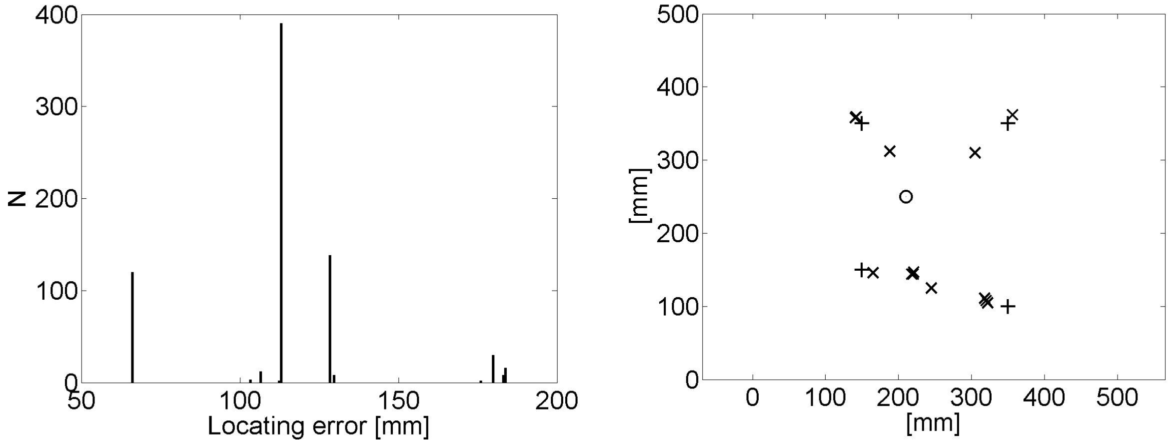

a) Error histogram, 1 mm

d) Estimated locations, 1 mm

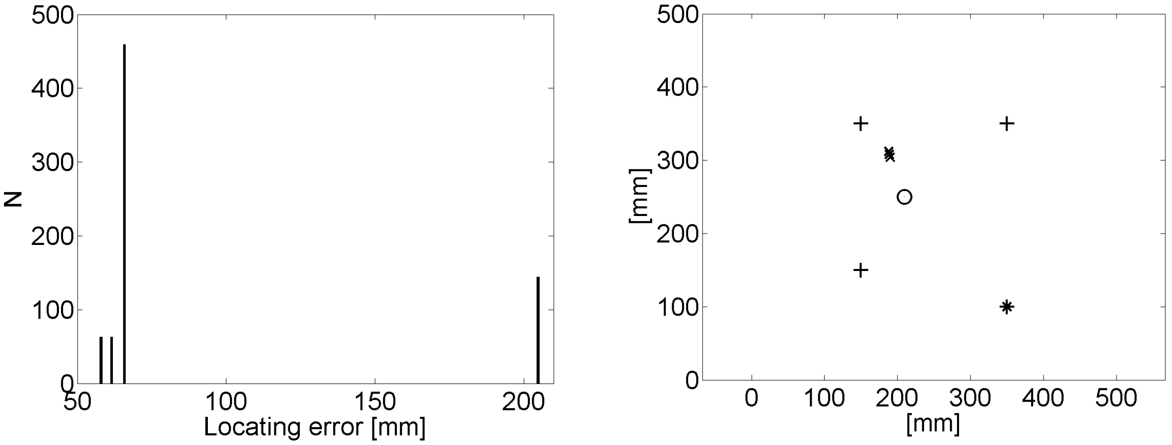

b) Error histogram, 3 mm

e) Estimated locations, 3 mm

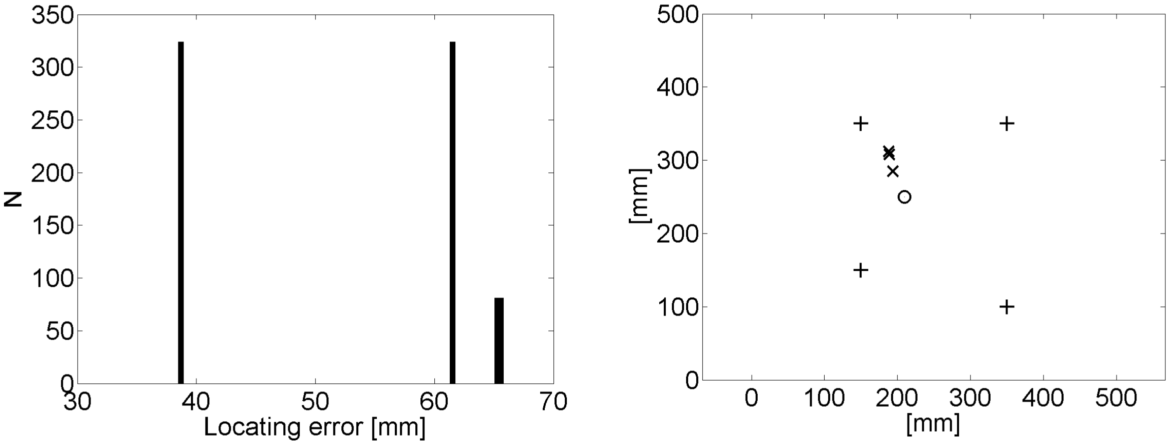

c) Error histogram, 5 mm

f) Estimated locations, 5 mm

Figure 85. Defect location estimate error histograms (a…c) and estimated locations (d...f) with defect diameters 1mm, 3 mm and 5 mm for test plate 2. The circle marks the correct defect location, the plus signs mark the locations of PWASs, and the defect location estimates are marked with crosses.

In both cases, 1 mm defect is too small to be located correctly. In test plate 1, all location estimates for 1 mm defect coincide either with P1, i.e. (150,350) mm, or with P2, i.e. (350,350) mm. In test plate 2, there is large variation in location estimates. The results show the tendency of the location algorithm to reach a global maximum at one of the PWASs when the changes in burst variance are small. For 3mm and 5 mm defects, the location results are in both test plates clustered either at a single point or at few different points. This shows that the estimation algorithm is consistent. The defect locating repeatability is better in test plate 1, where relative variation of the responses and the S_0 mode burst variance is small. Averaging a few repeated measurements improves the defect locating repeatability by reducing the effect of random variations in the responses.

7.8 Defect locating repeatability with the suggested method

The repeatability of defect locating with the method suggested in Chapter 5 was tested by simulating the effect of the measurement system prototype on the PWAS responses analyzed in 7.7. The responses were first band-pass filtered with the filter shown in Figure 29. This results in approximately 30-fold increase in the signal amplitude. Then the filtered responses were resampled at 12.5 MHz approximating the clock rate of the FPSLIC timer used in the prototype, approximate peak values of the half-periods were measured using the constant period length assumption, and finally the signal was reconstructed from these samples.

Table 20 shows the results for relative variance repeatability analysis for test plate 1 (1 mm aluminium) when the variance calculated from the measured samples without signal reconstruction is used as a parameter. Coupled *t*-test results for 1 mm and 5 mm defect size for each signal path are also shown. The corresponding analysis results for reconstructed waveform are shown in Table 21. In the first case, the number of peak value samples used for variance calculation is only approximately 30 - 40, in the second case number of samples used is in the range of 700 - 1100. The inaccuracy in the peak value detection results in higher variation of the burst variance in the reference state compared with the results in Table 16 (the original responses measured using high sampling rate). Signal reconstruction reduces this variation, but not to the level of the original signal. The distribution normality test also gives worse results than with the original signal. The coupled Student's *t*-test results can not reliably separate defect existence/non-existence near the signal path, but this was also the case with the original signal (see Tables 17 and 19). Improving the peak detection accuracy would improve the results with respect to the signals measured at high sampling rate; e.g. the 95% confidence interval of the variance would be much narrower than with the current peak detection based on the constant period assumption, and the variance distribution at each signal path could be assumed normal (see Table 22).

Table 20. Repeatability results for relative sample variance for test plate 1, when samples are taken using the constant period assumption. χ^2 is the value of chi-squared statistics. If $\chi^2 < 14.07$, the distribution is normal with 95% level of significance. *t* is the result for coupled *t*-test. If $t > 2.01$, defect on or near the signal path is assumed with 95% confidence level. CI = confidence interval, $\mu_x \pm 1.96\sigma_x$.

Path	σ^2, intact plate			1 mm defect			5 mm defect		
	Ref. [V^2]	χ^2	95% CI	m_2	σ_2	t	m_2	σ_2	t
A1 → S4	736	14.82	0.999±0.062	0.896	0.019	7.10	0.917	0.026	5.63
A2 → S3	298	18.43	0.985±0.057	0.934	0.025	3.84	0.786	0.023	14.81
A1 → S2	769	17.37	0.971±0.038	0.845	0.010	14.27	0.906	0.018	7.20
A3 → S4	1469	25.43	1.002±0.055	0.955	0.028	3.43	1.179	0.004	14.16
A1 → S3	779	2.17	1.013±0.034	0.955	0.021	7.12	1.171	0.014	19.70
A2 → S4	952	8.55	1.002±0.036	0.934	0.015	7.86	0.982	0.019	2.30

Table 21. Repeatability results for relative burst variance for test plate 1, when signal reconstruction based on the constant period assumption is used. If $\chi^2 < 14.07$, the distribution is normal with 95% level of significance. If $t > 2.01$, defect on or near the signal path is assumed with 95% confidence level. CI = confidence interval, $\mu_x \pm 1.96\sigma_x$.

Path	σ^2, intact plate			1 mm defect			5 mm defect		
	Ref. [V^2]	χ^2	95% CI	m_2	σ_2	t	m_2	σ_2	t
A1 → S4	335	17.2	1.016±0.034	0.935	0.010	10.22	0.984	0.014	4.08
A2 → S3	142	19.6	0.984±0.056	0.915	0.027	5.19	0.765	0.008	16.83
A1 → S2	317	3.00	0.996±0.024	0.939	0.011	9.83	0.976	0.016	3.34
A3 → S4	685	4.96	1.002±0.038	0.970	0.022	3.41	1.123	0.009	13.72
A1 → S3	363	8.89	0.999±0.021	0.945	0.023	9.36	1.144	0.028	23.62
A2 → S4	404	18.29	0.973±0.023	0.898	0.016	13.25	0.959	0.019	2.30

Table 22. Repeatability results for relative burst variance for test plate 1, when signal reconstruction based on accurate peak detection is used. If χ^2 < 14.07, the distribution is normal with 95% level of significance. If t > 2.01, defect on or near the signal path is assumed with 95% confidence level. CI = confidence interval, $\mu_x \pm 1.96\sigma_x$.

Path	σ^2, intact plate			1 mm defect			5 mm defect		
	Ref. [V^2]	χ^2	95% CI	m_2	σ_2	t	m_2	σ_2	t
A1 → S4	379	1.89	1.001±0.006	0.926	0.003	50.87	0.978	0.005	14.63
A2 → S3	173	4.13	1.000±0.005	0.930	0.009	46.16	0.774	0.007	167.32
A1 → S2	386	7.07	1.002±0.006	0.930	0.007	44.63	0.965	0.008	21.36
A3 → S4	776	5.64	1.004±0.003	0.966	0.004	36.08	1.100	0.003	117.36
A1 → S3	416	3.00	1.002±0.005	0.958	0.005	35.10	1.144	0.008	95.93
A2 → S4	448	15.58	1.004±0.004	0.937	0.007	51.57	0.988	0.006	13.52

The corresponding results for test plate 2 (10 mm aluminium) for sample variance and reconstruction based on the constant period assumption are shown in Tables 23 and 24.

Table 23. Repeatability results for relative sample variance for test plate 2, when samples are taken using the constant period assumption. χ^2 is the value of chi-squared statistics. If χ^{22} < 14.07, the distribution is normal with 95% level of significance. t is the result for coupled t-test. If t > 2.01, defect on or near the signal path is assumed with 95% confidence level. CI = confidence interval, $\mu_x \pm 1.96\sigma_x$.

Path	σ^2, intact plate			1 mm defect			5 mm defect		
	Ref. [V^2]	χ^2	95% CI	m_2	σ_2	t	m_2	σ_2	t
A1 → S4	22.6	8.64	1.001±0.105	0.917	0.029	3.46	0.631	0.012	15.25
A2 → S3	59.9	6.68	1.038±0.103	0.870	0.034	6.98	1.034	0.045	0.17
A1 → S2	86.3	30.21	1.034±0.126	0.959	0.066	2.49	1.008	0.073	0.86
A3 → S4	59.6	12.42	1.020±0.122	0.674	0.018	12.27	0.741	0.011	9.91
A1 → S3	87.0	16.88	1.021±0.122	0.982	0.074	1.29	1.015	0.011	0.19
A2 → S4	52.6	34.70	1.007±0.077	0.943	0.023	3.49	0.966	0.023	2.29

Table 24. Repeatability results for relative sample variance for test plate 2, when signal reconstruction based on the constant period assumption is used. If $\chi^2 < 14.07$, the distribution is normal with 95% level of significance. If $t > 2.01$, defect on or near the signal path is assumed with 95% confidence level. CI = confidence interval, $\mu_x \pm 1.96\sigma_x$.

Path	σ^2, intact plate			1 mm defect			5 mm defect		
	Ref. [V^2]	χ^2	95% CI	m_2	σ_2	t	m_2	σ_2	t
A1 → S4	10.0	5.94	1.010±0.094	0.920	0.033	4.10	0.677	0.013	15.35
A2 → S3	27.6	5.86	1.013±0.077	0.817	0.018	10.97	0.990	0.016	1.29
A1 → S2	39.2	42.36	0.994±0.065	0.910	0.030	5.40	0.980	0.025	0.88
A3 → S4	25.6	4.79	1.004±0.075	0.692	0.021	17.85	0.759	0.010	14.11
A1 → S3	39.1	4.50	1.012±0.068	0.979	0.024	2.07	1.067	0.015	3.48
A2 → S4	22.0	12.69	1.011±0.059	0.946	0.033	4.55	0.970	0.022	2.96

The repeatability of defect locating using reconstructed signals was then tested using the $3^6 = 729$ data sets used for analysis shown Figures 84 and 85. The histograms of the estimation errors (red bars) and the estimated locations (red crosses) for test plates 1 and 2 with different defect diameters are shown in Figures 86 and 87, respectively. Defect location was also estimated without reconstructing the response, using the variance calculated directly from the peak value samples. The results are shown as blue bars and crosses in Figures 86 and 87. The corresponding results for the original responses measured with high sampling frequency are shown as black bars in estimation error histograms and black crosses in location estimates.

The results with reconstructed signals resemble those of the original signals. With the 1 mm and 3 mm defects, the location is more often estimated at one of the PWASs. With 5 mm defect, the estimated locations match those resulting from the original signals. Even if the responses are not reconstructed, but the variance calculated directly from the peak value samples is used as defect indicator instead, the locating results for 5 mm defect are comparable to those obtained with reconstruction method. This is a promising result considering the future development of the system in the sense of improved energy efficiency. Again, averaging a few measured responses would reduce the effect of random variation on the results, but at the cost of increased energy consumption.

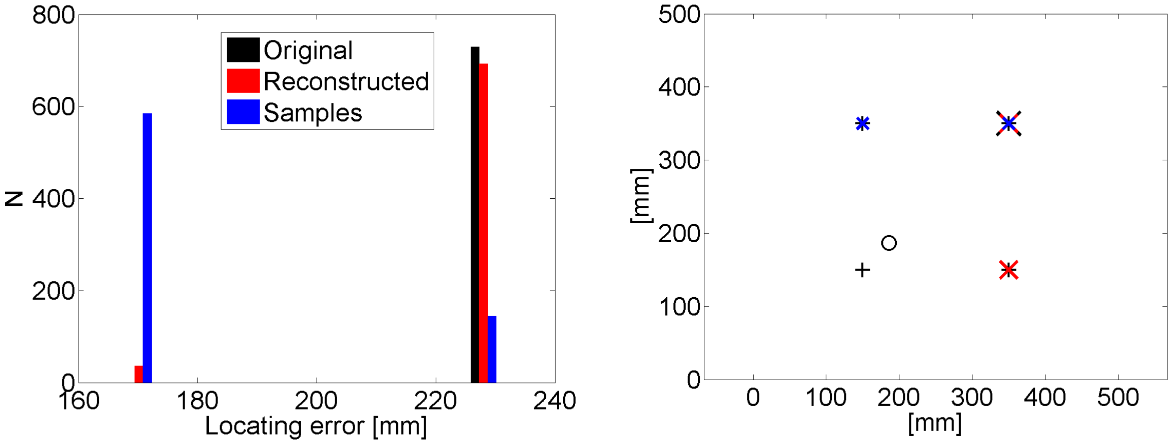

a) Error histogram, 1 mm

d) Estimated locations, 1 mm

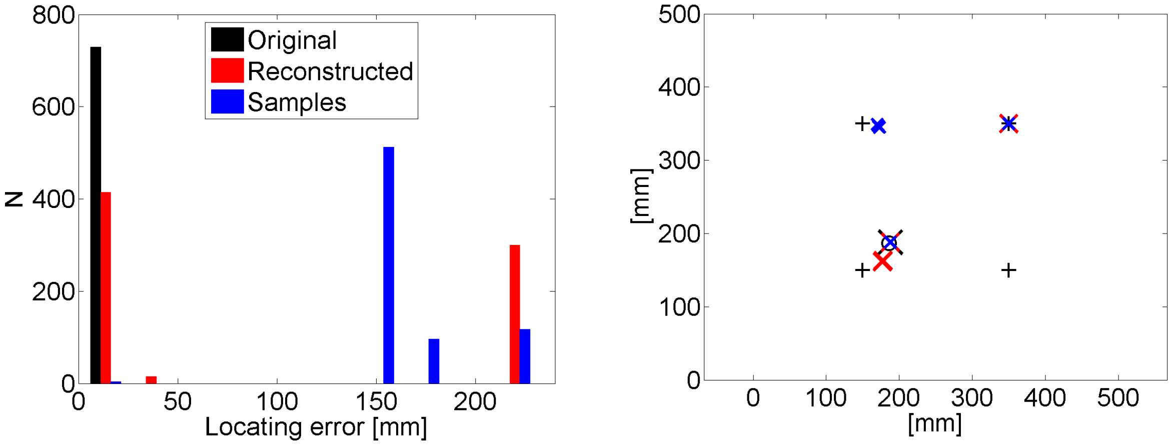

b) Error histogram, 3 mm

e) Estimated locations, 3 mm

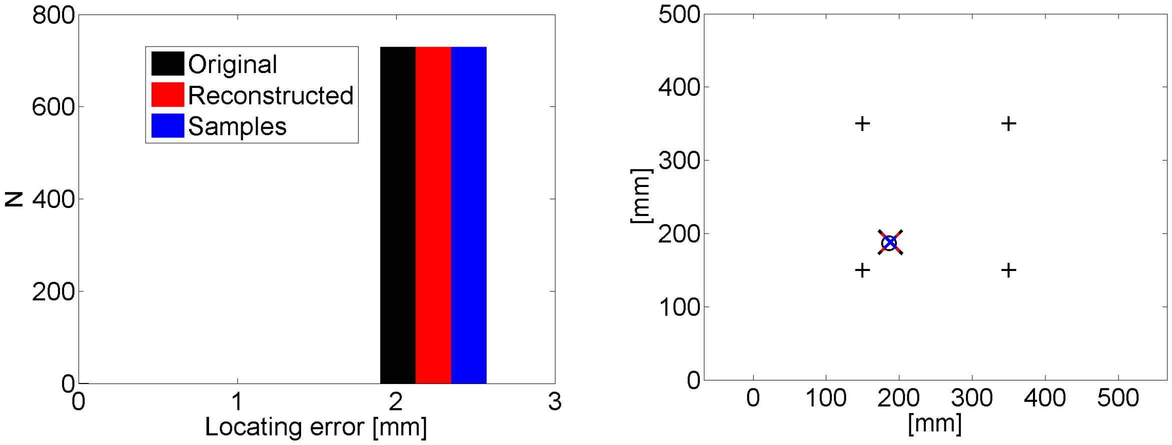

c) Error histogram, 5 mm

f) Estimated locations, 5 mm

Figure 86. Defect location estimate error histograms (a…c) and estimated locations (d...f) with defect diameters 1mm, 3 mm and 5 mm for test plate 1. The circle marks the correct defect location, the plus signs mark the locations of PWASs, and the defect location estimates are marked with crosses.

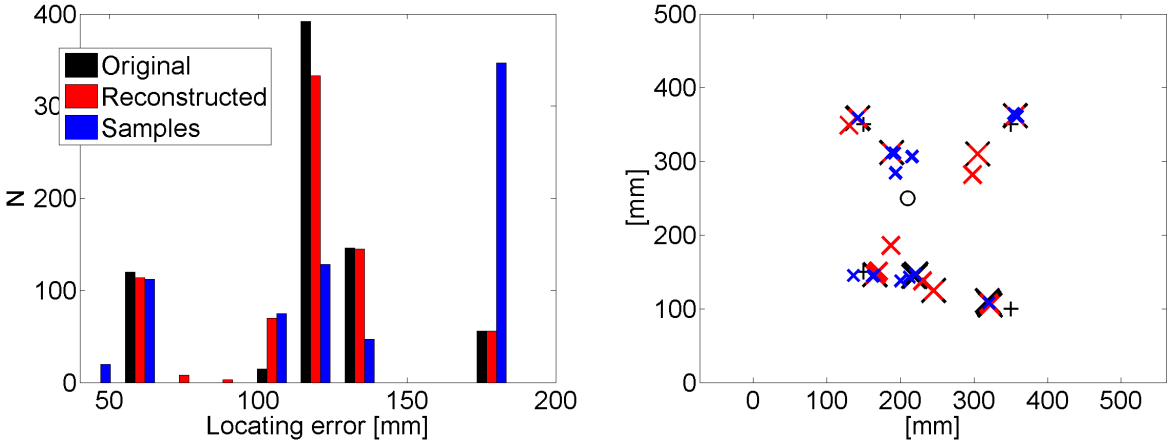

a) Error histogram, 1 mm

d) Estimated locations, 1 mm

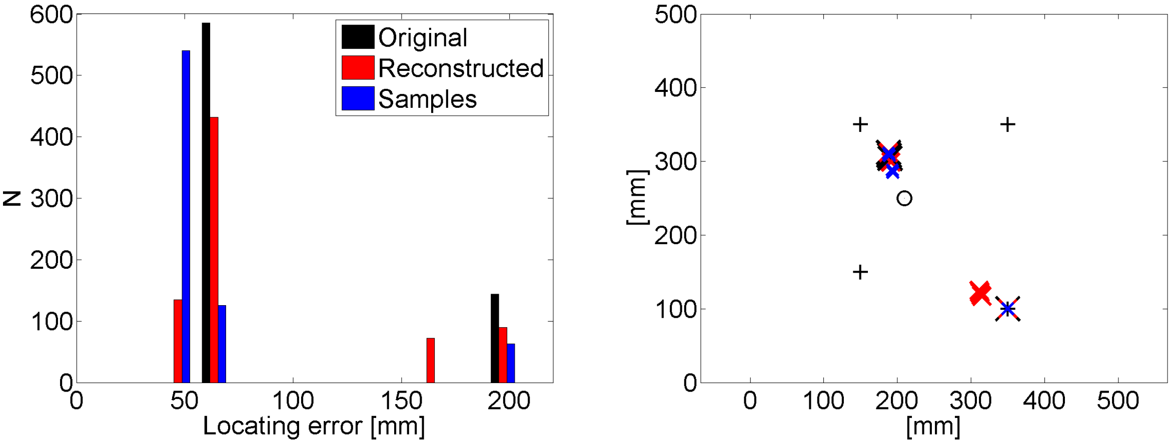

b) Error histogram, 3 mm

e) Estimated locations, 3 mm

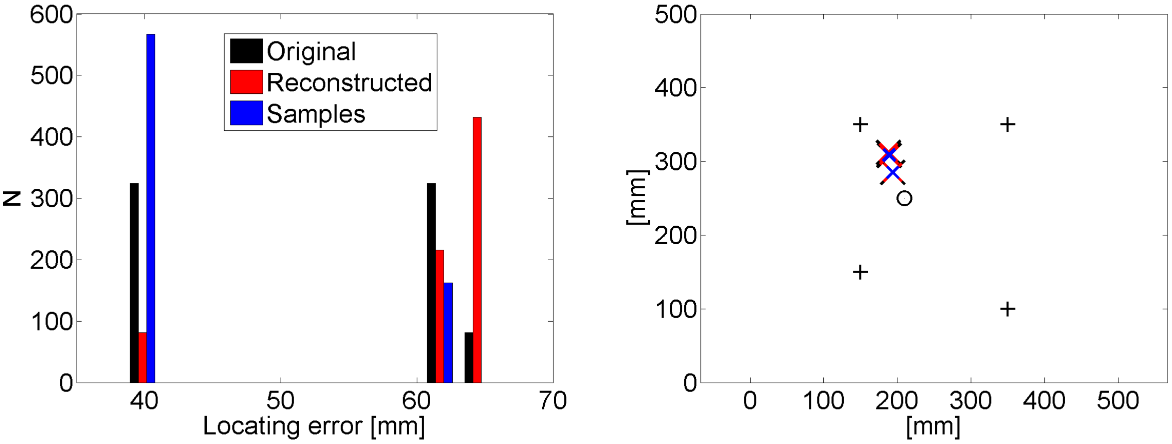

c) Error histogram, 5 mm

f) Estimated locations, 5 mm

Figure 87. Defect location estimate error histograms (a…c) and estimated locations (d...f) with defect diameters 1mm, 3 mm and 5 mm for test plate 2. The circle marks the correct defect location, the plus signs mark the locations of PWASs, and the defect location estimates are marked with crosses.

7.9 Summary

In this chapter, the repeatability of the PWAS response measurements, defect indicating statistical parameters and defect locating in thin (1 mm) and thick (10 mm) aluminium plates was studied. It was found that in thin plates the repeatability of all these variables is better due to less complicated waveform structure: only two wave modes, S_0 and A_0 exist within the studied frequency range, and the modes can be separated from each other. In thick plates, up to eight wave modes coexist and they are generally superposed.

The chi-squared test was used for analyzing the normality of the distributions of statistical parameters estimated from the 50 reference measurements taken from an intact structure. Then the coupled Student's *t*-test was applied to the parameters to analyze the separability of a damaged structure (5 repeated measurements on each signal path) from an intact structure. It was found that the *t*-test does not in this case give a reliable indication of the existence of a defect on or near the signal path, especially in the case of the thick plate where the parameter variation in an intact structure is large enough to cover the effect of small defects on the PWAS response. The range of relative change in burst variance considered as undamaged structure was set to $[\sigma^2_{\min}, \sigma^2_{\max}] = [0.99, 1.01]$ based on 95% confidence interval in the thin plate (see Table 16).

Defect locating repeatability was tested using 729 different PWAS response combinations for each defect size. The analysis was repeated using three different estimates for burst variance: 1) estimate calculated from a response measured using 25 MHz sampling frequency, 2) estimate calculated from a response reconstructed from local peak values, and 3) estimate calculated from local peak values without signal reconstruction. It was found that even the peak value variance suffices for indicating and locating defects, if the peak values are measured accurately.

8. Discussion and Conclusions

Guided wave based condition monitoring is nowadays widely used in several technology fields. Development in sensor and wireless data transfer technologies has led to an increasing number of possible application areas, for example in rotating machinery. Problems with sensor wiring combined with the increasing demand for energy efficiency have brought forward the question of self-powered SHM systems with low energy consumption. Generally the use of replaceable batteries is not a welcome option in industrial applications since the replacements are not generally simple and cheap to do or easy to predict.

The goal of the research project to which this thesis contributes was to develop a self-powered structural health monitoring system suitable for continuous use in industrial applications. The requirements for the system were as follows:

- energy efficiency
- piezoelectric actuating and sensing of Lamb waves
- simple actuation burst generation
- minimized data sampling
- wireless data transfer
- self-powering through power harvesting
- detecting and locating defects through efficient signal analysis

In this thesis, it was shown that a PWAS driven SHM system for metallic and composite structures can be constructed in such way that the number of measured data points as well as total energy consumption of the measurement procedure is minimized, and the system can be powered by harvesting energy from the surroundings. Location of the possible defects can be estimated using signal reconstruction technique and simple statistical parameter analysis. The sensitivity and accuracy of the method depends on actuated wavelengths with respect to the size of both defect and the used PWAS, the distance between sensors, and the accuracy of waveform peak detection in the measurement phase. Thus all the pre-set requirements were met in the developed measurement system prototype.

Zhao’s and Lallart’s systems [Zha2007a,b, Lal2008] presented in Chapter 6, and the measurement system prototype presented in this thesis are difficult to compare with each other directly. They use different energy harvesting/sensor powering, different actuation bursts, and different amount of local signal processing. Compared with these competing technologies, the suggested measurement system is competitive when the energy efficiency is considered. The most important difference between the presented system prototype and Zhao’s and Lallart’s systems is that in the presented prototype the PWASs are wired for actuating and sensing the Lamb waves. The only wireless function is the data transmission. The wiring required for PWASs was not considered a major issue in the planned application targets within this project, but wireless actuation and sensing wirelessly is a strongly emerging concept and could be an important feature in the future development. However, it would require radical changes to the overall system design. The idea of local energy harvesting in each sensor unit presented in Lallart’s system is better suited for many industrial applications than the Zhao’s RF or microwave antenna based method of supplying power to the sensors. However, the cost for AWR and AWT type sensors per unit is much higher than for a single PWAS, and thus it may still be more economical to use wired PWASs, if possible.

The artificial defects in the test plates used were relatively large. Generally, the purpose of the SHM system is to detect defects which are not visible to the naked eye, e.g. cracks initiating at a critical point of a structure, or delaminations in composite structures. Capability of guided waves to detect these hidden defects depends on their wavelength, which in its turn depends on the frequency-thickness product of a structure and is different for each Lamb wave mode. Increasing frequency results in shorter wavelengths but it possibly also increases the number of different wave modes in the structures. The more there are modes in the structure, superposing with each other, the more complicated the analysis becomes. This problem can be avoided by using only the first wave mode burst arriving at the sensor directly from the actuator. Experiments with the aluminium test beam shown in Figure 4 showed that even invisible cracks can be detected using the burst variance based detection and location method.

The question of long term reproducibility of the responses, i.e. the variations in results that do not originate from changes in the monitored structure but e.g. from changes in the PWAS contact to the structure, requires more research in the future. Another issue is the requirement of storing reference data from a healthy structure for SHM. In an ideal system, there would be no need for stored reference data. The defects could be detected e.g. by comparing the responses measured successively from two separate but physically identical signal paths. This would remove e.g. the problem of temperature effects on responses. However, implementing such paths with PWASs is difficult, because the PWAS responses are different if the PWASs do not have identical contact with the structure. Ensuring the identical contact of all the PWASs with the surface in a large scale application, especially when the PWASs are embedded in the structure, is extremely difficult.

To conclude, despite the promising results obtained in the measurement system development project and this thesis, more research is needed and the developed measurement system prototype can be further improved in several ways:

- The ongoing development in electronic components makes it possible to implement the system with even better energy efficiency.
- The PWAS response peak detection accuracy can be improved by giving up the constant frequency assumption, triggering the peak detection both at the rising and falling edges of the response, and using max/min circuits instead of picking a sample of the response at an estimated time instant for the local peak.
- The battery charging efficiency of the energy harvesting module can be increased, and also other energy sources than vibration can be utilized.
- The defect detection could be implemented as a built-in function of a smart sensor node.
- The defect detection algorithm can be further improved to remove the tendency for the global probability maximum to be located at one of the PWASs.
- Feasibility of wireless actuation and sensing of the PWASs could be studied.

Bibliography

[Ace2009] http://www.acellent.com/ (11.5.2009)

[Ach1975] Achenbach, J.D. (1975): *Wave propagation in elastic solids*. Elsevier, 425 p.

[Adh2009] Adhikari, S., Friswell, M.I. and Inman, D.J. (2009): ”Piezoelectric energy harvesting from broadband random vibrations.” *Smart Mater. Struct.* 18, 7 pp.

[Ale1987] Alers, G. A., and Burns, L. R. (1987). “EMAT Designs for Special Applications”. *Materials Evaluation*, 45(10), pp. 1184-1194.

[All1992] Alleyne, D.N., Cawley, P. (1992): “Interaction of Lamb waves with defects.” *IEEE Trans Ultrason Ferroelectr Freq Control*. 39(3), pp. 381-387.

[Ant2008] Anton, S.R. (2008): *Baseline-Free and Self-Powered Structural Health Monitoring*. M. Sc. Thesis. Department of Mechanical Engineering, Virginia Polytechnic Institute and State University, Virginia, 154 p.

[APC2009] http://www.americanpiezo.com/materials/apc_properties.html, (14.5.2009)

[Arn1986] Arnold, J.M., and Felsen, L.B. (1986): “Coupled mode theory of intrinsic modes in a wedge.” *J. Acoust. Soc. Am.* 79(1), pp. 31-40.

[Ban2007] Banerjee, S., Ricci, F., Monaco, E., Lecce, L., and Mal, A. (2007): ”Autonomous Impact Damage Monitoring in a Stiffened Composite Panel.” *Journal of Intelligent Material Systems and Structures*, 18, pp. 623-633.

[Ban2009] Banerjee, S., Ricci, F., Monaco, E., and Mal, A. (2009): ”A wave propagation and vibration-based approach for damage indentification in structural composites.” *Journal of Sound and Vibration*, 322, pp. 167-183.

[Ben1986] Bendat, J. and Piersol, A. (1986): *Random data. Analysis and measurement procedures*, 2nd ed. John Wiley & Sons, 566 p.

[Bie2001] Biemans, C., Staszewski, W.J., Boller, C., and Tomlinson, G.R. (2001): “Crack Detection in Metallic Structures Using Broadband Excitation of Acousto-Ultrasonics.” *Journal of Intelligent Material Systems and Structures*, 12, pp. 589-597.

[Cha1996] Challis, R. E., Bork, U., and Todd, P. C. D. (1996): "Ultrasonic NDE of Adhered T-joints Using Lamb Waves and Intelligent Signal Processing". *Ultrasonics*, 34(2-5), pp. 455-459.

[Cha1999] Chang, Z. and Mal, A. (1999): "Scattering of Lamb waves from a rivet hole with edge cracks." *Mechanics of Materials* 31, pp. 197-204.

[Cha2003] Chang, P. C., Flatau, A. and Liu, S.C. (2003): "Review Paper: Health Monitoring of Civil Infrastructure." *Structural Health Monitoring,* 2(3), pp. 257-267.

[Cho1996] Cho, Y., and Rose, J.L. (1996): "A boundary element solution for a mode conversion study on the edge reflection of Lamb waves." *J. Acoust. Soc. Am.* 99(4), pp. 2097-2109.

[Chr2005] Christensen, R.M. (2005): *Mechanics of Composite Materials*. Revised edition, Dover, 348 p.

[Cia2008] Ciang, C.C., Lee J.-R., and Bang, H.-J. (2008): "Structural health monitoring for a wind turbine system: a review of damage detection methods." *Meas. Sci. Technol.* 19 122001, 20 p. (doi:10.1088/0957-0233/19/12/12200)

[Dau1992] Daubechies, I. (1992): *Ten lectures on wavelets*. SIAM, Philadelphia.

[Deg1996] Degerketin, F. L., and Khuri-Yakub, B. T. (1996): "Single Mode Lamb Wave Excitation in Thin Plates by Hertzian Contacts". *Applied Physics Letters*, 69(2), pp. 146-148.

[Elk2004] El-Kettani, M.E., Luppé, F., and Guillet, A. (2004): "Guided waves in a plate with linearly varying thickness: experimental and numerical results." Ultrasonics 42(1-9), pp. 807-812.

[Flo2006] Flores-López, M.A. and Gregory, R.D. (2006): "Scattering of Rayleigh-Lamb waves by a surface breaking crack in an elastic plate." *J. Acoust. Soc. Am.* 119(4), pp. 2041-1049.

[Fri1980] Fritsch, F.N., and Carlson, R.E. (1980): "Monotone Piecewise Cubic Interpolation." *SIAM J. Numer. Anal*. Vol. 17, No. 2, pp. 238-246.

[Fri2008] Fritzen, C.-P., Kraemer, P., and Klinkov, M. (2008): "Structural health monitoring of offshore wind energy plants." *Proceedings of 4th European Workshop on Structural Health Monitoring*. Edited by T. Uhl, W. Ostachowitcz, J. Holnicki-Szulc. DEStech Publications, pp. 3-20.

[Fro2002] Fromme, P. and Sayir, M.B. (2002); “Measurement of the scattering of a Lamb wave by a through hole in a plate.” *J. Acoust. Soc. Am.* 111(3), pp. 1165-1170.

[GaG2009] http://www.gage-applied.com/, referred 18.11.2009

[Gal1998] Galanenko, V.B. (1998): “On coupled modes theory of two-dimensional wave motion in elastic wave guides with slowly varying parameters in curvilinear orthogonal coordinates.” *J. Acoust. Soc. Am.* 103(4), pp. 1752-1762.

[Giu2002a] Giurgiutiu, V. (2002): “Lamb Wave Generation with Piezoelectric Wafer Active Sensors for Structural Health Monitoring.” *SPIE's 10th Annual International Symposium on Smart Structures and Materials and 8th Annual International Symposium on NDE for Health Monitoring and Diagnostics*, CA, USA. Paper # 5056-17.

[Giu2002b] Giurgiutiu, V. and Bao, J. (2002): “Embedded Ultrasonic Structural Radar for the Nondestructive Evaluation of Thin-Wall Structures,” In: *Proceedings of the 2002 ASME International Mechanical Engineering Congress*, November 17-22, 2002, New Orleans, LA, Paper # IMECE2002-39017.

[Giu2003] Giurgiutiu, V. (2003): “Embedded Ultrasonics NDE with Piezoelectric Wafer Active Sensors.” *Instrumentation, Mesure, Metrologie*, Lavoisier Pub., Paris, France, RS series 12M, 3(3-4), pp. 149-180.

[Giu2005] Giurgiutiu, V. (2005): “Tuned Lamb Wave Excitation and Detection with Piezoelectric Wafer Active Sensors for Structural Health Monitoring.” *Journal of Intelligent Material Systems and Structures*, Vol. 16, pp. 291-305.

[Giu2008a] Giurgiutiu, V. (2008): *Structural health monitoring with piezoelectric wafer active sensors*, Academic Press (Elsevier), 747 p.

[Giu2008b] Giurgiutiu, V. (2008): “Structural health monitoring and NDE – an Air Force Office of Scientific Research structural health mechanics program perspective.” *Proceedings of 4th European Workshop on Structural Health Monitoring*. Edited by T. Uhl, W. Ostachowitcz, J. Holnicki-Szulc. DEStech Publications, pp. 35-42

[Gol1996] Golub, G.H. and Van Loan, C.F. (1996): *Matrix computations* (3rd ed.). The Johns Hopkins University Press, Baltimore, 694 p.

[Gos2007] Goswami, D.Y. and Kreith, F. (eds.) (2007): *Energy conversion*, CRC Press, pp. 20-1 – 20-2.

[Gre2005] Greve, D.W., Neumann, J.J., Nieuwenhuis, J.H., Oppenheim, I.J., and Tyson, N.L. (2005): "Use of Lamb Waves to Monitor Plates: Experiments and Simulations." Smart Structures and Materials 2005: Sensors and Smart Structures Technologies for Civil, Mechanical, and Aerospace Systems. Edited by Tomizuka, Masayoshi. *Proceedings of the SPIE*, Volume 5765, pp. 281-292.

[Gri2001] Gribonval, R. (2001): "Fast Matching Pursuit With a Multiscale Dictionary of Gaussian Chirps". *IEEE Transactions on Signal Processing*, 49(5), pp. 994-1001.

[Her2005] Herzberg, I., Li, H.C.H., Dharmawan, F., Mouritz, A.P., Nguyen, M. and Bayandor, J. (2005): "Damage assessment and monitoring of composite ship joints", *Composite Structures* 67(2), pp. 205-216.

[Hla1991] Hlawatsch, F. (1991): "Time-frequency methods for signal processing." Technical Report 1291-0001, Dept of Electrical Engineering, University of Rhode Island.

[Hyt2008] Hytti, H. (2008): "Efficient signal reconstruction and analysis for integrated SHM System." *Proceedings of 4th European Workshop on Structural Health Monitoring*. Edited by T. Uhl, W. Ostachowitcz, J. Holnicki-Szulc. DEStech Publications, pp. 316-323.

[Ihn2004] Ihn, J-B., and Chang, F-K. (2004): "Detection and monitoring of hidden fatigue crack growth using a built-in piezoelectric sensor/actuator network: I. Diagnostics." *Smart Mater. Struct.* 13, pp. 609-620.

[IUP1997] McNaught, A.D. and Wilkinson, A. (eds.) (1997): *IUPAC Compendium of Chemical Terminology. The Gold Book*, Second Edition, Blackwell Science, 464 p.

[Jol2002] Jolliffe, I. T. (2002): *Principal Component Analysis. Second edition.* Springer-Verlag.

[Jon1975] Jones, R.M. (1975): *Mechanics of composite materials*. Hemisphere, New York, 355 p.

[Kaw2006] Kaw, A.K. (2006): *Mechanics of Composite Materials, 2nd edition*, CRC Press, 457 p.

[Kel2010] Kelzenberg, M.D., Boettcher, S.W., Petykiewicz, J.A., Turner-Evans, D.B., Putnam, M.C., Warren, E.L., Spurgeon, J.M., Briggs, R.M., Lewis, N.S. and Atwater, H.A. (2010); "Enhanced absorption and carrier collection in Si wire arrays for photovoltaic applications." *Nature Materials* 9, pp. 239 – 244.

[Kid2002] Kiddy, J., Baldwin, C., Salter, T. and Chen, P. (2002): "Structural load monitoring of RV Triton using Fiber Optic Sensors," *Proceedings: Smart Structures and Materials: Industrial and Commercial Applications of Smart Structures Technologies*, SPIE Vol. 4698, pp. 462-472.

[Kol2002] Kolecki, J.C. (2002): "An Introduction to Tensors for Students of Physics and Engineering", *NASA /TM*-2002-211716.

[Kun2004] Kundu, T. (2004): Ultrasonic Nondestructive Evaluation: Engineering and Biological Material Characterization. CRC Press, 872 p.

[Lal2008] Lallart, M., Guyomar, D., Jayet, Y., Petit, L., Lefeuvre, E., Monnier, T., Guy, P., and Richard, C. (2008) : "Synchronized switch harvesting applied to self-powered smart systems: Piezoactive microgenerators for autonomous wireless receivers." *Sensors and Actuators A: Physical* 147, pp. 263-272.

[Lam1917] Lamb, H. (1917): "On waves in an elastic plate." *Proc. Roy. Soc. (London)*, Ser. A, 93, p. 114.

[Lan2007] Lanza di Scalea, F., Matt, H., and Bartoli, I. (2007) : "The response of rectangular piezoelectric sensors to Rayleigh and Lamb ultrasonic waves", *J. Acoust. Soc. Am.* 121(1), pp. 175-187.

[Lee2003] Lee, B.C., and Staszewski, W.J. (2003): "Modelling of Lamb waves for damage detection in metallic structures: Part II. Wave interactions with damage." *Smart Mater. Struct.* 12, pp. 815-824.

[Lee2007a] Lee, B.C., and Staszewski, W.J. (2007): "Lamb wave propagation modelling for damage detection: I. Two-dimensional analysis", *Smart Mater. Struct.* 16, pp. 249-259.

[Lee2007b] Lee, B.C., and Staszewski, W.J. (2007): "Lamb wave propagation modelling for damage detection: II. Damage monitoring strategy." *Smart Mater. Struct.* 16, pp. 260-274.

[Leg2001] Legendre, S., Massicotte, D., Goyette, J., and Bose, T. K. (2001): “Neural Classification of Lamb Wave Ultrasonic Weld Testing Signals Using Wavelet Coefficients”. *IEEE Transactions on Instrumentation and Measurement*, 50(3), pp. 672-678.

[Lew2007] Lewis, N.S. (2007): “Toward Cost-Effective Solar energy Use.” *Nature* 315, pp. 798-801.

[Lu2006] Lu, Y., Ye, L., and Su, Z. (2006): “Crack identification in aluminium plates using Lamb wave signals of a PZT sensor network.” *Smart. Mater. Struct.* 15, pp. 839-849.

[Mal1993] Mallat, S.G. and Zhang, Z. (1993): “Matching Pursuits With Time-Frequency Dictionaries.” *IEEE Trans. Sig. Proc.* Vol 41, No 12, pp. 3397-3415.

[Mal2005] Mal, A., Ricci, F., Banerjee, S. and Shih, F. (2005): “An Conceptual Structural Health Monitoring System based on Vibration and Wave Propagation.” *Structural Health Monitoring* 4(3), pp. 283-293.

[Mal2009] Mal, A., Banerjee, S. and Ricci, F. (2009): “An automated damage identification technique based on vibration and wave propagation data.” *Phil. Trans. R. Soc. A* 365, pp. 479-491.

[Mas2006] Masry, E. (2006): “Random Sampling of Deterministic Signals: Statistical Analysis of Fourier Transform Estimates.” *IEEE Trans. Sig. Proc.* Vol 54, No 5, pp. 1750-1761.

[Mas2009] Masry, E. and Vadrevu, A. (2009): “Random Sampling Estimates of Fourier Transforms: Antithetical Stratified Monte Carlo.” *IEEE Trans. Sig. Proc.* Vol 57, No 1, pp. 194-204.

[Mat2009] www.mathworks.com, referred 30.11.2009

[McK1999] McKeon, J.C.P., and Hinders, M.K. (1999): “Lamb wave scattering from a through hole.” Journal of Sound and Vibration 224(5), pp. 843-862.

[MIL2003] MIL-HDBK-5J. Department of Defense Handbook: Metallic materials and elements for aerospace vehicle structures. Department of Defense, USA, January 2003.

[Mon2000] Monaco, E., Franco, F. and Lecce, L. (2000): "Experimental and Numerical Activities on Damage Detection Using Magnetostrictive Actuators and Statistical Analysis." *Journal of Intelligent Material Systems and Structures*, Vol. 11, No. 7, pp. 567-578.

[Muf2008] Mufti, A. and Neale, K. (2008): “State-of-the Art of FRP and SHM Applications in Bridge Structures in Canada”. *Composites Research Journal* 2(2), pp. 60-69.

[Muj2008] Mujica, L.E., Rodellar, J., Güemes, A., and López-Diez, J. (2008): “PCA based measures: Q-statistics and T2-statistics for assessing damages in structures”. *Proceedings of 4th European Workshop on Structural Health Monitoring*. Edited by T. Uhl, W. Ostachowitcz, J. Holnicki-Szulc. DEStech Publications, pp. 1088-1095.

[Muu2008] Muukkonen, T., Hytti, H., Huovila, H., Känsälä, K., and Lehtonen, M. (2008): “Adaptable integrated SHM system for metallic and composite structures.” *Proceedings of 4th European Workshop on Structural Health Monitoring*. Edited by T. Uhl, W. Ostachowitcz, J. Holnicki-Szulc. DEStech Publications, pp. 349-356.

[Nan2006] Nanotron nanoNET TRX Transceiver (NA1TR8) datasheet version 2.08.

[Nay1995] Nayfeh, A.H. (1995): *Wave Propagation in Layered Anisotropic Media: with Applications to Composites*, Elsevier Science, North-Holland Series in Applied Mathematics and Mechanics, Volume 39, 332 p.

[Ng2009] Ng, C.T. and Veidt, M. (2009): “A Lamb-wave-based technique for damage detection in composite laminates.” *Smart Mater. Struct.* 18, 074006, 12 p.

[Nie2005] Nieuwenhuis, J., Neumann J Jr., Greve D., and Oppenheim I. (2005): “Generation and detection of guided waves using PZT wafer transducers.” *IEEE Trans Ultrason Ferroelectr Freq Control*. 52(11), pp. 2103-2111.

[O’Ne1998] O’Neill, J.C., and Flandrin, P. (1998): “Chirp hunting.” In: *Proceedings of the IEEE-SP International Symposium on Time-Frequency and Time-Scale Analysis*, 6-9 Oct., pp. 425 – 428.

[Opp1989] Oppenheim, A.W., and Schafer, R.W. (1989): *Discrete-Time Signal processing*, Prentice-Hall, 879 p.

[Pel1996] Pelts, S.P., and Rose, J.L. (1996): “Source influence parameters on elastic guided waves in an orthotropic plate.” *J. Acoust. Soc. Am*. (99)4, pp. 2124-2129.

[Pel1996] Pelts, S. P., Jiao, D., and Rose, J. L. (1996): “A Comb Transducer for Guided Wave Generation and Mode Selection”. Proceedings of the IEEE Ultrasonics Symposium, Vol. 2, San Antonio, TX, pp. 857- 860.

[Pie1998] Pierce, S. G., and Culshaw, B. (1998): "Laser Generation of Ultrasonic Lamb Waves Using Low Power Optical Sources". *IEE Proceedings: Science, Measurement and Technology*, 145(5), pp. 244-249.

[Pra2003] Prasad, M. S., Kumar, V. R., Balasubramaniam, K., and KrishnaMoorthy, C. V. (2003). "Imaging of Defects in Composite Structures Using Guided Ultrasonics". *Proceedings of the SPIE*, 5062, pp. 700-703.

[Pri1981] Priestley, M.B. (1981): *Spectral Analysis and time Series*, London: Academic Press Ltd., pp. 504-510.

[Pri2009] Priya, S. and Inman, D.J. (eds.) (2009): *Energy Harvesting Technologies*. Springer US (doi: 10.1007/978-0-387-76464-1).

[Pur2004] Purekar, A.S., Pines, D.J., Sundararaman, S., and Adams, D.E. (2004): "Directional piezoelectric phased array filters for detecting damage in isotropic plates." *Smart Mater. Struct.* 13, pp. 838-850.

[Pur2007] Puri Andrews, J. (2007): *Lamb wave propagation in varying thermal environments*. M. Sc. Thesis. Department of Aeronautical and Astronautical Engineering, Air Force Institute of Technology, Wright-Patterson Air Force Base, Ohio, 184 p.

[Qia1994] Qian, S., and Chen, D. (1994): "Signal Representation Via Adaptive Normalized Gaussian Functions", *Signal Processing*, 36(1), pp. 1-11.

[Qia1996] Qian, S., and Chen, D. (1996): *Joint Time-Frequency Analysis. Methods and Applications*, Prentice-Hall PTR, 302 p.

[Rag2004] Raghavan, A., and Cesnik, C. E. S. (2004): "Modeling of piezoelectric-based Lamb-wave generation and sensing for structural health monitoring." *Smart Structures and Materials 2004: Sensors and Smart Structures Technologies for Civil, Mechanical, and Aerospace Systems, Shih-Chi Liu, Editor, Proc. of SPIE*, Vol. 5391 (SPIE, Bellingham, WA, 2004), pp. 419-430.

[Rag2007a] Raghavan, A., and Cesnik, C.E.S. (2007): "Guided-wave signal processing using chirplet matching pursuits and mode correlation for structural health monitoring." *Smart Mater. Struct.* 16, pp. 355-366.

[Rag2007b] Raghavan, A., and Cesnik, C.E.S. (2007): "Review of Guided-wave Structural Health Monitoring", *The Shock and Vibration Digest*, Vol. 39, No. 2, pp. 91-114.

[Ray1885] Lord Rayleigh (1885): "On waves propagated along the plane surfaces of an elastic solid." *Proc. London Math. Soc.*, 17, pp. 4-11.

[Roh1999] Roh, Y.S. and Chang, F.-K. (1999): "Built in diagnostics for identifying an anomaly in plates using wave scattering". *PhD Dissertation,* Department of Aeronautics and Astronautics, Stanford University.

[Ros1999] Rose, J.L. (1999): *Ultrasonic Waves in Solid Media*. Cambridge University Press, Cambridge, 454 p.

[Sch1942] Scholte, J.G. (1942): "On the Stonely wave equation". *Proc. Kon. Noderl. Akad. Wetensch*, 45, pp. 159-164.

[Sta2004] Staszewski, W., Boller, C., and Tomlinson, G. (eds) (2004): *Health Monitoring of Aerospace Structures. Smart Sensor Technologies and Signal Processing.* John Wiley & Sons, Ltd, 266 p. (pp. 163-206)

[Sto1924] Stonely, R. (1924): "Elastic waves at the surface of separation of two solids". *Proc. R. Soc. London*, 106, pp. 416-428.

[Su2004] Su, Z., and Ye, L. (2004): "An Intelligent Signal Processing and Pattern Recognition Technique for Defect Identification Using an Active Sensor Network". *Smart Materials and Structures*, 13(4), pp. 957-969.

[Su2005] Su, Z., and Ye, L. (2005): "A fast damage locating approach using digital damage fingerprints extracted from Lamb wave signals." *Smart Materials and Structures*, 14(5), pp. 1047-1054.

[TFD1999] http://tfd.sourceforge.net/, referred 18.11.2009

[TFT2008] http://tftb.nongnu.org/, referred 18.11.2009

[Vik1967] Viktorov, I. (1967): *Rayleigh and Lamb Waves: Physical Theory and Applications*. Plenum Press, New York, 154 p.

[Vil1948] Ville, J. (1948): "Thovrie et applications de la notion de signal analylique", (in French). *Câbles et Transmission*, vol. 2, pp. 61-74.

[Wan2007] Wang, L. and Yuan, F. (2007): "Group velocity and characteristic wave curves of Lamb waves in composites: Modeling and experiments." *Composite Science and Technology* 67, pp. 1370-1384.

[Wig1932] Wigner, E.P. (1932): "On the Quantum Correction for Thermodynamic Equilibrium", *Phys. Rev.*, vol. 40, p. 749.

[Wil2001] Wilcox, P. D., Lowe, M. J. S., and Cawley, P. (2001). "Mode and Transducer Selection for Long Range Lamb Wave Inspection". *Journal of Intelligent Material Systems and Structures*, 12(8), pp. 553-565.

[Yan2005] Yang, M., and Qiao, P. (2005) : "Modeling and experimental detection of damage in various materials using the pulse-echo method and piezoelectric sensors/actuators." *Smart. Mater. Struct.* 14, pp. 1083-1100.

[Yu2005] Yu, L., and Giurgiutiu, V. (2005): "Advanced signal processing for enhanced damage detection with piezoelectric wafer active sensors." *Smart Structures and Systems* (1)2, pp. 185-215.

[Zha2004] Zhao, X., Kwan, C., Xu, R., Qian, T., Hay, T., Rose, J. L., Raju, B. B., Maier, R., and Hexemer, R. (2004): "Non-destructive Inspection of Metal Matrix Composites Using Guided Waves". *Review of Quantitative Nondestructive Evaluation*, Vol. 23, D. O. Thompson and D. E. Chimenti, eds, American Institute of Physics, Melville, NY, pp. 914-920.

[Zha2007a] Zhao, X., Gao, H., Zhang, G., Ayhan, B., Yan, F., Kwan, C. and Rose, J. L. (2007): "Active health monitoring of an aircraft wing with embedded piezoelectric sensor/actuator network: I. Defect detection, localization and growth monitoring." *Smart Mater. Struct.* 16, pp. 1208-1217.

[Zha2007b] Zhao, X., Gao, H., Zhang, G., Ayhan, B., Yan, F., Kwan, C. and Rose, J. L. (2007): "Active health monitoring of an aircraft wing with embedded piezoelectric sensor/actuator network: II. Wireless approaches." *Smart Mater. Struct.* 16, pp. 1218-1225.

[Zhu1998] Zhu, W., Rose, J. L., Barshinger, J. N., and Agarwala, V. S. (1998): "Ultrasonic Guided Wave NDT for Hidden Corrosion Detection". *Research in Nondestructive Evaluation*, 10(4), pp. 205-225.

[Zhu2008] Zhu, M., Reid, A., Finney, S., and Judd, M. (2008): "Energy Scavenging Technique for Powering Wireless Sensors." *International Conference on Condition Monitoring and Diagnosis* (CMD 2008), Beijing, China.

[Zhu2009] Zhu, M., Baker, P.C., Roscoe, N.M., Judd, M.D. and Fitch, J. (2009): "Alternative Power Sources for Autonomous Sensors in High Voltage Plant." *IEEE Electrical Insulation Conference*, Montreal, QC, Canada.